



An International ICT Journal
Featuring Industry-University-Institute Cooperation and
Indexed in Scopus

ISSN 1673-5188
CN 34-1294/TN

ZTE COMMUNICATIONS

中兴通讯技术(英文版)

<http://zte.magtechjournal.com>

September 2024, Vol. 22 No. 3

Special Topic: Integrated Sensing and Communication (ISAC) Technologies for Future Wireless Communication



(See Fig. 3 on P. 44)

ISSN 1673-5188



The 10th Editorial Board of ZTE Communications

Chairman GAO Wen, Peking University (China)
Vice Chairmen XU Ziyang, ZTE Corporation (China) | XU Chengzhong, University of Macau (China)

Members (Surname in Alphabetical Order)

AI Bo	Beijing Jiaotong University (China)
CAO Jiannong	The Hong Kong Polytechnic University (China)
CHEN Chang Wen	The Hong Kong Polytechnic University (China)
CHEN Yan	Northwestern University (USA)
CHI Nan	Fudan University (China)
CUI Shuguang	UC Davis (USA) and The Chinese University of Hong Kong, Shenzhen (China)
GAO Wen	Peking University (China)
GAO Yang	Nanjing University (China)
GAO Yue	Fudan University (China)
GE Xiaohu	Huazhong University of Science and Technology (China)
HE Yejun	Shenzhen University (China)
Victor C. M. LEUNG	The University of British Columbia (Canada)
LI Xiangyang	University of Science and Technology of China (China)
LI Zixue	ZTE Corporation (China)
LIAO Yong	Chongqing University (China)
LIN Xiaodong	ZTE Corporation (China)
LIU Chi	Beijing Institute of Technology (China)
LIU Jian	ZTE Corporation (China)
LIU Yue	Beijing Institute of Technology (China)
MA Jianhua	Hosei University (Japan)
MA Zheng	Southwest Jiaotong University (China)
PAN Yi	Shenzhen University of Advanced Technology, Chinese Academy of Sciences (China)
PENG Mugen	Beijing University of Posts and Telecommunications (China)
REN Fuji	Tokushima University (Japan)
REN Kui	Zhejiang University (China)
SHENG Min	Xidian University (China)
SU Zhou	Xi'an Jiaotong University (China)
SUN Huifang	Pengcheng Laboratory (China)
SUN Zhili	University of Surrey (UK)
TAO Meixia	Shanghai Jiao Tong University (China)
WANG Chengxiang	Southeast University (China)
WANG Haiming	Southeast University (China)
WANG Xiang	ZTE Corporation (China)
WANG Xiyu	ZTE Corporation (China)
WANG Yongjin	Nanjing University of Posts and Telecommunications (China)
XU Chengzhong	University of Macau (China)
XU Ziyang	ZTE Corporation (China)
YANG Kun	University of Essex (UK)
YU Hongfang	University of Electronic Science and Technology of China (China)
YUAN Jinhong	University of New South Wales (Australia)
ZENG Wenjun	Eastern Institute of Technology, Ningbo (China)
ZHANG Honggang	Zhejiang Lab (China)
ZHANG Jianhua	Beijing University of Posts and Telecommunications (China)
ZHANG Rui	The Chinese University of Hong Kong, Shenzhen (China)
ZHANG Wenqiang	Fudan University (China)
ZHANG Yueping	Nanyang Technological University (Singapore)
ZHOU Wanlei	City University of Macau (China)
ZHUANG Weihua	University of Waterloo (Canada)

CONGRATULATIONS



ZTE Communications
has been indexed in
Scopus

More information about the journal



Website



Submission guidelines

Special Topic ▶

Integrated Sensing and Communication (ISAC) Technologies for Future Wireless Communication

- 01 Guest Editorial YUAN Jinhong, FEI Zesong, WEI Zhiqiang
- 04 Kullback-Leibler Divergence Based ISAC Constellation and Beamforming Design in the Presence of Clutter TANG Shuntian, WANG Xinyi, XIA Fanghao, FEI Zesong
- 13 Joint Beamforming Design for Dual-Functional Radar-Communication Systems Under Beamforming Gain Constraints CHEN Guangyi, ZHANG Ruoyu, REN Hong, LIN Xu, WU Wen
- 21 On Normalized Least Mean Square Based Interference Cancellation Algorithm for Integrated Sensing and Communication Systems YU Xiaohui, YU Shucheng, LIU Xiqing, PENG Mugen
- 29 Trajectory Tracking for MmWave Communication Systems via Cooperative Passive Sensing YU Chao, LYU Bojie, QIU Haoyu, WANG Rui
- 37 Integrated Sensing and Communication: Who Benefits More? DU Ruolin, WEI Zhiqiang, YANG Zai
- 48 Low-Complexity Integrated Super-Resolution Sensing and Communication with Signal Decimation and Ambiguity Removal DAI Qianglong, ZHOU Zhiwen, XIAO Zhiqiang, ZENG Yong, YANG Fei, CHEN Yan
- 56 Tensor Decomposition-Based Channel Estimation and Sensing for Millimeter Wave MIMO-OFDM V2I Systems WANG Jilin, ZENG Xianlong, YANG Yonghui, PENG Lin, LI Lingxiang
- 69 Sensing and Communication Integrated Fast Neighbor Discovery for UAV Networks WEI Zhiqing, ZHANG Yongji, JI Danna, LI Chenfei
- 83 A Survey on Task Scheduling of CPU-GPU Heterogeneous Cluster ZHOU Yiheng, ZENG Wei, ZHENG Qingfang, LIU Zhilong, CHEN Jianping
- 91 Multi-View Image-Based 3D Reconstruction in Indoor Scenes: A Survey LU Ping, SHI Wenzhe, QIAO Xiuquan
- 99 Intelligence Driven Wireless Networks in 5G and 6G Era: A Survey GAO Yin, CHEN Jiajun, LI Dapeng
- 106 Secure SSL/TLS Communication System Based on Quantum Keys WANG Jigang, LU Yuqian, WEI Liping, JIANG Xinzao, ZHANG Han
- 116 Differential Spatial Modulation Mapping Algorithms WANG Chanfei, CHAI Jianxin, XU Yamei

Review ▶

Research Papers ▶

Serial parameters: CN 34-1294/TN*2003*q*16*122*en*P*¥20.00*2200*14*2024-09

Submission of a manuscript implies that the submitted work has not been published before (except as part of a thesis or lecture note or report or in the form of an abstract); that it is not under consideration for publication elsewhere; that its publication has been approved by all co-authors as well as by the authorities at the institute where the work has been carried out; that, if and when the manuscript is accepted for publication, the authors hand over the transferable copyrights of the accepted manuscript to *ZTE Communications*; and that the manuscript or parts thereof will not be published elsewhere in any language without the consent of the copyright holder. Copyrights include, without spatial or timely limitation, the mechanical, electronic and visual reproduction and distribution; electronic storage and retrieval; and all other forms of electronic publication or any other types of publication including all subsidiary rights.

Responsibility for content rests on authors of signed articles and not on the editorial board of *ZTE Communications* or its sponsors.

Statement

This magazine is a free publication for you. If you do not want to receive it in the future, you can send the "TD unsubscribe" mail to magazine@zte.com.cn. We will not send you this magazine again after receiving your email. Thank you for your support.

ZTE Communications Guidelines for Authors

Remit of Journal

ZTE Communications publishes original theoretical papers, research findings, and surveys on a broad range of communications topics, including communications and information system design, optical fiber and electro-optical engineering, microwave technology, radio wave propagation, antenna engineering, electromagnetics, signal and image processing, and power engineering. The journal is designed to be an integrated forum for university academics and industry researchers from around the world.

Manuscript Preparation

Manuscripts must be typed in English and submitted electronically in MS Word (or compatible) format. The word length is approximately 3 000 to 8 000, and no more than 8 figures or tables should be included. Authors are requested to submit mathematical material and graphics in an editable format.

Abstract and Keywords

Each manuscript must include an abstract of approximately 150 words written as a single paragraph. The abstract should not include mathematics or references and should not be repeated verbatim in the introduction. The abstract should be a self-contained overview of the aims, methods, experimental results, and significance of research outlined in the paper. Three to eight carefully chosen keywords must be provided with the abstract.

References

Manuscripts must be referenced at a level that conforms to international academic standards. All references must be numbered sequentially in-text and listed in corresponding order at the end of the paper. References that are not cited in-text should not be included in the reference list. References must be complete and formatted according to *ZTE Communications* Editorial Style. A minimum of 10 references should be provided. Footnotes should be avoided or kept to a minimum.

Copyright and Declaration

Authors are responsible for obtaining permission to reproduce any material for which they do not hold copyright. Permission to reproduce any part of this publication for commercial use must be obtained in advance from the editorial office of *ZTE Communications*. Authors agree that a) the manuscript is a product of research conducted by themselves and the stated co-authors; b) the manuscript has not been published elsewhere in its submitted form; c) the manuscript is not currently being considered for publication elsewhere. If the paper is an adaptation of a speech or presentation, acknowledgement of this is required within the paper. The number of co-authors should not exceed five.

Content and Structure

ZTE Communications seeks to publish original content that may build on existing literature in any field of communications. Authors should not dedicate a disproportionate amount of a paper to fundamental background, historical overviews, or chronologies that may be sufficiently dealt with by references. Authors are also requested to avoid the overuse of bullet points when structuring papers. The conclusion should include a commentary on the significance/future implications of the research as well as an overview of the material presented.

Peer Review and Editing

All manuscripts will be subject to a two-stage anonymous peer review as well as copyediting, and formatting. Authors may be asked to revise parts of a manuscript prior to publication.

Biographical Information

All authors are requested to provide a brief biography (approx. 100 words) that includes email address, educational background, career experience, research interests, awards, and publications.

Acknowledgements and Funding

A manuscript based on funded research must clearly state the program name, funding body, and grant number. Individuals who contributed to the manuscript should be acknowledged in a brief statement.

Address for Submission

<http://mc03.manuscriptcentral.com/ztecom>



Guest Editorial >>>

Special Topic on Integrated Sensing and Communication (ISAC) Technologies for Future Wireless Communication

Guest Editors


 YUAN Jinhong

 FEI Zesong

 WEI Zhiqiang

The radio communication division of the International Telecommunication Union (ITU-R) has recently adopted Integrated Sensing and Communication (ISAC) as a key usage scenario for IMT-2030/6G. The synergy of these two functionalities can facilitate a wide array of applications such as autonomous driving, smart cities, and industrial automation, where simultaneous data transmission and environmental sensing are crucial. The rationale of the ISAC is that a radio emission can simultaneously convey communication data from the transmitter to the receiver and extract environmental information from the scattered echoes. From a research perspective, ISAC opens new avenues for innovation in signal processing, hardware design, and network architecture, facilitating efficient utilization of system spectrum/power/hardware resources and pursuit of mutual benefits. It is anticipated that ISAC can improve spectral efficiency, reduce hardware costs, and enhance overall system capabilities. Despite the promising advantages above, ISAC imposes unique technical challenges on future wireless communications, including the dual-functional signaling strat-

egy, the low-complexity sensing and communication reception technique, the potential resource management and protocols tailored for the ISAC network, the information-theoretic limits of ISAC, etc.

The call-for-paper of this special issue has attracted high-quality submissions. After two-round reviews, eight papers are presented to address some of the aforementioned challenges, and innovative solutions to facilitating the ISAC technology are proposed. These papers cover a wide range of topics, including the signaling design, resource allocation design, and reception algorithm design.

The first paper titled “Kullback-Leibler Divergence Based ISAC Constellation and Beamforming Design in the Presence of Clutter” presents a novel approach to constellation and beamforming design for ISAC systems in the presence of clutter, employing the Kullback-Leibler divergence (KLD) as the unified ISAC performance metric. The constellation design problem is solved via the successive convex approximation (SCA) technique, while the optimal beamforming in terms of sensing KLD is proven to be equivalent to maximizing the signal-to-interference-plus-noise ratio (SINR) of echo signals. The proposed scheme achieves significant clutter suppression and higher SINR of echo signals compared with the conventional schemes.

The second paper titled “Joint Beamforming Design for Dual-Functional Radar-Communication Systems Under Beampattern Gain Constraints” proposes a joint beamforming design to maximize the sum rate of multi-user communication while ensuring the beampattern gain at specific sensing

DOI: 10.12142/ZTECOM.202403001

Citation (Format 1): YUAN J H, FEI Z S, WEI Z Q. Integrated sensing and communication (ISAC) technologies for future wireless communication [J]. *ZTE Communications*, 2024, 22(3): 1 – 3. DOI: 10.12142/ZTECOM.202403001Citation (Format 2): J. H. Yuan, Z. S. Fei, and Z. Q. Wei, “Integrated sensing and communication (ISAC) technologies for future wireless communication,” *ZTE Communications*, vol. 22, no. 3, pp. 1–3, Sept. 2024. doi: 10.12142/ZTECOM.202403001.

angles of interest under the transmit power budget constraint. Utilizing fractional programming and semidefinite relaxation, the study introduces an iterative algorithm that balances the performance of both communication and sensing. The results demonstrate significant performance gain in terms of communication sum rate and radar detection capability.

The third paper titled “On Normalized Least Mean Square Based Interference Cancellation Algorithm for Integrated Sensing and Communication Systems” addresses the co-site interference issue for practical ISAC systems by proposing an interference cancellation scheme using a normalized least mean square (NLMS) algorithm. The scheme reconstructs the interference from the local transmitter and cancels it from the received signal. The proposed NLMS algorithm effectively cancels co-site interference and achieves a good balance between computational complexity and convergence performance.

The fourth paper titled “Trajectory Tracking for MmWave Communication Systems via Cooperative Passive Sensing” proposes a cooperative passive sensing framework for millimeter wave (mmWave) communication systems and demonstrates it in the presence of a mobile signal blocker. A gradient-descent-based algorithm is proposed to track the blocker’s trajectory, localize the transmitters, and detect the potential link blockage jointly. The study demonstrates that the system can achieve decimeter-level localization and trajectory estimation, and predict the blockage time with an error of less than 0.1 s.

The fifth paper titled “Integrated Sensing and Communication: Who Benefits More?” examines the benefits of communication-assisted sensing and sensing-assisted communication in the context of ISAC. The paper reveals that communication-assisted sensing may offer greater development potential due to the wide coverage and cost-effectiveness of wireless infrastructure in a large range of applications. As an instance, the paper presents a channel knowledge map (CKM)-assisted beam tracking scheme and demonstrates the practical advantages of incorporating CKM in enhancing beam tracking accuracy.

The sixth paper titled “Low-Complexity Integrated Super-Resolution Sensing and Communication with Signal Decimation and Ambiguity Removal” introduces a low-complexity method for super-resolution sensing based on communication signals. The proposed scheme performs signal decimation in the frequency domain to reduce the computational complexity and uses the collocated subcarrier data to remove the pseudo peaks due to range ambiguity. The proposed scheme reduces computational complexity by two orders of magnitude while maintaining the range resolution and unambiguity.

The seventh paper titled “Tensor Decomposition-Based Channel Estimation and Sensing for Millimeter Wave MIMO-OFDM V2I Systems” utilizes tensor decomposition tech-

niques for channel estimation and sensing in millimeter-wave MIMO-OFDM vehicle-to-infrastructure (V2I) systems. A CANDECOMP/PARAFAC (CP) decomposition-based method is proposed for time-varying channel parameter extraction and then a nonlinear weighted least-square problem is proposed to accurately recover the location, heading and velocity of vehicles. The proposed methods are effective and efficient in time-varying channel estimation as well as vehicle sensing in mmWave MIMO-OFDM V2I systems.

The eighth paper titled “Sensing and Communication Integrated Fast Neighbor Discovery for UAV Networks” addresses the challenge of fast neighbor discovery in UAV networks through integrated sensing and communication. The learning automata (LA) is applied to interact with the environment and continuously adjust the probability to select beams to accelerate the convergence speed of ND algorithms. The method reduces the neighbor discovery (ND) time by up to 32% compared with the conventional scan-based algorithm (SBA).

To conclude, the papers presented in this special issue underscore some fundamental challenges of ISAC technology for future wireless communication systems. The diverse research contributions provide valuable insights and innovative solutions, serving as a valuable resource for researchers, practitioners, and students who are interested in ISAC. We also hope this special issue inspires further research and collaboration in this exciting and rapidly evolving field. Finally, we would like to express our sincere gratitude to all the authors and reviewers who have contributed to the success of this special issue.

Biographies

YUAN Jinhong received his BE and PhD degrees in electronics engineering from Beijing Institute of Technology, China in 1991 and 1997, respectively. From 1997 to 1999, he was a research fellow at the School of Electrical Engineering, University of Sydney, Australia. In 2000, he joined the School of Electrical Engineering and Telecommunications, The University of New South Wales, Australia, where he is currently a professor and the Acting Head of the School. He has published two books, five book chapters, over 300 papers in telecommunications journals and conference proceedings, and 50 industrial reports. He is a co-inventor of one patent on MIMO systems and four patents on low-density-parity-check codes. His current research interests include error control coding and information theory, communication theory, and wireless communications. He has coauthored four Best Paper Awards and one Best Poster Award, including the Best Paper Award from the IEEE International Conference on Communications, Kansas City, USA in 2018, the Best Paper Award from IEEE Wireless Communications and Networking Conference, Cancun, Mexico in 2011, and the Best Paper Award from the IEEE International Symposium on Wireless Communications Systems, Trondheim, Norway in 2007. He served as the IEEE NSW Chapter Chair of Joint Communications/Signal Processing/Ocean Engineering Chapter from 2011 to 2014 and served as an associate editor for the *IEEE Transac-*

tions on Communications from 2012 to 2017. He is currently serving as an associate editor for the *IEEE Transactions on Wireless Communications* and *IEEE Transactions on Communications*.

FEI Zesong received his PhD degree in electronic engineering from Beijing Institute of Technology (BIT), China in 2004. He is currently a professor with the Research Institute of Communication Technology, BIT. His research interests are in the area of wireless communications and signal processing, including integrated sensing and communications, physical layer security, UAV communications, intelligent reflecting surface, channel coding, and multiple access. He has authored or co-authored over 200 journal and conference papers, and was the co-receipt of the Best Paper Award in WCSP 2012, Chinacom 2012, Chinacom 2013, and PIMRC 2015. He serves as an associate editor for *IEEE Open Journal of the Communications Society*.

WEI Zhiqiang received his BE degree in information engineering from Northwestern Polytechnical University (NPU), China in 2012, and PhD de-

gree in electrical engineering and telecommunications from The University of New South Wales (UNSW), Australia in 2019. From 2019 to 2020, he was a postdoctoral research fellow with UNSW. From 2021 to 2022, he was a Humboldt postdoctoral research fellow with the Institute for Digital Communications, Friedrich-Alexander University Erlangen-Nuremberg (FAU), Germany. He is currently a professor with the School of Mathematics and Statistics, Xi'an Jiaotong University, China. He is the founding co-chair (publications) of the IEEE ComSoc special interest group on OTFS (OTFS-SIG). He received the Best Paper Award at the IEEE ICC 2018 and IEEE WCNC 2023. He was the organizer/chair for several workshops and tutorials on related topics of orthogonal time frequency space (OTFS) in IEEE flagship conferences, including IEEE ICC, IEEE WCNC, IEEE VTC, and IEEE ICC. He also co-authored the IEEE ComSoc Best Readings on OTFS and Delay Doppler Signal Processing. He is now serving as the associate editor of the *IEEE Open Journal of the Communications Society*. His current research interests include delay-Doppler communications, resource allocation optimization, and statistic and array signal processing.

Kullback-Leibler Divergence Based ISAC Constellation and Beamforming Design in the Presence of Clutter



TANG Shuntian, WANG Xinyi, XIA Fanghao,
FEI Zesong
(Beijing Institute of Technology, Beijing 100081, China)

DOI: 10.12142/ZTECOM.202403002

<https://kns.cnki.net/kcms/detail/34.1294.TN.20240816.1728.002.html>,
published online August 19, 2024

Manuscript received: 2024-07-02

Abstract: Integrated sensing and communication (ISAC) is regarded as a pivotal technology for 6G communication. In this paper, we employ Kullback-Leibler divergence (KLD) as the unified performance metric for ISAC systems and investigate constellation and beamforming design in the presence of clutters. In particular, the constellation design problem is solved via the successive convex approximation (SCA) technique, and the optimal beamforming in terms of sensing KLD is proven to be equivalent to maximizing the signal-to-interference-plus-noise ratio (SINR) of echo signals. Numerical results demonstrate the tradeoff between sensing and communication performance under different parameter setups. Additionally, the beampattern generated by the proposed algorithm achieves significant clutter suppression and higher SINR of echo signals compared with the conventional scheme.

Keywords: constellation design; clutter suppression; integrated sensing and communications; Kullback-Leibler divergence

Citation (Format 1): TIAN S T, WANG X Y, XIA F H, et al. Kullback-Leibler divergence based ISAC constellation and beamforming design in the presence of clutter [J]. *ZTE Communications*, 2024, 22(3): 4 - 12. DOI: 10.12142/ZTECOM.202403002

Citation (Format 2): S. T. Tian, X. Y. Wang, F. H. Xia, et al., "Kullback-Leibler divergence based ISAC constellation and beamforming design in the presence of clutter," *ZTE Communications*, vol. 22, no. 3, pp. 4 - 12, Sept. 2024. doi: 10.12142/ZTECOM.202403002.

1 Introduction

Integrated sensing and communication (ISAC) technology is emerging as a pivotal component for 6G communications, significantly advancing the development of the Intelligent Internet of Everything. By enabling simultaneous sensing and communication functionalities on the same spectrum and hardware platform, ISAC enhances both spectrum and energy efficiency. This technology not only optimizes resource utilization but also opens the door to new applications and services that demand high precision and low latency. As a dual-capability technology, ISAC stands as a cornerstone for future communication networks, meeting the growing need for more efficient and intelligent connectivity solutions in a world increasingly defined by the Internet of Everything^[1]. Consequently, ISAC has garnered considerable attention from researchers in recent years.

As ISAC integrates both communication and sensing func-

tionalties, the tradeoff between communication and sensing performance is crucial in ISAC system design. Current research regarding the tradeoff between communication and sensing performance focuses on their typical performance indicators, e.g., capacity and bit error rates (BER) for communications, e.g., capacity and bit error rates (BER) for communications, and detection probability and the Cramer-Rao bound (CRB) for sensing. For instance, in Ref. [2], the authors considered a Multi-Input Multi-Output (MIMO) ISAC scenario with imperfect knowledge of the channel state information (CSI). They designed robust beamforming using the communication signal-to-interference-plus-noise ratio (SINR) as a constraint, involving the simultaneous design of both digital and analog beamformers. In Ref. [3], the authors collaboratively designed transmitting hybrid beamformers and digital receiving beamformers for ISAC systems to meet SINR constraints for communication users. The simulation results demonstrated that the communication requirements were strictly satisfied. Similarly, in Ref. [4], the authors aimed to achieve optimal beamforming using communication quality-of-service (QoS) as a performance metric. Specifically, they considered the Euclidean distance between the received noise-free signal and its closest decision boundary requirements. In addition, the authors in Ref. [5] employed intelligent reflecting surfaces

This work was supported in part by National Key R&D Program of China under Grant No. 2021YFB2900200, in part by National Natural Science Foundation of China under Grant Nos. U20B2039 and 62301032, and in part by China Postdoctoral Science Foundation under Grant No. 2023TQ0028.

(IRS) to enhance an orthogonal frequency division multiplexing (OFDM) based ISAC system, ensuring the communication rate of the desired user was maintained. The authors in Ref. [6] investigated the robust beamforming design under the statistical CSI, focusing on SINR requirements. They proposed a double-loop deep unfolding (DU) approach to address this challenge, and simulation results underscored the effectiveness of their proposed robust beamforming design algorithm. From the sensing perspective, the authors in Ref. [7] proposed a robust beamforming scheme by adopting the CRB for angle estimation as the sensing performance metric, and the simulation results demonstrated that the proposed scheme maintained robust direction of arrival (DoA) estimation performance across various targets, indicating its effectiveness. As a step further, the authors in Ref. [8] explored the impact of reconfigurable intelligent surfaces (RIS) in mitigating multi-user interference (MUI) while satisfying CRB constraints. Their simulation results demonstrated superior estimation performance compared with previous works based on SINR of echo signals. The authors in Ref. [9] focused on sidelobe control in sensing to enhance target detection performance. Additionally, authors in Ref. [10] investigated the detection probability in radar sensing with binary detection, incorporating Minorize-Maximize (MM) algorithms to achieve optimal sensing beam-patterns across diverse scenarios.

It can be seen that the aforementioned existing work utilizes different metrics for sensing and communication to achieve the performance tradeoff in ISAC systems. In the absence of a unified metric for ISAC system design, the authors in Refs. [11] and [12] employed mutual information (MI) to evaluate the performance of communication and sensing. Simulation results showed MI could be used to assess the efficiency of transmission and achieve the performance tradeoff in ISAC systems. From the perspective of detection, the authors in Refs. [13] and [14] respectively employed Kullback-Leibler (KL) divergence to analyze ISAC systems, thereby formulating a unified design framework. Furthermore, the authors in Ref. [15] proposed a novel allocation approach to ISAC systems using KLD. Simulation results demonstrated that the proposed scheme achieved a higher KLD compared with the uniform power allocation scheme. These approaches provide a comprehensive method to balance and optimize both sensing and communication functionalities within ISAC systems. However, all the above studies overlook the interference caused by clutter in the environment, potentially degrading the sensing performance in realistic ISAC systems.

In this paper, we employ KLD as a unified performance metric to design ISAC systems and construct a model that accounts for the presence of static clutter for ISAC scenarios. In particular, we focus on constellation and beamforming design with the aim of investigating the performance tradeoff and achieving clutter suppression. A successive convex approxima-

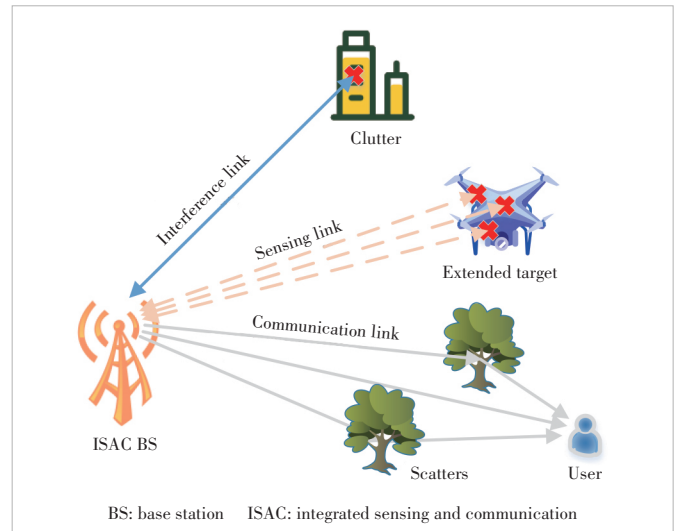
tion (SCA) method is used for constellation design, and the fractional optimization technique is employed for beamforming design. Simulation results reveal the tradeoff in terms of sensing, communication KLD, and the SINR of echo signals and BER in ISAC systems, validating that the proposed beamforming design can suppress the clutter and enhance sensing performance.

2 ISAC System Model with Clutter

We present the ISAC system model in the presence of static clutter and employ the KLD as a criterion to define a unified performance metric. This unified metric illustrates the relationship between KLD and demodulation error as well as detection probability.

2.1 System Model and Signal Model

As depicted in Fig. 1, we consider an ISAC system comprising one base station (BS), one single-antenna communication user, one sensing target, and static clutter. The ISAC BS is equipped with two uniform linear arrays (ULAs), each with M antennas. Besides serving the communication user, the BS also exploits the echoes of communication signals to detect the potential sensing target in a specific direction. Specifically, we denote the distance between the target and the BS as d_s , while the distance from BS to user is d_c . To enhance the realism of the model, the Saleh-Valenzuela channel model is considered for communication, comprising one line-of-sight (LoS) path and p non-LoS (NLoS) paths, and the extended target model is considered for sensing. Compared with the sensing target, the radar cross section (RCS) of scatters in communication links and users is much smaller, which is thus ignored in this paper. The angles of departure (AoD) for the LoS path and the p -th NLoS path of the BS-user link are denoted as θ_c and θ_p , respectively, while the AoD for the j -th sensing path is denoted as θ_j . Besides, the clutter is located at a distance of d_u



▲ Figure 1. An illustration of the considered ISAC system

from the BS in the direction of θ_u . Since the clutter is typically static, its AoD and distance information are assumed to be known at the BS, and a point model is employed to depict it. Besides, the clutter is passive and far away from the communication user, and therefore its impact on communication performance can be omitted.

With the ISAC waveform transmitted by the BS denoted as $\mathbf{s} = [s_1, \dots, s_L] \in \mathbb{C}^{1 \times L}$, where L denotes the number of snapshots, the discrete-time received signals $\mathbf{y}_c \in \mathbb{C}^{1 \times L}$ at the user can be expressed as

$$\mathbf{y}_c = \sqrt{\rho_0 d_c^{-2} P_t} \left(\mathbf{a}^H(\theta_c) + \sum_{p=1}^P \alpha_p \mathbf{a}^H(\theta_p) \right) \mathbf{w} \mathbf{s} + \mathbf{n}_c \triangleq \sqrt{\rho_0 d_c^{-2} P_t} \mathbf{h}_c \mathbf{w} \mathbf{s} + \mathbf{n}_c, \quad (1)$$

where ρ_0 denotes the path loss at the reference distance $d_0 = 1$ m, $\mathbf{a}(\theta) = [1, e^{j2\pi\delta \sin(\theta)}, \dots, e^{j2\pi(M-1)\delta \sin(\theta)}]^T \in \mathbb{C}^{M \times 1}$ is the transmit antenna steering vector with δ denoting the normalized antenna spacing, α_p denotes the small-scale fading of the p -th NLoS path, $\mathbf{w} \in \mathbb{C}^{M \times 1}$ denotes the normalized beamforming vector with $\mathbf{w}^H \mathbf{w} = 1$, and $\mathbf{n}_c \sim \mathcal{CN}(0, \sigma_c^2 \mathbf{I}_L)$ denotes the additive white Gaussian noise (AWGN) vector at the communication user.

As for sensing, the received sensing echo signals $\mathbf{Y}_r \in \mathbb{C}^{M \times L}$ at the BS can be expressed as:

$$\mathbf{Y}_r = \underbrace{\sqrt{\rho_0 d_t^{-4} P_t} \sum_{j=1}^J \mathbf{b}^*(\theta_j) \mathbf{a}^H(\theta_j) \mathbf{w} \mathbf{s}}_{\text{target component}} + \underbrace{\sqrt{\rho_0 d_u^{-4} P_t} \mathbf{b}^*(\theta_u) \mathbf{a}^H(\theta_u) \mathbf{w} \mathbf{s}}_{\text{clutter component}} + \underbrace{\mathbf{N}_r}_{\text{noise}}, \quad (2)$$

where $\mathbf{b}(\theta) \triangleq \mathbf{a}(\theta)$ denotes the receiving antenna steering vector, and $\mathbf{N}_r = [\mathbf{n}_{r,1}, \dots, \mathbf{n}_{r,L}]^T \in \mathbb{C}^{M \times L}$ denotes the AWGN at the BS with $\mathbf{n}_{r,l} \sim \mathcal{CN}(0, \sigma_r^2 \mathbf{I}_M), \forall 1 \leq l \leq L$. The detection of the potential target at the l -th frame can be cast as the binary hypothesis testing as follows:

$$\mathbf{y}_r = \begin{cases} \sqrt{\rho_0 d_u^{-4} P_t} \mathbf{b}^*(\theta_u) \mathbf{a}^H(\theta_u) \mathbf{w} \mathbf{s} + \mathbf{n}_r & \mathcal{H}_0 \\ \sqrt{\rho_0 d_t^{-4} P_t} \sum_{j=1}^J \mathbf{b}^*(\theta_j) \mathbf{a}^H(\theta_j) \mathbf{w} \mathbf{s} + \sqrt{\rho_0 d_u^{-4} P_t} \mathbf{b}^*(\theta_u) \mathbf{a}^H(\theta_u) \mathbf{w} \mathbf{s} + \mathbf{n}_r & \mathcal{H}_1 \end{cases}. \quad (3)$$

As evident from Eqs. (2) and (3), the existence of clutter can significantly affect the detection, indicating the necessity of clutter suppression.

2.2 KLD-Based Unified Performance Metric

For a pair of probability density functions (PDFs), KLD is defined as the relative entropy from one PDF $f_n(x)$ to another

PDF $f_m(x)$ to measure the information gain achieved by employing the distribution f_m instead of $f_n^{[13]}$, hence, the KLD can be defined as:

$$\text{KLD}_{n \rightarrow m} = \int_{-\infty}^{\infty} f_m(x) \log_2 \frac{f_m(x)}{f_n(x)} dx. \quad (4)$$

To compare the differences among multiple PDFs, one can consider the KLD between each pair of PDFs and take either the average or the minimum of all the comparison results. In communication systems, the KLD can be employed to assess the demodulation performance, as the error performance is significantly influenced by the pair of closest symbols. Specifically, for each pair of different data symbols $\{s_m, s_n\} (m \neq n)$ in a Q-ary signal constellation, the KLD in communication demodulation can be represented as:

$$\text{KLD}_c = \min_{n \neq m} \int_{-\infty}^{\infty} f_m(x) \log_2 \frac{f_m(x)}{f_n(x)} dx. \quad (5)$$

From the perspective of sensing systems, the KLD can be utilized to evaluate the difference between \mathcal{H}_0 and \mathcal{H}_1 , as Stein's Lemmas state that for any fixed false alarm probability, the maximization of the KLD between \mathcal{H}_0 and \mathcal{H}_1 leads to an asymptotic maximization of detection probability^[16], and hence, the KLD in sensing detection can be expressed as

$$\text{KLD}_r = \text{KLD}(\mathcal{H}_0 \| \mathcal{H}_1). \quad (6)$$

2.2.1 KLD for Communication

For communications, based on Eq. (1), the PDF of the received symbol y_c is given as

$$f_m(x) \triangleq f(y_c | \{s_m, \mathbf{w}\}) = \frac{\exp(-(\mathbf{y}_c - \boldsymbol{\mu}_m)^T \boldsymbol{\Sigma}^{-1} (\mathbf{y}_c - \boldsymbol{\mu}_m))}{\sqrt{(2\pi)^2 |\boldsymbol{\Sigma}_c|}}, \quad (7)$$

where $\mathbf{y}_c \triangleq [y_{c,R}, y_{c,I}]^T$ with $y_{c,R}$ and $y_{c,I}$ denoting the real and imaginary components of y_c , $\boldsymbol{\mu}_m \triangleq [\mu_{c,R}, \mu_{c,I}]^T$ with $\mu_{c,R} = \sqrt{\rho_0 d_c^{-2} P_t} \text{Re}\{\mathbf{h}_c \mathbf{w} s_m\}$ and $\mu_{c,I} = \sqrt{\rho_0 d_c^{-2} P_t} \text{Im}\{\mathbf{h}_c \mathbf{w} s_m\}$, and $\boldsymbol{\Sigma}_c = \sigma_c^2 \mathbf{I}_2$.

Substituting Eq. (7) into Eqs. (1) and (5), the KLD in communication can be expressed as

$$\text{KLD}_c = \min_{m \neq n} \frac{1}{2 \ln 2} \left(\text{tr}(\boldsymbol{\Sigma}_c^{-1} \boldsymbol{\Sigma}_c) - 2 + (\boldsymbol{\mu}_m - \boldsymbol{\mu}_n)^H \boldsymbol{\Sigma}_c^{-1} (\boldsymbol{\mu}_m - \boldsymbol{\mu}_n) + \ln \frac{|\boldsymbol{\Sigma}_c|}{|\boldsymbol{\Sigma}_c|} \right) = \min_{m \neq n} \frac{1}{2 \sigma_c^2 \ln 2} (\boldsymbol{\mu}_m - \boldsymbol{\mu}_n)^H (\boldsymbol{\mu}_m - \boldsymbol{\mu}_n). \quad (8)$$

It can be readily seen that an ISAC system with a larger

KLD_c value exhibits superior demodulation performance as corresponding transmit symbols mixed with noise can be more easily distinguished by the receiver.

2.2.2 KLD for Sensing

Based on Eq. (3), the PDFs of \mathbf{y}_r under \mathcal{H}_0 and \mathcal{H}_1 are expressed as:

$$\begin{aligned} f_0(\mathbf{y}_r) &= \frac{1}{\pi^M |\boldsymbol{\Sigma}_u|} \exp(-\mathbf{y}_r^H \boldsymbol{\Sigma}_u^{-1} \mathbf{y}_r), \\ f_1(\mathbf{y}_r) &= \frac{1}{\pi^M |\boldsymbol{\Sigma}_u + \boldsymbol{\Sigma}_s|} \exp(-\mathbf{y}_r^H (\boldsymbol{\Sigma}_u + \boldsymbol{\Sigma}_s)^{-1} \mathbf{y}_r), \end{aligned} \quad (9)$$

where $\boldsymbol{\Sigma}_s = \rho_0 d_t^{-4} P_t \mathbb{E}\{|s|^2\} \mathbf{A}_s \mathbf{W} \mathbf{A}_s^H$, $\mathbb{E}\{|s|^2\} = \sum_{m=1}^Q P_r(s_m) |s_m|^2$, $\mathbf{A}_s = \sum_{j=1}^J \mathbf{b}^s(\theta_j) \mathbf{a}^H(\theta_j)$, $\mathbf{W} = \mathbf{w} \mathbf{w}^H$ and $\boldsymbol{\Sigma}_u = \rho_0 d_t^{-4} P_t \mathbb{E}\{|s|^2\} \mathbf{A}_u \mathbf{W} \mathbf{A}_u^H + \sigma_r^2 \mathbf{I}_M$, $\mathbf{A}_u = \mathbf{b}^*(\theta_u) \mathbf{a}^H(\theta_u)$.

By substituting Eq. (9) into Eqs. (1) and (6), the KLD for target detection can be derived as

$$\begin{aligned} \text{KLD}_r &= \ln \left| \mathbf{I}_M + \boldsymbol{\Sigma}_u^{-1/2} \boldsymbol{\Sigma}_s \boldsymbol{\Sigma}_u^{-1/2} \right| + \\ &\text{tr} \left((\mathbf{I}_M + \boldsymbol{\Sigma}_u^{-1/2} \boldsymbol{\Sigma}_s \boldsymbol{\Sigma}_u^{-1/2})^{-1} - \mathbf{I}_M \right). \end{aligned} \quad (10)$$

The waveform design for detection can be addressed by maximizing KLD_r in Eq. (10) in order to obtain the optimal detection probability performance in terms of Stein's Lemmas^[16].

3 ISAC Constellation Design Under KLD Performance Metric

We investigate the methodology of constellation design under the KLD metrics in Eqs. (8) and (10) to achieve a tradeoff between sensing and communication performance in this section. Additionally, the maximum instantaneous transmit power constraint is considered to ensure the transmit power remains within the linear dynamic range of the amplifier.

The constellation design can be formulated as a max-min optimization problem with power constraints, which can be solved by the SCA algorithm. It's worth noting that the optimization of constellation reveals the inherent trade-off between sensing and communication performance.

3.1 Constellation Design Under Single-Antenna Setup

Based on the expressions in Eqs. (8) and (10), it is evident that the KLD performance metric is influenced by both the constellation set and the beamforming vector. In practice, the constellation set is fixed and shared between the transmitter and the receiver to minimize signaling overhead. Therefore, constellation design can be analyzed in a single-antenna setup, allowing for a separation of the constellation design from the beamforming design.

First, based on the KLD performance metrics in Eqs. (8) and (10), while ensuring the amplitude of the transmit symbol remains within the linear dynamic range of the amplifier, the ISAC constellation design problem can be formulated as

$$\begin{aligned} \max_{\{s_m\}} \text{KLD}_c \\ \text{s.t. } \text{KLD}_r \geq \text{KLD}_{r,\text{thresh.}} \\ |s_m|^2 \leq 1, m = 1, 2, \dots, Q, \end{aligned} \quad (11)$$

where $\text{KLD}_{r,\text{thresh.}}$ denotes the lower boundary of KLD_r in order to ensure the sensing performance.

To decouple the constellation design from the beamforming design, we consider a single-antenna scenario setup while substituting the expressions of the intermediate variables, and the KLD for communication in Eq. (8) can be simplified as follows.

$$\begin{aligned} \text{KLD}_c &= \min_{m \neq n} \frac{1}{2\sigma_c^2 \ln 2} (\boldsymbol{\mu}_m - \boldsymbol{\mu}_n)^H (\boldsymbol{\mu}_m - \boldsymbol{\mu}_n) = \\ &\frac{\rho_0 d_c^{-2} P_t}{2\sigma_c^2 \ln 2} \min_{m \neq n} |s_m - s_n|^2. \end{aligned} \quad (12)$$

We can see from Eq. (12) that the minimum distance among the inner points in the constellation determines the communication demodulation performance. This result makes sense as the minimum distance dictates the noise margin of the constellation.

Similarly, for a single-antenna scenario setup, the KLD for radar sensing in Eq. (10) can be simplified as^[17]:

$$\text{KLD}_r = \ln \left(1 + \frac{\zeta}{\sigma_r^2} \right) + \frac{\sigma_r^2}{\zeta + \sigma_r^2} - 1, \quad (13)$$

where $\zeta = \mathbb{E}\{|s_m|^2\} \rho_0 d_t^{-4} P_t$ denotes the power of echo signals. It can be readily seen from Eq. (12) that the KLD for sensing is positively related to $\mathbb{E}\{|s_m|^2\}$ as $f'(x) = 1/(1+x) - 1/(1+x)^2$ is always greater than 0 when $x > 0$ and KLD_r can be reformulated as $f(\mathbb{E}\{|s_m|^2\} \rho_0 d_t^{-4} P_t / \sigma_r^2)$, indicating the average power of inner points in the constellation determines the sensing performance.

Based on Eqs. (12) and (13), Problem (11) can be reformulated as

$$\begin{aligned} \max_{\{s_m\}} \min_{m \neq n} |s_m - s_n|^2 \\ \text{s.t. } r^2 \leq |s_m|^2 \leq 1, m = 1, 2, \dots, Q, \end{aligned} \quad (14)$$

where r constraints the average power of the constellation to ensure the difference between the echo signals and noise in the detection. The setting of r is intended to ensure the lower bound of the sensing performance of the ISAC system.

Problem (14) is non-convex and to address this, we utilize the SCA technique in the following discussion^[18].

3.2 Constellation Design with SCA

For ease of description and intuitive understanding, Problem (14) can be reformulated as

$$\begin{aligned} & \max_{\mathbf{S}} t \\ & \text{s.t. } r^2 \leq |s_m|^2 \leq 1, m = 1, 2, \dots, Q, \\ & |s_m - s_n|^2 \geq t^2, m, n = 1, 2, \dots, Q; m \neq n, \end{aligned} \quad (15)$$

where $\mathbf{S} = [s_1, \dots, s_Q] \in \mathbb{R}^{Q \times 2}$ with $s_i = [\text{Re}(s_i), \text{Im}(s_i)]^T$ denotes the point location in the constellation.

By introducing superscripts (l) to represent the value of variables at the l -th iteration and applying a first-order Taylor expansion to the constraints at $\mathbf{S}^{(l)}$, Problem (15) can be approximated as

$$\begin{aligned} & \max_{\Delta \mathbf{S}^{(l)}} t^{(l)} \\ & \text{s.t. } s_m^{(l)T} s_m^{(l)} + 2s_m^{(l)T} \Delta s_m^{(l)} + \Delta s_m^{(l)T} \Delta s_m^{(l)} \leq 1, m = 1, 2, \dots, Q \\ & s_m^{(l)T} s_m^{(l)} + 2s_m^{(l)T} \Delta s_m^{(l)} \geq r^2, m = 1, 2, \dots, Q \\ & s_m^{(l)T} s_m^{(l)} + s_n^{(l)T} s_n^{(l)} - 2s_m^{(l)T} s_n^{(l)} + \\ & 2(s_m^{(l)T} - s_n^{(l)T})(\Delta s_m^{(l)} - \Delta s_n^{(l)}) \geq t^{(l)}, \\ & m, n = 1, 2, \dots, Q; m \neq n \\ & t^{(l)} \geq t^{(l-1)}, \end{aligned} \quad (16)$$

where the second and third constraints are first-order Taylor approximations of the original expressions and the fourth is employed to ensure the minimum distance among inner points can continually increase with each iteration. By utilizing the optimal solution $\Delta \mathbf{S}_{\text{opt}}^{(l)}$ to update the original term with $\mathbf{S}^{(l+1)} = \mathbf{S}^{(l)} + \Delta \mathbf{S}_{\text{opt}}^{(l)}$ and repeatedly solving Problem (16) until it converges, we can eventually obtain \mathbf{S}^* .

The complexity of the constellation design mainly comes from the application of interior within each iteration, which is $O(I \times \ln(1/\varepsilon)Q^3)$, where I denotes the number of iterations, Q denotes the order of constellation and ε denotes the duality gap of the interior point method^[19]. It can be seen that the complexity of this algorithm primarily increases cubically with the dimension of variables.

As for the convergence of this algorithm, within each iteration, we have

$$\begin{aligned} & s_m^{(l)T} s_m^{(l)} + s_n^{(l)T} s_n^{(l)} - 2s_m^{(l)T} s_n^{(l)} + 2(s_m^{(l)T} - s_n^{(l)T})(\Delta s_m^{(l)} - \\ & \Delta s_n^{(l)}) \geq t^{(l)} \geq t^{(l-1)}, m, n = 1, 2, \dots, Q; m \neq n. \end{aligned} \quad (17)$$

The right side of Problem (17) shows that the value of objective function monotonically increases during the SCA process. Based on the first constraint in Problems (16) and (17), we have

$$\begin{aligned} t^{(l)} & \leq s_m^{(l)T} s_m^{(l)} + s_n^{(l)T} s_n^{(l)} - 2s_m^{(l)T} s_n^{(l)} + 2(s_m^{(l)T} - s_n^{(l)T})(\Delta s_m^{(l)} - \Delta s_n^{(l)}) = \\ & (s_m^{(l)T} s_m^{(l)} + 2s_m^{(l)T} \Delta s_m^{(l)} + (s_n^{(l)T} s_n^{(l)} + 2s_n^{(l)T} \Delta s_n^{(l)}) - \\ & 2(s_m^{(l)T} s_n^{(l)} + s_m^{(l)T} \Delta s_n^{(l)} + s_n^{(l)T} \Delta s_m^{(l)}) < \\ & 2 - 2(s_m^{(l)T} s_n^{(l)} + s_m^{(l)T} \Delta s_n^{(l)} + s_n^{(l)T} \Delta s_m^{(l)}) < \\ & 2 + 2(|s_m^{(l)}| |s_n^{(l)}| + |s_m^{(l)}| |\Delta s_n^{(l)}| + |s_n^{(l)}| |\Delta s_m^{(l)}|) = b_u. \end{aligned} \quad (18)$$

Note that the value of b_u is limited; hence, the alternating optimization is guaranteed to converge.

By setting different values of r , we can obtain the corresponding constellation to achieve various tradeoffs between sensing and communication performance as a larger r represents a higher average power for better detection, which also results in a smaller inner-constellation distance and poorer communication performance.

4 Sensing Clutter Suppression Design Based on KLD

In this section, we study the beamforming design in the presence of clutter as depicted in Fig. 1 with a fixed constellation set designed in Section 3. The aim of beamforming focuses more on clutter suppression, as the tradeoff between sensing and communication performance is adjusted by setting different values of r in the constellation design. We will show that the maximization of KLD in terms of sensing in the presence of clutter is eventually equivalent to maximizing the SINR of echo signals.

With the fixed constellation mapping designed in the previous section, the BS can achieve various tradeoffs between sensing and communication performance by setting different inner radii r in Problem (14). However, as indicated by Eq. (2), the influence of clutter still exists. To address this issue, we explore optimal beamforming to mitigate the impact of clutter based on Eq. (10) shown as follows.

In the presence of clutter, the KLD for sensing in Eq. (10) can be further derived as:

$$\begin{aligned} \text{KLD}_r & = \ln \left| (\boldsymbol{\Sigma}_u + \boldsymbol{\Sigma}_s) \boldsymbol{\Sigma}_s^{-1} \right| + \text{tr} \left[(\boldsymbol{\Sigma}_u + \boldsymbol{\Sigma}_s)^{-1} \boldsymbol{\Sigma}_s \right] = \\ & \ln \left| \mathbf{I}_M + \beta_s \mathbf{A}_s \mathbf{W} \mathbf{A}_s^H (\beta_u \mathbf{A}_u \mathbf{W} \mathbf{A}_u^H + \mathbf{I}_M)^{-1} \right| + \\ & \text{tr} \left[(\mathbf{I}_M + \beta_u \mathbf{A}_u \mathbf{W} \mathbf{A}_u^H)^{-1} \beta_s \mathbf{A}_s \mathbf{W} \mathbf{A}_s^H + \mathbf{I}_M \right]^{-1}, \end{aligned} \quad (19)$$

$$\text{where } \beta_s = \frac{\rho_0 d_s^{-4} P_t \mathbb{E} \left\{ |s_m|^2 \right\}}{\sigma_r^2} \text{ and } \beta_u = \frac{\rho_0 d_u^{-4} P_t \mathbb{E} \left\{ |s_m|^2 \right\}}{\sigma_r^2}.$$

In the following, we employ the KLD for sensing in the presence of clutter in Eq. (10) to explore the optimal beampattern to achieve clutter suppression. To further simplify KLD, we apply the Woodbury identity as follows^[20].

$$(\mathbf{A} + \mathbf{UCV})^{-1} = \mathbf{A}^{-1} - \mathbf{A}^{-1} \mathbf{U} (\mathbf{C}^{-1} + \mathbf{V} \mathbf{A}^{-1} \mathbf{U})^{-1} \mathbf{V} \mathbf{A}^{-1}, \quad (20)$$

where $\mathbf{A} \in \mathbb{C}^{M \times M}$, $\mathbf{U} \in \mathbb{C}^{M \times K}$, $\mathbf{C} \in \mathbb{C}^{K \times K}$ and $\mathbf{V} \in \mathbb{C}^{K \times M}$. By re-

placing matrices \mathbf{A} and \mathbf{C} with identity matrices, we can obtain

$$(\mathbf{I} + \mathbf{UV})^{-1} = \mathbf{I} - \mathbf{U}(\mathbf{I} + \mathbf{VU})^{-1}\mathbf{V}. \quad (21)$$

Then, let $\mathbf{U} = (\beta_u \mathbf{A}_u \mathbf{W} \mathbf{A}_u^H + \mathbf{I}_M)^{-1} \mathbf{A}_s \mathbf{w}$ and $\mathbf{V} = \beta_s \mathbf{w}^H \mathbf{A}_s^H$, we can obtain:

$$\text{KLD}_r = \ln \left(1 + \beta_s \mathbf{w}^H \mathbf{A}_s^H (\beta_u \mathbf{A}_u \mathbf{w} \mathbf{w}^H \mathbf{A}_u^H + \mathbf{I}_M)^{-1} \mathbf{A}_s \mathbf{w} \right) + \frac{1}{1 + \beta_s \mathbf{w}^H \mathbf{A}_s^H (\beta_u \mathbf{A}_u \mathbf{w} \mathbf{w}^H \mathbf{A}_u^H + \mathbf{I}_M)^{-1} \mathbf{A}_s \mathbf{w}}. \quad (22)$$

Again, note that $f(x) = \ln(1+x) + 1/(1+x)$ is monotonically increasing with the increase of x ; hence, the maximization of KLD_r can be formulated as:

$$\begin{aligned} \max_{\mathbf{w}} \quad & \beta_s \mathbf{w}^H \mathbf{A}_s^H (\beta_u \mathbf{A}_u \mathbf{w} \mathbf{w}^H \mathbf{A}_u^H + \mathbf{I}_M)^{-1} \mathbf{A}_s \mathbf{w} \\ \text{s.t.} \quad & \mathbf{w}^H \mathbf{w} = 1. \end{aligned} \quad (23)$$

It can be seen that the objective function of Problem (23) can be further transformed as follows.

$$\begin{aligned} & \beta_s \mathbf{w}^H \mathbf{A}_s^H (\beta_u \mathbf{A}_u \mathbf{w} \mathbf{w}^H \mathbf{A}_u^H + \mathbf{I}_M)^{-1} \mathbf{A}_s \mathbf{w} = \\ & \beta_s \mathbf{w}^H \mathbf{A}_s^H \mathbf{A}_s \mathbf{w} \operatorname{tr} \left[(\beta_u \mathbf{A}_u \mathbf{w} \mathbf{w}^H \mathbf{A}_u^H + \mathbf{I}_M)^{-1} \right] = \\ & \frac{\beta_s \mathbf{w}^H \mathbf{A}_s^H \mathbf{A}_s \mathbf{w}}{1 + \beta_u \mathbf{w}^H \mathbf{A}_u^H \mathbf{A}_u \mathbf{w}}. \end{aligned} \quad (24)$$

Based on the above results, Problem (23) can be reformulated as follows.

$$\begin{aligned} \max_{\mathbf{w}} \quad & \frac{\beta_s \mathbf{w}^H \mathbf{A}_s^H \mathbf{A}_s \mathbf{w}}{1 + \beta_u \mathbf{w}^H \mathbf{A}_u^H \mathbf{A}_u \mathbf{w}} \\ \text{s.t.} \quad & \mathbf{w}^H \mathbf{w} = 1. \end{aligned} \quad (25)$$

It can be observed that the KLD maximizing problem is eventually transformed to maximizing the SINR of echo signals, thereby achieving clutter suppression. To obtain the optimal beamforming vector of Problem (25), we first apply the constraint to transform the objective function of Problem (25) into

$$\frac{\beta_s \mathbf{w}^H \mathbf{A}_s^H \mathbf{A}_s \mathbf{w}}{1 + \beta_u \mathbf{w}^H \mathbf{A}_u^H \mathbf{A}_u \mathbf{w}} = \frac{\beta_s \mathbf{w}^H \mathbf{A}_s^H \mathbf{A}_s \mathbf{w}}{\beta_u \mathbf{w}^H \left(\frac{1}{\beta_u} \mathbf{I} + \mathbf{A}_u^H \mathbf{A}_u \right) \mathbf{w}}. \quad (26)$$

Since $\frac{1}{\beta_u} \mathbf{I} + \mathbf{A}_u^H \mathbf{A}_u$ is a positive semi-definite matrix, we consider its lower triangular Cholesky decomposition, i. e., $\mathbf{C}\mathbf{C}^H = \frac{1}{\beta_u} \mathbf{I} + \mathbf{A}_u^H \mathbf{A}_u$. Let $\mathbf{w} = (\mathbf{C}^H)^{-1} \mathbf{y}$, and we can obtain:

$$\frac{\beta_s \mathbf{w}^H \mathbf{A}_s^H \mathbf{A}_s \mathbf{w}}{\beta_u \mathbf{w}^H \left(\frac{1}{\beta_u} \mathbf{I} + \mathbf{A}_u^H \mathbf{A}_u \right) \mathbf{w}} = \frac{\beta_s \mathbf{y}^H \mathbf{C}^{-1} \mathbf{A}_s^H \mathbf{A}_s (\mathbf{C}^H)^{-1} \mathbf{y}}{\beta_u \mathbf{y}^H \mathbf{y}}. \quad (27)$$

According to the Rayleigh quotient^[21], Problem (25) has a closed-form solution as shown below.

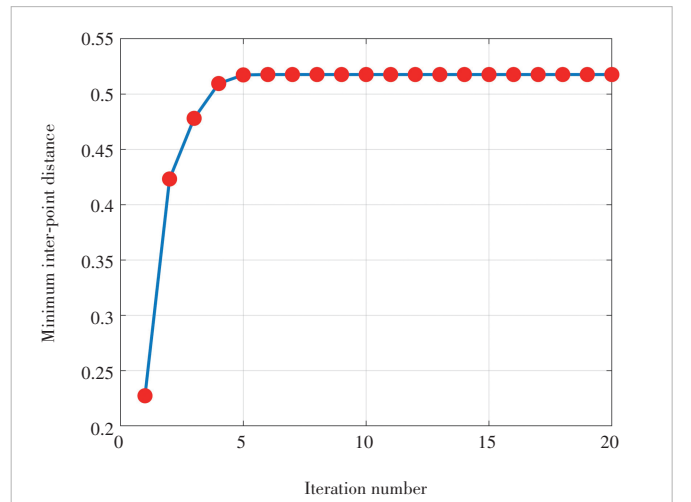
$$\mathbf{w}^* = \frac{(\mathbf{C}^H)^{-1} \mathbf{u}_{\max}}{\|(\mathbf{C}^H)^{-1} \mathbf{u}_{\max}\|}, \quad (28)$$

where \mathbf{u}_{\max} denotes the eigenvector of $\mathbf{C}^{-1} \mathbf{A}_s^H \mathbf{A}_s (\mathbf{C}^H)^{-1}$ corresponding to the largest eigenvalue λ_{\max} . By utilizing the optimal transmit beamforming vector in Eq. (25), the BS can effectively suppress clutter by maximizing the SINR of the echo signals, as demonstrated in Problem (25), which leads to enhanced sensing performance in the ISAC system.

5 Numerical Results

In this section, we provide numerical results to demonstrate the performance of the constellation and beamforming design methodology. The number of antennas is set as $M = 16$ and the inner-element spacing is $\lambda/2$ with λ denoting the wavelength of the transmit signal. The transmit power of BS is set as 30 dBm and the path loss at the reference distance of 1 m is set as -30 dBm. In addition, the DoAs of the target, user and static clutter are $\theta_s = 30^\circ$, $\theta_c = 18^\circ$ and $\theta_u = 45^\circ$, respectively. Besides, the BS-target, the BS-user and the BS-clutter distances are set as $d_s = 600$ m, $d_c = 800$ m and $d_u = 750$ m. The noise power at the BS and the user is set as -110 dBm and -70 dBm, respectively. The number of NLoS links is set as 4 while the number of scattering points on the extended target is set as 10.

The convergence behavior of the SCA algorithm for constellation design is shown in Fig. 2, illustrating the minimum inter-point distance t versus the iteration number for $Q = 16$ and $r = 0.4$. It is shown that the minimum inter-point distance stabilizes by the fourth iteration, indicating that the algorithm has converged. This demonstrates the good convergence of



▲ Figure 2. Minimum inter-point distance versus iteration number

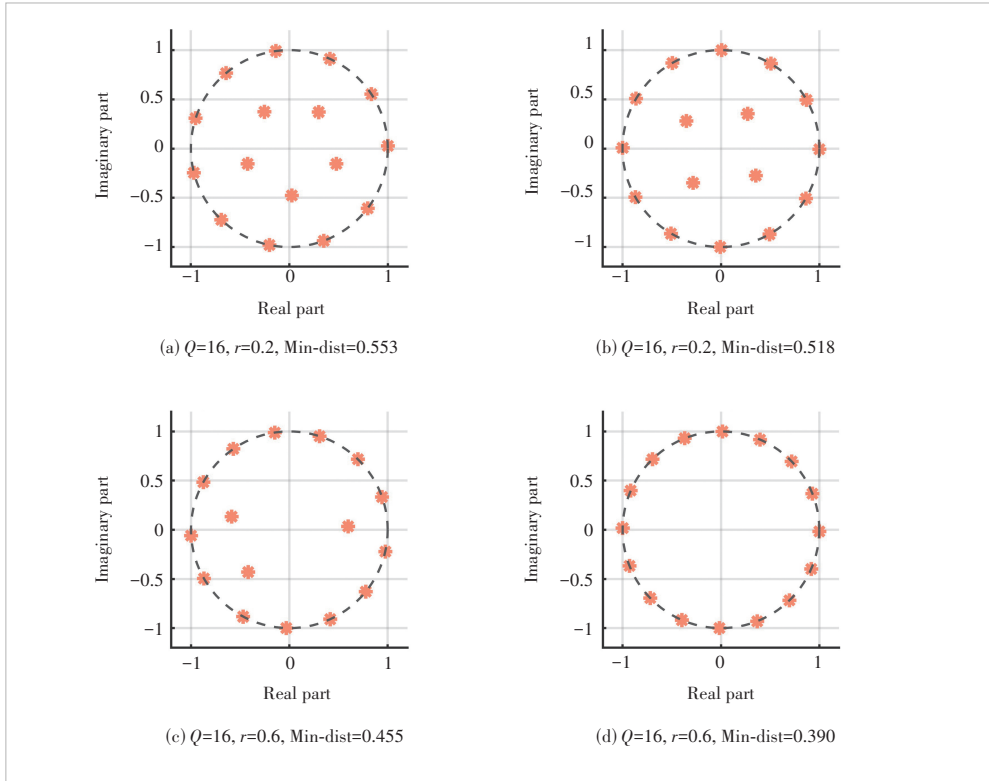
this SCA algorithm for constellation design algorithm.

Next, in Fig. 3, we provide the optimized constellation set with various inner ring radii r and the modulation order of $Q = 16$. A larger r results in a smaller minimum inter-point distance within the constellation. This results in more constellation points clustering at the edge of the unit circle, leading to a gradual transition of the constellation mapping from irregular to regular. This demonstrates tuning r can generate different constellations and the corresponding result can achieve different tradeoffs between sensing and communication performance.

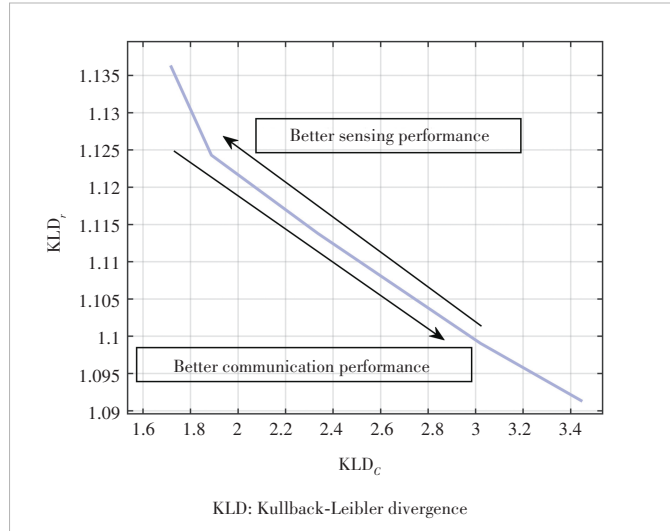
To further investigate the performance tradeoff, we illustrate the Pareto bound between sensing and communication from the perspective of KLD in Fig. 4. The constellations designed in Fig. 3 are taken into consideration. It can be seen that KLD_r strictly and monotonically decreases with the increase of KLD_c , indicating an inherent tradeoff in the ISAC system. With higher inner ring radii r , more constellation points cluster at the edge of the unit circle, shifting the tradeoff state from right bottom to left top in Fig. 4 and vice versa. Therefore, we can achieve the desired performance tradeoff to meet various needs by selecting corresponding constellations.

As a step further, we evaluate the performance of the transmit beampattern generated by the proposed design methodology compared with the beampattern generated by the Maximum Ratio Transmission (MRT) algorithm and the methods proposed in Ref. [14], as shown in Fig. 5. The beampattern generated by the MRT algorithm exhibits significant power gain in the direction of targets while the beampattern from Ref. [14] has high gain in both the direction of the user and the target as the ISAC system design in Ref. [14] considers the tradeoff between sensing and communication through beamforming. However, the influence of static clutter is overlooked in these schemes. In contrast, the transmitted waveform generated by our proposed algorithm is predominantly focused in the desired direction, while a deep fading occurs in the clutter direction. This indicates that the proposed scheme effectively achieves clutter suppression, thereby enhancing overall sensing performance.

In Fig. 6, we further evaluate the performance of the pro-



▲ Figure 3. Constellation under different inner ring radii r



▲ Figure 4. Tradeoff between sensing and communication

posed design by comparing the SINR of echo signals with other algorithms. The optimized ISAC constellation under various r is employed in this example. As it can be seen, the proposed algorithm achieves 0.7 dB gain over the MRT algorithm and 3 dB gain over the method in Ref. [14], indicating the proposed algorithm can successfully achieve clutter suppression better. The method in Ref. [14] allocates more power to the user direction but less power to the target direction to balance

- ternational Conference on Acoustics, Speech and Signal Processing (ICASSP). IEEE, 2024: 8651 - 8655. DOI: 10.1109/ICASSP48485.2024.10447252
- [4] LIU R, LI M, LIU Q, et al. Dual-functional radar-communication waveform design: a symbol-level precoding approach [J]. IEEE journal of selected topics in signal processing, 2021, 15(6): 1316 - 1331. DOI: 10.1109/JSTSP.2021.3111438
- [5] ZHANG Y, QI H T, LU W D, et al. Beamforming design for IRS-assisted OFDM-ISAC system in C-RAN [J]. IEEE wireless communications letters, 2024, 13(6): 1626 - 1630. DOI: 10.1109/LWC.2024.3384249
- [6] LIU W X, XU H B, HE X L, et al. Bi-level deep unfolding based robust beamforming design for IRS-assisted ISAC system [J]. IEEE access, 2024, 12: 76663 - 76672. DOI: 10.1109/ACCESS.2024.3406527
- [7] ZHAO Z Y, ZHANG L, JIANG R, et al. Joint beamforming scheme for ISAC systems via robust Cramér-Rao bound optimization [J]. IEEE wireless communications letters, 2024, 13(3): 889 - 893. DOI: 10.1109/LWC.2024.3349488
- [8] WANG X Y, FEI Z S, HUANG J X, et al. Joint waveform and discrete phase shift design for RIS-assisted integrated sensing and communication system under cramer-Rao bound constraint [J]. IEEE transactions on vehicular technology, 2022, 71(1): 1004 - 1009. DOI: 10.1109/TVT.2021.3122889
- [9] FUHRMANN D R, SAN ANTONIO G. Transmit beamforming for MIMO radar systems using signal cross-correlation [J]. IEEE transactions on aerospace and electronic systems, 2008, 44(1): 171 - 186. DOI: 10.1109/TAES.2008.4516997
- [10] TANG B, NAGHSH M M, TANG J. Relative entropy-based waveform design for MIMO radar detection in the presence of clutter and interference [J]. IEEE transactions on signal processing, 2015, 63(14): 3783 - 3796. DOI: 10.1109/TSP.2015.2423257
- [11] LI J, ZHOU G, GONG T T, et al. A framework for mutual information-based MIMO integrated sensing and communication beamforming design [J]. IEEE transactions on vehicular technology, 2024, 73(6): 8352 - 8366. DOI: 10.1109/TVT.2024.3355899
- [12] PIAO J H, WEI Z Q, YUAN X, et al. Mutual information metrics for up-link MIMO-OFDM integrated sensing and communication system [C]// IEEE Global Communications Conference. IEEE, 2023: 7387 - 7392. DOI: 10.1109/GLOBECOM54140.2023.10437900
- [13] AL-JARRAH M, ALSUSA E, MASOUIROS C. A unified performance framework for integrated sensing-communications based on KL-divergence [J]. IEEE transactions on wireless communications, 2023, 22(12): 9390 - 9411. DOI: 10.1109/TWC.2023.3270390
- [14] FEI Z, TANG S, WANG X, et al. Revealing the trade-off in ISAC systems: the KL divergence perspective [J]. IEEE wireless communications letters, 2024, 13(10): 2747 - 2751. DOI: 10.1109/LWC.2024.3443409
- [15] KLOOB Y, AL-JARRAH M, ALSUSA E, et al. Novel KLD-based resource allocation for integrated sensing and communication [J]. IEEE transactions on signal processing, 2024, 72: 2292 - 2307. DOI: 10.1109/TSP.2024.3392350
- [16] KAILATH T. The divergence and bhattacharyya distance measures in signal selection [J]. IEEE transactions on communication technology, 1967, 15(1): 52 - 60. DOI: 10.1109/TCOM.1967.1089532
- [17] WANG X Y, FEI Z S, LIU P, et al. Sensing aided covert communications: turning interference into allies [J]. IEEE transactions on wireless communications, 2024, PP(99): 1. DOI: 10.1109/TWC.2024.3374775
- [18] JEANNE R S, SAMUNDISWARY P. Power minimization in MIMO-OFDM network with energy harvesting node using Successive Convex Approximation (SCA) technique [C]//Proceedings of International Conference on Control, Instrumentation, Communication and Computational Technologies (ICCICT). IEEE, 2016: 431 - 436. DOI: 10.1109/ICCICT.2016.7987988
- [19] WALDSPURGER I, D' ASPREMONTE A, MALLAT S. Phase recovery, MaxCut and complex semidefinite programming [J]. Mathematical programming, 2015, 149(1): 47 - 81. DOI: 10.1007/s10107-013-0738-9
- [20] BUDHU J, GRBIC A. Accelerated optimization of metasurfaces with the Woodbury matrix identity [C]//International Applied Computational Electromagnetics Society Symposium (ACES). IEEE, 2021: 1 - 3
- [21] SUN J G. Eigenvalues of Rayleigh quotient matrices [J]. Numerische mathematik, 1991, 59(1): 603 - 614. DOI: 10.1007/BF01385798

Biographies

TANG Shuntian received his BE degree in electronic engineering from Beijing Institute of Technology (BIT), China in 2024. He is currently pursuing his master's degree with BIT. His research interests include integrated sensing and communications and AFDM modulation.

WANG Xinyi (bit_wangxy@163.com) received his BE and PhD degrees in electronic engineering from Beijing Institute of Technology (BIT), China in 2017 and 2022, respectively. He is currently a postdoctoral researcher at BIT. He was a recipient of the Best Paper Award in WOCC 2019 and has been recognized as an exemplary reviewer for the *IEEE Transactions on Communications*. His research interests include integrated sensing and communications, UAV communications, intelligent reflecting surface, polar codes, and OTFS modulation. He has published over 50 journals and conference papers in these areas.

XIA Fanghao received his BS degree in electronic engineering from Beijing Institute of Technology (BIT), China in 2021. He is currently pursuing his PhD degree with the Research Institute of Communication Technology, BIT. His research interests include integrated sensing and communications, intelligent reflection surface, and physical layer security.

FEI Zesong received his PhD degree in electronic engineering from Beijing Institute of Technology (BIT), China in 2004. He is currently a professor with the Research Institute of Communication Technology, BIT, where he is involved in the design of the next generation high-speed wireless communication. He is the chief investigator with the National Natural Science Foundation of China. His research interests include wireless communications and multimedia signal processing. He is a senior member of the Chinese Institute of Electronics and China Institute of Communications.



Joint Beamforming Design for Dual-Functional Radar-Communication Systems Under Beampattern Gain Constraints

CHEN Guangyi¹, ZHANG Ruoyu¹, REN Hong¹,
LIN Xu², WU Wen¹

(1. Key Laboratory of Near-Range RF Sensing ICs Microsystems, Ministry of Education, School of Electronic and Optical Engineering, Nanjing University of Science and Technology, Nanjing 210094, China;
2. School of Electronics and Information Engineering, Harbin Institute of Technology, Harbin 150001, China)

DOI: 10.12142/ZTECOM.202403003

<https://kns.cnki.net/kcms/detail/34.1294.TN.20240814.1632.002.html>,
published online August 15, 2024

Manuscript received: 2024-06-22

Abstract: The joint beamforming design challenge for dual-functional radar-communication systems is addressed in this paper. The base station in these systems is tasked with simultaneously sending shared signals for both multi-user communication and target sensing. The primary objective is to maximize the sum rate of multi-user communication, while also ensuring sufficient beampattern gain at particular angles that are of interest for sensing, all within the constraints of the transmit power budget. To tackle this complex non-convex problem, an effective algorithm that iteratively optimizes the joint beamformers is developed. This algorithm leverages the techniques of fractional programming and semidefinite relaxation to achieve its goals. The numerical results confirm the effectiveness of the proposed algorithm.

Keywords: dual-functional radar-communication; joint beamforming design; beampattern gain constraints; semidefinite relaxation; fractional programming

Citation (Format 1): CHEN G Y, ZHANG R Y, REN H, et al. Joint beamforming design for dual-functional radar-communication systems under beampattern gain constraints [J]. *ZTE Communications*, 2024, 22(3): 13 – 20. DOI: 10.12142/ZTECOM.202403003

Citation (Format 2): G. Y. Chen, R. Y. Zhang, H. Ren, et al., “Joint beamforming design for dual-functional radar-communication systems under beampattern gain constraints,” *ZTE Communications*, vol. 22, no. 3, pp. 13 – 20, Sept. 2024. doi: 10.12142/ZTECOM.202403003.

1 Introduction

In future 6G wireless networks, we expect that the scarcity of spectrum resources will be exacerbated by the increasing number of wireless communication devices and higher demands for transmission rates^[1–3]. The growing sensing requirements in applications such as unmanned aerial vehicles and intelligent vehicles have made the coexistence of radar-communication spectrum a vital issue^[4–6]. Due to the benefits of low hardware complexity reduction, spectrum sharing, low power consumption, and joint signal processing, dual-functional radar-communication (DFRC) is now regarded as a key enabling technology in 6G systems^[7–8].

In the DFRC systems where radar and communication share a platform, the joint beamforming design enables multi-user communication and radar sensing by exploiting the spa-

tial degree of freedom (DoF)^[9]. In Ref. [10], the goal was to minimize the radar beampattern mean square error while satisfying communication quality of service constraints. In Ref. [11], the beamforming design was proposed to maximize the worst signal-to-interference-noise ratio (SINR) among all users, while satisfying the transmit waveform covariance and power constraints. The Cramér-Rao bound was used as the radar performance metric and the SINR as the communication metric to optimize beamformers^[12]. Under constraints of power and signal-clutter-noise ratio, a low-complexity beamforming scheme to maximize the sum rate was investigated in Ref. [13].

While these works considered the communication metrics as the objective function, the authors investigated the joint beamforming design using the radar metrics as the objective function in Refs. [14 – 16]. In Ref. [14], an approach to minimizing the radar beampattern mean squared error under the SINR constraints was proposed. In Ref. [15], under the same SINR constraint, the authors developed the joint beamformer by matching the radar detection beampattern. In Ref. [16], the authors compared the beamforming designs of the beampat-

This work was supported in part by the National Natural Science Foundation of China under Grant No. 62201266, and in part by the Natural Science Foundation of Jiangsu Province under Grant No. BK20210335.

tern matching error minimization and the beampattern gain maximization under the power and SINR constraints. A shortcoming of the conventional beampattern matching design is that a fine grid of points covering the location sectors of interest is required to approximate the desired beampattern. In contrast, the beampattern gain maximization design focuses on the direct optimizing of the radar direction gain without requiring complex dense grids, which inspires us to leverage this characteristic for DFRC beamforming design.

In this work, we study the joint beamforming design problem for the DFRC systems in which a base station (BS) transmits the shared signals for both multi-user communication and radar target sensing. Our goal is to maximize the sum rate under the constraints of the radar beampattern gain and the transmit power budget. To tackle the non-convexity of the problem at hand, we employ the fractional programming (FP) method to obtain a tractable form of the objective function^[17]. Additionally, the non-convex radar beampattern gain constraints are handled using the semidefinite relaxation (SDR) technique^[18]. By doing so, we design an iterative algorithm to obtain the joint beamformers for radar sensing and multi-user communication. Numerical results demonstrate that a flexible trade-off between the communication sum rate and radar beampattern gain performance can be achieved by the proposed algorithm.

Notations are as follows: \mathbf{A} and \mathbf{a} denote a matrix and a column vector; Superscripts $(\cdot)^T$, $(\cdot)^*$ and $(\cdot)^H$ denote the matrix transpose, the conjugate and the conjugate transpose, respectively. Expectation and the real part of a complex variable are denoted by $\mathbb{E}\{\cdot\}$ and $\Re\{\cdot\}$; $\text{Tr}(\cdot)$ stands for the trace of a matrix. \mathbf{I}_N is an $N \times N$ identity matrix; $\text{rank}(\mathbf{A})$ denotes the rank of \mathbf{A} , and $\mathbf{A} \succeq \mathbf{0}$ indicates that \mathbf{A} is positive semidefinite.

2 System Model and Problem Formulation

As shown in Fig. 1, we consider a DFRC system in which the BS is equipped with an N -antenna uniform linear array (ULA). The BS simultaneously serves K single-antenna users and senses Q potential targets. The shared transmit signal from the BS can be expressed as

$$\mathbf{x} = \sum_{k=1}^K \mathbf{w}_k s_k, \quad (1)$$

where $\mathbf{w}_k \in \mathbb{C}^{N \times 1}$ is the beamforming vector for the k -th user, and s_k is the transmitted data symbol satisfying $\mathbb{E}\{s_k s_k^*\} = 1$ and $\mathbb{E}\{s_i s_j^*\} = 0$, $\forall i \neq j$. The power constraint at the BS is $\sum_{k=1}^K \|\mathbf{w}_k\|^2 \leq P_{\max}$, where P_{\max} is the maximum transmit power budget. The received signal of the k -th communication

user can be given by

$$y_k = \mathbf{h}_k^H \mathbf{x} + n_k, \quad \forall k, \quad (2)$$

where $n_k \sim \mathcal{CN}(0, \sigma_k^2)$ is the independent identically distributed (i.i.d) complex Gaussian noise with the variance σ_k^2 . In this work, we consider the widely adopted geometric channel model given by Ref. [19]¹:

$$\mathbf{h}_k = \sqrt{\frac{N}{L_k}} \sum_{l=1}^{L_k} \alpha_{k,l} \mathbf{a}(\phi_{k,l}) \in \mathbb{C}^{N \times 1}, \quad \forall k, \quad (3)$$

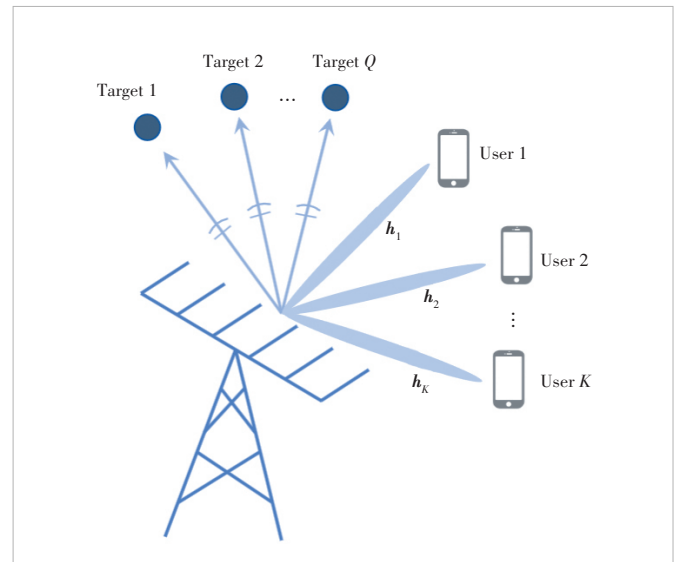
where L_k is the number of paths between the BS and the k -th user, $\alpha_{k,l}$ is the gain of the l -th path for the k -th user, $\phi_{k,l}$ is the angle of departure (AoD) of the k -th user of the l -th path. The transmit steering vector of direction θ is specified as

$$\mathbf{a}(\theta) = \frac{1}{\sqrt{N}} \left[1, e^{j\frac{2\pi}{\lambda}d \cos \theta}, \dots, e^{j\frac{2\pi}{\lambda}d(N-1)\cos \theta} \right]^T, \quad (4)$$

where d and λ are the antenna spacing and signal wavelength. Under this setup, the sum rate of all k users is expressed as

$$R = B \sum_{k=1}^K \log_2(1 + \gamma_k), \quad (5)$$

where B is a constant denoting the channel bandwidth. Besides, γ_k is the SINR of the k -th user and is given by



▲ Figure 1. Illustration of the considered dual-functional radar-communication (DFRC) system

¹ The line-of-sight component is part of the channel model, making it easier to observe the impact of the user's direction on the beam gain. The proposed method is applicable to various types of channels.

$$\gamma_k = \frac{|\mathbf{h}_k^H \mathbf{w}_k|^2}{\sum_{i \neq k}^K |\mathbf{h}_k^H \mathbf{w}_i|^2 + \sigma_k^2}, \forall k \quad (6)$$

For the radar sensing, the detection performance of potential targets can be enhanced by forming highly directional beams towards the target directions. The transmit beampattern gain at a particular angle is given by Ref. [20] as

$$p(\theta) = \mathbb{E}\{\mathbf{a}^H(\theta) \mathbf{x}^2\} = \mathbf{a}^H(\theta) (\mathbf{w}_k \mathbf{w}_k^H) \mathbf{a}(\theta). \quad (7)$$

Our goal in this work is to design the beamforming vectors $\{\mathbf{w}_k\}_{k=1}^K$, such that the sum rate is maximized under the constraints of the transmit power budget and the radar beampattern gain of Q directions is guaranteed. The corresponding optimization problem can be formulated as

$$\max_{\{\mathbf{w}_k\}} \sum_{k=1}^K \log_2(1 + \gamma_k), \quad (8a)$$

$$\text{s.t.} \quad \sum_{k=1}^K \|\mathbf{w}_k\|^2 \leq P_{\max}, \quad (8b)$$

$$\mathbf{a}^H(\theta_q) \left(\sum_{k=1}^K \mathbf{w}_k \mathbf{w}_k^H \right) \mathbf{a}(\theta_q) \geq \Gamma_q P_{\max}, \forall q, \quad (8c)$$

where θ_q is the direction of the q -th target, $\Gamma_q P_{\max}$ represents the required beampattern gain towards the q -th target, Γ_q is a weighting coefficient satisfying $\Gamma_1 + \dots + \Gamma_Q \leq 1$. It should be noted that due to the logarithmic and fractional terms in Eq. (8a) and the non-convex radar beampattern gain constraints in Eq. (8c), it is challenging to directly handle the optimization problem.

3 Proposed Joint Beamforming Design for DFRC Systems

In this section, we present an iterative algorithm for solving the considered optimization problem (8). We first use the FP method to tackle the complex objective function (8a) and then transform a considered problem into the tractable form based on the SDR technique.

3.1 Transformation of Objective Function

We study the properties of the objective function (8a), a typical function with multiple fractional terms. Our goal is to convert the objective function to a tractable form. Using the Lagrangian duality transformation^[17], we take the fractional term γ_k out of the logarithm and then transform the function (8a) into a polynomial expression.

Proposition 1: The objective function (8a) can be converted into

$$\sum_{k=1}^K \log_2(1 + \nu_k) - \nu_k + \sum_{k=1}^K \frac{(1 + \nu_k) |\mathbf{h}_k^H \mathbf{w}_k|^2}{\sum_{i=1}^K |\mathbf{h}_k^H \mathbf{w}_i|^2 + \sigma_k^2}, \quad (9)$$

where ν_k is an auxiliary variable satisfying $\nu_k = \gamma_k, \forall k$.

Proof: See Appendix A.

Proposition 1 illustrates that the objective function (8a) is equivalent to Eq. (9) as long as $\nu_k = \gamma_k$. Even after this transform, solving the problem remains challenging due to the last term in the objective function (9), which is the sum of k fractional terms. To address this issue, we use the multidimensional quadratic transform^[17].

Proposition 2: The fractional term in Eq. (9), that is

$$\frac{(1 + \nu_k) |\mathbf{h}_k^H \mathbf{w}_k|^2}{\sum_{i=1}^K |\mathbf{h}_k^H \mathbf{w}_i|^2 + \sigma_k^2}, \forall k \quad (10)$$

which can be quadratically transformed into

$$2\sqrt{1 + \nu_k} \Re\{\tau_k^* \mathbf{h}_k^H \mathbf{w}_k\} - \sum_{i=1}^K |\tau_i|^2 |\mathbf{h}_k^H \mathbf{w}_i|^2 - |\tau_k|^2 \sigma_k^2, \quad (11)$$

where $\{\tau_k\}_{k=1}^K$ is the fractional programming auxiliary variable expressed as

$$\tau_k = \frac{\sqrt{1 + \nu_k} \mathbf{h}_k^H \mathbf{w}_k}{\sum_{i=1}^K |\mathbf{h}_k^H \mathbf{w}_i|^2 + \sigma_k^2}, \forall k \quad (12)$$

Proof: See Appendix B.

Using Proposition 2, Eq. (9) can be further reformulated as

$$\sum_{k=1}^K \log(1 + \nu_k) - \sum_{k=1}^K \nu_k + \sum_{k=1}^K \left(2\sqrt{1 + \nu_k} \Re\{\tau_k^* \mathbf{h}_k^H \mathbf{w}_k\} - \sum_{i=1}^K |\tau_i|^2 |\mathbf{h}_k^H \mathbf{w}_i|^2 - |\tau_k|^2 \sigma_k^2 \right). \quad (13)$$

To facilitate the beamforming design, we determine the optimal auxiliary variables ν_k and τ_k by applying $\nu_k = \gamma_k$ and Eq. (12). Then, we extract the term containing \mathbf{w}_k from the objective function (13) and rewrite the objective function as

$$\sum_{k=1}^K \left(2\sqrt{1 + \nu_k} \Re\{\tau_k^* \mathbf{h}_k^H \mathbf{w}_k\} - \sum_{i=1}^K |\tau_i|^2 |\mathbf{h}_i^H \mathbf{w}_k|^2 \right) = \sum_{k=1}^K \left(\sqrt{1 + \nu_k} (\tau_k^* \mathbf{h}_k^H \mathbf{w}_k + \mathbf{w}_k^H \mathbf{h}_k \tau_k) - \mathbf{w}_k^H \sum_{i=1}^K |\tau_i|^2 \mathbf{h}_i \mathbf{h}_i^H \mathbf{w}_k \right), \quad (14)$$

where the equality holds due to $2\Re\{A\} = A + A^H$. By defin-

ing $\boldsymbol{\beta}_k = \sqrt{1 + \nu_k} \mathbf{h}_k \tau_k$ and $\Lambda = \sum_{i=1}^K |\tau_i|^2 \mathbf{h}_i \mathbf{h}_i^H$, the optimization problem can be compactly formulated as

$$\max_{\{\mathbf{w}_k\}} \sum_{k=1}^K (\boldsymbol{\beta}_k^H \mathbf{w}_k + \mathbf{w}_k^H \boldsymbol{\beta}_k - \mathbf{w}_k^H \Lambda \mathbf{w}_k), \quad (15a)$$

$$\text{s.t.} \quad \sum_{k=1}^K |\mathbf{w}_k|^2 \leq P_{\max}, \quad (15b)$$

$$\mathbf{a}^H(\theta_q) \left(\sum_{k=1}^K \mathbf{w}_k \mathbf{w}_k^H \right) \mathbf{a}(\theta_q) \geq \Gamma_q P_{\max}, \forall q. \quad (15c)$$

One can see that (15) is a non-homogeneous quadratic constrained quadratic programming (QCQP) problem. In the next subsection, we reformulate the problem (15) as a homogeneous QCQP problem and adopt the SDR technique to obtain the optimized DFRC beamformers.

3.2 Solution via SDR

We first derive the equivalent form of beampattern gain constraint (15c) by introducing the auxiliary variable t , i.e.,

$$\sum_{k=1}^K \mathbf{a}^H(\theta_q) \left(\sum_{i=1}^K \mathbf{w}_i \mathbf{w}_i^H \right) \mathbf{a}(\theta_q) = \sum_{k=1}^K \begin{bmatrix} \mathbf{a}^H(\theta_q), 0 \end{bmatrix} \begin{bmatrix} \mathbf{w}_k \\ t \end{bmatrix} \begin{bmatrix} \mathbf{w}_k^H, t \end{bmatrix} \begin{bmatrix} \mathbf{a}(\theta_q) \\ 0 \end{bmatrix} = \sum_{i=1}^K \mathbf{x}_i^H \mathbf{C}_q \mathbf{x}_i, \quad (16)$$

where the last equality holds by defining

$$\mathbf{x}_k = \begin{bmatrix} \mathbf{w}_k \\ t \end{bmatrix}, \mathbf{C}_q = \begin{bmatrix} \mathbf{a}(\theta_q) \mathbf{a}(\theta_q)^H & 0 \\ 0 & 0 \end{bmatrix}, \mathbf{X}_k = \mathbf{x}_k \mathbf{x}_k^H. \quad (17)$$

The non-homogeneous objection function (15a) can be equivalently expressed as the following homogeneous form:

$$\sum_{k=1}^K \left(\begin{bmatrix} \mathbf{w}_k^H, t \end{bmatrix} \begin{bmatrix} -\Lambda & \boldsymbol{\beta}_k \\ \boldsymbol{\beta}_k^H & 0 \end{bmatrix} \begin{bmatrix} \mathbf{w}_k \\ t \end{bmatrix} \right), \quad (18)$$

where Eq. (18) equals to the objective function (15a) by introducing the constraint $t^2 = 1$, which can be equivalently written by

$$t^2 = \begin{bmatrix} \mathbf{w}_k^H, t \end{bmatrix} \begin{bmatrix} 0_N & 0 \\ 0 & 1 \end{bmatrix} \begin{bmatrix} \mathbf{w}_k \\ t \end{bmatrix} = 1. \quad (19)$$

Also, the power constraint (15b) can be manipulated as

$$\sum_{k=1}^K \begin{bmatrix} \mathbf{w}_k^H, t \end{bmatrix} \begin{bmatrix} \mathbf{I}_N & 0 \\ 0 & 0 \end{bmatrix} \begin{bmatrix} \mathbf{w}_k \\ t \end{bmatrix} \leq P_{\max}. \quad (20)$$

For simplicity, we define

$$\mathbf{A}_k = \begin{bmatrix} -\Lambda & \boldsymbol{\beta}_k \\ \boldsymbol{\beta}_k^H & 0 \end{bmatrix}, \mathbf{B} = \begin{bmatrix} \mathbf{I}_N & 0 \\ 0 & 0 \end{bmatrix}, \mathbf{D} = \begin{bmatrix} 0_N & 0 \\ 0 & 1 \end{bmatrix}. \quad (21)$$

Optimization problem (15) can be restated as

$$\begin{aligned} & \max_{\{\mathbf{X}_k\} \in \mathbb{H}^{N+1}} \sum_{k=1}^K \text{Tr}(\mathbf{A}_k \mathbf{X}_k), \\ & \text{s.t.} \quad \sum_{k=1}^K \text{Tr}(\mathbf{B} \mathbf{X}_k) \leq P_{\max}, \\ & \quad \sum_{k=1}^K \text{Tr}(\mathbf{C}_q \mathbf{X}_k) \geq \Gamma_q P_{\max}, \forall q, \\ & \quad \text{Tr}(\mathbf{D} \mathbf{X}_k) = 1, \text{rank}(\mathbf{X}_k) = 1, \\ & \quad \mathbf{X}_k \succeq 0, \end{aligned} \quad (22)$$

where \mathbb{H}^{N+1} is the set of $N+1$ dimensional complex Hermitian matrices. Note that Eq. (22) is still a non-convex optimization problem due to the existence of rank-one constraints. We relax the non-convex constraints and then transform problem (22) into a convex one. Then, we can solve the converted problem using the CVX toolbox in MATLAB^[21]. Finally, by applying the Gaussian randomization technique to reduce the rank of the \mathbf{X}_k matrix to one^[18], we obtain the beamforming vectors $\{\mathbf{w}_k\}_{k=1}^K$. Algorithm 1 summarizes the proposed algorithm for problem (8).

Algorithm 1. The Proposed Algorithm for Problem (8)

Input: $N, K, \mathbf{h}_1, \dots, \mathbf{h}_K$, maximum iteration number iter_{\max} , and threshold $\varepsilon > 0$

Output: $\{\mathbf{w}_k\}_{k=1}^K$

1. Initialize randomly $\{\mathbf{w}_k^{(0)}\}_{k=1}^K$, compute the sum rate $R^{(0)}$;
 2. **While** $\text{iter} \leq \text{iter}_{\max}$ and $|R^{(\text{iter})} - R^{(\text{iter}-1)}|/B \geq \varepsilon$ **do**
 3. Update $\{\nu_k^{(\text{iter})}\}_{k=1}^K$ via $\nu_k = \gamma_k, \forall k$;
 4. Update $\{\tau_k^{(\text{iter})}\}_{k=1}^K$ via (12);
 5. Update $\{\mathbf{w}_k^{(\text{iter})}\}_{k=1}^K$ via (22) and Gaussian randomization technique;
 6. Compute $R^{(\text{iter})}$ via (5);
 7. $\text{iter} = \text{iter} + 1$;
 8. **End while.**
-

The main computational complexity of the overall algorithm is dominated by Step 5 of Algorithm 1. For solving problem (22), the interior-point method is commonly utilized^[12]. The computational complexity of updating $\{\mathbf{X}_k\}_{k=1}^K$ is $\mathcal{O}(K^{3.5} N^7 \log(1/\varepsilon))$, where ε is the given accuracy level. The Gaussian randomization technique is then employed to recover the beamforming vectors, which adds a complexity of

$\mathcal{O}(K^{2.5}N^3)$. The overall complexity is of order $\mathcal{O}(K^{3.5}N^7 \log(1/\epsilon) + \mathcal{O}(K^{2.5}N^3))^{[22]}$.

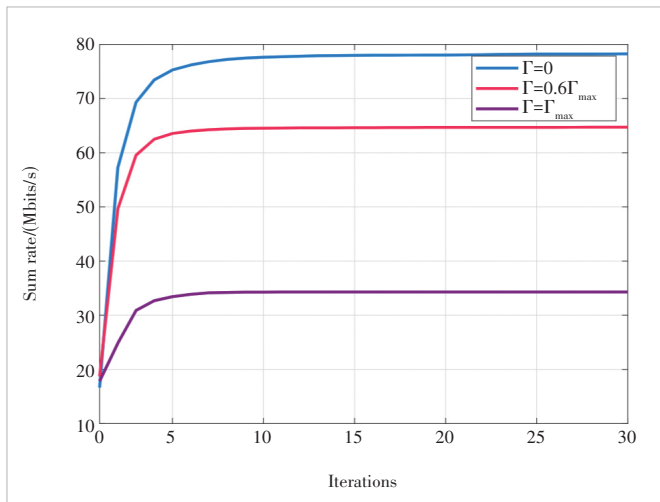
4 Numerical Results

In this section, we present the numerical results to investigate the performance of the proposed DFRC joint beamforming design.

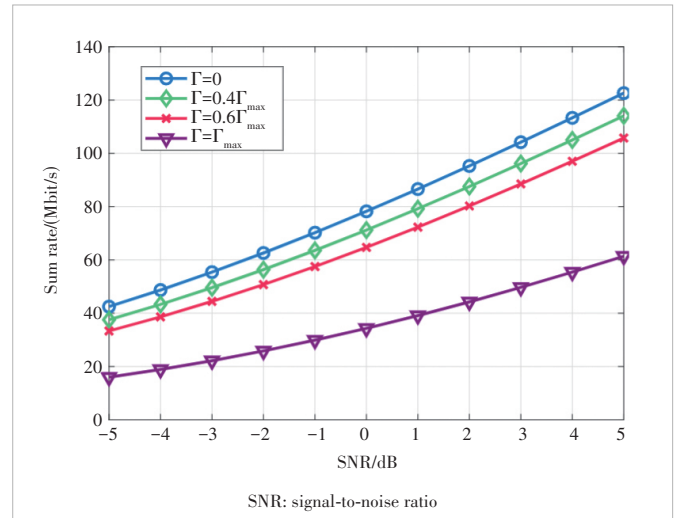
Unless stated otherwise, we assume that the BS equipped with $N = 16$ antennas is serving $K = 4$ users^[23], and the antenna spacing is set to $d = \lambda/2$. As for the channel model, we consider $L_k = 5$ paths with $\alpha_{k,l} \sim \mathcal{CN}(0, 1)$. The AoDs follow the Laplacian distribution with uniformly distributed in $[0, \pi)$ and angular spread of five degrees^[24]. We set the bandwidth as $B = 10$ MHz. In addition, we set $Q = 3$ sensing directions with angles of 50° , 90° and 130° ^[13]. We assume that the beampattern gain is the same for all target directions ($\Gamma_q = \Gamma, \forall q$), which allows us to calculate the maximum weighting coefficient of beampattern gain for each direction as $\Gamma_{\max} = 1/Q$. The signal-to-noise ratio (SNR) is defined as P_{\max}/σ_k^2 , with $\sigma_k^2 = 1, \forall k$. We set the maximum iteration number $\text{iter}_{\max} = 100$ and threshold $\epsilon = 10^{-3}$. The performance of the proposed algorithm is averaged over 500 Monte-Carlo realizations.

In Fig. 2, we demonstrate the convergence behavior of the proposed algorithm under different beampattern gains, while holding a fixed SNR of 0 dB. It is evident that the proposed algorithm converges after 30 iterations. This trend is steady, indicating a robust and stable algorithm.

Fig. 3 illustrates the performance of sum rates versus SNR for different values of Γ . As seen in Fig. 3, the sum rate is the highest in the communication-only case ($\Gamma = 0$), which means there is no constraint imposed by the radar beampattern gain. Conversely, as Γ incrementally increases, a noticeable decline in the sum rate performance is observed. This trend can be attributed to the shifting design focus towards enhancing radar



▲ Figure 2. Sum rate convergence behavior of the proposed algorithm

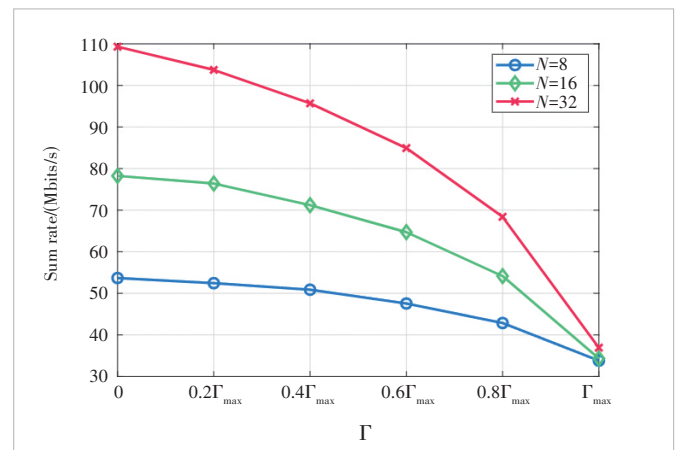


▲ Figure 3. Sum rate versus SNR for different Γ

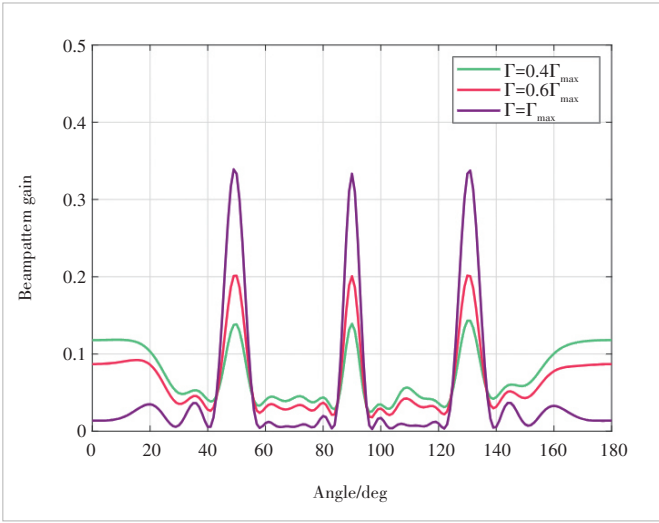
sensing capabilities. In essence, as the value of Γ escalates, the system's priority transitions from solely maximizing communication sum rate to a more balanced approach.

We evaluate the trade-off between the communication sum rate and the radar beampattern gain with different numbers of BS antennas in Fig. 4, where SNR is set to 0 dB. It can be seen that the sum rate performance increases with the number of antennas. Additionally, when the number of antennas increases, the beampattern gain increases as well due to the increased DoF.

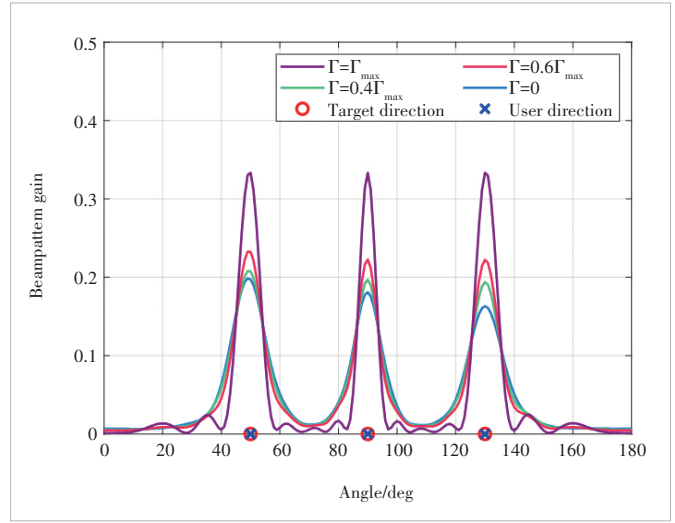
Fig. 5 depicts the beampattern gain of the proposed design when SNR = 0 dB. Our proposed DFRC design simultaneously allocates the beampattern gain to the directions of the sensing targets and communication users. Specifically, as the value of Γ increases, the beampattern gain weight becomes more tilted towards the radar, which is consistent with the results in Fig. 3, where the sum rate gradually decreases. In Fig. 6, we further present the beampattern performance, where users are located at $[30^\circ, 70^\circ, 110^\circ, 150^\circ]$. One can clearly ob-



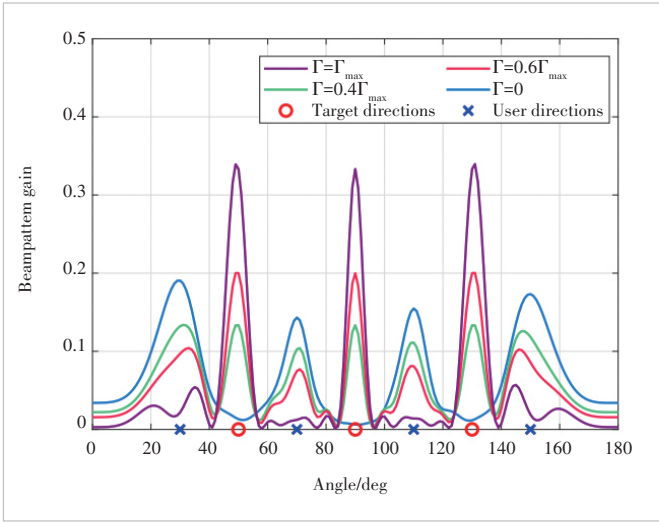
▲ Figure 4. Sum rate versus Γ for different numbers of antenna



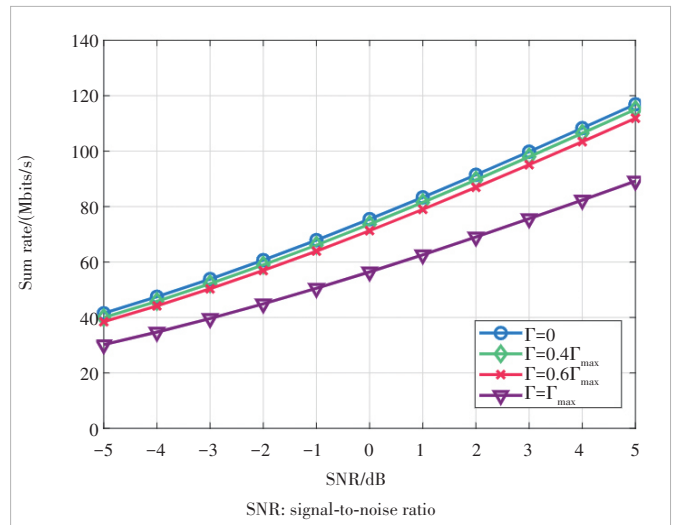
▲ Figure 5. Radar sensing beampattern performance comparison of different Γ , where user directions are uniformly distributed from $[0, \pi)$



▲ Figure 7. Radar sensing beampattern performance comparison of different Γ , where the positions of the communication users and radar targets coincide



▲ Figure 6. Radar sensing beampattern performance comparison of different Γ , where users are located at $[30^\circ, 70^\circ, 110^\circ, 150^\circ]$



▲ Figure 8. Sum rate versus SNR for different Γ , where the positions of the communication users and radar targets coincide

serve that the beampattern gain is allocated to the desired directions of the sensing targets and users in the radar-only ($\Gamma = \Gamma_{\max}$) and communication-only ($\Gamma = 0$) cases.

Fig. 7 depicts the radar sensing beampattern performance for different values when the positions of the communication users and radar targets coincide. One can see that, as the Γ value increases, the beampattern gain at the radar target and communication target directions ($50^\circ, 90^\circ, 130^\circ$) increases. In addition, compared to the case where users and targets are located at different directions in Figs. 5 and 6, the case where users and radar targets coincide shows higher beampattern gain at the same value of Γ . Fig. 8 shows that the proposed method achieves a balance between communication and sensing. In the radar-only case, compared to the scenario where the communication users and radar targets are separated, the

sum rate performance is better.

5 Conclusions

In this work, we study a joint beamforming design problem for the DFRC system and propose an iterative algorithm to maximize the sum rate under the radar beampattern gain and power constraints. Utilizing the FP technique, we transform the complex non-convex problem into a more tractable form and apply the SDR technique to solve this transformed problem. From our experimentation, we demonstrate that the proposed algorithm can achieve a flexible trade-off between the communication sum rate and the radar beampattern gain performance.

Appendix A

By introducing K auxiliary variables ν_k to replace each fractional term γ_k in Eq. (5), we can rewrite the unconstrained sum rate maximization problem as

$$\begin{aligned} & \max \sum_{k=1}^K \log(1 + \nu_k) \\ & \text{s.t. } \nu_k \leq \gamma_k, \forall k. \end{aligned} \quad (23)$$

Note that Eq. (23) is a convex optimization problem satisfying the strong duality^[25]. By introducing K multipliers λ_k , we can obtain a Lagrangian function as

$$\mathcal{L} = \sum_{k=1}^K \log(1 + \nu_k) - \sum_{k=1}^K \lambda_k (\nu_k - \gamma_k). \quad (24)$$

By setting $\partial \mathcal{L} / \partial \nu_k = 0$, we obtain the optimal $\nu_k^* = \gamma_k$. By setting $\partial \mathcal{L} / \partial \lambda_k = 0$, we can obtain the optimal λ_k^* as

$$\lambda_k^* = \frac{1}{1 + \gamma_k}. \quad (25)$$

With the optimal λ_k^* , Eq. (24) can be written as

$$\begin{aligned} \mathcal{L}^* &= \sum_{k=1}^K \log(1 + \nu_k) - \sum_{k=1}^K \lambda_k^* (\nu_k - \gamma_k) = \\ & \sum_{k=1}^K \log(1 + \nu_k) - \sum_{k=1}^K \frac{\nu_k}{1 + \gamma_k} + \sum_{k=1}^K \frac{\gamma_k}{1 + \gamma_k} = \\ & \sum_{k=1}^K \log(1 + \nu_k) - \sum_{k=1}^K \frac{\nu_k \left(\sum_{i \neq k}^K |\mathbf{h}_k^H \mathbf{w}_i|^2 + \sigma_k^2 + |\mathbf{h}_k^H \mathbf{w}_k|^2 \right)}{\sum_{i=1}^K |\mathbf{h}_k^H \mathbf{w}_i|^2 + \sigma_k^2} + \\ & \sum_{k=1}^K \frac{\nu_k |\mathbf{h}_k^H \mathbf{w}_k|^2}{\sum_{i=1}^K |\mathbf{h}_k^H \mathbf{w}_i|^2 + \sigma_k^2} + \sum_{k=1}^K \frac{|\mathbf{h}_k^H \mathbf{w}_k|^2}{\sum_{i=1}^K |\mathbf{h}_k^H \mathbf{w}_i|^2 + \sigma_k^2} = \\ & \sum_{k=1}^K \log(1 + \nu_k) - \sum_{k=1}^K \nu_k + \sum_{k=1}^K \frac{(1 + \nu_k) |\mathbf{h}_k^H \mathbf{w}_k|^2}{\sum_{i=1}^K |\mathbf{h}_k^H \mathbf{w}_i|^2 + \sigma_k^2}, \end{aligned} \quad (26)$$

where the second equation holds by substituting the expression of γ_k in Eq. (6). Expression (26) has the same form as Eq. (9) in Proposition 1. By substituting ν_k^* back into Eq. (9), we can obtain objective function (8a), which completes the proof.

Appendix B

To obtain an equivalent form of Eq. (10), we can rewrite Eq. (11) as

$$\begin{aligned} & \sqrt{1 + \nu_k} \Re \{ \tau_k^* \mathbf{h}_k^H \mathbf{w}_k \} - \sum_{i=1}^K |\tau_i|^2 |\mathbf{h}_k^H \mathbf{w}_i|^2 - |\tau_k|^2 \sigma_k^2 = \\ & \left(\sum_{i=1}^K |\mathbf{h}_k^H \mathbf{w}_i|^2 + \sigma_k^2 \right) \left[\frac{2 \sqrt{1 + \nu_k} \Re \{ \tau_k^* \mathbf{h}_k^H \mathbf{w}_k \}}{\sum_{i=1}^K |\mathbf{h}_k^H \mathbf{w}_i|^2 + \sigma_k^2} - |\tau_k|^2 \right] = \\ & \left(\sum_{i=1}^K |\mathbf{h}_k^H \mathbf{w}_i|^2 + \sigma_k^2 \right) \left[\frac{(1 + \nu_k) |\mathbf{h}_k^H \mathbf{w}_k|^2}{\left(\sum_{i=1}^K |\mathbf{h}_k^H \mathbf{w}_i|^2 + \sigma_k^2 \right)^2} - \left| \frac{\sqrt{1 + \nu_k} \mathbf{h}_k^H \mathbf{w}_k}{\sum_{i=1}^K |\mathbf{h}_k^H \mathbf{w}_i|^2 + \sigma_k^2} - \tau_k \right|^2 \right], \forall k. \end{aligned} \quad (27)$$

where the first equation holds by factoring out the common terms from $\sum_{i=1}^K |\mathbf{h}_k^H \mathbf{w}_i|^2 + \sigma_k^2$. Note that, when we have

$$\tau_k^* = \frac{\sqrt{1 + \nu_k} \mathbf{h}_k^H \mathbf{w}_k}{\sum_{i=1}^K |\mathbf{h}_k^H \mathbf{w}_i|^2 + \sigma_k^2}, \forall k, \quad (28)$$

Eq. (27) becomes equivalent to Eq. (10) in Proposition 2, which completes the proof.

References

- [1] LIU F, CUI Y H, MASOUIROS C, et al. Integrated sensing and communications: toward dual-functional wireless networks for 6G and beyond [J]. *IEEE journal on selected areas in communications*, 2022, 40(6): 1728 - 1767. DOI: 10.1109/jsac.2022.3156632
- [2] YUAN W J, WEI Z Q, LI S Y, et al. Integrated sensing and communication-assisted orthogonal time frequency space transmission for vehicular networks [J]. *IEEE journal of selected topics in signal processing*, 2021, 15(6): 1515 - 1528. DOI: 10.1109/JSTSP.2021.3117404
- [3] LI J P, SHAO X D, CHEN F, et al. Networked integrated sensing and communications for 6G wireless systems [J]. *IEEE Internet of Things journal*, 2024, PP(99): 1. DOI: 10.1109/JIOT.2024.3406598
- [4] ZHOU W X, ZHANG R Y, CHEN G Y, et al. Integrated sensing and communication waveform design: a survey [J]. *IEEE open journal of the communications society*, 2022, 3: 1930 - 1949. DOI: 10.1109/OJCOMS.2022.3215683
- [5] ZHANG R Y, SHIM B, YUAN W J, et al. Integrated sensing and communication waveform design with sparse vector coding: low sidelobes and ultra reliability [J]. *IEEE transactions on vehicular technology*, 2022, 71(4): 4489 - 4494. DOI: 10.1109/TVT.2022.3146280
- [6] ZHANG R Y, CHENG L, WANG S, et al. Integrated sensing and communication with massive MIMO: a unified tensor approach for channel and target parameter estimation [J]. *IEEE transactions on wireless communications*, 2024. DOI: 10.1109/TWC.2024.3351856
- [7] HASSANIEN A, AMIN M G, ABOUTANIOS E, et al. Dual-function radar communication systems: a solution to the spectrum congestion problem [J]. *IEEE signal processing magazine*, 2019, 36(5): 115 - 126. DOI: 10.1109/MSP.2019.2900571
- [8] CHEN G Y, ZHANG R Y, REN H, et al. Hybrid beamforming design with overlapped subarrays for massive MIMO-ISAC systems [C]//Proc. 2023 IEEE Global Communications Conference. IEEE, 2023: 528 - 533. DOI:

- 10.1109/GLOBECOM54140.2023.10437590
- [9] MA D Y, SHLEZINGER N, HUANG T Y, et al. Joint radar-communication strategies for autonomous vehicles: combining two key automotive technologies [J]. *IEEE signal processing magazine*, 2020, 37(4): 85 – 97. DOI: 10.1109/MSP.2020.2983832
- [10] LIU F, MASOUIROS C, LI A, et al. MU-MIMO communications with MIMO radar: from co-existence to joint transmission [J]. *IEEE transactions on wireless communications*, 2018, 17(4): 2755 – 2770. DOI: 10.1109/TWC.2018.2803045
- [11] LIU X, HUANG T Y, LIU Y M. Transmit design for joint MIMO radar and multiuser communications with transmit covariance constraint [J]. *IEEE journal on selected areas in communications*, 2022, 40(6): 1932 – 1950. DOI: 10.1109/JSAC.2022.3155512
- [12] WANG X Y, FEI Z S, ZHANG J A, et al. Partially-connected hybrid beamforming design for integrated sensing and communication systems [J]. *IEEE transactions on communications*, 2022, 70(10): 6648 – 6660. DOI: 10.1109/TCOMM.2022.3202215
- [13] CHEN L, WANG Z Q, DU Y, et al. Generalized transceiver beamforming for DFRC with MIMO radar and MU-MIMO communication [J]. *IEEE journal on selected areas in communications*, 2022, 40(6): 1795 – 1808. DOI: 10.1109/JSAC.2022.3155515
- [14] LIU F, MASOUIROS C, PETROPULU A P, et al. Joint radar and communication design: applications, state-of-the-art, and the road ahead [J]. *IEEE transactions on communications*, 2020, 68(6): 3834 – 3862. DOI: 10.1109/TCOMM.2020.2973976
- [15] DONG F W, WANG W, HU Z Y, et al. Low-complexity beamformer design for joint radar and communications systems [J]. *IEEE communications letters*, 2021, 25(1): 259 – 263. DOI: 10.1109/LCOMM.2020.3024574
- [16] HUA H C, XU J, HAN T X. Optimal transmit beamforming for integrated sensing and communication [J]. *IEEE transactions on vehicular technology*, 2023, 72(8): 10588 – 10603. DOI: 10.1109/TVT.2023.3262513
- [17] SHEN K M, YU W. Fractional programming for communication systems: part I: power control and beamforming [J]. *IEEE transactions on signal processing*, 2018, 66(10): 2616 – 2630. DOI: 10.1109/TSP.2018.2812733
- [18] LUO Z Q, MA W K, SO A M C, et al. Semidefinite relaxation of quadratic optimization problems [J]. *IEEE signal processing magazine*, 2010, 27(3): 20 – 34. DOI: 10.1109/MSP.2010.936019
- [19] ZHANG R Y, SHIM B, ZHAO H L. Downlink compressive channel estimation with phase noise in massive MIMO systems [J]. *IEEE transactions on communications*, 2020, 68(9): 5534 – 5548. DOI: 10.1109/TCOMM.2020.2998141
- [20] STOICA P, LI J, XIE Y. On probing signal design for MIMO radar [J]. *IEEE transactions on signal processing*, 2007, 55(8): 4151 – 4161. DOI: 10.1109/tsp.2007.894398
- [21] GRANT M, BOYD S. CVX: MATLAB software for disciplined convex programming, version 2.1 [R]. 2014
- [22] BEN-TAL A, NEMIROVSKI A. *Lectures on modern convex optimization* [M]. Philadelphia, USA: Society for Industrial and Applied Mathematics, 2001. DOI: 10.1137/1.9780898718829
- [23] LIU X, HUANG T Y, SHLEZINGER N, et al. Joint transmit beamforming for multiuser MIMO communications and MIMO radar [J]. *IEEE transactions on signal processing*, 2020, 68: 3929 – 3944. DOI: 10.1109/TSP.2020.3004739
- [24] EL AYACH O, RAJAGOPAL S, ABU-SURRA S, et al. Spatially sparse precoding in millimeter wave MIMO systems [J]. *IEEE transactions on wireless communications*, 2014, 13(3): 1499 – 1513. DOI: 10.1109/TWC.2014.011714.130846
- [25] BOYD S, VANDENBERGHE L. *Convex optimization* [M]. Cambridge, UK: Cambridge University Press, 2004. DOI: 10.1017/cbo9780511804441

Biographies

CHEN Guangyi received his BE degree in electronic science and technology from Chongqing University of Posts and Telecommunications, China in 2021, MS degree from Nanjing University of Science and Technology, China. He is currently pursuing a PhD degree with the Department of Electronics and Communications Engineering, Nanjing University of Science and Technology. His current research interests include MIMO systems, hybrid precoding, and integrated sensing and communication.

ZHANG Ruoyu (ryzhang19@njjust.edu.cn) received his BE and PhD degrees in information and communication engineering from Harbin Institute of Technology, China in 2014 and 2019, respectively. From 2017 to 2018, he was a visiting student with the Department of Electrical and Computer Engineering, The University of British Columbia, Canada. He is currently an associate professor with the School of Electronic and Optical Engineering, Nanjing University of Science and Technology, China. His research interests include integrated sensing and communication, massive MIMO, millimeter-wave communications, and sparse signal processing.

REN Hong received her bachelor's degree in electronic information engineering from Jiangsu University, China in 2022. She is currently pursuing a master's degree in the School of Electronic and Optical Engineering, Nanjing University of Science and Technology, China. Her main research focus is integrated sensing and communication beamforming.

LIN Xu received his BS degree from Harbin Institute of Technology, China in 2014, and MS degree from the China Academy of Telecommunications Technology in 2017. He is currently pursuing a PhD degree with the School of Electronics and Information Engineering, Harbin Institute of Technology. From 2019 to 2020, he was a research trainee with the Department of Electrical and Computer Engineering, McGill University, Canada. His research interests include communication signal processing, physical waveform design, transform domain communication systems, and synchronization.

WU Wen received his PhD degree in electromagnetic field and microwave technology from Southeast University, China in 1997. He is currently a professor with the School of Electronic and Optical Engineering, Nanjing University of Science and Technology, China, where he is also a director with the Key Laboratory of Near-Range RF Sensing ICs & Microsystems (NJUST), Ministry of Education of the People's Republic of China. He has authored or co-authored over 300 journal articles and conference papers, and has submitted over 30 patent applications. His current research interests include microwave and millimeter-wave theories and technologies, microwave and millimeter-wave detection, and multimode compound detection. He was a recipient of six Ministerial and Provincial-Level Science and Technology Awards.



On Normalized Least Mean Square Based Interference Cancellation Algorithm for Integrated Sensing and Communication Systems

YU Xiaohui, YU Shucheng, LIU Xiqing, PENG Mugen

(Beijing University of Posts and Telecommunications, Beijing 100876, China)

DOI: 10.12142/ZTECOM.202403004

<https://kns.cnki.net/kcms/detail/34.1294.TN.20240919.1205.004.html>, published online September 19, 2024

Manuscript received: 2024-08-04

Abstract: Integrated sensing and communication (ISAC) technology is a promising candidate for next-generation communication systems. However, severe co-site interference in existing ISAC systems limits the communication and sensing performance, posing significant challenges for ISAC interference management. In this work, we propose a novel interference management scheme based on the normalized least mean square (NLMS) algorithm, which mitigates the impact of co-site interference by reconstructing the interference from the local transmitter and canceling it from the received signal. Simulation results demonstrate that, compared to typical adaptive interference management schemes based on recursive least square (RLS) and stochastic gradient descent (SGD) algorithms, the proposed NLMS algorithm effectively cancels co-site interference and achieves a good balance between computational complexity and convergence performance.

Keywords: interference management; OFDM; 5G new radio; interference cancellation; radio frequency domain

Citation (Format 1): YU X H, YU S C, LIU X Q, et al. On normalized least mean square based interference cancellation algorithm for integrated sensing and communication systems [J]. *ZTE Communications*, 2024, 22(3): 21 – 28. DOI: 10.12142/ZTECOM.202403004

Citation (Format 2): X. H. Yu, S. C. Yu, X. Q. Liu, et al., “On normalized least mean square based interference cancellation algorithm for integrated sensing and communication systems,” *ZTE Communications*, vol. 22, no. 3, pp. 21 – 28, Sept. 2024. doi: 10.12142/ZTECOM.202403004.

1 Introduction

With the development of wireless communication technologies, the number of users and access devices is rapidly increasing, leading to an urgent shortage of communication spectrum resources. Traditionally, communication and sensing systems have been designed, developed and deployed independently. However, the congestion of the available radio spectrum has stimulated interest in combining communication and sensing functions within shared frequency bands and potentially on the same hardware platforms. In frequency bands below 10 GHz, such as the L-band (1 – 2 GHz), S-band (2 – 4 GHz), and C-band (4 – 8 GHz), radar systems, Long-Term Evolution (LTE), and wireless local area network (WLAN) communication systems are widely favored. Above 10 GHz, the operating frequencies of 5G millimeter-wave communication systems are very close to those of automotive millimeter-wave radars. Therefore, realiz-

ing integrated sensing and communication (ISAC) has become necessary and feasible^[1]. Currently, ISAC can be classified into two categories: One focuses on the coexistence of communication and sensing signals within the same frequency bands^[2]; the other aims to use a unified hardware platform with ISAC signals^[3].

Interference management is a critical challenge for the above ISAC implementation approaches. In coexistence-based ISAC systems, communication and sensing are implemented by independent hardware that transmits different signals. These systems are often not scheduled or synchronized with each other, resulting in severe mutual interference between communication and sensing signals. Consequently, dual-function radar-communication systems face high hardware complexity and difficulties in joint optimization of radar and communication functions. A current mainstream research direction is to design integrated waveforms based on existing communication signals to achieve communication and sensing simultaneously. In such ISAC systems, interference management becomes even more complex.

Many studies have focused on interference management in ISAC systems^[4], where opportunistic spectrum sharing^[5] and

This work were supported in part by the National Key Research and Development Program of China under Grant No. 2021YFB2900200, in part by National Natural Science Foundation of China under Grant Nos. 61925101 and 62271085, and in part by Beijing Natural Science Foundation under Grant No. L223007-2.

null space projection^[6] are the two typical methods for mitigating interference between communication and sensing signals. Recently, optimization theory has been widely investigated for its effectiveness in interference management in ISAC systems^[7-8]. The authors in Ref. [9] studied the spectrum sharing between multiple-input multiple-output (MIMO) based radar and communication systems in cluttered environments. To achieve effective clutter suppression, the ISAC system was designed by jointly optimizing the communication covariance matrix and the radar sub-sampling matrix. This scheme minimizes the interference power at the receiver of the radar system while maintaining the communication performance^[10]. In Ref. [11], a novel coexistence architecture for communication systems and pulse radars was proposed, together with a comprehensive performance evaluation. Different from the coordinated coexistence of communication and radar in most existing ISAC systems, the authors in Ref. [12] investigated the coexistence of communication and sensing functions in uncoordinated scenarios, with a particular focus on the dynamics of information sharing.

Additionally, interference cancellation in full-duplex systems has been a hot topic for long^[13]. An iterative successive nonlinear co-site interference cancellation method for in-band full-duplex communication was proposed in Ref. [14], which significantly improves co-site interference cancellation through multiple iterations. In Ref. [15], a low-latency precoding strategy for in-band full-duplex MIMO relay systems was introduced to achieve interference cancellation through time, space, and radio-frequency (RF) domains^[16]. The authors in Ref. [17] discussed joint analog and digital co-site interference cancellation techniques in full-duplex transceivers with frequency-dependent in-phase/quadrature (I/Q) imbalance. KIAYANI et al. studied adaptive nonlinear RF interference cancellation techniques to improve system isolation performance^[18]. In fact, interference management in ISAC systems is similar to that in full-duplex systems^[19]. Some works have designed dual-function radar and communication systems based on orthogonal frequency division multiplexing (OFDM) signals. In Ref. [20], monostatic sensing using OFDM in the presence of phase noise was investigated. The results show that with appropriate processing strategies, phase noise can not only be mitigated but also exploited to improve the sensing accuracy. In Ref. [21], the beam-domain full-duplex massive MIMO technology was investigated, where a precise beamforming scheme and a co-site interference cancellation strategy were proposed to improve spectrum utilization. LIU et al. proposed an effective channel estimation method for interference channel estimation in the coexistence of radar and communication systems^[22]. Moreover, the authors in Ref. [23] investigated integrating sensing capabilities into communication systems without significantly increasing system complexity.

In this work, we delve into interference management in

ISAC systems and propose a normalized least mean square (NLMS) algorithm to mitigate co-site interference. Specifically, we begin with a brief review of the widely implemented OFDM-based ISAC system models. Different from most existing works on ISAC technologies, we perform a detailed modeling and analysis of co-site interference in ISAC systems. On this basis, we propose the NLMS algorithm to reconstruct and cancel the co-site interference received from the local transmitter (Tx) at the integrated receiver (Rx). Simulation results demonstrate that the proposed algorithm effectively cancels interference and strikes a good balance between computational complexity and algorithm convergence performance. This work further advances the theory of ISAC interference management and has significant implications for guiding engineering practice.

2 System Model

Most existing works on ISAC have generally assumed that the signals received at the integrated receiver consist only of echoes and noise, neglecting the co-site interference caused by the local transmitter. To briefly illustrate the OFDM-based integrated signal processing, we first introduce the ideal interference-free ISAC system model. In this work, we investigate an OFDM-ISAC system with N subcarriers, where each subcarrier carries M OFDM symbols per frame. The subcarrier spacing is assumed to be Δf , and the symbol time can be obtained by $T = 1/\Delta f$. The transmitted OFDM symbol matrix is written as

$$\mathbf{F}_{\text{Tx}} = \begin{pmatrix} x_{0,0} & \cdots & x_{0,l} & \cdots & x_{0,M-1} \\ \vdots & \ddots & \vdots & \ddots & \vdots \\ x_{k,0} & \cdots & x_{k,l} & \cdots & x_{k,M-1} \\ \vdots & \ddots & \vdots & \ddots & \vdots \\ x_{N-1,0} & \cdots & x_{N-1,l} & \cdots & x_{N-1,M-1} \end{pmatrix}, \mathbf{F}_{\text{Tx}} \in \mathcal{A}^{N \times M} \quad (1)$$

The Doppler shift causes a phase shift in each element of \mathbf{F}_{Tx} , and each subcarrier experiences a different phase shift. For a delay of τ , the phase shift on the k -th subcarrier is expressed as $e^{j2\pi(k\Delta f + f_0)\tau}$, where f_0 is the carrier frequency. Hence, the echo signal of the l -th symbol on the k -th subcarrier is given as

$$(\mathbf{F}_{\text{Rx}})_{k,l} = b_0(\mathbf{F}_{\text{Tx}})_{k,l} \cdot \exp(j2\pi T f_D l - j2\pi\tau(k\Delta f + f_0)) + (\tilde{\mathbf{Z}})_{k,l} \quad (2)$$

where f_D is the Doppler shift and b_0 is the round-trip path loss. The matrix $\tilde{\mathbf{Z}} \in \mathbb{C}^{N \times M}$ represents the additive white Gaussian noise (AWGN) with power σ^2 . Clearly, \mathbf{F}_{Rx} contains the parameters τ, f_D and b_0 to be estimated. As \mathbf{F}_{Tx} is also known to the integrated receiver, the transmitted symbols are removed from the received echo signal by symbol-wise division as

$$(\mathbf{F})_{k,l} = \frac{(\mathbf{F}_{\text{Rx}})_{k,l}}{(\mathbf{F}_{\text{Tx}})_{k,l}} = b_0 \cdot \exp\left(j2\pi T f_D l - j2\pi\tau(k\Delta f + f_0)\right) + (\mathbf{Z})_{k,l}. \quad (3)$$

Here, $(\mathbf{Z})_{k,l} = (\tilde{\mathbf{Z}})_{k,l}/(\mathbf{F}_{\text{Tx}})_{k,l}$ is the noise sample after symbol-wise division. The Doppler shift f_D and the target distance R are obtained by discrete Fourier transform (DFT) for each row and inverse discrete Fourier transform (IDFT) for each column of $(\mathbf{F})_{k,l}$, respectively. Here, we denote the peak index of the n -th row of \mathbf{F} after DFT as $\tilde{m}_{F,n}$, and the speed of the target v can be obtained by

$$\tilde{m}_{F,n} = \lfloor f_D T M \rfloor, \quad v = \frac{f_D c}{2f_c}, \quad (4)$$

where $\lfloor \cdot \rfloor$ is the floor function, c is the light of speed, and f_c is the carrier frequency. Then, we denote the peak index of IDFT on the m -th column of \mathbf{F} as $\tilde{n}_{F,m}$, and the distance R between the sensing target and the base station is derived using^[24]

$$\tilde{n}_{F,m} = \left\lfloor \frac{2BR}{c} \right\rfloor, \quad (5)$$

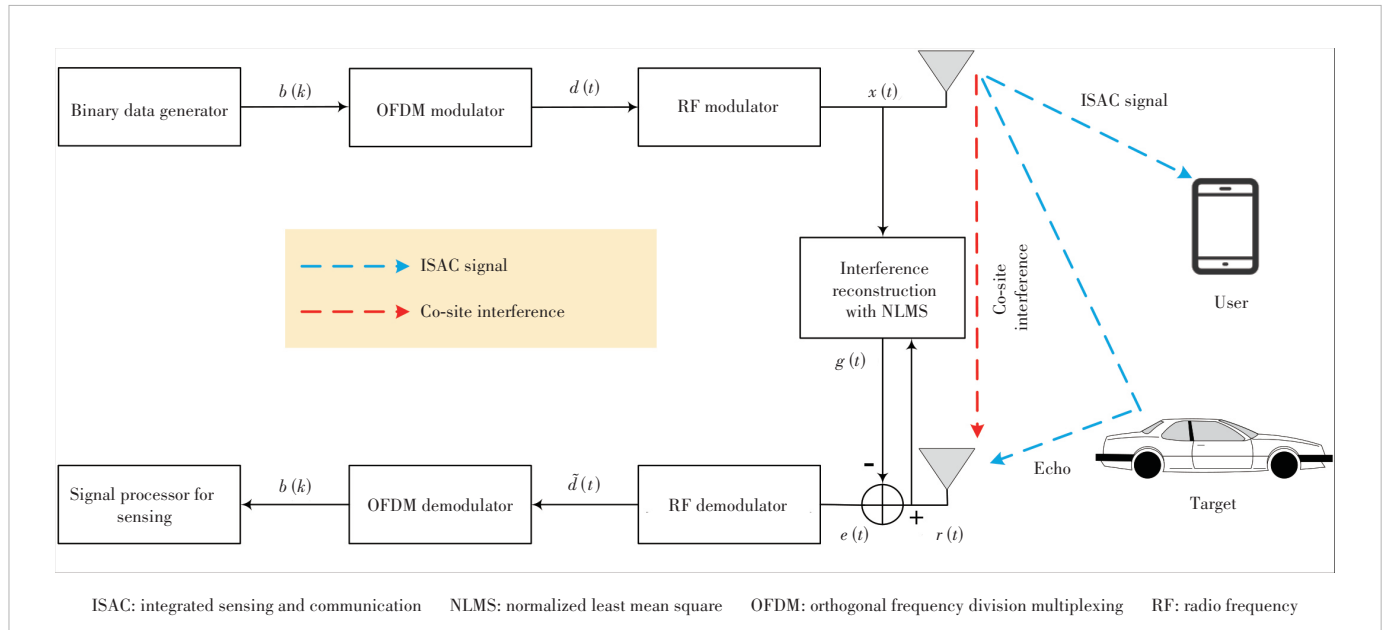
where B is the bandwidth of the ISAC signal.

Practically, the transmitted signals leaked from the local transmitter can cause significant co-site interference at the integrated receiver. To address this issue, we propose the NLMS algorithm with a decreasing convergence parameter. Fig. 1 il-

lustrates the ISAC system model with the proposed interference reconstruction and cancellation scheme. The NLMS algorithm reconstructs the co-site interference in the RF domain using a multi-tap circuit consisting of delayers, attenuators, and phase shifters. Interference cancellation is then performed at the receiver to eliminate the co-site interference. At the receiver of a communication user, the received signal undergoes RF demodulation, analog-to-digital conversion, cyclic prefix removal, and serial-to-parallel conversion. It is then transformed from the time domain to the frequency domain by the fast Fourier transform (FFT). Subsequently, we perform channel equalization, symbol decision, and symbol demapping on the frequency-domain signal to obtain the recovered communication data.

Next, we model the co-site interference received by the integrated receiver. As shown in Fig. 1, the Tx and Rx antennas are co-located, and mutual interference steps in the signal processing of the sensing receiver through the Tx-Rx channel. In this work, we term this mutual interference as the co-site interference, and the Tx-Rx channel can be modeled as a Rician fading channel^[25-27]. Thus, the co-site interference can be denoted as $\mathbf{Y}_{\text{ci}} = \mathbf{H} \cdot \mathbf{F}_{\text{Tx}}$. The channel matrix is written as

$$\mathbf{H} = \begin{bmatrix} h_0 & \cdots & h_0 \\ \vdots & & \vdots \\ h_k & \cdots & h_k \\ \vdots & & \vdots \\ h_{N-1} & \cdots & h_{N-1} \end{bmatrix}, \quad \mathbf{H} \in \mathcal{A}^{N \times M}, \quad (6)$$



▲ Figure 1. Schematic diagram of the ISAC system with interference reconstruction and cancellation

where the (k, l) -th element can be expressed as $h_k = \sqrt{r/(r+1)} h_k^{\text{los}} + \sqrt{1/(r+1)} h_k^{\text{nlos}}$, where r is the Rician factor. The terms h_k^{los} and h_k^{nlos} represent the line of sight (LoS) and non-LoS components, respectively. In a co-site interference channel, the LoS signal is relatively strong, resulting in a large value of r . Here, we express the received signal, including the echo signal, the co-site interference, and the noise, as

$$\begin{aligned} (\mathbf{F}_{\text{Rx}})_{k,l} &= b_0 (\mathbf{F}_{\text{Tx}})_{k,l} \cdot \exp(j2\pi T f_D l - j2\pi\tau(k\Delta f + f_0)) + \\ &h_k (\mathbf{F}_{\text{Tx}})_{k,l} \cdot \exp(-j2\pi\tau_{\text{SI}}(k\Delta f + f_0)) + (\tilde{\mathbf{Z}})_{k,l}, \end{aligned} \quad (7)$$

where τ_{SI} represents the co-site interference delay.

3 Normalized Least Mean Square Algorithm

A solution to cancelling the co-site interference is to establish a multi-tap circuit between the transmitter and receiver. Based on the known transmitted signal, the signal's amplitude and phase parameters are changed through the multi-tap circuit. Fig. 2 depicts the signal processing of the multi-tap circuit. The input signal $x(t)$ from the RF modulator can be expressed as

$$x(t) = \sqrt{2P} d(t) \cos(2\pi f_c t + \phi), \quad (8)$$

where P denotes the power of the transmitted signal, ϕ is the initial phase of the carrier, and $d(t)$ is the signal generated by the OFDM modulator. For simplicity, we assume that the signal power and the initial phase satisfy $P = 1/2$ and $\phi = 0$, and

then we have $x(t) = d(t) \cos(2\pi f_c t)$. Next, $x(t)$ goes through the delayer, attenuator, and phase shifter. The output signal of the l -th tap in the i -th iteration, denoted by $g_l^{(i)}(t)$, can be obtained as

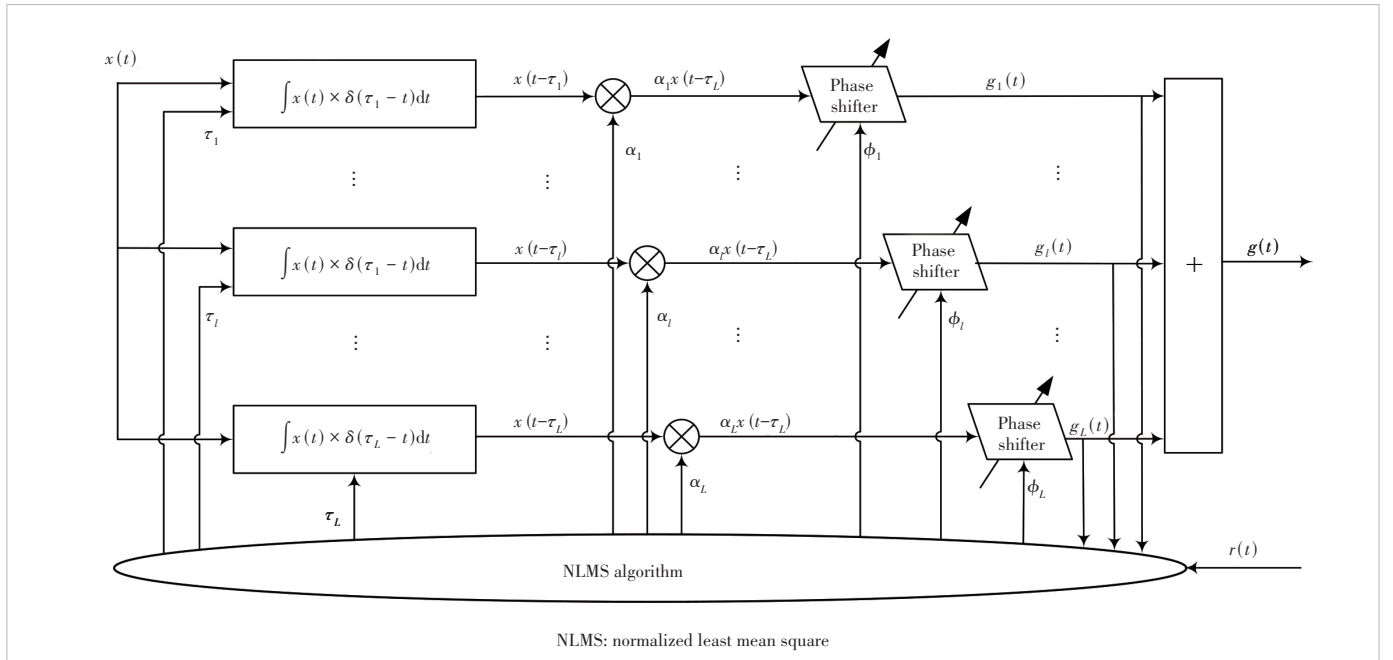
$$g_l^{(i)}(t) \triangleq \alpha_l^{(i)} x(t - \tau_l^{(i)}) e^{j\phi_l^{(i)}}, \quad i = 1, 2, \dots, I, \quad (9)$$

where $\alpha_l^{(i)}$, $\tau_l^{(i)}$ and $\phi_l^{(i)}$ are the attenuation component, delay and phase shift of the l -th path at the i -th iteration, respectively. The output signals of L paths undergo an adder to get the reconstructed interference signal $g(t)$. Then, by subtracting it from the received signal, the co-site interference cancellation is achieved. Within a time-frequency resource block, the complex amplitude of the signal can be approximated as a constant and the received signal can be simplified as

$$r(t) = b_0 x(t - \tau) \exp(j2\pi f_D t) + b_1 x(t - \tau_{\text{SI}}) + w(t), \quad (10)$$

where b_1 is the complex amplitude of the co-site interference. The first term in Eq. (10) is the sensing signal reflected by the target and the second term is the co-site interference. It is worth mentioning that the value of b_1 is much larger than b_0 , since b_0 refers to the round-trip path loss, which is proportional to the square of the distance between the transmitter and receiver. For the l -th tap, the error signal $e_l^{(i)}(t)$ and cost function $J_l^{(i)}(t)$ are defined respectively as

$$e_l^{(i)}(t) \triangleq r(t) - g_l^{(i)}(t), \quad (11)$$



▲ Figure 2. Interference reconstruction with NLMS

$$J_l^{(i)}(t) \triangleq \mathbb{E} \left[\left(e_l^{(i)}(t) \right)^2 \right] = \mathbb{E} \left[(r(t) - g_l^{(i)}(t))^2 \right]. \quad (12)$$

In the traditional least mean square (LMS) algorithm^[28], the reconstructed interference signal $g_l^{(i+1)}(t)$ is updated by

$$g_l^{(i+1)}(t) = g_l^{(i)}(t) - \frac{1}{2} \mu \nabla J_l^{(i)}(t) = g_l^{(i)}(t) + \mu e_l^{(i)}(t) x(t), \quad (13)$$

where μ is the step size factor.

Specifically, the LMS algorithm uses a stochastic gradient descent (SGD) algorithm to update $g_l^{(i+1)}(t)$. At each adaptation moment, the gradient of the cost function is calculated from the difference between the reconstructed and real interference signals and multiplied by an appropriate step size factor μ . It is worth mentioning that when $x(t)$ is large, the LMS algorithm suffers from a problem of gradient noise amplification. To overcome this difficulty and achieve a balance between convergence speed and steady-state error, the updated equation in the proposed RF interference cancellation algorithm is

$$g_l^{(i+1)}(t) = g_l^{(i)}(t) + \left[\frac{\mu}{\rho + x^2(t)} \right] e_l^{(i)}(t) x(t), \quad (14)$$

where ρ is a very small value, preventing the denominator from being zero. By introducing $\tilde{\mu}(t) = \mu / [\rho + x^2(t)]$, we can view NLMS as a variable step-size algorithm. Small $x^2(t)$ results in large $\tilde{\mu}(t)$, accelerating the convergence for the NLMS algorithm. Conversely, large $x^2(t)$ and small $\tilde{\mu}(t)$ can avoid instability and divergence. Thus, by adaptively selecting an appropriate step size, NLMS can improve the robustness across different input signals.

4 Simulation Results and Discussions

In this section, we conduct simulations to verify the interference cancellation capability of the proposed NLMS algorithm and compare it with mainstream algorithms such as SGD and recursive least squares (RLS). In the simulation experiments, quadrature phase shift keying (QPSK) and 16-quadrature amplitude modulation (16 QAM) are used for modulation. The channel models include extended pedestrian A (EPA), extended typical urban (ETU), and extended vehicular A (EVA), with minimum mean square error (MMSE) employed for channel equalization. The rest of the simulation parameters are listed in Table 1.

The core idea of the RLS algorithm is to recursively update the filter parameters to make the output signal as close to the desired signal as possible. The forgetting factor λ determines the weight of new and old data during iterations. A higher forgetting factor gives more weight to new data, allowing the algorithm to track rapidly changing system parameters, while a

lower forgetting factor is suitable for systems with slowly varying parameters. The SGD algorithm uses gradient descent to update the filter weights, minimizing the mean squared error between the desired and actual signals. The SGD algorithm exhibits the lowest computational complexity among the three algorithms, followed by the NLMS and RLS algorithms. Given an L -tap circuit, the computational complexities of SGD and NLMS are $\mathcal{O}(L)$, while the complexity for RLS is up to $\mathcal{O}(L^2)$. Table 2 shows a detailed analysis of the computational complexities with respect to the three algorithms mentioned.

Fig. 3 plots the interference estimation error (IEE) versus the number of iterations for different algorithms, where the signal-to-interference ratio (SIR) is assumed to be -60 dB and the maximum number of iterations I is set to 1 000. The RLS algorithm with $\lambda = 0.99$ demonstrates the most excellent interference reconstruction capability, followed by the proposed NLMS algorithm. The SGD with $\mu = 0.1$ exhibits the worst interference reconstruction capability. In the SGD algorithm, a tradeoff can be observed between the convergence speed and the IEE. A large step size factor μ accelerates convergence but leads to a higher IEE, since SGD may miss the optimal solution in each update. To reduce the IEE, we can select a small step size, which however consumes much longer time.

▼ **Table 1. Simulation parameters**

Parameter	Value
Rician factor	13 dB
Channel taps	10
Modulation	QPSK, 16 QAM
Subcarrier space (Δf)	30 kHz
FFT length	512
Communication channel type	EPA, ETU, EVA
Equalizer	MMSE
SIR	-60 dB
SGD step size (μ)	0.01, 0.1
RLS forgetting factor (λ)	0.99, 0.9
NLMS small value (ρ)	0.001

16 QAM: 16-quadrature amplitude modulation

EPA: extended pedestrian A

ETU: extended typical urban

EVA: extended vehicular A

FFT: fast Fourier transform

MMSE: minimum mean square error

NLMS: normalized least mean square

QPSK: quadrature phase shift keying

RLS: recursive least squares

SGD: stochastic gradient descent

SIR: signal-to-interference ratio

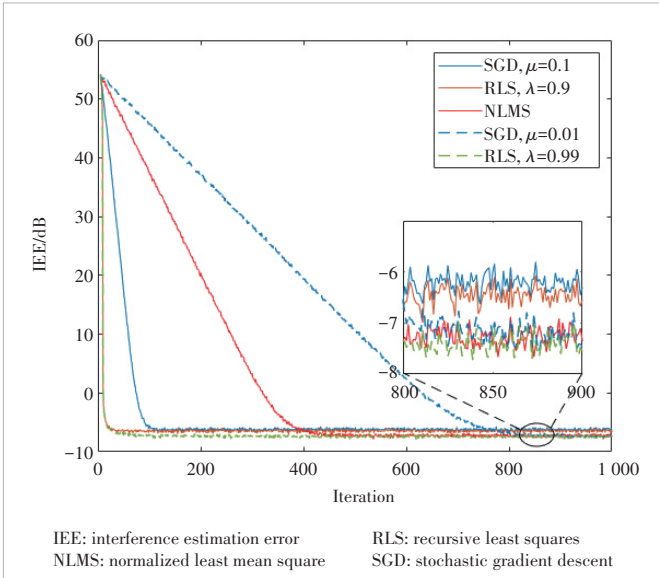
▼ **Table 2. Computational complexity of SGD, NLMS, and RLS algorithm^[29]**

Algorithm	Number of Additions per Iteration	Number of Multiplications per Iteration
SGD	$L + 1$	$2L$
NLMS	$2L + 1$	$3L + 50$
RLS	$L^2 + L$	$2L^2 + 3L + 50$

NLMS: normalized least mean square

RLS: recursive least squares

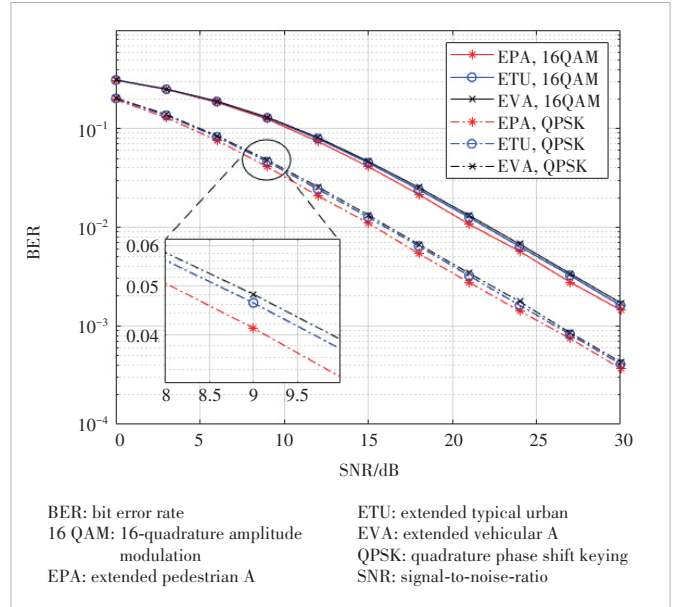
SGD: stochastic gradient descent



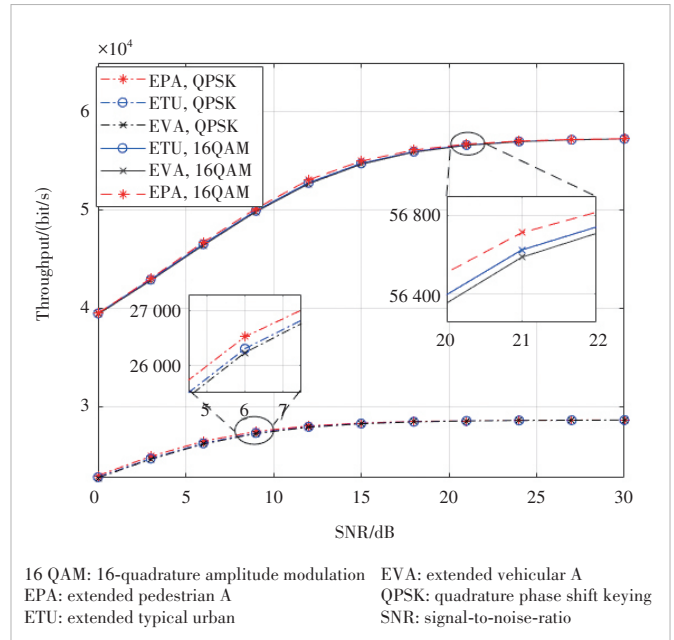
▲ Figure 3. IEEs of SGD, RLS and NLMS, with signal-to-interference ratio (SIR)=-60 dB

The SGD algorithm with $\mu = 0.1$ converges to an IEE of around -6 dB after 120 iterations. When the step size is reduced to 0.01, the SGD algorithm achieves a lower IEE of -7 dB at the cost of a slower convergence speed, i.e., 780 iterations. The NLMS can better handle this tradeoff and halves the iteration time. For the RLS algorithm, setting the forgetting factor to $\lambda = 0.99$ allows for more accurate interference reconstruction, yielding the lowest IEE. However, it does so at the cost of the greatly increased computational complexity $\mathcal{O}(L^2)$. In contrast, the proposed NLMS algorithm provides comparable interference reconstruction capability while keeping a low computational complexity $\mathcal{O}(L)$.

Next, we simulate the bit error rate (BER) and throughput of the ISAC system with the proposed NLMS algorithm under different modulation types and channels to evaluate its communication performance. As shown in Fig. 4, the BER of the ISAC system gradually decreases with increasing SNR. The EPA channel, with fewer multi-paths and lower average power attenuation per path compared to the ETU and EVA channels, results in the lowest BER. Compared to QPSK, the higher modulation order of QAM means that symbols are placed closer to each other in the constellation diagram, making the communication signal more sensitive to noise and resulting in a higher BER at the same SNR. Additionally, we present the throughput simulation results under different channel models and modulation types in Fig. 5. It can be observed that the ISAC system exhibits similar throughput across different channel models, with EPA and EVA yielding the highest and lowest throughput, respectively. Furthermore, 16 QAM achieves higher throughput than QPSK due to its higher modulation order.



▲ Figure 4. BER versus SNR under EPA, ETU, EVA channels, with two modulation types: QPSK and 16 QAM



▲ Figure 5. Throughput versus SNR under EPA, ETU, EVA channels, with two modulation types: QPSK and 16QAM

5 Conclusions and Future Work

In this work, we investigate the co-site interference problem in 5G NR ISAC systems. We model an OFDM-based ISAC system and provide a detailed overview of the corresponding ISAC signal processing flow. By modeling and analyzing the co-site interference in a single BS ISAC scenario, we propose an RF domain interference cancellation algorithm called the NLMS algorithm. By substituting μ for $\tilde{\mu}(t) = \mu / [\rho + x^2(t)]$,

the NLMS algorithm could adaptively adjust the step size factor, accelerating the convergence at a low cost of computing. Simulation results and analysis demonstrate that the NLMS algorithm could effectively cancel RF domain co-site interference. It also achieves a good balance among the iterations required for convergence, the computational complexity, and the capability of interference reconstruction. Compared to the RLS algorithm, the NLMS algorithm demonstrates similar interference reconstruction capability while maintaining a lower computational complexity $\mathcal{O}(L)$. In comparison to the SGD algorithm, it can better handle the tradeoff between the convergence speed and the IEE. Thus, the NLMS algorithm is a promising solution to co-site interference cancellation in ISAC systems. Our future work will focus on the joint design of more advanced interference cancellation algorithms in both the RF domain and baseband domain.

References

- [1] BAQUERO BARNETO C, RIIHONEN T, TURUNEN M, et al. Full-duplex OFDM radar with LTE and 5G NR waveforms: challenges, solutions, and measurements [J]. *IEEE transactions on microwave theory and techniques*, 2019, 67(10): 4042 – 4054. DOI: 10.1109/TMTT.2019.2930510
- [2] ZHENG L, LOPS M, EL-DAR Y C, et al. Radar and communication coexistence: an overview: a review of recent methods [J]. *IEEE signal processing magazine*, 2019, 36(5): 85 – 99. DOI: 10.1109/MSP.2019.2907329
- [3] LIU F, CUI Y H, MASOUIROS C, et al. Integrated sensing and communications: toward dual-functional wireless networks for 6G and beyond [J]. *IEEE journal on selected areas in communications*, 2022, 40(6): 1728 – 1767. DOI: 10.1109/JSAC.2022.3156632
- [4] CHEN S J, CHENG R S. Clustering for interference alignment in multiuser interference network [J]. *IEEE transactions on vehicular technology*, 2014, 63(6): 2613 – 2624. DOI: 10.1109/TVT.2013.2292897
- [5] HONG B Q, WANG W Q, LIU C C. Interference utilization for spectrum sharing radar-communication systems [J]. *IEEE transactions on vehicular technology*, 2021, 70(8): 8304 – 8308. DOI: 10.1109/TVT.2021.3092410
- [6] BABAIE A, TRANTER W H, BOSE T. A nullspace-based precoder with subspace expansion for radar/communications coexistence [C]//Proc. IEEE Global Communications Conference (GLOBECOM). IEEE, 2013: 3487 – 3492. DOI: 10.1109/GLOCOM.2013.6831613
- [7] MAHAL J A, KHAWAR A, ABDELHADI A, et al. Spectral coexistence of MIMO radar and MIMO cellular system [J]. *IEEE transactions on aerospace and electronic systems*, 2017, 53(2): 655 – 668. DOI: 10.1109/TAES.2017.2651698
- [8] CADAMBE V R, ALI JAFAR S. Interference alignment and degrees of freedom of the K-user interference channel [J]. *IEEE transactions on information theory*, 2008, 54(8): 3425 – 3441. DOI: 10.1109/TIT.2008.926344
- [9] LI B, PETROPULU A P. Joint transmit designs for coexistence of MIMO wireless communications and sparse sensing radars in clutter [J]. *IEEE transactions on aerospace and electronic systems*, 2017, 53(6): 2846 – 2864. DOI: 10.1109/TAES.2017.2717518
- [10] QIAN J H, HE Z S, HUANG N, et al. Transmit designs for spectral coexistence of MIMO radar and MIMO communication systems [J]. *IEEE transactions on circuits and systems II: express briefs*, 2018, 65(12): 2072 – 2076. DOI: 10.1109/TCSII.2018.2822845
- [11] CHENG Z Y, LIAO B, SHI S N, et al. Co-design for overlaid MIMO radar and downlink MISO communication systems via Cramér-Rao bound minimization [J]. *IEEE transactions on signal processing*, 2019, 67(24): 6227 – 6240. DOI: 10.1109/TSP.2019.2952048
- [12] ZHENG L, LOPS M, WANG X D, et al. Joint design of overlaid communication systems and pulsed radars [J]. *IEEE transactions on signal processing*, 2018, 66(1): 139 – 154. DOI: 10.1109/TSP.2017.2755603
- [13] TUYEN LE A, HUANG X J, DING C, et al. An in-band full-duplex prototype with joint self-interference cancellation in antenna, analog, and digital domains [J]. *IEEE transactions on microwave theory and techniques*, 2024, 72(9): 5540 – 5549. DOI: 10.1109/TMTT.2024.3364113
- [14] HONG Z H, ZHANG L, WU Y Y, et al. Iterative successive nonlinear self-interference cancellation for In-band full-duplex communications [J]. *IEEE transactions on broadcasting*, 2024, 70(1): 2 – 13. DOI: 10.1109/TBC.2023.3291136
- [15] MALAYTER J R, LOVE D J. A low-latency precoding strategy for In-band full-duplex MIMO relay systems [J]. *IEEE transactions on wireless communications*, 2024, 23(3): 1899 – 1912. DOI: 10.1109/TWC.2023.3292985
- [16] HONG Z H, ZHANG L, LI W, et al. Frequency-domain RF self-interference cancellation for in-band full-duplex communications [J]. *IEEE transactions on wireless communications*, 2023, 22(4): 2352 – 2363. DOI: 10.1109/TWC.2022.3211196
- [17] HUANG X J, TUYEN LE A, GUO Y J. Joint analog and digital self-interference cancellation for full duplex transceiver with frequency-dependent I/Q imbalance [J]. *IEEE transactions on wireless communications*, 2023, 22(4): 2364 – 2378. DOI: 10.1109/TWC.2022.3211316
- [18] KIAYANI A, WAHEED M Z, ANTTILA L, et al. Adaptive nonlinear RF cancellation for improved isolation in simultaneous transmit – receive systems [J]. *IEEE transactions on microwave theory and techniques*, 2018, 66(5): 2299 – 2312. DOI: 10.1109/TMTT.2017.2786729
- [19] STURM C, WIESBECK W. Waveform design and signal processing aspects for fusion of wireless communications and radar sensing [J]. *Proceedings of the IEEE*, 2011, 99(7): 1236 – 1259. DOI: 10.1109/JPROC.2011.2131110
- [20] KESKIN M F, WYMEERSCH H, KOIVUNEN V. Monostatic sensing with OFDM under phase noise: From mitigation to exploitation [J]. *IEEE transactions on signal processing*, 2023, 71: 1363 – 1378. DOI: 10.1109/TSP.2023.3266976
- [21] XIA X C, XU K, ZHANG D M, et al. Beam-domain full-duplex massive MIMO: realizing co-time co-frequency uplink and downlink transmission in the cellular system [J]. *IEEE transactions on vehicular technology*, 2017, 66(10): 8845 – 8862. DOI: 10.1109/TVT.2017.2698160
- [22] LIU F, GARCIA-RODRIGUEZ A, MASOUIROS C, et al. Interfering channel estimation for radar and communication coexistence [C]//Proc. IEEE 20th International Workshop on Signal Processing Advances in Wireless Communications (SPAWC). IEEE, 2019: 1 – 5. DOI: 10.1109/SPAWC.2019.8815575
- [23] WU K, ZHANG J A, HUANG X J, et al. Integrating low-complexity and flexible sensing into communication systems [J]. *IEEE journal on selected areas in communications*, 2022, 40(6): 1873 – 1889. DOI: 10.1109/JSAC.2022.3156649
- [24] WEI Z Q, QU H Y, WANG Y, et al. Integrated sensing and communication signals toward 5G-A and 6G: a survey [J]. *IEEE Internet of Things journal*, 2023, 10(13): 11068 – 11092. DOI: 10.1109/JIOT.2023.3235618
- [25] LUO Y J, BI L H, ZHAO D. Adaptive digital self-interference cancellation based on fractional order LMS in LFM CW radar [J]. *Journal of systems engineering and electronics*, 2021, 32(3): 573 – 583. DOI: 10.23919/JSEE.2021.000049
- [26] QUAN X, LIU Y, PAN W S, et al. A two-stage analog cancellation architecture for self-interference suppression in full-duplex communications [C]//Proc. IEEE MTT-S International Microwave Symposium (IMS). IEEE, 2017: 1169 – 1172. DOI: 10.1109/MWSYM.2017.8058808
- [27] DOTY J M, JACKSON R W, GOECKEL D L. Analog cancellation of a known remote interference: Hardware realization and analysis [J]. *IEEE wireless communications letters*, 2024, 13(3): 829 – 833. DOI: 10.1109/LWC.2023.3346290

- [28] HAYKIN S. Adaptive Filter Theory (5th Ed.)[M]. Upper Saddle River, USA: Prentice Hall, 2014.
- [29] CIOLINO S. On the use of wavelet packets in ultra wideband pulse shape modulation systems [J]. IEICE transactions on fundamentals of electronics, communications and computer sciences, 2005, E88-A(9): 2310 – 2317. DOI: 10.1093/ietfec/e88-a.9.2310

Biographies

YU Xiaohui received his BS degree from the School of Information Engineering, Guangdong University of Technology, China in 2023. He is currently working toward an MS degree at Beijing University of Posts and Telecommunications, China. His research interests include integrated sensing and communication, and wireless communication.

YU Shucheng received his BS and MS degrees from the School of Information and Communication Engineering, Beijing University of Posts and Telecommunications, China in 2021 and 2024, respectively. His research interests include integrated sensing and communication and wireless communication.

LIU Xiqing (liuxiqing@bupt.edu.cn) received his MS and PhD degrees from Harbin University of Science and Technology, China and Harbin Institute of Technology, China in 2012 and 2017, respectively. Currently, he is an associate professor with the State Key Laboratory of Networking and Switching Technology, School of Information and Communication Engineering, Beijing University of Posts and Telecommunications, China. His research interests include integrated sensing and communications, waveform designs for wireless transmission, and multiple access technologies. He has served as a technical editor of *IEEE Wireless communications*.

PENG Mugen received his PhD degree in communication and information systems from Beijing University of Posts and Telecommunications (BUPT), China in 2005. Afterward, he joined BUPT, where he has been the deputy director with the State Key Laboratory of Networking and Switching Technology since 2018. Currently, he is the vice president of BUPT. During 2014, he was also an academic visiting fellow with Princeton University, USA. His research interests include integrated sensing and communication, wireless communication theory, and radio signal processing. He was a recipient of the 2018 Heinrich Hertz Prize Paper Award, the 2014 IEEE ComSoc AP Outstanding Young Researcher Award, the Best Paper Award in the ICC 2024 and ICC 2022, etc. He is currently on the Editorial/Associate Editorial Board of the *IEEE Network*, *IEEE Internet of Things Journal*, *IEEE Transactions on Vehicular Technology*, *IEEE Transactions on Network Science and Engineering*, etc.



Trajectory Tracking for MmWave Communication Systems via Cooperative Passive Sensing

YU Chao, LYU Bojie, QIU Haoyu, WANG Rui

(Department of Electronic and Electrical Engineering, Southern University of Science and Technology, Shenzhen 518000, China)

DOI: 10.12142/ZTECOM.202403005

<https://kns.cnki.net/kcms/detail/34.1294.TN.20240919.0834.002.html>, published online September 19, 2024

Manuscript received: 2024-08-20

Abstract: A cooperative passive sensing framework for millimeter wave (mmWave) communication systems is proposed and demonstrated in a scenario with one mobile signal blocker. Specifically, in the uplink communication with at least two transmitters, a cooperative detection method is proposed for the receiver to track the blocker's trajectory, localize the transmitters and detect the potential link blockage jointly. To facilitate detection, the receiver collects the signal of each transmitter along a line-of-sight (LoS) path and a non-line-of-sight (NLoS) path separately via two narrow-beam phased arrays. The NLoS path involves scattering at the mobile blocker, allowing its identification through the Doppler frequency. By comparing the received signals of both paths, the Doppler frequency and angle-of-arrival (AoA) of the NLoS path can be estimated. To resolve the blocker's trajectory and the transmitters' locations, the receiver should continuously track the mobile blocker to accumulate sufficient numbers of the Doppler frequency and AoA versus time observations. Finally, a gradient-descent-based algorithm is proposed for joint detection. With the reconstructed trajectory, the potential link blockage can be predicted. It is demonstrated that the system can achieve decimeter-level localization and trajectory estimation, and predict the blockage time with an error of less than 0.1 s.

Keywords: mmWave communications; integrated sensing and communication; trajectory tracking; passive sensing

Citation (Format 1): YU C, LYU B J, QIU H Y, et al. Trajectory tracking for mmWave communication systems via cooperative passive sensing [J]. *ZTE Communications*, 2024, 22(3): 29 – 36. DOI: 10.12142/ZTECOM.202403005

Citation (Format 2): C. Yu, B. J. Lyu, H. Y. Qiu, et al., "Trajectory tracking for mmWave communication systems via cooperative passive sensing," *ZTE Communications*, vol. 22, no. 3, pp. 29 – 36, Sept. 2024. doi: 10.12142/ZTECOM.202403005.

1 Introduction

Due to the short wavelength, millimeter-wave (mmWave) wireless communication is fragile to link blockage^[1-3]. Fortunately, with the development of wireless sensing techniques, it is feasible to design a robust mmWave communication system that can predict the link blockage, detect backup signal propagation paths, and mitigate the impact of signal-to-noise ratio (SNR) loss via predictive scheduling.

There have been a number of research efforts on blockage prediction via out-of-band sensors^[4-6] or in-band channel information^[7-11]. For example, a camera was proposed to sense the communication environment and predict the mmWave link blockage via deep learning algorithms in Refs. [4-5]. A light detection and ranging (LiDAR) assisted proactive blockage prediction scheme was proposed in Ref. [6]. The use of out-of-band sensors not only increases the cost of communication systems, but also raises privacy issues, especially in indoor communication scenarios. With the in-band channel information, the variation of received signal strength (RSS) was proposed to predict

blockage in Refs. [7, 11], where deep learning algorithms were developed to track the RSS variation patterns right before blockage. It was found in Ref. [8] that the diffraction effects of mmWave signals could be exploited in blockage prediction. Moreover, a protective beam was proposed in Ref. [9] to monitor the Doppler effect in the communication environment, so that potential link blockage can be forecasted. However, none of the above in-band sensing methods can track the trajectory of mobile blockers. Without the trajectory, these methods may not provide sufficient warning time before blockage, or they may lead to a large false alarm probability. In our preliminary study^[12], an mmWave blockage prediction method via passive sensing architecture was proposed, which could predict 90% of the line-of-sight (LoS) blockage with a sensing time of 1.4 s. It assumed location knowledge of the transmitter and receiver, as well as the constant velocity of the mobile blocker.

In fact, passive sensing is a promising approach to facilitating simultaneous sensing and data communication with half-duplexing transceivers^[13]. By comparing the received signals of

reference and surveillance channels, multi-antenna passive sensing techniques can detect the direction, distance and the raised Doppler frequency of a mobile target. It has been used for localization or trajectory tracking via WiFi signals^[14] or long-term evolution (LTE) downlink signals^[15]. To further improve the tracking accuracy, multiple signal transmitters or sensing receivers can be adopted to detect the Doppler frequency in different dimensions. For example, a handwriting tracking method via cooperative passive sensing of two receivers was proposed in Ref. [16], where the accuracy of handwriting reconstruction was at the millimeter level. However, all these works assumed knowledge of the locations of signal transmitters and sensing receivers, which might not be easily obtained in mobile communication systems, especially in indoor scenarios.

In this paper, we would like to address the above issue by proposing a cooperative passive sensing method for joint trajectory tracking and device localization. Specifically, at least two uplink transmitters simultaneously transmit uplink signals to one receiver in different frequency bands, and there is one mobile blocker in the communication environment. The receiver adopts two narrow beams to receive the uplink signal of each transmitter. One beam is aligned with the transmitter directly, and the other is aimed at the mobile blocker. Thus, the signal of LoS path is received by the former beam, and the scattered signal from the mobile blocker, which is with non-zero Doppler frequencies, is received by the latter one. By comparing the signals of the above two beams, the Doppler frequencies and angles-of-arrival (AoA) of the mobile blocker can be continuously observed. Accumulating the above observations from two transmitters, we find the transmitters' locations and the blocker's trajectory can be jointly detected via a proposed gradient-descent-based algorithm. It is demonstrated that the system can achieve decimeter-level localization and trajectory estimation, and predict the blockage time with an error of less than 0.1 s.

The remainder of this paper is organized as follows. In Section 2, an overview of the system is provided. In Section 3, the signal processing for passive sensing is introduced. Section 4 introduces the algorithms for joint trajectory tracking and transmitter localization, followed by the method of blockage prediction. The experiment results and analysis are provided in Section 5. Finally, conclusions are drawn in Section 6.

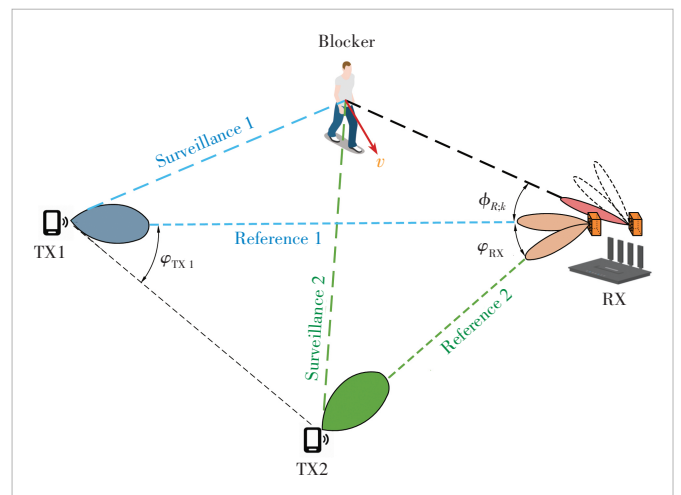
2 System Overview

In this paper, a trajectory tracking and blockage prediction method is proposed for mmWave uplink communications. Without a priori location knowledge of the transmitters and receiver, the proposed method can simultaneously track the trajectory of a mobile signal blocker and detect the locations of the transmitters with respect to the receiver. As a result, the potential blockage of the LoS path can be predicted. The overall system architecture is illustrated in Fig. 1. The proposed system consists of one mmWave receiver and at least two transmitters, where the

receiver receives signals from all transmitters simultaneously by frequency division. The two transmitters are referred to as transmitters 1 and 2, and their orthogonal communication bands are referred to as bands 1 and 2, respectively. The transmitters and receiver can be the user equipment (UE) and base station (BS) of uplink communications, respectively.

Each mmWave transmitter delivers an information-bearing signal via a transmission beam. The signal arrives at the receiver via both the LoS path and the non-line-of-sight (NLoS) path scattered at the mobile blocker, as illustrated in Fig. 1. The receiver has at least two RF chains, each with a phased array. One of the phased arrays generates a receiving beam, namely a surveillance beam, to capture the NLoS signal in both frequency bands. Due to the mobility of the blocker, this receiving beam should periodically sweep the surrounding region. The other phased array generates two receiving beams towards the two transmitters, respectively. They could capture the LoS signals of the two transmitters in two frequency bands with a high signal-to-noise ratio (SNR), respectively. The LoS paths from the two transmitters are referred to as reference channels 1 and 2, and their receiving beams are referred to as reference beams 1 and 2, respectively. Additionally, the signal propagation paths from both transmitters and scattered by the mobile blocker are called surveillance channels 1 and 2, respectively.

By comparing the signals received from a pair of reference and surveillance channels, the Doppler frequencies raised by the mobile blocker can be detected at a particular AoA. Due to the carrier frequency offset (CFO) and the sampling clock frequency offset (SFO) between the transmitter and the receiver, the time-of-fly (ToF) measurement of reference channels or surveillance channels could be difficult. It is therefore infeasible to localize the mobile blocker at the receiver via a single capture of the blocker. Instead, the Doppler frequency and AoA of the mobile blocker are successively tracked in the proposed method, so that the trajectory of the mobile blocker and the lo-



▲ Figure 1. Overview of the integrated sensing and communication system

cations of the two transmitters can be jointly detected with a sufficient number of observations.

3 Signal Processing of Cooperative Passive Sensing

3.1 Signal Model

It is assumed that the transmission and receiving beams of the two reference channels have been aligned via the existing method, e.g., exhaustive beam search. On the other hand, the surveillance beam switches sequentially and periodically among Q -directions, denoted as $\Phi = \{\phi_1, \phi_2, \dots, \phi_Q\}$. In each direction, signals of both frequency bands are received via the surveillance beam for a duration of T_b s. Thus, it takes the surveillance beam $T_d = QT_b$ s to complete a sweeping period.

In the k -th sweeping period ($\forall k$), let $s_{m,k,q}(t)$ be the transmit baseband signal of the m -th transmitter ($m = 1, 2$) when the surveillance beam is at the direction ϕ_q , and the received signal via the m -th reference beam in the m -th frequency band can be written as :

$$y_{m,k,q}^{\text{ref}}(t) = \alpha_{m,k,q}^{\text{ref}} s_{m,k,q}(t - \tau_{m,k,q}^{\text{ref}}) + n_{m,k,q}^{\text{ref}}(t), 0 \leq t \leq T_b, \quad (1)$$

where $\alpha_{m,k,q}^{\text{ref}}$ and $\tau_{m,k,q}^{\text{ref}}$ denote the complex gain and delay of the LoS path, and $n_{m,k,q}^{\text{ref}}(t)$ denotes the superposition of noise and NLoS echoes. As a remark, the scattered signal of $s_{m,k,q}(t)$ may also be received by the reference beam.

Simultaneously, the received signal of the surveillance beam in the m -th frequency band, denoted as $y_{m,k,q}^{\text{sur}}(t)$, includes the scattered signals from the mobile blocker and static scattering clusters. Thus,

$$y_{m,k,q}^{\text{sur}}(t) = \alpha_{m,k,q}^{\text{tar}}(t) s_{m,k,q}(t - \tau_{m,k,q}^{\text{tar}}(t)) e^{-j2\pi f_{m,k,q}^{\text{tar}}(t)t} + \sum_{l=1}^{L_{m,q}} \alpha_{m,k,q}^l s_{m,k,q}(t - \tau_{m,k,q}^l) + n_{m,k,q}^{\text{sur}}(t), 0 \leq t \leq T_b, \quad (2)$$

where $\alpha_{m,k,q}^{\text{tar}}(t)$, $\tau_{m,k,q}^{\text{tar}}(t)$ and $f_{m,k,q}^{\text{tar}}(t)$ denote the time-varying complex gain, delay and Doppler frequency of the surveillance channel, respectively, $L_{m,q}$ denotes the number of NLoS paths via static scattering clusters, $\alpha_{m,k,q}^l$ and $\tau_{m,k,q}^l$ are the complex gain and delay of the l -th one, and $n_{m,k,q}^{\text{sur}}(t)$ denotes the noise. As a remark, the signal from the LoS path may also be received by the surveillance beam, which can be treated as a special static scattering cluster in the second term of the above equation.

The received signals from both reference and surveillance beams in the two frequency bands are sampled with a period T_s , which can be expressed by $y_{m,k,q}^{\text{ref}}[n] = y_{m,k,q}^{\text{ref}}(nT_s)$ and $y_{m,k,q}^{\text{sur}}[n] = y_{m,k,q}^{\text{sur}}(nT_s)$, where $n = 1, 2, \dots, T_b/T_s$, and $m = 1, 2, q = 1, 2, \dots, Q$. Note that the signal components in $y_{m,k,q}^{\text{sur}}[n]$ with non-zero Doppler frequencies from the moving blocker may be overwhelmed by the strong scattered signals with zero Doppler frequency.

Specifically, in Eq. (2), the first term on the right side is far smaller than the second term. This can disrupt the estimation of the Doppler frequency. Hence, the least-square-based (LS-based) clutter cancellation in Ref. [17] is applied to suppress the signal components with zero Doppler frequency in $y_{m,k,q}^{\text{sur}}[n]$. The surveillance signal after clutter cancellation is denoted as $\hat{y}_{m,k,q}^{\text{sur}}[n]$.

3.2 Doppler Frequency and AoA Estimation

The Doppler frequency estimation in passive sensing is based on the cross-ambiguity function (CAF) between the reference signals and surveillance signals. Particularly, the CAF of the received signals in the m -th frequency band, k -th sweeping period, and q -th surveillance beam's direction is defined as

$$R_{m,k}(q, f_d) = \max_{\tau_{m,k,q}} \sum_{n=1}^{N_0} \hat{y}_{m,k,q}^{\text{sur}}[n] \left\{ y_{m,k,q}^{\text{ref}}[n - \tau_{m,k,q}] \right\}^* e^{j2\pi f_d n T_s}, \quad (3)$$

where $\{.\}^*$ is the complex conjugate; $N_0 = T_b/T_s$ denotes the number of samples when the surveillance beam is in one direction. Since we only focus on the estimation of the Doppler frequency, the delay $\tau_{m,k,q}$ is not considered a parameter of the CAF. There should be a peak value of $R_{m,k}(q, f_d)$ at $f_d = f_{m,k,q}^{\text{tar}}(kN_0T_s)$. Thus, Doppler frequencies of the mobile blocker could be detected by finding the peak values of $R_{m,k}(q, f_d)$. As a remark, note that estimating the Doppler frequency in Eq. (3) does not request a priori knowledge of the path gains $\alpha_{m,k,q}^{\text{tar}}$ and $\alpha_{m,k,q}^l$.

There might be more than one peak value of $R_{m,k}(q, f_d)$ in the k -th sweeping period. This is because there might be multiple scattering points on the blocker with different velocities. The scattering between the blocker and the surrounding clutters would also generate weak peaks on $R_{m,k}(q, f_d)$. An adaptive-threshold-based method is adopted to detect the Doppler frequencies with the dominant receiving power from the CAF. First, the threshold for the Doppler frequency f_d in the q -th surveillance beam's direction can be calculated as:

$$T_{m,k}(q, f_d) = \frac{\gamma}{2W + 1} \sum_{p=-W_T}^{W_T} R_{m,k}(q, f_d + p\Delta f), \quad (4)$$

where W_T is the half length of training cells, $\gamma > 1$ is a scaling factor for the detection threshold, and $\Delta f = 1/(N_0T_s)$ is the resolution of the Doppler frequency. Thus, in the k -th sweeping period, a Doppler frequency f_d is detected in the q -th surveillance beam's direction when $R_{m,k}(q, f_d) \geq T_{m,k}(q, f_d)$.

Note that the scattered signal from the mobile blocker might be captured by multiple beam directions, leading to a false alarm in the AoA detection. In the proposed system, we treat the surveillance beam's direction maximizing the CAF as the

estimated AoA of each sweeping period. Particularly, denoting $\tilde{f}_{m,k}$ and $\tilde{\phi}_k$ as the estimated Doppler frequency and AoA in the k -th sweeping period, we have

$$\begin{aligned} (\tilde{f}_{m,k}, \tilde{q}_{m,k}) &= \underset{f_d, q}{\operatorname{argmax}} R_{m,k}(q, f_d) \\ \text{s.t. } R_{m,k}(q, f_d) &\geq T_{m,k}(q, f_d), \end{aligned} \quad (5)$$

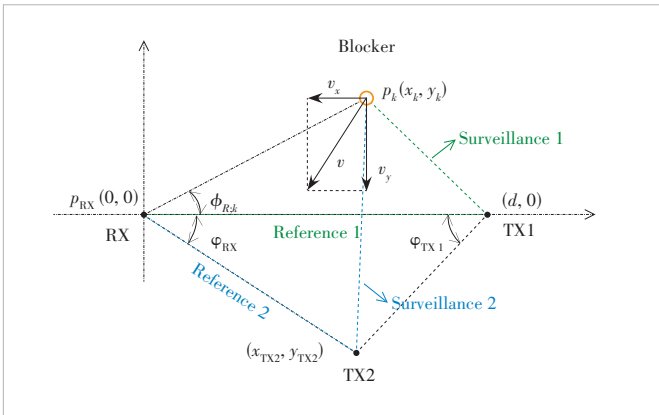
and $\tilde{\phi}_k = \phi_{\tilde{q}_{m,k}}$, respectively. Note that the AoA of blockers is independent of the frequency bands. Finally, we define the measured feature vector z_k of the k -th sweeping periods as

$$z_k = [\tilde{\phi}_k, \tilde{f}_{1,k}, \tilde{f}_{2,k}]^T. \quad (6)$$

4 Localization and Blockage Prediction

In this section, a joint estimation method is proposed to detect the positions of the two transmitters and the trajectory of the mobile blocker based on the measured AoAs and Doppler frequencies in a number of sweeping periods. The geometric relation among the two transmitters, the receiver and the mobile blocker is illustrated in Fig. 2. Without loss of generality, the coordinates of the receiver and the two transmitters are represented by vectors $\mathbf{p}^{\text{RX}} = [0, 0]^T$, $\mathbf{p}_1^{\text{TX}} = [d, 0]^T$, $\mathbf{p}_2^{\text{TX}} = [x_{\text{TX}2}, y_{\text{TX}2}]^T$, respectively, and the coordinates of the mobile blocker in the k -th sweeping period are represented by $\mathbf{p}_k = [x_k, y_k]^T$. There is no a priori knowledge of the locations of the two transmitters at the receiver. Thus, d , $x_{\text{TX}2}$ and $y_{\text{TX}2}$ are unknown.

To facilitate the joint estimation, it is assumed that the two transmitters and a receiver have sent and received signals to and from each other, so that the angles-difference-of-arrival (ADoA) between them have been estimated via the spatial smoothing multiple signal classification (MUSIC) algorithm^[18]. Thus, the angles φ_{RX} and $\varphi_{\text{TX}1}$ in Fig. 2 are known at the receiver. Note that $x_{\text{TX}2}$ and $y_{\text{TX}2}$ are functions of d , φ_{RX} and $\varphi_{\text{TX}1}$, the joint estimation of d and \mathbf{p}_k , where $k = 1, 2, 3, \dots$, is



▲ Figure 2. Illustration of the blocker tracking system in the coordinate system with two transmitters

elaborated in this section, followed by the blockage prediction. In the following, we first elaborate on the motion model of the mobile blocker.

4.1 Motion Model

According to the geometric relation, ADoA φ_{RX} and $\varphi_{\text{TX}1}$ can be expressed in terms of the coordinates of the two transmitters and the receiver as:

$$\begin{cases} \varphi_{\text{RX}} = \cos^{-1} \frac{(\mathbf{p}_1^{\text{TX}} - \mathbf{p}^{\text{RX}})^T (\mathbf{p}_2^{\text{TX}} - \mathbf{p}^{\text{RX}})}{\|\mathbf{p}_1^{\text{TX}} - \mathbf{p}^{\text{RX}}\| \|\mathbf{p}_2^{\text{TX}} - \mathbf{p}^{\text{RX}}\|} \\ \varphi_{\text{TX}1} = \cos^{-1} \frac{(\mathbf{p}^{\text{RX}} - \mathbf{p}_1^{\text{TX}})^T (\mathbf{p}_2^{\text{TX}} - \mathbf{p}_1^{\text{TX}})}{\|\mathbf{p}^{\text{RX}} - \mathbf{p}_1^{\text{TX}}\| \|\mathbf{p}_2^{\text{TX}} - \mathbf{p}_1^{\text{TX}}\|}. \end{cases} \quad (7)$$

Since the sweeping period is very short, it can be approximated that the mobile blocker is moving with a constant velocity in a sweeping period. Hence, the trajectory of the mobile block can be expressed as:

$$\mathbf{p}_k = \mathbf{p}_{k-1} + \mathbf{v}_{k-1} T_d = \mathbf{p}_1 + \sum_{n=1}^{k-1} \mathbf{v}_n T_d, \quad (8)$$

where $\mathbf{v}_k = [v_{x;k}, v_{y;k}]^T$ is the vector of velocity in the k -th sweeping period; $v_{x;k}$ and $v_{y;k}$ denote the velocity components in the x -axis and y -axis, respectively.

Hence, the AoA of the surveillance channel in the k -th sweeping period $\phi_{R;k}$ can be written as

$$\phi_{R;k} = \cos^{-1} \frac{\mathbf{p}_k}{\|\mathbf{p}_k\|} = \cos^{-1} \frac{\mathbf{p}_1 + \sum_{n=1}^{k-1} \mathbf{v}_n T_d}{\|\mathbf{p}_1 + \sum_{n=1}^{k-1} \mathbf{v}_n T_d\|}. \quad (9)$$

Moreover, the Doppler frequency of the m -th surveillance channel is given by

$$f_{d;m,k} = \frac{1}{\lambda_m} \left(\frac{\mathbf{p}_k - \mathbf{p}_m^{\text{TX}}}{\|\mathbf{p}_k - \mathbf{p}_m^{\text{TX}}\|} + \frac{\mathbf{p}_k - \mathbf{p}^{\text{RX}}}{\|\mathbf{p}_k - \mathbf{p}^{\text{RX}}\|} \right)^T \mathbf{v}_k, \quad (10)$$

where λ_m is the carrier frequency of the m -th transmitter.

4.2 Joint Localization and Trajectory Estimation

It can be observed from the above motion model that, given the distance d , the initial position \mathbf{p}_1 and the velocity vectors $\mathbf{v}_1, \mathbf{v}_2, \dots, \mathbf{v}_k$ of the blocker, the AoAs and Doppler frequencies of all the sweeping periods can be calculated according to Eqs. (9) and (10). Let $\mathbf{x}_k = [d, \mathbf{p}_1^T, \mathbf{v}_1^T, \mathbf{v}_2^T, \dots, \mathbf{v}_k^T]^T$ be the vector of all the motion parameters to be estimated in the first k sweeping periods; $\mathbf{h}_k = [\phi_{R;k}, f_{d;1,k}, f_{d;2,k}]^T$ is the true feature vector of k -th sweeping period with motion parameters \mathbf{x}_k ; $\mathbf{H}(\mathbf{x}_k) = [h(\mathbf{x}_1), h(\mathbf{x}_2), \dots, h(\mathbf{x}_k)]^T$ and $\mathbf{Z}_k = [z_1, z_2, \dots, z_k]^T$ are the aggregation of the true feature vectors and measured feature

vectors, respectively. The trajectory of the mobile blocker and the positions of transmitters can be estimated via minimizing the difference between true features and the measured ones in the first K sweeping periods. Thus,

$$\hat{\mathbf{x}}_K = \underset{\mathbf{x}_K}{\operatorname{argmin}} \operatorname{tr} \left\{ \mathbf{W} \left[\mathbf{Z}_K - \mathbf{H}(\mathbf{x}_K) \right]^\top \left[\mathbf{Z}_K - \mathbf{H}(\mathbf{x}_K) \right] \right\}, \quad (11)$$

where $\operatorname{tr}\{\cdot\}$ denotes the matrix trace. $\mathbf{W} = \operatorname{diag}(\alpha_1, \alpha_2, \alpha_3)$ is the weighting matrix, and α_1, α_2 , and α_3 denote the weights of different features, respectively.

Although the above problem is nonlinear, we can find local optimal solutions by the classical Levenberg-Marquardt (LM) optimization algorithm^[19-20] with multiple initial solutions. Particularly, we first define function $f(\mathbf{x}_K) = \operatorname{tr} \left\{ \mathbf{W} \left[\mathbf{Z}_K - \mathbf{H}(\mathbf{x}_K) \right]^\top \left[\mathbf{Z}_K - \mathbf{H}(\mathbf{x}_K) \right] \right\}$, and let $\mathbf{x}_{K,1}^0, \mathbf{x}_{K,2}^0, \dots, \mathbf{x}_{K,S}^0$ be the S initial estimations of the motion parameters \mathbf{x}_K . In the l -th iteration ($l = 1, 2, 3, \dots$), the estimations of motion parameters \mathbf{x}_K are updated as $\mathbf{x}_{K,s}^l = \mathbf{x}_{K,s}^{l-1} + \mathbf{J}(\mathbf{x}_{K,s}^{l-1})\Delta$, $s = 1, 2, 3, \dots, S$, where $\mathbf{J}(\mathbf{x}_K) = \frac{\partial f(\mathbf{x}_K)}{\partial \mathbf{x}_K}$ is the Jacobian matrix and Δ is the step size. Finally, let L be the total number of iterations, and the estimated motion parameters are given by

$$\hat{\mathbf{x}}_K = \underset{\mathbf{x}_K \in \{\mathbf{x}_{K,1}^L, \mathbf{x}_{K,2}^L, \dots, \mathbf{x}_{K,S}^L\}}{\operatorname{argmin}} f(\mathbf{x}_K). \quad (12)$$

4.3 Blockage Detection

Based on the estimated trajectory and velocities of the blocker in the K sweeping periods, it is feasible to predict whether and when the LoS between transmitters and the receiver would be blocked. Assuming that the mobile blocker keeps the average velocity of the previous n sweeping periods, the predicted trajectory $\mathbf{p}(t)$ of the blocker after the K -th sweeping period can be expressed as

$$\mathbf{p}(t) = \hat{\mathbf{p}}_K + \bar{\mathbf{v}}t, \quad (13)$$

where $\bar{\mathbf{v}} = \sum_{k=K-n+1}^K \hat{\mathbf{v}}_k$ is the average velocity in previous n sweeping periods, and $\hat{\mathbf{v}}_k$ is the estimated velocity of the blocker in the k -th sweeping period according to Eq. (12).

Let $\mathbf{b}_m \in \{0, 1\}$, $m = 1, 2$, be the blockage indicator, where $\mathbf{b}_m = 1$ denotes that the m -th LoS will be

blocked in the future and $\mathbf{b}_m = 0$, otherwise. We have

$$\mathbf{b}_m = \begin{cases} 1, & \det \left(\left[\bar{\mathbf{v}}, \mathbf{p}^{\text{RX}} - \hat{\mathbf{p}}_K \right] \right) \det \left(\left[\bar{\mathbf{v}}, \mathbf{p}_m^{\text{TX}} - \hat{\mathbf{p}}_K \right] \right) < 0 \\ 0, & \text{otherwise.} \end{cases} \quad (14)$$

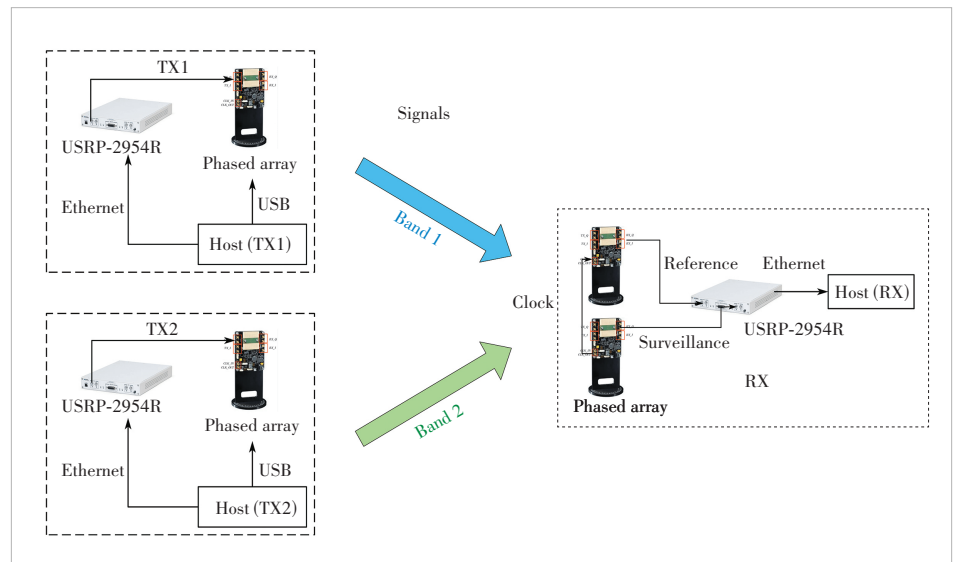
Moreover, let \hat{t}_m be the estimated blockage time, after which the link blockage will happen. Let $\mu \mathbf{p}_m^{\text{TX}}$ be the position of the intersection point in the m -th LoS path, where $\mu \in [0, 1]$. The blockage time \hat{t}_m and μ can be calculated by

$$\begin{bmatrix} \mu \\ \hat{t}_m \end{bmatrix} = \left[\mathbf{p}_m^{\text{TX}}, -\bar{\mathbf{v}} \right]^{-1} \hat{\mathbf{p}}_K, \quad (15)$$

where $\det \left(\left[\mathbf{p}_m^{\text{TX}}, -\bar{\mathbf{v}} \right] \right) \neq 0$.

5 Experiment Results and Analysis

In the experiments, the implementation of the proposed system is shown in Fig. 3. Both transmitters 1 and 2 are implemented with one NI USRP-2954R connected with one Sivers 60 GHz phased array. In both transmitters, the transmitting signal with a bandwidth of 1 MHz consists of a training sequence and an orthogonal frequency division multiplexing (OFDM)-modulated data payload. The carrier frequencies of transmitters 1 and 2 are 60.98 GHz and 60.985 GHz, and the width of transmitting beams are both 90° . At the receiver, two Sivers 60 GHz phased arrays, with a clock of 45 MHz, are connected to one NI USRP-2954R. One of the phased arrays adopts a two-lobe receiving beam towards transmitters 1 and 2, respectively, which receives signals of reference channels 1 and 2 in two different frequency bands. The surveillance beam is implemented via the other phased array, covering both frequency bands. Signals from two transmitters can be separated at the USRP of the receiver via two bandpass filters. Moreover,



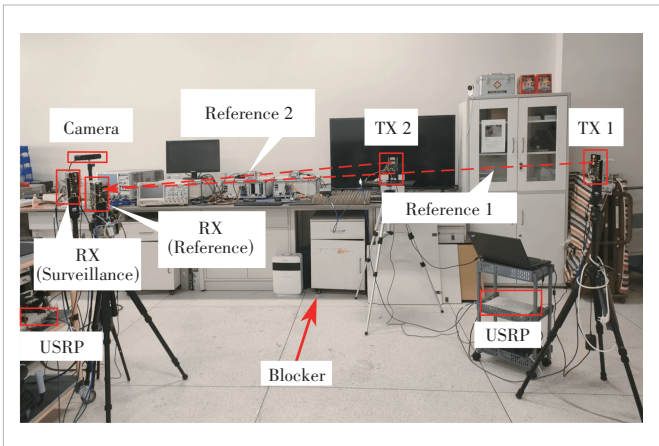
▲ Figure 3. Block diagram of system implementation

the surveillance beam is switched periodically among $Q=4$ directions, which are 40° , 27° , 18° and 10° , with a beamwidth of about 10° . The sensing duration of one direction is $T_b=50$ ms and the duration of one sweeping period is $T_d = 200$ ms which implies the minimum detectable speed is around 0.025 m/s. The sampling frequency at the baseband is 10 MHz.

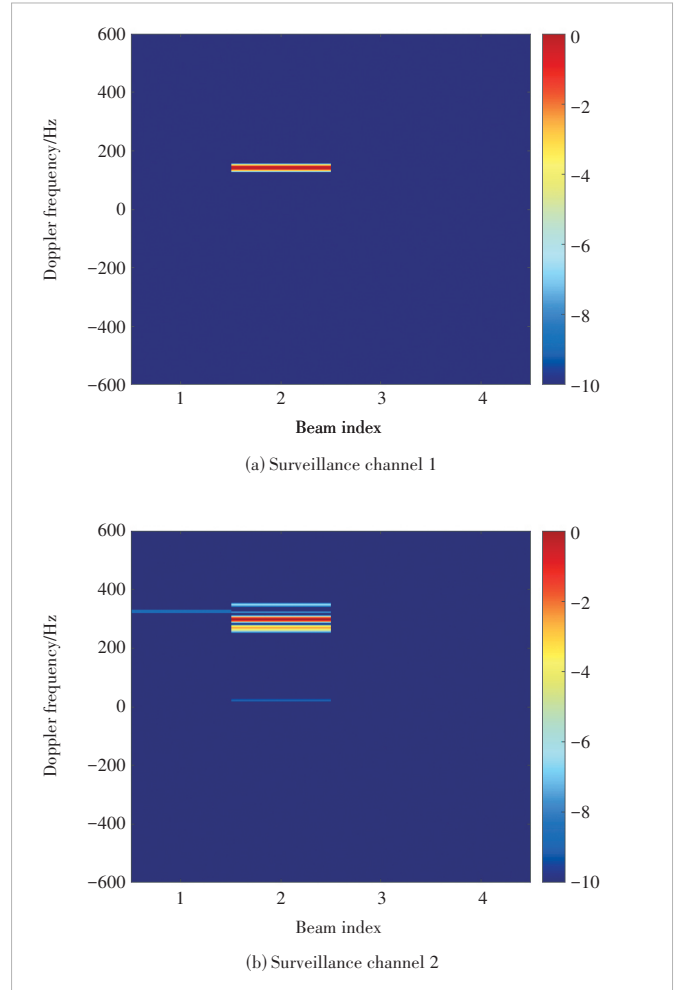
The experiments are conducted in a laboratory environment with rich scattering clusters, e.g., displays and metallic cabinets. The placement of the two transmitters and the receiver platform is illustrated in Fig. 4, where all of the phased arrays are placed at a height of 1.5 m. Taking the receiver as the origin, the coordinates of transmitters 1 and 2 are $\mathbf{p}_1^{\text{TX}} = [2.7 \text{ m}, 0]^\text{T}$ and $\mathbf{p}_2^{\text{TX}} = [1.8 \text{ m}, -1.4 \text{ m}]^\text{T}$. A volunteer is walking in this region as a mobile blocker. A depth camera system (ZED) is deployed behind the receiver to record the true trajectory of the blocker. It is synchronized with the receiver at the millisecond level. Since different parts of the body have different trajectories, we extract the trajectory information of 21 key points of the human body from the depth camera^[21] with centimeter-level accuracy, and represent the real trajectory of the human body by that of the “neck” keypoint. This is because the key point of “neck” is at the same height as the phased array.

5.1 Detection of Doppler Frequency and AoA

An example of the Doppler-angle spectrograms of two surveillance channels in one sweeping period is shown in Fig. 5. In both spectrograms, the strengths of the signal components versus beam directions (AoAs) and Doppler frequencies are illustrated by colors. It can be observed that a Doppler frequency of 140 Hz is detected in surveillance channel 1, and a Doppler frequency of 300 Hz is detected in surveillance 2. Thus, the same movement of the blocker would generate different Doppler frequencies at the two surveillance channels due to different locations of the transmitters. It can also be observed that there are multiple peaks of Doppler frequencies in Fig. 5 (b) that are caused by different movements of scattering points on the human body, e.g.,



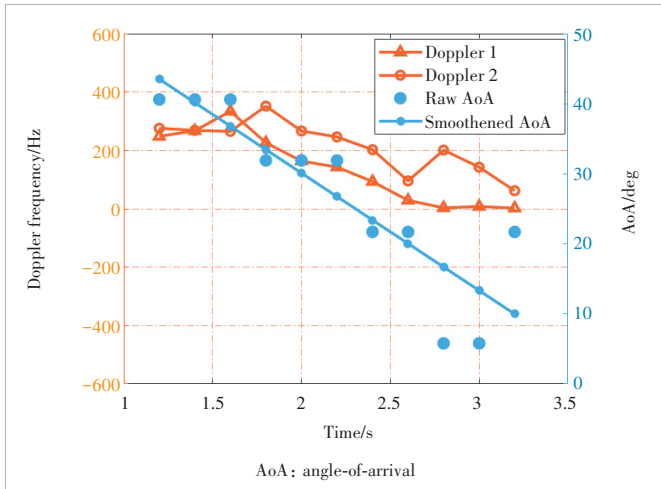
▲ Figure 4. Illustration of the experiment environment



▲ Figure 5. Doppler frequencies of 4 beams (beams 1 to 4 indicate angles-of-arrival of 40° , 27° , 18° and 10°) in a sweeping period

350 Hz, 300 Hz and 270 Hz. According to Eq. (5), we will choose the Doppler frequency with the highest signal strength as the feature of the sweeping period. As a result, since the Doppler frequencies are mainly captured by the second beam direction, the AoA of the sweeping period is 27° .

All detected Doppler frequencies and AoAs versus time of a trajectory are shown in Fig. 6. It can be observed that there is no moving target in the time interval $[0, 1.2 \text{ s}]$, since no significant Doppler frequency can be detected. The Doppler frequencies of surveillance channel 1 is consistently greater than that of surveillance channel 2, and the Doppler frequency of the first surveillance channel is close to 0 in $[2.8 \text{ s}, 3.2 \text{ s}]$. This is because the projection of velocity along surveillance channel 2 is more significant according to the locations of both transmitters. Furthermore, since the estimation error of AoAs could be large, it is necessary to smooth AoAs via polynomials as shown by the blue line. After the detection of Doppler frequencies and AoAs of the two surveillance channels, the trajectory of the blocker and the positions of transmitters can be obtained by solving the problem in Eq. (12).



▲ Figure 6. Estimated Doppler frequencies of two surveillance channels and AoAs

5.2 Trajectory Estimation and Transmitter's Localization

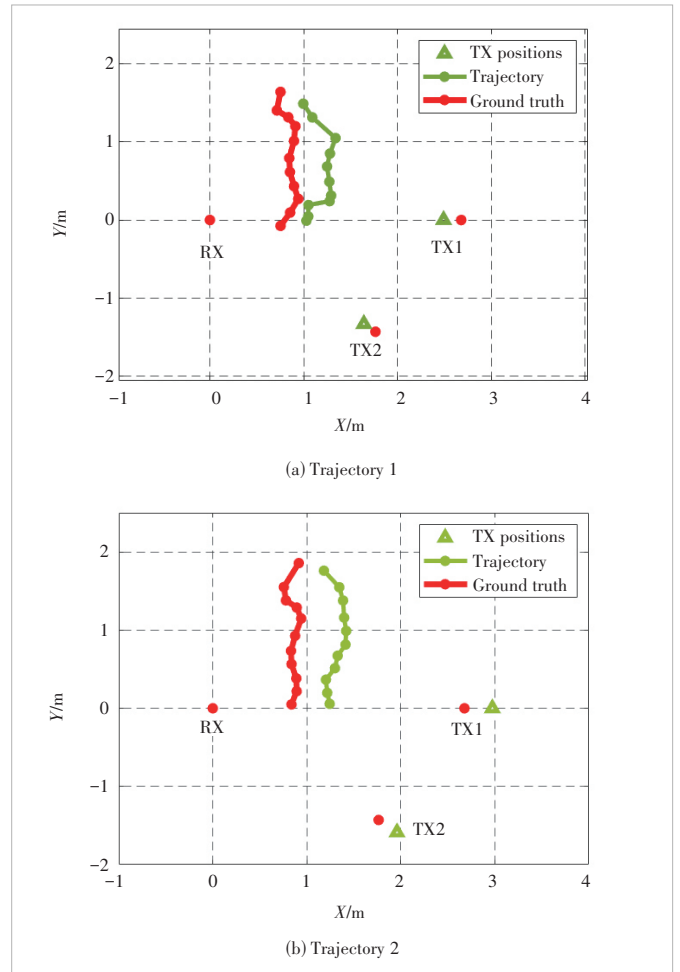
In the experiments, it is estimated that the ADoAs are $\varphi_{RX} = 39^\circ$ and $\varphi_{RX} = 58^\circ$. Hence, the locations of the two transmitters and the trajectory of the mobile blocker can be estimated jointly according to the above estimated Doppler frequencies and AoAs. The trajectories of the two trails are illustrated in Figs. 7(a) and 7(b), respectively, where the red curve is the true trajectory of the blocker recorded by the ZED and the green one is the estimated one. Moreover, the true and estimated locations of the two transmitters are also differentiated by colors. It can be observed that the localization errors of the two transmitters are within 0.2 m. The estimated trajectory is almost parallel to the real trajectory, but with an offset in the x -axis. The average error in the blocker's trajectory and raw AoA estimation is 0.39 m and 7.8 degrees, respectively, with corresponding mean squared errors of 0.48^2 and 9.4^2 . Nevertheless, the estimated trajectory is sufficiently accurate in the blockage prediction.

5.3 Blockage Prediction

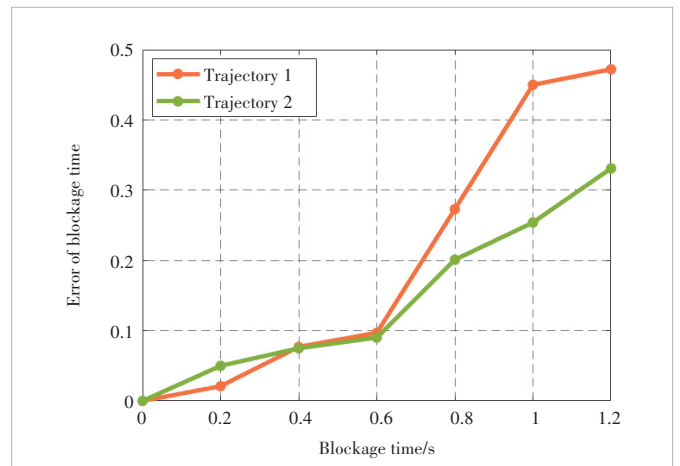
The prediction of blockage time, which measures the remaining time duration until link blockage, for the above two trajectories is illustrated in Fig. 8. Due to the placement of transmitters and the receiver, the link blockage will happen in reference channel 1. It can be observed that the error of blockage time \hat{t}_1 is less than 0.1 s when the blockage time is less than 0.6 s. Moreover, larger blockage time leads to larger prediction errors. This is due to the time-varying velocity of the volunteer.

6 Conclusions

In the paper, a method that employs passive sensing techniques to jointly estimate transmitter positions and blocker trajectories is proposed for mmWave communication systems, so that the link blockage and the blockage time can be predicted. The method can be deployed in the uplink transmission sce-



▲ Figure 7. Estimated trajectory of the blocker and the positions of transmitters



▲ Figure 8. Error of predicted blockage time \hat{t}_1

nario with one mobile blocker and at least two transmitters. Without a priori knowledge of the positions of transmitters, the trajectory of the mobile blocker is estimated by tracking its Doppler frequencies and AoAs in a number of sweeping periods,

where a gradient-descent algorithm is proposed to suppress the estimation error. It is demonstrated that the system can achieve decimeter-level localization and trajectory estimation, and the blockage time prediction error is within 0.1 s when the blockage time is less than 0.6 s.

While this paper considers the tracking of a single blocker, the proposed system has the potential to identify and track multiple blockers with distinct Doppler frequencies or AoAs. Moreover, it is possible to improve the detection accuracy of the distances between the transmitters and the receiver by observing a number of trajectories of a single blocker in different trials. Hence, the detection accuracy of a single blocker's trajectory could also be further improved. We would like to investigate the above extensions in our future research.

References

- [1] BAI T Y, HEATH R W. Coverage and rate analysis for millimeter-wave cellular networks [J]. *IEEE transactions on wireless communications*, 2015, 14 (2): 1100 - 1114. DOI: 10.1109/TWC.2014.2364267
- [2] MACCARTNEY G R, RAPPAPORT T S, RANGAN S. Rapid fading due to human blockage in pedestrian crowds at 5G millimeter-wave frequencies [C]//*IEEE Global Communications Conference. IEEE*, 2017: 1 - 7. DOI: 10.1109/GLOCOM.2017.8254900
- [3] RAPPAPORT T S, XING Y C, KANHERE O, et al. Wireless communications and applications above 100 GHz: opportunities and challenges for 6G and beyond [J]. *IEEE access*, 2019, 7: 78729 - 78757. DOI: 10.1109/ACCESS.2019.2921522
- [4] CHARAN G, ALRABEIAH M, ALKHATEEB A. Vision-aided 6G wireless communications: blockage prediction and proactive handoff [J]. *IEEE transactions on vehicular technology*, 2021, 70(10): 10193 - 10208. DOI: 10.1109/TVT.2021.3104219
- [5] YANG Y W, GAO F F, TAO X M, et al. Environment semantics aided wireless communications: a case study of mmWave beam prediction and blockage prediction [J]. *IEEE journal on selected areas in communications*, 2023, 41(7): 2025 - 2040. DOI: 10.1109/JSAC.2023.3280966
- [6] WU S Y, CHAKRABARTI C, ALKHATEEB A. Proactively predicting dynamic 6G link blockages using LiDAR and in-band signatures [J]. *IEEE open journal of the communications society*, 2023, 4: 392 - 412. DOI: 10.1109/OJCOMS.2023.3239434
- [7] WU S Y, ALRABEIAH M, CHAKRABARTI C, et al. Blockage prediction using wireless signatures: deep learning enables real-world demonstration [J]. *IEEE open journal of the communications society*, 2022, 3: 776 - 796. DOI: 10.1109/OJCOMS.2022.3162591
- [8] FALLAH DIZCHE A, DUEL-HALLEN A, HALLEN H. Early warning of mmWave signal blockage using diffraction properties and machine learning [J]. *IEEE communications letters*, 2022, 26(12): 2944 - 2948. DOI: 10.1109/LCOMM.2022.3204636
- [9] HERSYANDIKA R, MIAO Y, POLLIN S. Guard beam: protecting mmWave communication through In-band early blockage prediction [C]//*IEEE Global Communications Conference. IEEE*, 2022: 4093 - 4098. DOI: 10.1109/GLOBECOM48099.2022.10001163
- [10] TANG R S, QI C H, SUN Y. Blockage prediction and fast handover of base station for millimeter wave communications [J]. *IEEE communications letters*, 2023, 27(8): 2142 - 2146. DOI: 10.1109/LCOMM.2023.3289581
- [11] ALKHATEEB A, BELTAGY I, ALEX S. Machine learning for reliable mmwave systems: blockage prediction and proactive handoff [C]//*Global Conference on Signal and Information Processing (GlobalSIP). IEEE*, 2018: 1055 - 1059. DOI: 10.1109/GlobalSIP.2018.8646438
- [12] YU C, SUN Y F, LUO Y, et al. MmAlert: mmWave link blockage prediction via passive sensing [J]. *IEEE wireless communications letters*, 2023, 12 (12): 2008 - 2012. DOI: 10.1109/LWC.2023.3304320
- [13] COLONE F, FILIPPINI F, PASTINA D. Passive radar: past, present, and future challenges [J]. *IEEE aerospace and electronic systems magazine*, 2023, 38(1): 54 - 69. DOI: 10.1109/maes.2022.3221685
- [14] SUN H B, CHIA L G, RAZUL S G. Through-wall human sensing with WiFi passive radar [J]. *IEEE transactions on aerospace and electronic systems*, 2021, 57(4): 2135 - 2148. DOI: 10.1109/taes.2021.3069767
- [15] RAJA ABDULLAH R S A, SALAH A A, ISMAIL A, et al. Experimental investigation on target detection and tracking in passive radar using long-term evolution signal [J]. *IET radar, sonar & navigation*, 2016, 10(3): 577 - 585. DOI: 10.1049/iet-rsn.2015.0346
- [16] YU C, LUO Y, CHEN R Q, et al. Passive handwriting tracking via weak mmWave communication signals [J]. *IEEE wireless communications letters*, 2024, 13(3): 874 - 878. DOI: 10.1109/LWC.2023.3348875
- [17] TAN D K P, SUN H, LU Y, et al. Passive radar using global system for mobile communication signal: theory, implementation and measurements [J]. *IEE proceedings, radar, sonar and navigation*, 2005, 152(3): 116. DOI: 10.1049/ip-rsn: 20055038
- [18] SUN Y F, LI J, ZHANG T, et al. An indoor environment sensing and localization system via mmWave phased array [J]. *Journal of communications and information networks*, 2022, 7(4): 383 - 393. DOI: 10.23919/JCIN.2022.10005216
- [19] LEVENBERG K. A method for the solution of certain non-linear problems in least squares [J]. *Quarterly of applied mathematics*, 1944, 2(2): 164 - 168. DOI: 10.1090/qam/10666
- [20] MARQUARDT D W. An algorithm for least-squares estimation of nonlinear parameters [J]. *Journal of the society for industrial and applied mathematics*, 1963, 11(2): 431 - 441. DOI: 10.1137/0111030
- [21] Stereolabs. Stereolabs docs: API reference, tutorials, and integration [EB/OL]. [2024-07-07]. <https://www.stereolabs.com/docs>

Biographies

YU Chao received his BS degree from Qingdao University of Technology, China in 2019 and ME degree from the Southern University of Science and Technology (SUSTech), China in 2023. He is currently a research assistant with SUSTech. His research interests include integrated sensing and communication (ISAC) and passive sensing.

LYU Bojie received his BE degree in communication engineering from Southern University of Science and Technology (SUSTech), China in 2018, and M.Phil degree (ranked top 2) in information and communication engineering from Harbin Institute of Technology, China in 2020. He is currently pursuing his PhD degree in mathematics with SUSTech.

QIU Haoyu received his BE degree from the Southern University of Science and Technology, China in 2023, where he is currently pursuing his ME degree with the Department of Electronic and Electrical Engineering. His research interests include wireless sensing, passive mmWave communication and sensing system and optimization in the WiFi system.

WANG Rui (wangr@sustech.edu.cn) received his BS degree from the University of Science and Technology of China in 2004, and PhD degree in wireless communications from The Hong Kong University of Science and Technology, China in 2008. From 2009 to 2012, he was a senior research engineer with Huawei Technologies, Co., Ltd. Since 2012, he has joined Southern University of Science and Technology, China as an associate professor. He has research experience in both academia and industry. He has authored over 100 papers in top-level IEEE journals and flagship international conferences, especially in the area of wireless radio resource optimization and interference management. He has contributed over 20 US patent applications and over 100 Chinese patent applications (50 of them have been granted).



Integrated Sensing and Communication: Who Benefits More?

DU Ruolin, WEI Zhiqiang, YANG Zai

(Xi'an Jiaotong University, Xi'an 710049, China)

DOI: 10.12142/ZTECOM.202403006

<https://kns.cnki.net/kcms/detail/34.1294.TN.20240911.0853.002.html>,
published online September 11, 2024

Manuscript received: 2024-08-26

Abstract: This paper compares the benefits of communication-assisted sensing and sensing-assisted communication in the context of integrated sensing and communication (ISAC). Communication-assisted sensing leverages the extensive cellular infrastructure to create a vast and cooperative sensor network, enhancing environmental perception accuracy and coverage. On the other hand, sensing-assisted communication utilizes advanced sensing technologies to improve predictive beamforming and channel estimation performance in high-frequency and high-mobility scenarios, thereby increasing communication efficiency and reliability. To validate our analysis, we present an example of channel knowledge map (CKM)-assisted beam tracking. This example demonstrates the practical advantages of incorporating CKM in enhancing beam tracking accuracy. Our analysis confirms that communication-assisted sensing may offer greater development potential due to its wide coverage and cost-effectiveness in large-scale applications.

Keywords: communication-assisted sensing; integrated sensing and communication (ISAC); sensing-assisted communication; 6G; vehicle-to-everything (V2X)

Citation (Format 1): DU R L, WEI Z Q, YANG Z. Integrated sensing and communication: who benefits more? [J]. *ZTE Communications*, 2024, 22(3): 37 - 47. DOI: 10.12142/ZTECOM.202403006

Citation (Format 2): R. L. Du, Z. Q. Wei, and Z. Yang, "Integrated sensing and communication: who benefits more?" *ZTE Communications*, vol. 22, no. 3, pp. 37 - 47, Sept. 2024. doi: 10.12142/ZTECOM.202403006.

1 Introduction

Integrated sensing and communication (ISAC) is gaining widespread attention as a crucial technology for future wireless systems^[1]. The International Telecommunication Union (ITU) has regarded ISAC as one of the key potential technologies for the 6G mobile communication systems^[2]. Future 6G networks are expected to utilize wide-bandwidth radio signals, large-scale antenna arrays, and multiple network nodes to offer efficient sensing capabilities including detection, localization, tracking, activity recognition, and environmental reconstruction, which brings the ultimate vision of the interconnected, intelligent, and perceptive world into reality^[3-6]. Moreover, in future 6G wireless networks, ISAC will support higher data rates, enhanced communication reliability, and improved network coverage.

ISAC provides substantial gains by combining communication and sensing functions into a unified framework. This integration results in increased spectrum and hardware utilization efficiency, collectively known as integration gain. More importantly, coordination gain is achieved through the mutual assistance of communication and sensing, enhancing overall system performance^[1]. ISAC allows the communication system to

serve as a sensor^[3], utilizing radio wave transmission, reflection, and scattering to perceive and understand the physical environment^[7], thereby offering a broader range of new services. Additionally, high-precision localization, imaging, and environmental reconstruction can significantly improve communication performance by enabling more accurate predictive beamforming^[8], faster link recovery^[9], and reduced overhead for tracking channel state information (CSI)^[10-11].

To enhance the integration gain, researchers have considered three design approaches: communication-centric design, radar-centric design, and joint optimization design^[12-13]. On the other hand, to enhance the collaborative gain, two approaches have been adopted^[1]: communication-assisted sensing and sensing-assisted communication. In particular, communication-assisted sensing leverages existing cellular network protocols and architectures to utilize available radio resources for sensing based on communication signals. Wireless communication networks enable distributed sensing and enhance sensing performance to address the limitations of monostatic sensing. In perceptive mobile networks (PMN), existing works have shown that distributed ISAC systems can improve localization accuracy and moving target detection probability by offering extensive angle observations and a wide

range of spatial diversity^[14].

However, distributed ISAC imposes a demanding requirement on time and frequency synchronization among distributed sensing nodes^[14]. The main challenges of communication-assisted sensing include self-interference cancellation, interference management, network resource scheduling, and synchronization^[1, 5, 14], which will be detailed later. Sensing-assisted communication refers to the use of radar sensing to assist communication in high-mobility scenarios, effectively reducing communication overhead and improving communication reliability^[15-16]. In sensing-assisted wireless networks, the estimated location and speed of a moving terminal can be utilized for fast link establishment and handover, thus reducing access delay^[17-19]. The main challenges of sensing-assisted communication include the limited sensing range, the mismatch between the sensed state and CSI, and the requirement for full-duplex operation to eliminate strong interference from transmitted signals to the echoes.

This paper investigates the comparative analysis of communication-assisted sensing and sensing-assisted communication, including their applicable scenarios, sources of benefits, and technical details. We aim to determine which method holds greater research significance and performance gain in future 6G scenarios, such as intelligent transportation systems and smart cities. In this paper, we first introduce the basic concepts, main challenges and usage scenarios of ISAC. Then, we discuss the mutual benefits of sensing and communication, and investigate which one benefits more. In the end, we present an example of channel knowledge map (CKM)-assisted beam tracking to illustrate how communication-assisted sensing enhances beam tracking accuracy in complex vehicle-to-everything (V2X) scenarios in the presence of multipath and channel variations.

2 Fundamentals of ISAC

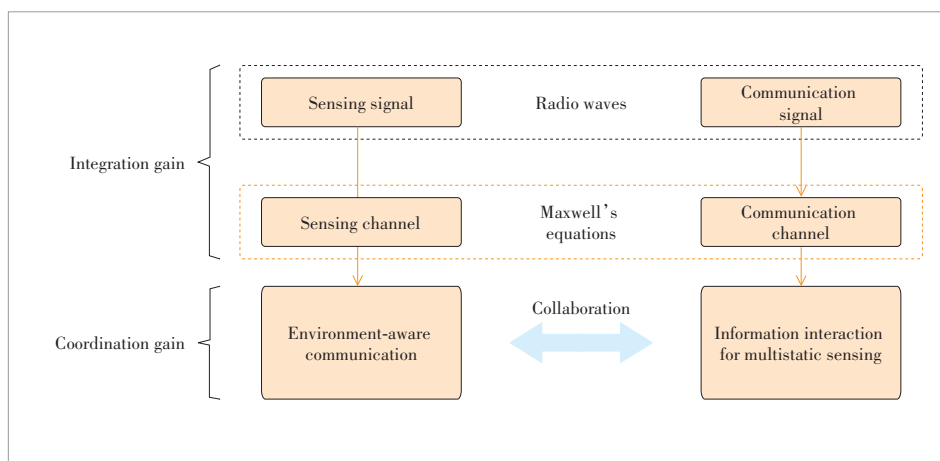
2.1 ISAC Definition and Models

ISAC aims to achieve dual functions of communication and radar through integrated design in hardware platforms, resource allocation, and signal processing, addressing the issue of scarce spectrum resources^[3].

The main advantage of ISAC over independent sensing or communication is integration gain. As shown in Fig. 1, both sensing and communication (S&C) utilize radio waves as their signal carriers, and the propagation of these signals follows Maxwell's equations. This commonality implies that the components or re-

sources used for sensing and communication can be effectively coupled to achieve more efficient resource utilization. For example, ISAC can divide the antenna array into two groups, one for communication and the other for sensing, using the same hardware to fulfill their respective purposes. Spectral efficiency can be readily pursued by employing a dual-mission signal^[13]. Consequently, by sharing spectrum and hardware, system spectral efficiency, energy efficiency, and hardware efficiency can be improved, thereby achieving integration gain. Furthermore, the mutual assistance between sensing and communication functions can further enhance their respective performances, leading to coordination gain. As depicted in Fig. 1, environment-aware communication can be achieved by incorporating the sensed information, such as the user terminal state and the environment radio map^[4, 8], into the communication design. Multistatic sensing can be achieved via proper information interaction among distributed sensing nodes.

Fig. 2 illustrates three types of ISAC systems, including monostatic sensing, bistatic sensing, and multistatic sensing. In all these scenarios, the base station (BS) transmits ISAC signals to perform communication and sensing tasks simultaneously. The red arrows represent communication channels, while the yellow arrows indicate sensing channels. The BS communicates with users via the communication channels and detects the position, speed, and other kinematic parameters of targets through sensing channels. In a monostatic ISAC system, the BS receives echoes reflected from targets at the same time. Nevertheless, a full-duplex BS is necessary for the simultaneous transmission and receiving of signals, as any remaining interference signal could deteriorate the BS's sensing capabilities^[3]. To circumvent this limitation, bistatic and multistatic ISAC systems have been proposed, where the sensing receiver is physically separated from the transmitter and almost does not suffer from the residual interference, and thus hardware modifications for a full-duplex BS are avoided. The bi-



▲ Figure 1. Two main advantages of integrated sensing and communication (ISAC): integration gain and coordination gain

static ISAC system includes one BS and one sensing receiver. The multistatic ISAC system comprises multiple base stations that together form a sensing cluster. This configuration includes various combinations, such as several transmitters with multiple receivers, a single transmitter with multiple receivers, or multiple transmitters with one receiver, to provide sensing services.

Based on whether the sensing target has the requirement and capability of communication, targets can be categorized into communication objects and non-communication objects. Communication objects refer to cooperative targets that can transmit, receive, and process signals, allowing the BS to sense them by receiving signals sent or reflected by the targets. Sensing based on communication objects is common in vehicle-to-everything (V2X) or unmanned aerial vehicle (UAV) networks, where the BS aims to communicate with the car or UAV while simultaneously acquiring and tracking their location and velocity. Communication objects within a scenario can also be classified based on their sensing requirements. For instance, between fixed BSs, only the channel state information (CSI) needs to be sensed. However, in more complex scenarios with dynamic interference, it is necessary to sense not only the CSI but also the radar cross-section, movement velocity, and other kinematic parameters of the targets^[11, 20-21]. Non-communication objects, on the other hand, lack baseband functionality and cannot send or receive signals. They can only reflect signals to the BS, enabling the BS

to sense their states. Non-communication targets are usually considered a part of the surrounding environment and their information can facilitate environment-aware communication^[4].

2.2 Challenges of ISAC

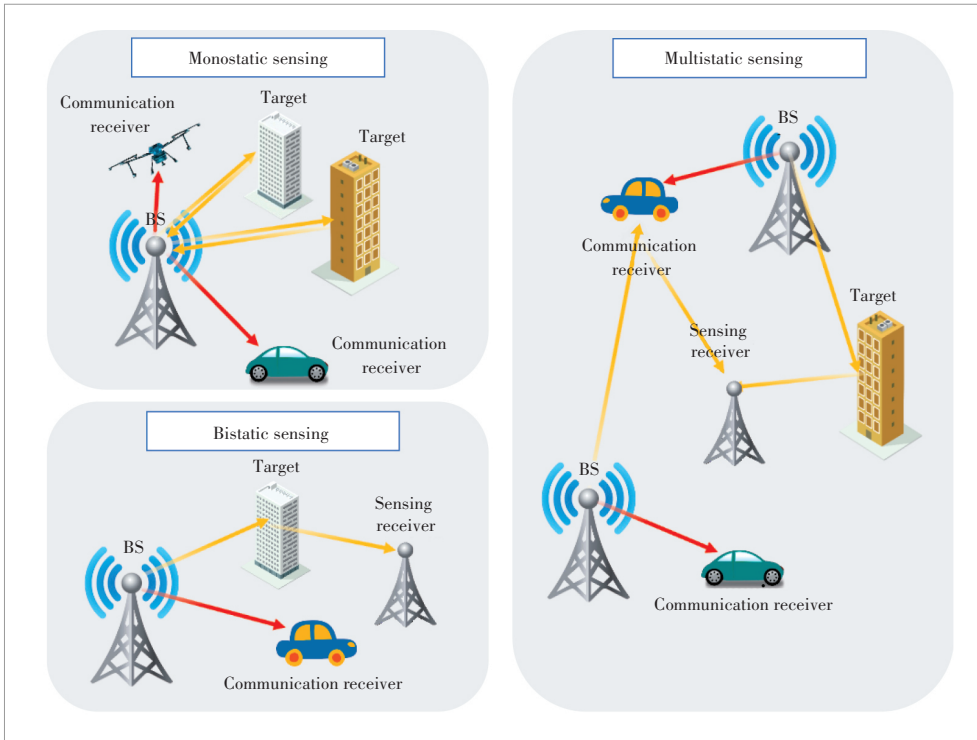
2.2.1 Joint Waveform Design and S&C Tradeoff

One of the primary challenges in ISAC is designing a unified waveform that can perform both target sensing and information transmission. The design methodologies can typically be categorized into three approaches: radar-centric design, communication-centric design, and joint design. The inherent similarities in channel parameters between sensing and communication serve as a primary driving force behind the design of ISAC waveforms. For example, in the monostatic ISAC system shown in Fig. 2, communication signal detection is based on one-way transmission from the BS to the user, while sensing relies on echoes received at the BS following round-trip propagation. But for both sensing and communication, the physical environment between the user and the BS is the same. Despite this, there is an inevitable tradeoff between sensing and communication due to different performance metric priorities for each function. We consider a general linear Gaussian channel model as follows^[22]:

$$Y = H(\eta)S(\xi) + Z, \quad (1)$$

where Y , H , S , and Z represent the received signal at the BS, the channel, the transmitted signal, and the Gaussian noise, respectively. These elements can be in the form of scalars, vectors, or matrices. The channel H is dependent on the physical parameters, e.g., range, angle, and velocity. The transmit signal S may be encoded/modulated with some information codeword ξ .

From the communication perspective, the fundamental problem is getting the codewords ξ back from Y . The channel H can be estimated a priori via pilot training. On the other hand, from the sensing perspective, the primary objective is to accurately estimate the target parameter η contained within H based on the known Y and S . When S is a known deterministic signal, ξ can be left out because the radar waveform does not contain any information. Then, the ISAC sys-



▲ Figure 2. Typical integrated sensing and communication (ISAC) systems, where the sensing target can be the communication receiver itself in all the scenarios

tem model can be written as^[3, 22]:

$$\begin{cases} \text{Sensing signal model: } Y_r = H_r(\eta)S + Z_r \\ \text{Communication signal model: } Y_c = H_cS + Z_c, \end{cases} \quad (2)$$

where S is the ISAC signal's discrete representation. To distinguish between sensing and communication channels, we use the subscripts $(\cdot)_r$ and $(\cdot)_c$, respectively.

Since sensing and communication have distinct performance metrics and prefer different signal distributions, it is crucial to achieve a balance between these two functions. In ISAC systems, there are two types of tradeoffs: the time-frequency tradeoff and the spatial tradeoff, also known as the deterministic random tradeoff (DRT) and the subspace tradeoff (ST)^[22]. Sensing systems prefer deterministic signals to achieve steady sensing performance, but communication systems need random signals send as much information as feasible. Choosing the modulation order for random data results in a tradeoff between time and frequency: higher-order modulation improves communication rates but degrades sensing performance because the random and non-constant-modulus data raise side-lobe levels in the ambiguity function^[3, 19, 22]. However, the choice of ISAC beamforming strategies is related to the spatial tradeoff. Aligning sensing-optimal and communication-optimal signals to their respective subspaces and managing resource allocation accordingly can enhance efficiency if their subspaces overlap. Conversely, no resources may be reused if two subspaces are orthogonal to each other, nulling any performance gain. More resources may be utilized between sensing and communication when there is a larger overlapping degree between two subspaces, which improves tradeoff performance^[12].

2.2.2 Artificial Intelligence (AI) Enabled ISAC

Powerful AI algorithms offer new opportunities to ISAC. A large volume of data generated by ISAC at the BS need to be processed rapidly and accurately by AI algorithms, potentially in conjunction with sensing data from other model sensors such as cameras and LiDARs^[18], to support applications with ultra-low latency requirements for sensing, communication, computation, and control. In data-rich and complex ISAC scenarios such as urban outdoor propagation environments, there exist plenty of noisy, discontinuous, or multimodal objective observations. The physical formulation of the system's nonlinear signal characteristics may be unknown or challenging to the model. In such cases, AI can be employed to simulate intricate communication/sensing channels, the surrounding environment, and even the system uncertainties. This approach addresses challenges that cannot be resolved solely through traditional mathematical models or signal-processing techniques.

However, integrating AI with ISAC systems poses significant challenges. The ISAC system can leverage its powerful sensing and communication capabilities to provide rich input

data for the training AI models. Additionally, AI-enabled ISAC introduces complex tradeoffs between sensing, communication, and computation^[1]. Firstly, defining performance metrics for an AI-enhanced ISAC system is challenging. This may involve integrating metrics such as AI model complexity, convergence speed, generalization ability, data dependency, and training computational cost with ISAC performance metrics. For example, it is necessary to define the overall latency for AI-enabled ISAC integrated services. If the processes of communication, sensing, and AI computation are sequential, the combined communication, sensing, and computation latency must not exceed the overall latency. Secondly, establishing an AI model dedicated to ISAC systems is challenging. For instance, the recently developed channel semantics provide an innovative perspective to ISAC signal processing. By combining the advantages of data-driven and model-driven techniques, a more reliable and effective ISAC system can be developed based on specific AI models^[23]. Furthermore, data security and privacy protection within the AI-enabled ISAC integrated architecture are critical concerns that cannot be overlooked.

2.2.3 Collaborative ISAC

In multi-user and multi-target scenarios, collaborative ISAC systems face the challenge of coordinating multiple cooperative nodes to optimize resource utilization and improve sensing performance. Effective collaboration requires sophisticated algorithms to manage interactions among users and share sensing data. Cloud radio access networks (C-RAN) offer greater flexibility for ISAC through cooperation among multiple BSs, especially in resource-limited situations, providing additional cooperative gains for both communication and sensing functions^[24].

To this end, it is crucial to develop advanced optimization algorithms and distributed sensing technologies to minimize information interaction overhead and enhance the efficiency of collaborative ISAC systems. For example, a joint communication and radar optimization resource allocation scheme is introduced, which supports the fusion of vast numbers of sensing data from both wireless infrastructure and vehicles to achieve optimal computation and resource allocation decisions^[25]. High-precision clock synchronization among nodes is also necessary for collaborative sensing. Imperfect clock synchronization can deteriorate the ambiguity function of the sensing signals in distributed systems, leading to reduced localization accuracy. The synchronization error in several clocks must be within tens of picoseconds in order to achieve centimeter-level resolution precision^[26]. This is a very strict synchronization requirement. While certain synchronization protocols, such as precision time protocol (PTP) and master-slave closed-up, can achieve a high degree of synchronization accuracy^[27], advanced methods are expected to support higher precision sensing functions.

2.2.4 Privacy and Security Issues

Privacy and security issues are significant considerations. Integrating sensing and communication functions involve collecting and transmitting a large volume of user data and environmental information^[28]. In practice, the sensed targets can potentially use the information-bearing signals to detect confidential information sent to the communication destination. This presents a significant tradeoff issue for the transmitter in ISAC systems. On one hand, the transmitter aims to enhance target sensing by focusing power on the target. On the other hand, it must limit the communication signal power reaching the target to prevent potential eavesdropping. Therefore, effective privacy protection measures and security mechanisms must be implemented to prevent information leakage and malicious attacks. Research and exploration in these areas are crucial for advancing the development and application of sensing and communication technologies.

2.3 Use Cases for ISAC in 6G

The most prominent scenarios and use cases for ISAC span both civilian and military domains^[1, 16]. From a civilian perspective, numerous emerging applications necessitate the joint design of sensing and communication, such as smart cities, smart homes, and intelligent manufacturing^[5], as well as intelligent transportation applications like vehicular networks and autonomous driving^[18]. From a military perspective, the development of radar, communication, and remote sensing systems has historically been isolated. By applying ISAC technologies, it is possible to significantly reduce the consumption of spectrum and hardware resources and enhance the performance of both communication and sensing.

2.3.1 V2X High-Accuracy Localization and Beam Tracking

V2X enhances traffic efficiency, road safety, and the availability of infotainment services. It encompasses vehicle-to-vehicle (V2V), vehicle-to-pedestrian (V2P), vehicle-to-infrastructure (V2I), and vehicle-to-network (V2N) communications. V2X requires Gbit/s-class data transmission with low latency and precise sensing for vehicle positioning^[29]. Traditional technologies like global navigation satellite systems (GNSS) and dedicated short range communications (DSRC) are inadequate for these needs^[30]. Robust beam tracking is essential in dynamic vehicular environments and millimeter-wave (mmWave) communications, extending the network coverage effectively^[16].

Within the ISAC framework, the roadside units (RSUs) can predict and estimate the vehicle's state at each epoch and the beamforming can be designed to match the predicted channel. For example, a novel extended Kalman filtering (EKF)-based predictive beamforming was proposed to effectively track and predict movements^[16, 21, 29, 31 - 32], employing ISAC echo signals for real-time vehicle position detection and state parameter estimation. With the use of the vehicles' state transition models

and echo signals, a distribution of the estimated parameters is generated in a novel beamforming system based on probabilistic prediction^[10]. However, many algorithms presuppose the availability of line-of-sight (LoS) links that are often obstructed in urban environments by high-rise buildings or other vehicles, leading to degraded channel time correlation and significantly impacting performance^[18]. ISAC in a non-line-of-sight (NLoS) scenario deserves to be studied further.

2.3.2 Human Activity Recognition and Smart Home

ISAC-based Internet of Things (IoT) systems show great potential in various applications, including daily activity recognition, healthcare monitoring, home security, and driver attention monitoring^[13]. Compared with sensor-based methods (such as cameras, Lidars, and ultrasonic sensors), current mmWave sensing has several benefits, such as a wider sensing range, fine-grained and directed sensing capacity, and resistance to illumination conditions^[33]. Evaluating variations in the amplitude and phase of wireless signals can facilitate a range of human sensing activities, including human tracking and localization, activity recognition, monitoring vital signs, sound recovery, and human imaging. Integrating sensing capabilities into existing wireless communication devices will significantly enhance the quality of life by improving the living environment and ensuring better safety and health monitoring.

2.3.3 ISAC for IRS-Assisted System

Intelligent reflecting surface (IRS) adjusts the phase, amplitude, frequency, and polarization of incident signals using numerous low-cost reflecting elements, thereby modifying signal propagation^[34]. The IRS usage is more appropriate for sensing and communication tasks because the ISAC system uses a common transmitter^[1]. The LoS path between the radar and the target is critical for sensing functionality. In scenarios where the LoS path is obstructed, resulting in weak or non-existent signals, a virtual LoS channel can be established between the radar and the target using IRS to cover blind spots. This ensures reliable sensing performance and utilizes the NLoS channels established by the IRS for downlink multi-user communication. For changing the direction of the signal that arrives from the BS towards the users, the BS uses a backhaul control connection to reconfigure the phase shift corresponding to each element in real time via external signals^[34]. This particular application of the IRS increases the BS's coverage area and improves the received signal energy at distant users. By simply adjusting these phase shifts to allow the BS to only do digital beamforming with fewer antennas, the IRS-assisted systems enable analog beamforming, lowering hardware costs and increasing energy efficiency.

However, the combined design issue including IRS is computationally hard, especially when designing optimal waveforms and allocating resources efficiently.

2.3.4 ISAC for UAV Networks

UAVs are characterized by high mobility, long range, wide coverage, and ease of deployment^[35]. UAVs constantly serve as temporary BSs or relays for potential improvements in communication coverage when employed as an auxiliary communication platform in airspace^[36]. Numerous advantages can be realized if the independent communication load and sensing load are replaced by the ISAC load. Because of the decreased load weight, UAVs will be more durable and flexible. Secondly, the ISAC UAV platform can achieve coordination gains. On the one hand, when the integrated waveform in the downlink communication channel between the BS and the UAVs encounters possible targets (such as buildings or uncooperative UAVs) during transmission, it will immediately be reflected back. The echo signal can then be cooperatively processed by the UAV network to detect the presence of a non-cooperative UAV and even pinpoint its location. This feature lowers the possibility of mishaps brought on by uncooperative UAVs, including privacy violations and flight disturbances. A more stable beam between UAVs and BS can be formed with the help of sensing the geographical relationship between the UAVs and the ground, which reduces the likelihood of mismatching in the beam management process.

3 Mutual Benefits of Communication and Sensing

3.1 Communication-Assisted Sensing

Integrated with sensing capabilities, 6G networks can function as a vast sensor network, continuously perceiving the physical world. A massive number of data provided by these networks contain rich channel knowledge, laying a solid foundation for communication-assisted sensing.

3.1.1 Networked Sensing

Communication-assisted sensing achieves gains in ISAC systems through sensing networks and cooperative sensing^[14]. Due to the significant influence of incident angles on the scattering and reflection intensity of electromagnetic waves on object surfaces and the potential presence of obstacles obstructing LoS, the sensing capability of individual nodes is limited^[11, 29, 37]. Existing communication devices reduce costs for establishing sensing platforms and provide numerous nodes and data sources. Through communication networks supporting multi-node cooperative sensing, nodes share sensing results and collectively sense their surrounding environment. This approach utilizes data fusion to reduce measurement uncertainties, expand coverage areas, enhance sensing accuracy and resolution, and even achieve sensing under NLoS conditions. Achieving optimal fusion of sensing results poses challenges in current research, focusing on addressing issues such as synchronization, joint signal and data processing, and efficient allocation of network resources.

3.1.2 CKM-Assisted Sensing

CKM is a comprehensive database that integrates environmental and channel state data to significantly enhance spatial coherence by correlating geographic positions with channel states^[4]. This supports precise beam alignment and tracking^[4, 38-39]. CKM is essentially a mapping between the location and CSI, which can facilitate environment-aware communication by providing a priori information on channels for transceiver design. Moreover, CKM can also be used in the opposite direction to improving sensing performance based on the measured CSI or channel parameters. Unlike traditional methods that rely on angle and signal energy^[37], CKM uses a priori information for hypothesis testing in LoS link identification^[11, 15]. This approach not only improves LoS detection but also aids in clutter suppression and interference elimination within ISAC systems. NLoS anchor nodes are known to be ineffective in improving localization accuracy, and when no prior knowledge of their NLoS pathways is available, they can even impair localization. In time-of-arrival wireless localization in complex environments that lack prior knowledge of NLoS path, only anchors with LoS paths to the agent increase localization accuracy. Based on the target's prior distribution, a unique CKM, i. e., LoS map^[7], could greatly reduce the localization error by selecting anchor nodes that are suitable for position estimation. Besides, the channel features included in the CKM are usually more stable than the directly measured CSI. Thus, CKM-assisted sensing could be more robust to environment dynamics. Besides, the channel features included in the CKM are usually more stable than the directly measured CSI. Thus, CKM-assisted sensing could be more robust to environment dynamics. While real-time training overhead can be reduced by radar/LiDAR/vision-aided communications without consuming communication resources, the cost, size, and complexity of communication systems are increased due to the need for extra hardware, waveforms, and signal processing complexity. CKM-enabled communications leverage environment awareness and can be implemented without these additional requirements. Furthermore, CKM can leverage vision, LiDAR, and radar observations to provide more precise predictions.

3.1.3 Wi-Fi Sensing

Due to the widespread usage and growing popularity of Wi-Fi devices, Wi-Fi signals, a part of the electromagnetic spectrum, can be found everywhere in everyday life and work^[3]. In addition to traditional communication functions, Wi-Fi signals contain a wealth of environmental information that can be exploited to sense and locate people and objects. Wi-Fi sensing can be categorized into three types: estimation, recognition, and detection^[40]. In a Wi-Fi system employing multiple-input and multiple-output orthogonal frequency division multiplexing (MIMO-OFDM), the CSI is a 3D matrix of complex numbers representing the amplitude attenuation and phase shift of

multiple-path Wi-Fi channels that can be used for different wireless sensing applications^[41]. For instance, CSI amplitude fluctuations in the time domain exhibit different trends for various humans, activities, gestures, and so on. These patterns may be applied to motion detection, human identification, fall detection, human presence detection, activity recognition, and gesture recognition. Human localization and tracking can be facilitated by CSI phase changes in the spatial and frequency domains, i.e., transmitting/receiving antennas and carrier frequencies, which are connected to signal transmission delay and direction^[41]. However, using a Wi-Fi device for sensing can degrade network performance and the sensing performance can be influenced by network settings. This interplay between Wi-Fi sensing and networking poses challenges but also highlights future trends in Wi-Fi technology, where seamless coexistence of both functions will be essential.

3.2 Sensing-Assisted Communication

Sensing-assisted communication demonstrates significant technical advantages and application potentials in high-frequency and high-mobility scenarios.

3.2.1 High-Frequency Communication

High-frequency ISAC signal propagation exhibits two primary characteristics:

- It shows rapid energy attenuation and significant energy loss due to reflection;
- The communication channel highly depends on the geometrical features of the environment.

These two characteristics underscore the potential to bolster communication robustness through precise environmental sensing. In high-frequency environments, sensing-assisted communication derives substantial benefits from several factors. Firstly, high-frequency waves almost completely lose their capacity to pass through common obstacles like walls and human bodies. This could block the LoS path between user equipment to an access point, thereby limiting the coverage distance. In scenarios characterized by complex and obstructive environments, high-accuracy localization and map reconstruction become pivotal to optimizing access. These sensing services can proactively design beam directions that minimize blockage by acquiring channel information a priori, thereby reducing disruptions^[11,15]. Secondly, the extensive bandwidth in the high-frequency band enables the system to distinguish between different scattering points along the distance axis with centimeter-level resolution^[42]. Given that channel parameters in high-frequency scenarios are intimately linked to the physical environment, a realistically reconstructed scenario from accurate sensing data can faithfully mirror the propagation dynamics of communication signals. Consequently, this allows for tailored energy allocation and beamforming to significantly enhance the achievable communication rate.

3.2.2 High-Mobility Communication

In high-mobility environments, beam training results in considerable overhead and significant latency^[41-42]. Owing beam tracking capacity is essential to adapt to fast-changing channels. In the context of V2I networks, sensing-assisted communication can reduce frequent beam sweeping overheads, while improving localization accuracy and robustness in high-mobility scenarios. Leveraging ISAC signals, RSUs can extract angle parameters from reflected echoes, thereby predicting angles and beam directions for the next moment^[10,21]. In high-mobility scenarios, the users may need to handover frequently between different BSs. Different from traditional detect-and-correct methods, a predict-and-prevent process that reduces the beam scanning area and offers early interventions for timely cell switching can be rendered possible by the sensing-assisted beam management method.

In summary, sensing-assisted communication in high-frequency and high-mobility scenarios not only significantly enhances the performance and reliability of communication systems through optimized beamforming and alignment strategies but also effectively reduces communication costs and complexity. The application potential of this technology promises substantial technological advancements and socio-economic benefits in future intelligent transportation, vehicular networks, and dense urban network domains.

3.3 Who Benefits More?

In summary, the relative advantages of communication-assisted sensing over sensing-assisted communication are highly dependent on the specific scenarios. In multistatic scenarios or at BSs with a priori information, such as networked sensing, ubiquitous sensing, and CKM-assisted sensing, which are particularly relevant to mmWave and intelligent transportation technologies, sensing typically derives greater benefits. Conversely, in environments characterized by high-mobility and high-frequency communication, the advantages predominantly favor communication.

Communication-assisted sensing offers significant benefits, particularly when the target is part of the surrounding environment. When BSs are connected via fronthaul links and participate in downlink bi-static sensing in a PMN framework, one BS's data payload can be directly acknowledged by another BS through coordination, which can be utilized for sensing functions. The high-capacity and low-latency optical fiber fronthaul also eliminates the need for complex phase noise compensation and synchronization methods.

On the other hand, sensing-assisted communication benefits more when the S&C channels are closely correlated and there are more wireless resources available for management. In general, sensing-assisted communication systems take advantage of the correlation between S&C channels to lower communication overheads and improve efficiency. Sensing-assisted V2X beam training, tracking, and prediction tech-

niques, for example, rely on the fact that a vehicle serves as both a radar target and a communication receiver, meaning that the S&C channels are highly linked. Sensing can be helpful in a high-mobility network not only for beam resources but also for allocating and managing more general wireless resources like power and bandwidth.

Given the existing communication networks and ubiquitous communication signals, communication-assisted sensing, with its broad coverage and capabilities for multi-node cooperative sensing, generally excels in more array of application scenarios. In the future, ISAC should progress from a monostatic to a multi-domain cooperative model. The exploration of methods to integrate as much sensory information as possible with minimal complexity to maximize cooperative gains remains a critical area of future research.

4 An Example: CKM-Assisted Multipath Beam Tracking

We provide an example of communication-assisted sensing in this section. In our example, tracking can be considered a sensing task, which aims to obtain the location of a moving target based on the angle and position measurements. Communication nodes record channel state information in a database known as the CKM, which can enhance sensing accuracy.

4.1 System Model

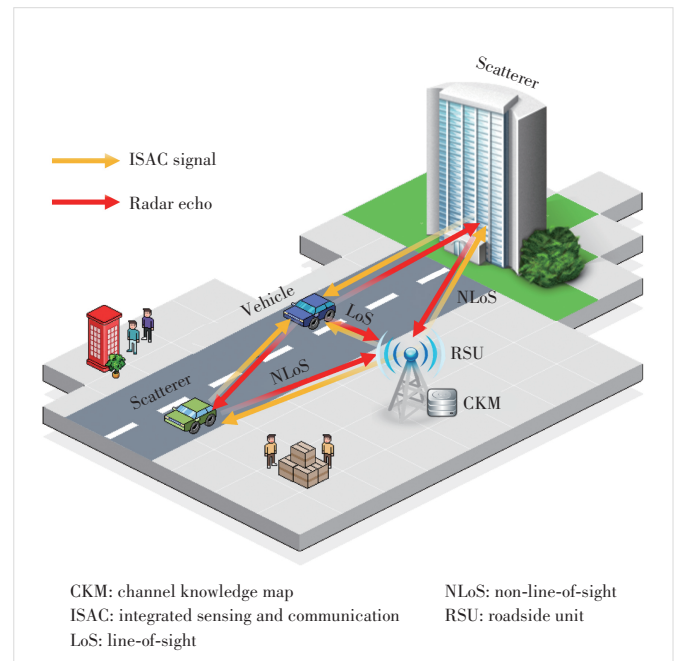
Robust beam tracking schemes are required due to the dynamic properties of vehicle motion and communication environments, as well as the high path loss and sensitivity to shadowing in mmWave communications^[42]. In the conventional beam tracking process, the receiver estimates the angle based on the received signal from the transmitter's pilot and returns it back to the transmitter. A tradeoff between the pilot overhead and the estimation accuracy is therefore needed^[20, 43 - 47]. In high-mobility communications, to achieve higher estimation accuracy, it is necessary to transmit more pilot signals, which incurs higher delay. A discrete Markov process has been proposed as a model for the temporal angle variations in a fast beam tracking strategy for mobile mmWave systems^[17].

We consider an mmWave MIMO system that includes an ISAC BS within an RSU. The RSU provides downlink communication services to user vehicles. Each user vehicle is equipped with a uniform linear array (ULA) for receiving signals from the RSU. The RSU itself functions both as a receiver and a transmitter, each end equipped with its own ULA.

Time is divided into slots, with each slot further divided into sub-slots. Within each slot, channel parameters remain constant. The transmitted ISAC signals are reflected back to the RSU after encountering scatterers, resulting in the RSU receiving a sum of paths, including reflections from various elements, such as buildings or other vehicles. The RSU exploits the echo signals and a priori information of CKM to align and track the beams accurately. The power of the reflected signal is not only

determined by the round-trip path-loss but also by the radar cross-section (RCS) of the target. In order to examine the RCS channel properties and environmental data, ZHANG et al.^[48] created an ISAC channel measurement platform. By approximating Maxwell's equations, extracting parameters through measurements, and estimating physical optics (PO), one can obtain the RCS. In target localization and tracking scenarios, the vehicle is usually modeled as a point, ignoring its volume and shape^[9]. The RCS of the vehicle is assumed to be constant within a short period of time while the RCS of buildings is considered to be known, attributed to the CKM^[9, 16 - 17]. The same assumptions as proposed in other articles are used in this paper, i.e. the RCS of structures is known and the RCS of vehicles is assumed to be constant throughout a short period of time.

From the view of the RSU, the radar sensing channel is both time and frequency selective, which is given by: $\mathbf{H}(t, \tau) = \sum_{i=1}^p \beta_i \mathbf{b}(\theta_i) \mathbf{a}^H(\theta_i) \delta(\tau - \tau_i) e^{j2\pi\mu_i t}$, where β_i , τ_i and μ_i denote the channel path gain, the round-trip delay, and the round-trip Doppler spread corresponding to the i -th path, respectively. We denote θ_i as the angle of the i -th path relative to the RSU. Tracking NLoS paths improves communication performance in wireless networks, despite their lower path gain compared with LoS paths. While NLoS pathways experience many reflections, resulting in lower signal strength, they, like LoS paths, contribute considerably to overall multipath propagation. To solve the difficulty of low NLoS path gain, we use angular a priori knowledge from the CKM and temporal correlation to track NLoS path directions more reliably.



▲ Figure 3. Considered scenario of CKM-assisted ISAC beam tracking system

4.2 Dual Domain Beam Tracking Framework

We have developed a robust multipath beam tracking method based on CKM. This method leverages prior information from CKM, which maps location to CSI, including parameters such as channel gains, angles, delays, and Doppler frequency shifts. By integrating this information, we propose an EKF-based tracking technique that is suitable for scenarios where the LoS path may disappear, allowing for precise continuous tracking.

The framework utilizes EKF to predict and track the state of vehicles, with state evolution and measurement models defined for both LoS-present and LoS-absent conditions. Under LoS-absent conditions, the measurement variables are time delays, Doppler shifts, and angle measurements for multiple reflectors, while the state variables are the vehicle's position and velocity. Essentially, the measurement model makes use of CKM, which records the channel parameters for each location. The proposed algorithmic framework bridges coordinate domain and beam domain information, effectively incorporating environmental awareness into the tracking process. The EKF measurement equations can maintain continuous beam tracking even when the LoS path is obscured, enabling robust multipath beam tracking.

4.3 Simulation Results

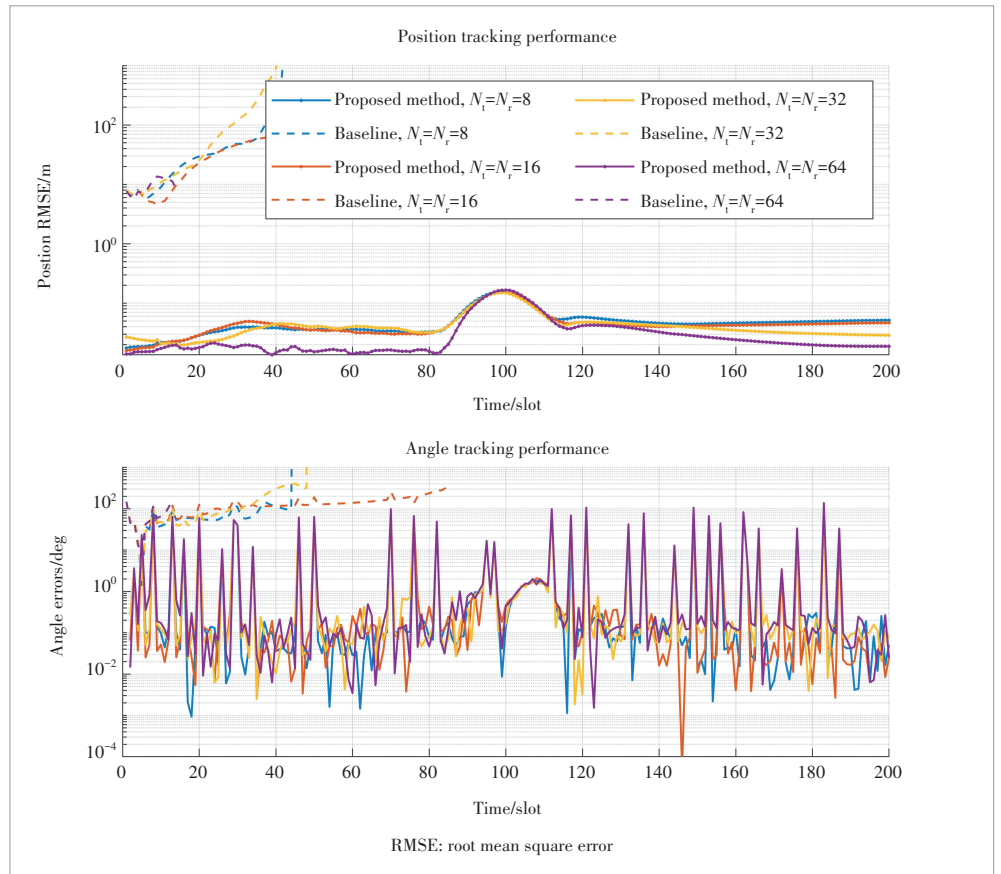
In this section, we present the numerical results to verify the performance of our proposed algorithm. The method described in Ref. [15], which does not utilize CKM's prior information to enhance angle estimation, is used as the baseline algorithm.

Fig. 4 demonstrates that our algorithm achieves the best sensing performance under different antenna configurations. In the scenario under consideration, the vehicle approaches the RSU from one side and then moves in front of it to the other. It is evident that as time goes on, the position tracking errors initially rise and subsequently fall. This pattern arises because as the vehicle approaches the BS, its relative angular velocity increases, heightening the likelihood of losing track of the vehicle. Notably, compared with the baseline, our algorithm's superior performance stems from utilizing prior information provided by CKM,

which significantly reduces angle estimation errors in multipath low signal-to-noise ratio (SNR) environments.

5 Conclusions and Outlook

ISAC is proposed to revolutionize the landscape of wireless communication and sensing systems. This paper offers a comprehensive overview of ISAC, detailing its foundational principles, system models, use cases, and main challenges. We began by elucidating the basic concepts of ISAC. Through various use cases, such as V2X applications, smart homes, and military scenarios, we demonstrated ISAC's vast potential and versatility. Our analysis delved into the significant performance gains from both sensing-assisted communication and communication-assisted sensing. Sensing-assisted communication enhances beamforming and channel estimation, especially crucial in high-frequency and high-mobility environments. Conversely, communication-assisted sensing leverages the expansive cellular infrastructure to create a cooperative sensor network, markedly improving environmental perception accuracy and coverage. We presented a practical example illustrating the benefits of ISAC integration. This example underscored the enhanced sensing accuracy, affirming its transformative impact on future wireless networks. In conclusion, while ISAC technology presents immense opportunities, sev-



▲ Figure 4. Performance of vehicle tracking

eral critical challenges still need to be addressed to fully realize the promise of ISAC in shaping the next generation of intelligent and interconnected systems.

References

- [1] LIU F, CUI Y H, MASOUIROS C, et al. Integrated sensing and communications: toward dual-functional wireless networks for 6G and beyond [J]. *IEEE journal on selected areas in communications*, 2022, 40(6): 1728 - 1767. DOI: 10.1109/JSAC.2022.3156632
- [2] ITU. Introduction to 6G: IMT-2030 [S]. 2020
- [3] ZHANG J A, LIU F, MASOUIROS C, et al. An overview of signal processing techniques for joint communication and radar sensing [J]. *IEEE journal of selected topics in signal processing*, 2021, 15(6): 1295 - 1315. DOI: 10.1109/JSTSP.2021.3113120
- [4] ZENG Y, CHEN J T, XU J, et al. A tutorial on environment-aware communications via channel knowledge map for 6G [J]. *IEEE communications surveys & tutorials*, 2024, 26(3): 1478 - 1519. DOI: 10.1109/COMST.2024.3364508
- [5] DING C F, WANG J B, ZHANG H, et al. Joint MIMO precoding and computation resource allocation for dual-function radar and communication systems with mobile edge computing [J]. *IEEE journal on selected areas in communications*, 2022, 40(7): 2085 - 2102. DOI: 10.1109/JSAC.2022.3157389
- [6] WANG R Y, KLAINE P V, ONIRETI O, et al. Deep learning enabled beam tracking for non-line of sight millimeter wave communications [J]. *IEEE open journal of the communications society*, 2021, 2: 1710 - 1720. DOI: 10.1109/OJCOMS.2021.3096118
- [7] LONG Y, ZENG Y, XU X L, et al. Environment-aware wireless localization enabled by channel knowledge map [C]//*IEEE Global Communications Conference*. IEEE, 2022: 5354 - 5359. DOI: 10.1109/GLOBECOM48099.2022.10001045
- [8] WU D, ZENG Y, JIN S, et al. Environment-aware and training-free beam alignment for mmWave massive MIMO via channel knowledge map [C]//*International Conference on Communications Workshops (ICC Workshops)*. IEEE, 2021: 1 - 7. DOI: 10.1109/ICCWorkshops50388.2021.9473871
- [9] CUI Y P, ZHANG Q X, FENG Z Y, et al. Seeing is not always believing: ISAC-assisted predictive beam tracking in multipath channels [J]. *IEEE wireless communications letters*, 2024, 13(1): 14 - 18. DOI: 10.1109/LWC.2023.3303949
- [10] YUAN W J, LIU F, MASOUIROS C, et al. Bayesian predictive beamforming for vehicular networks: A low-overhead joint radar-communication approach [J]. *IEEE transactions on wireless communications*, 2021, 20(3): 1442 - 1456. DOI: 10.1109/TWC.2020.3033776
- [11] ZENG S Q, XU X L, ZENG Y, et al. CKM-assisted LoS identification and predictive beamforming for cellular-connected UAV [C]//*International Conference on Communications*. IEEE, 2023: 2877 - 2882. DOI: 10.1109/ICC45041.2023.10278702
- [12] LIU F, LIU Y F, LI A, et al. Cramér-Rao bound optimization for joint radar-communication beamforming [J]. *IEEE transactions on signal processing*, 2021, 70: 240 - 253. DOI: 10.1109/TSP.2021.3135692
- [13] CUI Y H, LIU F, JING X J, et al. Integrating sensing and communications for ubiquitous IoT: applications, trends, and challenges [J]. *IEEE network*, 2021, 35(5): 158 - 167. DOI: 10.1109/MNET.010.2100152
- [14] ZHANG A, RAHMAN M L, HUANG X J, et al. Perceptive mobile networks: cellular networks with radio vision via joint communication and radar sensing [J]. *IEEE vehicular technology magazine*, 2021, 16(2): 20 - 30. DOI: 10.1109/MVT.2020.3037430
- [15] ZHAO Y K, XU X L, ZENG Y, et al. Sensing-assisted predictive beamforming with NLoS identification [C]//*International Conference on Communications*. IEEE, 2023: 6455 - 6460. DOI: 10.1109/ICC45041.2023.10278781
- [16] LI Y X, LIU F, DU Z, et al. ISAC-enabled V2I networks based on 5G NR: how much can the overhead be reduced? [C]//*International Conference on Communications Workshops*. IEEE, 2023: 691 - 696. DOI: 10.1109/ICCWorkshops57953.2023.10283528
- [17] ZHANG D Y, LI A, SHIRVANIMOGHADDAM M, et al. Fast beam tracking for millimeter-wave systems under high mobility [C]//*International Conference on Communications*. IEEE, 2019: 1 - 6. DOI: 10.1109/ICC.2019.8761896
- [18] TIAN Y, WANG C W. Vision-aided beam tracking: explore the proper use of camera images with deep learning [C]//*The 94th Vehicular Technology Conference*. IEEE, 2021: 1 - 5. DOI: 10.1109/VTC2021-Fall52928.2021.9625195
- [19] YUAN W J, WEI Z Q, LI S Y, et al. Integrated sensing and communication-assisted orthogonal time frequency space transmission for vehicular networks [J]. *IEEE journal of selected topics in signal processing*, 2021, 15(6): 1515 - 1528. DOI: 10.1109/JSTSP.2021.3117404
- [20] HYUN S H, SONG J, KIM K, et al. Adaptive beam design for V2I communications using vehicle tracking with extended Kalman filter [J]. *IEEE transactions on vehicular technology*, 2022, 71(1): 489 - 502. DOI: 10.1109/TVT.2021.3127696
- [21] LIU F, YUAN W J, MASOUIROS C, et al. Radar-assisted predictive beamforming for vehicular links: communication served by sensing [J]. *IEEE transactions on wireless communications*, 2020, 19(11): 7704 - 7719. DOI: 10.1109/TWC.2020.3015735
- [22] LIU F, ZHENG L, CUI Y H, et al. Seventy years of radar and communications: the road from separation to integration [J]. *IEEE signal processing magazine*, 2023, 40(5): 106 - 121. DOI: 10.1109/MSP.2023.3272881
- [23] GAO Z, LIU S C, SU Y, et al. Hybrid knowledge-data driven channel semantic acquisition and beamforming for cell-free massive MIMO [J]. *IEEE journal of selected topics in signal processing*, 2023, 17(5): 964 - 979. DOI: 10.1109/JSTSP.2023.3299175
- [24] GAO P, LIAN L X, YU J P. Cooperative ISAC with direct localization and rate-splitting multiple access communication: a Pareto optimization framework [J]. *IEEE journal on selected areas in communications*, 2023, 41(5): 1496 - 1515. DOI: 10.1109/JSAC.2023.3240714
- [25] LIU Q, LUO R, LIANG H R, et al. Energy-efficient joint computation offloading and resource allocation strategy for ISAC-aided 6G V2X networks [J]. *IEEE transactions on green communications and networking*, 2023, 7(1): 413 - 423. DOI: 10.1109/TGCN.2023.3234263
- [26] LEYVA L, CASTANHEIRA D, SILVA A, et al. Cooperative multi-terminal radar and communication: a new paradigm for 6G mobile networks [J]. *IEEE vehicular technology magazine*, 2021, 16(4): 38 - 47. DOI: 10.1109/MVT.2021.3114138
- [27] WU K, PEGORARO J, MENEGHELLO F, et al. Sensing in bi-static ISAC systems with clock asynchronism [EB/OL]. [2024-07-02]. <http://arxiv.org/abs/2402.09048>
- [28] JIA H B, LI X S, MA L. Physical layer security optimization with Cramér-Rao bound metric in ISAC systems under sensing-specific imperfect CSI model [J]. *IEEE transactions on vehicular technology*, 2024, 73(5): 6980 - 6992. DOI: 10.1109/TVT.2023.3347527
- [29] LIU F, MASOUIROS C. A tutorial on joint radar and communication transmission for vehicular networks: part I: background and fundamentals [J]. *IEEE communications letters*, 2021, 25(2): 322 - 326. DOI: 10.1109/LCOMM.2020.3025310
- [30] HOSSAIN M A, ELSHAFIEY I, AL-SANIE A. High accuracy GPS-free vehicular positioning based on V2V communications and RSU-assisted DOA estimation [C]//*The 9th IEEE-GCC Conference and Exhibition*. IEEE, 2017: 1 - 5. DOI: 10.1109/IEEEGCC.2017.8447999
- [31] CHEN K J, QI C H, WANG C X, et al. Beam training and tracking for extremely large-scale MIMO communications [J]. *IEEE transactions on wireless communications*, 2024, 23(5): 5048 - 5062. DOI: 10.1109/TWC.2023.3324176
- [32] MENG X, LIU F, MASOUIROS C, et al. Vehicular connectivity on com-

- plex trajectories: Roadway-geometry aware ISAC beam-tracking [J]. *IEEE transactions on wireless communications*, 2023, 22(11): 7408 – 7423. DOI: 10.1109/TWC.2023.3250442
- [33] ZHANG J, XI R, HE Y, et al. A survey of mmWave-based human sensing: technology, platforms and applications [J]. *IEEE communications surveys & tutorials*, 2023, 25(4): 2052 – 2087. DOI: 10.1109/COMST.2023.3298300
- [34] ZHENG B X, YOU C S, MEI W D, et al. A survey on channel estimation and practical passive beamforming design for intelligent reflecting surface aided wireless communications [J]. *IEEE communications surveys & tutorials*, 2022, 24(2): 1035 – 1071. DOI: 10.1109/COMST.2022.3155305
- [35] WEI Z Q, LIU F, LIU C, et al. Integrated sensing, navigation, and communication for secure UAV networks with a mobile eavesdropper [J]. *IEEE transactions on wireless communications*, 2024, 23(7): 7060 – 7078. DOI: 10.1109/TWC.2023.3337148
- [36] MU J S, ZHANG R H, CUI Y H, et al. UAV meets integrated sensing and communication: challenges and future directions [J]. *IEEE communications magazine*, 2023, 61(5): 62 – 67. DOI: 10.1109/MCOM.008.2200510
- [37] YU K G, GUO Y J. Statistical NLOS identification based on AOA, TOA, and signal strength [J]. *IEEE transactions on vehicular technology*, 2009, 58(1): 274 – 286. DOI: 10.1109/TVT.2008.924975
- [38] HE C, DONG Y R, WANG Z J. Radio map assisted multi-UAV target searching [J]. *IEEE transactions on wireless communications*, 2023, 22(7): 4698 – 4711. DOI: 10.1109/TWC.2022.3227933
- [39] ZENG Y, XU X L. Toward environment-aware 6G communications via channel knowledge map [J]. *IEEE wireless communications*, 2021, 28(3): 84 – 91. DOI: 10.1109/MWC.001.2000327
- [40] CHEN L Q, TIAN L P, XU Z M, et al. A survey of Wi-Fi sensing techniques with channel state information [J]. *ZTE communications*, 2020, 18(3): 57 – 63. DOI:10.12142/ZTECOM.202003009
- [41] MA Y S, ZHOU G, WANG S Q. WiFi sensing with channel state information: a survey [J]. *ACM computing surveys*, 2019, 52(3): 1 – 36. DOI: 10.1145/3310194
- [42] GONZÁLEZ-PRELCIC N, MÉNDEZ-RIAL R, HEATH R W. Radar aided beam alignment in MmWave V2I communications supporting antenna diversity [C]/*Information Theory and Applications Workshop (ITA)*. IEEE, 2016: 1 – 7. DOI: 10.1109/ITA.2016.7888145
- [43] ZHANG C, GUO D N, FAN P Y. Tracking angles of departure and arrival in a mobile millimeter wave channel [C]/*IEEE International Conference on Communications (ICC)*. IEEE, 2016: 1 – 6. DOI: 10.1109/ICC.2016.7510902
- [44] VA V, VIKALO H, HEATH R W. Beam tracking for mobile millimeter wave communication systems [C]/*IEEE Global Conference on Signal and Information Processing (GlobalSIP)*. IEEE, 2016: 743 – 747. DOI: 10.1109/GlobalSIP.2016.7905941
- [45] FRIEDLANDER B. On transmit beamforming for MIMO radar [J]. *IEEE transactions on aerospace and electronic systems*, 2012, 48(4): 3376 – 3388. DOI: 10.1109/TAES.2012.6324717
- [46] SEO J, SUNG Y, LEE G, et al. Training beam sequence design for millimeter-wave MIMO systems: a POMDP framework [J]. *IEEE transactions on signal processing*, 2016, 64(5): 1228 – 1242. DOI: 10.1109/TSP.2015.2496241
- [47] ZHANG D Y, LI A, SHIRVANIMOGHADDAM M, et al. Exploring AoA/AoD dynamics in beam alignment of mobile millimeter wave MIMO systems [J]. *IEEE transactions on vehicular technology*, 2019, 68(6): 6172 – 6176. DOI: 10.1109/TVT.2019.2910307
- [48] ZHANG J H, WANG J L, ZHANG Y X, et al. Integrated sensing and communication channel: measurements, characteristics, and modeling [J]. *IEEE communications magazine*, 2024, 62(6): 98-104. DOI: 10.1109/MCOM.020.2300165

Biographies

DU Ruolin received her BS degree from the School of Mathematics and Statistics at Northwestern Polytechnical University, China in 2021. She is currently pursuing her PhD degree at the School of Mathematics and Statistics, Xi'an Jiaotong University, China. Her research interests include integrated sensing and communications (ISAC) and channel knowledge map (CKM)-assisted sensing.

WEI Zhiqiang (zhiqiang.wei@xjtu.edu.cn) received his BE degree in information engineering from Northwestern Polytechnical University, China in 2012, and his PhD degree in electrical engineering and telecommunications from the University of New South Wales (UNSW), Australia in 2019. From 2019 to 2020, he was a post-doctoral research fellow with UNSW. From 2021 to 2022, he was a Humboldt post-doctoral research fellow with the Institute for Digital Communications, Friedrich-Alexander University Erlangen-Nuremberg (FAU), Germany. He is currently a professor with the School of Mathematics and Statistics, Xi'an Jiaotong University, China. He coauthored the IEEE ComSoc Best Readings on OTFS and Delay Doppler Signal Processing. His current research interests include delay-Doppler communications, resource allocation optimization, and statistic and array signal processing.

YANG Zai is a professor of the School of Mathematics and Statistics, Xi'an Jiaotong University, China. He received his BS degree in mathematics and MS degree in applied mathematics from Sun Yat-sen University, China in 2007 and 2009, respectively, and his PhD degree in electrical and electronic engineering from Nanyang Technological University (NTU), Singapore in 2014. He was a research associate and a research fellow of NTU from June 2013 to December 2015, and a professor of the School of Automation, Nanjing University of Science and Technology, China from 2016 to 2018. His research interests focus on mathematical foundations of information processing and wireless communications. He was a leading tutorial presenter at EUSIPCO 2017. He is an IEEE senior member.

Low-Complexity Integrated Super-Resolution Sensing and Communication with Signal Decimation and Ambiguity Removal



DAI Qianglong¹, ZHOU Zhiwen¹, XIAO Zhiqiang^{1,2},
ZENG Yong^{1,2}, YANG Fei³, CHEN Yan³

(1. National Mobile Communications Research Laboratory, Southeast University, Nanjing 210096, China;

2. Purple Mountain Laboratories, Nanjing 211111, China;

3. Wireless Technology Lab., 2012 Lab, Shanghai Huawei Technologies Co., Ltd, Shanghai 201206, China)

DOI: 10.12142/ZTECOM.202403007

<https://kns.cnki.net/kcms/detail/34.1294.TN.20240812.1649.002.html>,
published online August 13, 2024

Manuscript received: 2024-07-30

Abstract: Integrated sensing and communication (ISAC) is one of the main usage scenarios for 6G wireless networks. To most efficiently utilize the limited wireless resources, integrated super-resolution sensing and communication (ISSAC) has been recently proposed to significantly improve sensing performance with super-resolution algorithms for ISAC systems, such as the Multiple Signal Classification (MUSIC) algorithm. However, traditional super-resolution sensing algorithms suffer from prohibitive computational complexity of orthogonal-frequency division multiplexing (OFDM) systems due to the large dimensions of the signals in the subcarrier and symbol domains. To address such issues, we propose a novel two-stage approach to reduce the computational complexity for super-resolution range estimation significantly. The key idea of the proposed scheme is to first uniformly decimate signals in the subcarrier domain so that the computational complexity is significantly reduced without missing any target in the range domain. However, the decimation operation may result in range ambiguity due to pseudo peaks, which is addressed by the second stage where the total collocated subcarrier data are used to verify the detected peaks. Compared with traditional MUSIC algorithms, the proposed scheme reduces computational complexity by two orders of magnitude, while maintaining the range resolution and unambiguity. Simulation results verify the effectiveness of the proposed scheme.

Keywords: ISSAC; sparse decimation; range ambiguity; two-stage approach

Citation (Format 1): DAI Q L, ZHOU Z W, XIAO Z Q, et al. Low-complexity integrated super-resolution sensing and communication with signal decimation and ambiguity removal [J]. *ZTE Communications*, 2024, 22(3): 48 – 55. DOI: 10.12142/ZTECOM.202403007

Citation (Format 2): Q. L. Dai, Z. W. Zhou, Z. Q. Xiao, et al., “Low-complexity integrated super-resolution sensing and communication with signal decimation and ambiguity removal,” *ZTE Communications*, vol. 22, no. 3, pp. 48 – 55, Sept. 2024. doi: 10.12142/ZTECOM.202403007.

1 Introduction

Integrated sensing and communication (ISAC) has been identified as one of the key usage scenarios of the 6G communication systems^[1]. However, due to the limited available wireless resources, the resolution of the classical inverse discrete Fourier transform/discrete Fourier transform (IDFT/DFT) based methods for sensing usually leads to poor performance^[2]. To address such issues, integrated super-resolution sensing and communication (ISSAC) has been recently proposed to maximize the utilization of wireless resources and significantly enhance the sensing performance of ISAC systems^[3]. Specifically, the ISSAC system exploits super-resolution algorithms for radar signal processing to achieve

super-resolution parameter estimation, such as the angle-of-arrival (AoA), propagation delay, and the Doppler frequency shift of the targets.

On the other hand, orthogonal frequency division multiplexing (OFDM) is a dominate waveform in the 4G and 5G mobile communication systems, and it is expected to continue to play an important role in 6G. Consequently, besides dedicated waveform designs^[4], extensive works on ISAC are still based on OFDM systems^[2-3, 5-7]. For OFDM waveforms, the delay and Doppler estimation can be converted to spectral estimation problems due to the sum-of-complex-exponential structure of its channel matrix^[7]. Various methods are proposed for OFDM-based sensing, such as the IDFT/DFT-based and subspace-based methods. The IDFT/DFT-based methods such as the periodogram algorithm^[2] can be implemented easily but their resolution is limited by the wireless resources available for sensing, while the subspace-based methods, such as Mul-

This work was supported by the National Natural Science Foundation of China under Grant No. 62071114.

multiple Signal Classification (MUSIC)^[8] and Estimation of Signal Parameters via Rotational Invariance Techniques (ESPRIT)^[9], can achieve super-resolution but suffer from high computational complexity. Furthermore, compared with multiple-input multiple-output (MIMO) array signals for AoA estimation, the dimensions of OFDM signals in the subcarrier and symbol domains are extremely large. For example, when the number of antennas in an array reaches 128 or 512, it is called a massive array or an extremely large-scale array (XL-Array), but it is common for OFDM signals to have more than 512 subcarriers. Therefore, parameter estimation for OFDM waveforms suffers from prohibitive computational complexity if conventional super-resolution methods are directly applied. Extensive efforts have been devoted to reducing the complexity of such methods, like the ROOT-MUSIC^[10-11] algorithm which replaces the spectrum search in MUSIC with polynomial rooting, or the Propagator Method (PM)^[12-13] that replaces the eigenvalue decomposition by constructing a propagator. However, existing methods for complexity reduction are often tailored to specific algorithms, and thus their application scenarios are limited. Moreover, as these methods still struggle to address the high data dimension problem of OFDM signals, their complexity of delay and Doppler estimation remains high^[14-15]. Thus, how to reduce the computational complexity for ISSAC is still an important problem not fully solved yet.

To address the above issues, we propose a novel and universal complexity reduction method for ISSAC systems. The key idea of the proposed method is to first reduce the data dimensions of OFDM signals through uniform and sparse decimation of the signals in the subcarrier domain, which significantly reduces the computational complexity without missing any sensing target. However, the decimation operation involves sparse signal resampling, which causes range ambiguity due to pseudo peaks. Then, a second stage is conducted to remove any ambiguity by checking all potential points individually using the total collocated subcarrier data. Due to the periodicity of the outputs of both IDFT/DFT-based and subspace-based methods^[6], all the targets can be estimated using only a small subset of subcarriers, although range ambiguity may occur. Thus, we can first select a subset of the equidistance sparse subcarriers to reduce the data dimension, and then validate the estimated results using all the available subcarriers to remove any ambiguity. By utilizing the equidistance sparse data with lower subcarrier domain dimension in the first stage, the proposed method can achieve low-complexity range estimation with resolution equivalent to utilizing all the available data. Moreover, the proposed method is not only applicable to traditional super-resolution algorithms but also further reduces the complexity of existing low-complexity algorithms, e. g., PM-MUSIC and ROOT-MUSIC. Complexity analysis and simulation analysis are performed to verify the effectiveness of the proposed scheme. Numerical results demonstrate that the complexity of the proposed scheme is two orders of magnitude

lower than the traditional MUSIC algorithm in minimal sensing performance degradation.

2 System Model

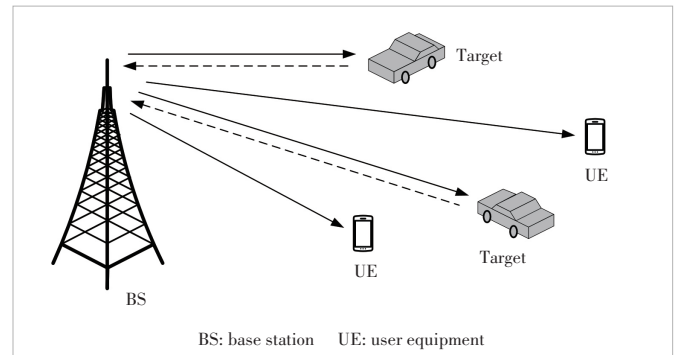
As shown in Fig. 1, we consider a mono-static OFDM-based ISSAC system, where a base station (BS) serves multiple communication user equipment (UE), and simultaneously senses multiple targets via the echoes of its transmitted signals. Note that the radar cross sections (RCSs) of communication UE are much smaller than those of the sensing targets, whose echoes are relatively small and can be neglected. The BS is equipped with M_t transmit antennas and a single radar receiving antenna. As we mainly focus on the range-Doppler sensing, analog beamforming is considered for the BS.

The BS transmits OFDM signals with N subcarriers and M OFDM symbols. The subcarrier spacing and the OFDM symbol duration with the cyclic prefix (CP) are denoted by Δf and T_s . The OFDM symbol duration without CP is $T = 1/\Delta f$, the duration of CP is $T_{cp} = T_s - T$, and the system bandwidth is $B = N\Delta f$. Therefore, the time-domain sequence of the m -th OFDM symbol transmitted by the BS before beamforming is

$$x_m[q] = \frac{1}{\sqrt{N}} \sum_{n=0}^{N-1} b_{n,m} e^{j2\pi nq/N}, \quad (1)$$

where $q = 0, 1, \dots, N-1$, and $b_{n,m}$ denotes the transmitted data on the n -th subcarrier of the m -th OFDM symbol.

Assuming that there are K targets for sensing. The range and the radial velocity of the k -th target are denoted by R_k and v_k , where $k = 1, 2, \dots, K$. Then, the delay and the Doppler frequency shift of the k -th target are $\tau_k = 2R_k/c = n_k \frac{1}{B}$ and $f_{dk} = 2f_c v_k/c$, where c denotes the signal propagation speed and f_c is the carrier frequency. To avoid inter-symbol interference (ISI), the maximum delay of the targets is assumed to be smaller than the CP duration. Moreover, the subcarrier spacing is assumed to be at least one order of magnitude larger than the largest Doppler frequency shift^[7]. Note that mono-static ISAC systems necessitate full-duplex operation of the transmitter



▲ Figure 1. An illustration of the mono-static integrated super-resolution sensing and communication (ISSAC) system

and the radar receiver, making them vulnerable to self-interference (SI) due to imperfect isolation. Various methods have been proposed to address this issue, such as a combination of analog and digital cancellers^[4]. After SI cancellation and CP removal, the time-domain sequence of the m -th received OFDM symbol is

$$y_m[q] = \sum_{k=1}^K \gamma_k x_m[q - n_k] e^{j2\pi m T_s f_{dk}} + \omega_m[q] = \sum_{k=1}^K \sum_{n=0}^{N-1} \gamma_k b_{n,m} e^{j2\pi \left(\frac{nq}{N} - n\Delta f \tau_k + m T_s f_{dk} \right)} + \omega_m[q], \quad (2)$$

where $\gamma_k = \frac{1}{\sqrt{N}} \mathbf{a}^H(\theta_k) \mathbf{w} \tilde{\gamma}_k$, $\mathbf{w} \in \mathbb{C}^{M \times 1}$ represents the transmit beamforming vector, $\mathbf{a}(\theta_k) \in \mathbb{C}^{M \times 1}$ and $\tilde{\gamma}_k$ denotes the array steering vector with angle of departure (AoD) θ_k and the complex reflection coefficient of the k -th target, and $\omega_m[q]$ is the corresponding additive white Gaussian noise (AWGN) plus the residual SI.

Then, $y_m[q]$ can be rearranged into a matrix $\mathbf{Y} \in \mathbb{C}^{N \times M}$ via DFT, and the (n, m) -th element of \mathbf{Y} is

$$\mathbf{Y}(n, m) = \frac{1}{N} \sum_{q=0}^{N-1} y_m[q] e^{-\frac{j2\pi n q}{N}} = b_{n,m} \sum_{k=1}^K \gamma_k e^{-j2\pi n \Delta f \tau_k} e^{j2\pi m T_s f_{dk}} + \bar{\omega}_{n,m}, \quad (3)$$

where $\bar{\omega}_{n,m}$ is the resulting noise.

Since the transmitted data $b_{n,m}$ is known by the BS, it can be removed via element-wise division. By doing so, the data matrix $\tilde{\mathbf{Y}}(n, m) \in \mathbb{C}^{N \times M}$ for radar processing is

$$\tilde{\mathbf{Y}}(n, m) = \frac{\mathbf{Y}(n, m)}{b_{n,m}} = \sum_{k=1}^K \gamma_k e^{-j2\pi n \Delta f \tau_k} e^{j2\pi m T_s f_{dk}} + \bar{\omega}'_{n,m} \in \mathbb{C}^{N \times M}, \quad (4)$$

where $\bar{\omega}'_{n,m} = \frac{\bar{\omega}_{n,m}}{b_{n,m}}$. Therefore, the amplitude γ_k , the propagation delay τ_k , and the Doppler f_{dk} can be estimated with various estimation algorithms by utilizing the data matrix $\tilde{\mathbf{Y}}$.

Due to the large dimensions of the data matrix $\tilde{\mathbf{Y}}$, the computational complexity for parameter estimation is significantly high, especially for super-resolution algorithms like MUSIC. However, by exploiting the periodicity of the outputs of both IDFT/DFT-based and subspace-based methods, all the targets in the range domain can be estimated through sparse data in lower dimensions, although ambiguity may occur. This motivates us to reduce the computational complexity for parameter estimation by decimation, if the ambiguity can be removed. In the following section, we uniformly decimate the subcarrier domain data of the data matrix $\tilde{\mathbf{Y}}$ in Eq. (4) to reduce data dimension, and then exploit the range peri-

odogram of decimated sparse data to analyze the relationship among the range resolution, the maximum unambiguous range and the decimation interval.

3 Ambiguity and Resolution Analysis

Since signal processing methods for range and Doppler estimations are similar, in the following, we focus on range estimation and assume all the targets are stationary, while the proposed method and analysis results can be directly applied to the Doppler counterparts. By uniformly decimating the subcarrier domain data of the data matrix $\tilde{\mathbf{Y}}$ in Eq. (4) with a step size of η , the decimated sparse data matrix can be expressed as

$$\tilde{\mathbf{Y}}^{\text{sp}}(n^{\text{sp}}, m) = \tilde{\mathbf{Y}}(n^{\text{sp}} \eta, m) = \sum_{k=1}^K \gamma_k e^{-j2\pi n^{\text{sp}} \eta \Delta f \tau_k} + \bar{\omega}'_{n^{\text{sp}} \eta, m}, \quad (5)$$

where $n^{\text{sp}} = 0, 1, \dots, N^{\text{sp}} - 1$, and $N^{\text{sp}} = \left\lfloor \frac{N}{\eta} \right\rfloor$ denotes the number of subcarriers in the decimated sparse data.

Then, the IDFT is applied to each column of $\tilde{\mathbf{Y}}^{\text{sp}}$, and the periodogram can be obtained by

$$\mathbf{F}(\tau; \eta) = \left| \frac{1}{M} \sum_{m=0}^{M-1} \frac{1}{N^{\text{sp}}} \sum_{n^{\text{sp}}=0}^{N^{\text{sp}}-1} \tilde{\mathbf{Y}}^{\text{sp}}(n^{\text{sp}}, m) e^{j2\pi n^{\text{sp}} \eta \Delta f \tau} \right|^2. \quad (6)$$

The peaks of $\mathbf{F}(\tau; \eta)$ correspond to the ranges of targets, where $\tau = \frac{2R}{c}$ denotes the observation delay, and R denotes the observation range. When $\eta = 1$, the ranges of targets are estimated with the total collected data, while for $\eta > 1$, they are obtained with the decimated sparse data.

By ignoring the noise and substituting Eq. (5) into Eq. (6), the periodogram of decimated sparse data for range sensing can be obtained by

$$\mathbf{F}(\Delta\tau_k; \eta) = \left| \sum_{k=1}^K \gamma_k e^{-j\pi(N^{\text{sp}}-1)\eta\Delta f\Delta\tau_k} \frac{\sin(\pi N \Delta f \Delta\tau_k)}{N^{\text{sp}} \sin(\pi \eta \Delta f \Delta\tau_k)} \right|^2, \quad (7)$$

where $\Delta\tau_k = \frac{2\Delta_k}{c}$ denotes the delay difference, $\Delta_k = R - R_k \in [-d_{\text{unamb}}, d_{\text{unamb}}]$ denotes the range difference between the observation range R and the target range R_k , and $d_{\text{unamb}} = \frac{c}{2\Delta f}$ denotes the maximum unambiguous range of OFDM radar with the subcarrier spacing Δf . It is observed from Eq. (7) that the range sensing for arbitrary target k is critically dependent on the function $G_\eta(\Delta_k) = \left| \frac{\sin(2\pi N \Delta f \Delta_k / c)}{N^{\text{sp}} \sin(2\pi \eta \Delta f \Delta_k / c)} \right|^2$, which has the following properties.

Main lobe: Let $2\pi N\Delta f\Delta/c = \pm\pi$ or $\Delta = \pm\frac{c}{2N\Delta f}$, $G_\eta(\Delta) = 0$.

Then the null-to-null width of the main lobe can be obtained as

$$\text{BW} = \frac{c}{N\Delta f}. \quad (8)$$

Typically, the range resolution can be defined as a half of the main lobe width. Therefore, the range resolution of decimated sparse data is:

$$\Delta_r^{\text{res}} = \frac{1}{2}\text{BW} = \frac{c}{2N\Delta f} = \frac{c}{2B}. \quad (9)$$

Grating lobe: When $\eta > 1$, grating lobes with the same amplitude and width as the main lobe exist, and the locations of the grating lobes can be obtained by letting $\frac{2\pi\eta\Delta f\Delta}{c} = n\pi$, $n = \pm 1, \pm 2, \dots, \pm\eta$. Then the n -th grating lobe is located at:

$$\Delta = \frac{nc}{2\eta\Delta f}, n = \pm 1, \pm 2, \dots, \pm\eta. \quad (10)$$

The grating lobes reflect the periodicity of the periodogram, which will cause range ambiguity. The maximum unambiguous range achieved utilizing the decimated sparse data is the grating lobe interval $d_{\text{unamb}}^{\text{sp}} = \frac{c}{2\eta\Delta f}$.

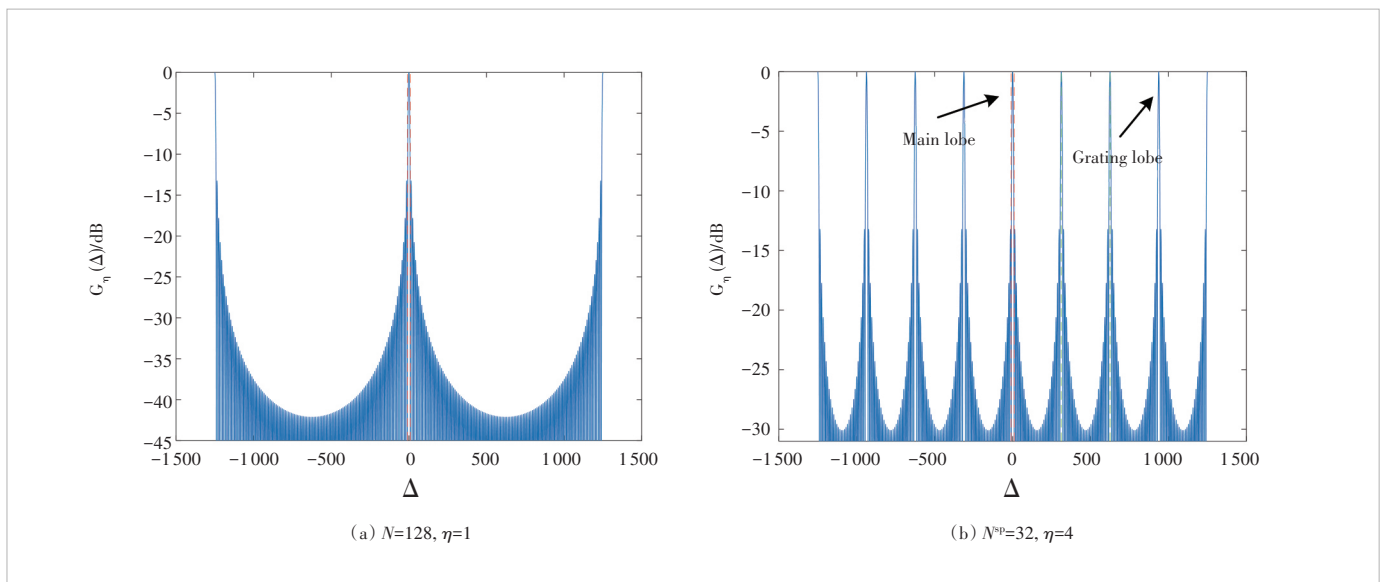
For $N = 128$ and $\Delta f = 120$ kHz, Figs. 2(a) and 2(b) illustrate the range periodograms for collocated subcarrier data and decimated sparse data. It is observed that the decimated sparse data can achieve the same range resolution as the total collocated subcarrier data, while the maximum unambiguous

range reduces inversely proportional to the decimation interval η . Similarly, when the decimated sparse data are applied in super-resolution algorithms, the range ambiguity exists and the range resolution remains. Moreover, the computational complexity of super-resolution algorithms is significantly high, especially for OFDM signals with high data dimensions. Therefore, it is necessary to propose low-complexity schemes utilizing lower-dimension decimated sparse data and periodic extension, while maintaining high range resolution. In the following section, we propose a two-stage scheme, which combines the advantages of collocated subcarrier data and decimated sparse data, to achieve low-complexity and unambiguous range sensing.

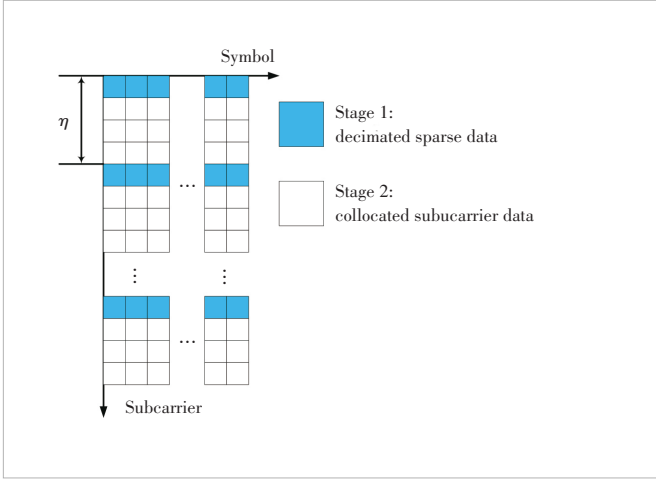
4 Range Sensing

4.1 Proposed Two-Stage Scheme

The two-stage scheme is shown in Fig. 3. In the first stage, we uniformly and sparsely decimate the subcarrier domain data from the matrix \tilde{Y} in Eq. (4) with decimation interval η . Thus, the range resolution and maximum unambiguous range of the decimated sparse data are $\Delta_r^{\text{res, sp}} = \frac{c}{2B}$ and $d_{\text{unamb}}^{\text{sp}} = \frac{c}{2\eta\Delta f}$, respectively. By utilizing the decimated sparse data, all the possible ranges with ambiguity can be estimated. In the second stage, the range resolution and maximum unambiguous range of the total collocated data are $\Delta_r^{\text{res}} = \frac{c}{2B}$ and $d_{\text{unamb}} = \frac{c}{2\Delta f}$, and thus the range ambiguity can be removed by exploiting the collocated subcarrier data to check each range estima-



▲ Figure 2. Range periodograms of: (a) Collocated subcarrier data with the number of subcarriers $N = 128$ and (b) Decimated sparse data with decimation interval $\eta = 4$



▲ Figure 3. Illustration of the two-stage scheme

tion obtained in the first stage individually. Therefore, the two-stage scheme can achieve range resolution equivalent to utilizing the total collocated data in Eq. (4) without range ambiguity, while the computational complexity is much lower.

4.2 Proposed Two-Stage Algorithm

In this subsection, a novel two-stage algorithm based on MUSIC is proposed. To eliminate high correlation between echo signals of the targets, modified spatial smoothing preprocessing (MSSP)^[16] is performed in the subcarrier domain of the data matrix \tilde{Y} . Specifically, the smoothing window size is $N_L = \rho N$, $\rho = 0.5$, and the number of submatrices is $N_{\text{sub}} = N - N_L + 1$. Thus, the data matrix $\hat{Y} \in \mathbb{C}^{N_L \times N_{\text{sub}} M}$ after MSSP can be obtained by:

$$\hat{Y} = \begin{bmatrix} \tilde{y}_1 & \cdots & \tilde{y}_{N_{\text{sub}}} \\ \vdots & \ddots & \vdots \\ \tilde{y}_{N_L} & \cdots & \tilde{y}_{N_{\text{sub}} + N_L} \end{bmatrix} \quad (11)$$

Then, the signal and noise subspaces can be obtained via eigenvalue decomposition (EVD) of the covariance matrix of the data matrix \hat{Y} , which is expressed as:

$$\mathbf{R}_{\hat{Y}} = \frac{1}{N_{\text{sub}} M} \hat{Y} \hat{Y}^H = \mathbf{E}_s \mathbf{A}_s \mathbf{E}_s^H + \mathbf{E}_n \mathbf{A}_n \mathbf{E}_n^H, \quad (12)$$

where \mathbf{A}_s denotes the diagonal matrix composed of the largest K eigenvalues, and \mathbf{E}_s and \mathbf{E}_n denote the signal subspace and noise subspace. Thus, the MUSIC spectrum for range estimation can be expressed as:

$$P_{\text{MUSIC}}(R) = \frac{1}{\mathbf{a}_r^H \mathbf{E}_n \mathbf{E}_n^H \mathbf{a}_r}, \quad (13)$$

where $\mathbf{a}_r = [1, e^{-j2\pi\Delta f\tau}, \dots, e^{-j2\pi(N_L-1)\Delta f\tau}]^T$, $\tau = \frac{2R}{c}$ denotes the

steering vector in delay dimension, R denotes the observation range, and c denotes the wave propagation speed. The peaks of the MUSIC spectrum correspond to the ranges of the targets. The proposed two-stage algorithm works as follows. In the first stage, the possible ranges of the targets are obtained by first utilizing the MUSIC algorithm on the decimated matrix \tilde{Y}^{sp} and then periodically extending the peaks with interval $d_{\text{unamb}}^{\text{sp}}$. In the second stage, the MUSIC spectrum of collocated subcarrier data matrix \tilde{Y} is exploited to remove the range ambiguity, where the spectral values remain large at the true peaks and sharply decrease at the pseudo peaks. The detailed steps of the proposed algorithm are shown in Algorithm 1.

Algorithm 1. MUSIC based low-complexity two-stage algorithm

Inputs: total collocated subcarrier data matrix \tilde{Y} ;
the decimation interval η .

Outputs: estimated range \hat{r} .

//Stage 1. Sparse estimation

1. $\tilde{Y}^{\text{sp}} = \tilde{Y}(1:\eta:N,:)$;
 2. $N_L^{\text{sp}} = \rho N^{\text{sp}}, N_{\text{sub}}^{\text{sp}} = N^{\text{sp}} - N_L^{\text{sp}} + 1$;
 3. Obtain sparse data matrix after MSSP \hat{Y}^{sp} ;
 4. $\mathbf{R}_{\hat{Y}^{\text{sp}}} = \frac{1}{N_{\text{sub}}^{\text{sp}} M} \hat{Y}^{\text{sp}} \hat{Y}^{\text{sp}H}$;
 5. $\mathbf{R}_{\hat{Y}^{\text{sp}}} = \mathbf{E}_s^{\text{sp}} \mathbf{A}_s^{\text{sp}} \mathbf{E}_s^{\text{sp}H} + \mathbf{E}_n^{\text{sp}} \mathbf{A}_n^{\text{sp}} \mathbf{E}_n^{\text{sp}H}$;
 6. $\hat{r}_1 = \text{findpeaks} \frac{1}{[0, d_{\text{unamb}}^{\text{sp}}] \mathbf{a}_r^{\text{sp}H} \mathbf{E}_n^{\text{sp}} \mathbf{E}_n^{\text{sp}H} \mathbf{a}_r^{\text{sp}}}$;
 7. $K = \text{length}(\hat{r}_1), P = \left\lceil \frac{d_{\text{max}}}{d_{\text{unamb}}^{\text{sp}}} \right\rceil$;
 8. $\hat{r}_1' = \text{ones}(1, P) \otimes \hat{r}_1 + d_{\text{unamb}}^{\text{sp}}(0:P-1) \otimes \text{ones}(1, K)$;
- // Stage 2. Ambiguity removal
9. $N_L = \rho N, N_{\text{sub}} = N - N_L + 1$;
 10. Obtain sparse data matrix after MSSP \hat{Y} ;
 11. $\mathbf{R}_{\hat{Y}} = \frac{1}{N_{\text{sub}} M} \hat{Y} \hat{Y}^H$;
 12. $\mathbf{R}_{\hat{Y}} = \mathbf{E}_s \mathbf{A}_s \mathbf{E}_s^H + \mathbf{E}_n \mathbf{A}_n \mathbf{E}_n^H$;
 13. $P_{\text{MUSIC}}(\hat{r}_1') = \frac{1}{\mathbf{a}_r^H \mathbf{E}_n \mathbf{E}_n^H \mathbf{a}_r}$;
 14. Obtain the verified spectral peaks \hat{r} ;
 15. **return** \hat{r} .

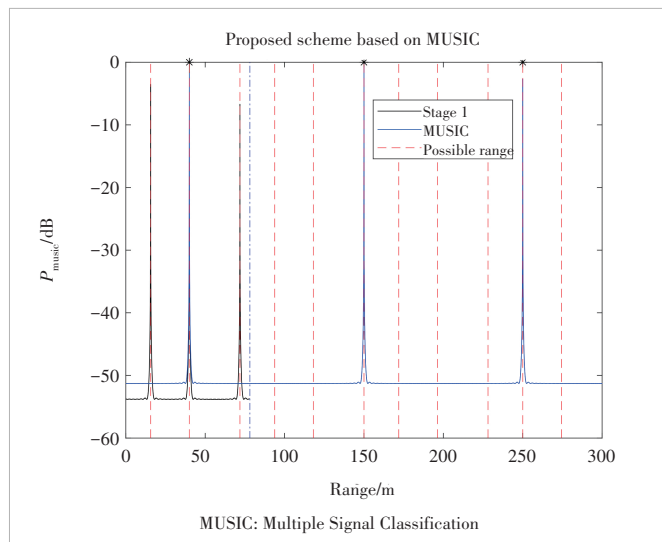
The two stages of Algorithm 1 can be explained as follows. In the first stage, all possible ranges of targets are found via the MUSIC spectrum of the decimated sparse data and periodic extension. Specifically, in Step 1, the decimated sparse data matrix \tilde{Y}^{sp} is obtained by uniformly decimating the total collocated OFDM data matrix \tilde{Y} with a step size of η . Then, MSSP is performed on \tilde{Y}^{sp} in Steps 2 - 3, and MUSIC is performed in the maximum unambiguous range of decimated sparse data $d_{\text{unamb}}^{\text{sp}} = \frac{c}{2\eta\Delta f}$ to obtain the coarse range estimation \hat{r}_1 in Steps 4 - 6. Subsequently, as shown in Steps 7 - 8, all

possible ranges of targets \hat{r}'_1 are obtained by periodic extension of spectral peaks \hat{r}_1 searched by MUSIC, where d_{\max} denotes the maximum detection range of OFDM radar, $P = \left\lfloor \frac{d_{\max}}{d_{\text{unamb}}^{\text{sp}}} \right\rfloor$ denotes the number of extended periods, and \otimes denotes the Kronecker product. In the second stage, all possible ranges of targets are verified by the MUSIC spectrum of the collocated subcarrier data individually to remove the range ambiguity. As is shown in Steps 9 – 10, MSSP is performed on \tilde{Y} . Then, calculation and eigenvalue decomposition of the covariance matrix are performed in Steps 11 – 12. Finally, all possible ranges in \hat{r}'_1 are verified by the MUSIC spectrum of the collocated subcarrier data point-by-point, where the spectral values at the true peaks are large, as is shown in Steps 13 – 14.

The range estimation result of the proposed scheme and traditional MUSIC is shown in Fig. 4. As shown by the black solid line, spectrum search is performed in the maximum unambiguous range for decimated sparse data in the first stage. Then, all possible ranges of targets are obtained by periodic extension, as shown by the red dashed line. Finally, in the second stage, the MUSIC pseudospectrum of the total collocated subcarrier data is used to check each possible range to remove any ambiguity, as shown by the blue solid line. The lower data dimension of decimated sparse data, smaller range for spectrum search, and limited points to be checked by the total collocated subcarrier data make the complexity of the proposed two-stage scheme much lower than that of the traditional MUSIC. In the following part, numerical results are provided to compare the complexity of the proposed scheme and the traditional MUSIC.

4.3 Computational Complexity Analysis

For the MUSIC algorithm, the computational complexity for



▲ Figure 4. Range estimation result of the proposed scheme and traditional MUSIC

calculating the covariance matrix is $\mathcal{O}(MN^2)$, and the complexity of eigenvalue decomposition and spectrum search is $\mathcal{O}(N^3)$ and $\mathcal{O}((2N(N-K)+N)r)$, respectively. Thus, the complexity of traditional MUSIC after spatial smoothing is $\mathcal{O}(N_{\text{sub}}MN_L^2 + N_L^3 + (2N_L(N_L-K) + N_L)r)$, where r denotes the number of points calculated in the peak search. Assuming the proposed scheme is applied to MUSIC, the complexity of the two stages of the proposed scheme is $\mathcal{O}(N_{\text{sub}}^{\text{sp}}MN_L^{\text{sp}2} + N_L^{\text{sp}3} + (2N_L^{\text{sp}}(N_L^{\text{sp}} - K) + N_L^{\text{sp}})r')$ and $\mathcal{O}(N_{\text{sub}}MN_L^2 + N_L^3 + (2N_L(N_L - K) + N_L)KP)$.

Assume the number of total collocated subcarriers is $N = 1024$, the number of OFDM symbols is $M = 112$, the maximum detection range of OFDM radar is $d_{\max} = 300$ m, the step size for spectrum search is 0.01 m, and the number of targets is $K = 3$. Then a comparison of the complexity of traditional MUSIC, PM-MUSIC and the proposed scheme with different decimation intervals η is provided in Table 1. It is observed that the PM-MUSIC algorithm can only slightly reduce the computational complexity of the MUSIC algorithm. The proposed scheme, however, can not only significantly reduce the complexity of MUSIC, but also further reduce the complexity of PM-MUSIC.

5 Simulation Results

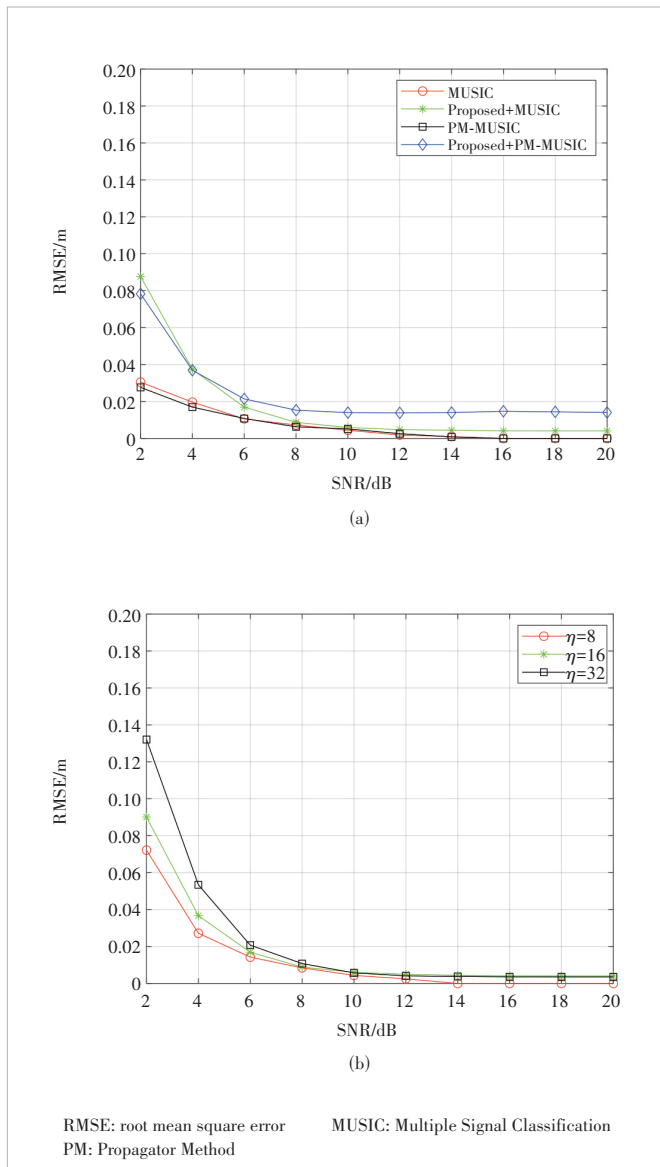
In this section, the performance of the two-stage algorithms is verified. The relevant parameter settings are as follows. The subcarrier spacing is $\Delta f = 120$ kHz, the total number of subcarriers is $N = 1024$, and thus the total bandwidth is $B = 122.88$ MHz. Moreover, the number of OFDM symbols is $M = 112$, the maximum detection range of OFDM radar is $d_{\max} = 300$ m, and the number of targets is $K = 3$.

As is shown in Fig. 5(a), a comparison of MUSIC, PM-MUSIC, and the proposed scheme in terms of root mean square error (RMSE) of the range estimations is provided. It is observed that the RMSEs of the proposed scheme are at the centimeter level, that is, the proposed algorithms can achieve comparable range estimation accuracy with traditional MUSIC and PM-MUSIC. In Fig. 5(b), the RMSEs of Algorithm 1 with different decimation intervals η are provided. It is observed that at low SNR levels, the estimation accuracy

▼ Table 1. Computational complexity analysis

Algorithms	Complexity of Different Decimation Intervals		
	$\eta = 8$	$\eta = 16$	$\eta = 32$
MUSIC		1.59e10	
Proposed+MUSIC	3.80e8	2.73e8	2.65e8
PM-MUSIC		1.57e10	
Proposed+PM-MUSIC	2.46e8	1.40e8	1.32e8

MUSIC: Multiple Signal Classification PM: Propagator Method



▲ Figure 5. (a) RMSE of MUSIC, PM-MUSIC, and the proposed scheme for range estimation; (b) RMSE of the proposed scheme with different decimation intervals for range estimation

of the proposed scheme slightly decreases as the decimation interval increases.

6 Conclusions

In this paper, we reduce the computational complexity of range estimation by uniformly decimating in the subcarrier domain, and derive the mathematical relationship between range resolution, maximum unambiguous range and the decimation interval. Then, a two-stage scheme is proposed to achieve low-complexity high-resolution range estimation while maintaining the unambiguous range, which first exploits the low-dimension data matrix to reduce computational complexity, and then removes the range ambiguity utilizing total collocated subcarrier

data. Finally, we compare the complexity and performance of the proposed scheme with traditional MUSIC and PM-MUSIC, and the results show that the proposed two-stage scheme can significantly reduce the complexity of range estimation with minimal performance degradation. Besides, the proposed scheme can be easily adapted to super-resolution algorithms for Doppler and AoA estimation.

References

- [1] ITU. Framework and overall objectives of the future development of IMT for 2030 and beyond [R]. 2023
- [2] SIT Y L, STURM C, REICHARDT L, et al. The OFDM joint radar-communication system: an overview [C]//Proceedings of the International Conference Advances in Satellite and Space Communications. IEEE, 2011: 69 - 74
- [3] ZHANG C Y, ZHOU Z W, WANG H Z, et al. Integrated super-resolution sensing and communication with 5G NR waveform: Signal processing with uneven CPs and experiments: (invited paper) [C]//The 21st International Symposium on Modeling and Optimization in Mobile, Ad Hoc, and Wireless Networks (WiOpt). IEEE, 2023: 681 - 688. DOI: 10.23919/wi-opt58741.2023.10349843
- [4] XIAO Z Q, ZENG Y. Waveform design and performance analysis for full-duplex integrated sensing and communication [J]. IEEE journal on selected areas in communications, 2022, 40(6): 1823 - 1837. DOI: 10.1109/JSAC.2022.3155509
- [5] CUI Y H, LIU F, JING X J, et al. Integrating sensing and communications for ubiquitous IoT: applications, trends, and challenges [J]. IEEE network, 2021, 35(5): 158 - 167. DOI: 10.1109/MNET.010.2100152
- [6] CHENG X, DUAN D L, GAO S J, et al. Integrated sensing and communications (ISAC) for vehicular communication networks (VCN) [J]. IEEE Internet of Things journal, 2022, 9(23): 23441 - 23451. DOI: 10.1109/JIOT.2022.3191386
- [7] BRAUN M. OFDM Radar algorithms in mobile communication networks [D]. Karlsruhe: Karlsruhe Institut für Technologie (KIT), 2014
- [8] SCHMIDT R. Multiple emitter location and signal parameter estimation [J]. IEEE transactions on antennas and propagation, 1986, 34(3): 276 - 280. DOI: 10.1109/TAP.1986.1143830
- [9] ROY R, KAILATH T. ESPRIT-estimation of signal parameters via rotational invariance techniques [J]. IEEE transactions on acoustics, speech, and signal processing, 1989, 37(7): 984 - 995. DOI: 10.1109/29.32276
- [10] RAO B D, HARI K V S. Performance analysis of Root-Music [J]. IEEE transactions on acoustics, speech, and signal processing, 1989, 37(12): 1939 - 1949. DOI: 10.1109/29.45540
- [11] PESAVENTO M, GERSHMAN A B, HAARDT M. Unitary root-MUSIC with a real-valued eigen decomposition: a theoretical and experimental performance study [J]. IEEE transactions on signal processing, 2000, 48(5): 1306 - 1314. DOI: 10.1109/78.839978
- [12] MARCOS S, MARSAL A, BENIDIR M. Performances analysis of the propagator method for source bearing estimation [C]//International Conference on Acoustics, Speech and Signal Processing. IEEE, 1994: IV/237 - IV/240. DOI: 10.1109/ICASSP.1994.389823
- [13] TAYEM N, KWON H M. L-shape 2-dimensional arrival angle estimation with propagator method [J]. IEEE transactions on antennas and propagation, 2005, 53(5): 1622 - 1630. DOI: 10.1109/TAP.2005.846804
- [14] NI Z T, ZHANG J A, HUANG X J, et al. Uplink sensing in perceptive mobile networks with asynchronous transceivers [J]. IEEE transactions on signal processing, 2021, 69: 1287 - 1300. DOI: 10.1109/TSP.2021.3057499
- [15] CHEN L L, QI W D, LIU P, et al. Low-complexity joint 2-D DOA and

TOA estimation for multipath OFDM signals [J]. *IEEE signal processing letters*, 2019, 26(11): 1583 – 1587. DOI: 10.1109/LSP.2019.2936292

- [16] YAMADA H, OHMIYA M, OGAWA Y, et al. Super-resolution techniques for time-domain measurements with a network analyzer [J]. *IEEE transactions on antennas and propagation*, 1991, 39(2): 177 – 183. DOI: 10.1109/8.68179

Biographies

DAI Qianglong received his BS degree in electronic and information engineering from Nanjing University of Posts and Telecommunications, China in 2023. He is currently pursuing his MS degree with the National Mobile Communications Research Laboratory, Southeast University, China. His research interests include ISAC and OFDM.

ZHOU Zhiwen received his BS degree in electronic and information engineering from Nanjing University of Posts and Telecommunications, China in 2022. He is currently pursuing his MS degree with the National Mobile Communications Research Laboratory, Southeast University, China. His research interests include ISAC and XL-arrays.

XIAO Zhiqiang received his BS and MS degrees from Nanjing University of Posts and Telecommunications, China in 2017 and 2020, respectively. He is currently pursuing his PhD degree with the National Mobile Communication Research Laboratory, Southeast University, China, and Purple Mountain Laboratories. His research interests include ISAC, waveform design and optimization, massive MIMO communications, and wireless localization.

ZENG Yong (yong_zeng@seu.edu.cn) is a full professor with the National Mo-

bile Communications Research Laboratory, Southeast University, China, and also with the Purple Mountain Laboratories. He received both the BE (First-Class Honours) and PhD degrees from Nanyang Technological University, Singapore. From 2013 to 2018, he was a research fellow and senior research fellow at the Department of Electrical and Computer Engineering, National University of Singapore. From 2018 to 2019, he was a lecturer at the School of Electrical and Information Engineering, the University of Sydney, Australia. Dr. ZENG was a highly cited researcher by Clarivate Analytics for five consecutive years (2019 – 2023). He is the recipient of the Australia Research Council (ARC) Discovery Early Career Researcher Award (DECRA), 2020 and 2024 IEEE Marconi Prize Paper Awards in Wireless Communications, 2018 IEEE Communications Society Asia-Pacific Outstanding Young Researcher Award, 2020 and 2017 IEEE Communications Society Heinrich Hertz Prize Paper Awards, 2021 IEEE ICC Best Paper Award, and 2021 China Communications Best Paper Award. He has published more than 170 papers, which have been cited by more than 26 000 times based on Google Scholar.

YANG Fei received his BS and PhD degrees in communication and information system in 2009 and 2014, respectively, both from University of Science and Technology of China (USTC). He joined Huawei Technologies Co., Ltd. since 2014. He has worked in departments of radio access network (RAN) chipset algorithm R&D and cell-phone communication protocol and technology. He is now a principal engineer in Wireless Technology Laboratory. His research interests include 6G channel modeling and integrated communication and sensing (ISAC) and their RAN simulation methodologies.

CHEN Yan is a senior expert of wireless communication at Huawei Technologies Co., Ltd. She received her BS and PhD degrees from Chu Kochen Honored College and Institute of Information and Communication Engineering, Zhejiang University, China in 2004 and 2009, respectively. Her research interests include 6G vision and enabling technology study (e.g., use cases, key capabilities, evaluation methodologies, and emerging technologies such as ISAC and collaborative robotics enabled by integrated sensing, artificial intelligence, and communications).

Tensor Decomposition-Based Channel Estimation and Sensing for Millimeter Wave MIMO-OFDM V2I Systems



WANG Jilin¹, ZENG Xianlong¹, YANG Yonghui^{2,3},
PENG Lin^{2,3}, LI Lingxiang¹

(1. National Key Laboratory of Wireless Communications, University of Electronic Science and Technology of China, Chengdu 611731, China;

2. ZTE Corporation, Shenzhen 518057, China;

3. State Key Laboratory of Mobile Network and Mobile Multimedia Technology, Shenzhen 518055, China)

DOI: 10.12142/ZTECOM.202403008

<https://kns.cnki.net/kcms/detail/34.1294.TN.20240723.1657.002.html>,
published online July 24, 2024

Manuscript received: 2024-03-01

Abstract: An integrated sensing and communication (ISAC) scheme for a millimeter wave (mmWave) multiple-input multiple-output orthogonal frequency division multiplexing (MIMO-OFDM) Vehicle-to-Infrastructure (V2I) system is presented, in which both the access point (AP) and the vehicle are equipped with large antenna arrays and employ hybrid analog and digital beamforming structures to compensate the path loss, meanwhile compromise between hardware complexity and system performance. Based on the sparse scattering nature of the mmWave channel, the received signal at the AP is organized to a four-order tensor by the introduced novel frame structure. A CANDECOMP/PARAFAC (CP) decomposition-based method is proposed for time-varying channel parameter extraction, including angles of departure/arrival (AoDs/AoAs), Doppler shift, time delay and path gain. Then leveraging the estimates of channel parameters, a nonlinear weighted least-square problem is proposed to recover the location accurately, heading and velocity of vehicles. Simulation results show that the proposed methods are effective and efficient in time-varying channel estimation and vehicle sensing in mmWave MIMO-OFDM V2I systems.

Keywords: MIMO-OFDM Vehicle-to-Infrastructure (V2I) systems; ISAC; time-varying channel estimation; CANDECOMP/PARAFAC (CP) decomposition

Citation (Format 1): WANG J L, ZENG X L, YANG Y H, et al. Tensor decomposition-based channel estimation and sensing for millimeter wave MIMO-OFDM V2I systems [J]. *ZTE Communications*, 2024, 22(3): 56 – 68. DOI: 10.12142/ZTECOM.202403008

Citation (Format 2): J. L. Wang, X. L. Zeng, Y. H. Yang, et al., “Tensor decomposition-based channel estimation and sensing for millimeter wave MIMO-OFDM V2I systems,” *ZTE Communications*, vol. 22, no. 3, pp. 56 – 68, Sept. 2024. doi: 10.12142/ZTECOM.202403008.

1 Introduction

Due to the large available bandwidth and small wavelength, millimeter wave (mmWave) communication technology has received much attention. To compensate for the severe path loss of mmWave systems, large antenna arrays are usually used at the transmitter and receiver to provide sufficient beamforming gain for mmWave communications. However, to obtain the directional beam gain, accurate channel information needs to be realized by channel estimation^[1-5].

In recent years, the millimeter-wave channel estimation problem has been widely investigated. By exploring its sparsity in the angular domain, the millimeter-wave channel estimation problem is equivalent to a sparse signal recovery problem, which can be solved with the help of compressive sensing tools^[6]. It has been shown in Refs. [6 – 7] that a sub-

stantial reduction in training overhead can be achieved via compressed sensing methods. Also, a low-complexity channel estimation algorithm was proposed by exploiting the strongest angles of arrival in mmWave channels^[8]. Besides, the authors in Ref. [9] exploited the delay-domain sparsity of wideband channels and a sparse signal recovery-based scheme was proposed for channel estimation. Moreover, tensor-based channel estimation was introduced in Refs. [10] and [11], which exploited the multi-dimensional characteristics of the mmWave multiple-input multiple-output (MIMO) channels with the low-rank property. Specifically, the received signal was organized to a third-order tensor, and a CANDECOMP/PARAFAC (CP) decomposition-based method was proposed to estimate channel parameters including angles of departure/arrival (AoDs/AoAs), time delays, and fading coefficients. However, in practice, the wireless

transceivers may have high-speed relative movements, e.g., high-speed trains^[12], unmanned aerial vehicles (UAVs)^[13] and vehicle-to-everything (V2X) networks^[14]. In particular, the high-speed relative movements introduce severe Doppler effects on the multiple propagating paths and result in a time-varying multipath mmWave channel. To enable high data rate transmissions for high mobility, the time-varying mmWave channel estimation has been studied in Refs. [15 – 16]. In Ref. [15], the time-varying channel estimation was divided into two separate stages including AoA/AoD estimation and followed by a path gain estimation. Also, by rearranging the received signal, a canonical polyadic decomposition (CPD)-based method was developed in Ref. [16] to estimate the time-varying mmWave channel.

The relative position and relative velocity of the transmitter and the receiver are known as channel estimations that give information on the AoA/AoD and the Doppler shift. Furthermore, the location information may be utilized as a stand-in for channel information to enable beamforming. This means that if the position of the mobile station (MS) is known, the AP can steer its transmission to the MS, either directly or via a reflective path. Further, the velocity information can be utilized to predict the position of MS, which helps the AP to perform beam alignment efficiently. This leads to synergies between communication and sensing. Previous works in Refs. [17 – 19] for millimeter waves and in Refs. [20 – 21] for massive MIMO explored using 5G techniques to acquire location and orientation. Ref. [17] considered estimating and tracking AoA by beam switching. The MS localization was formulated as a hypothesis-testing problem in Ref. [18]. Besides, Ref. [19] obtained meter-level positioning accuracy by measuring received signal strength levels. In the massive case, Ref. [20] addressed the estimation of angles, while Ref. [21] considered the joint delay and AoD/AoA estimation in the line-of-sight (LoS) conditions, and the impact of errors in delay and phase shifters was also analyzed.

In this paper, we consider the integrated sensing and communications for a millimeter wave MIMO-orthogonal frequency division multiplexing (MIMO-OFDM) Vehicle-to-Infrastructure (V2I) system. Specifically, we formulate the time-varying mmWave channel model for a MIMO-OFDM system and propose a novel frame structure. The received signal in the training stage is organized to a four-order tensor, and then a CP decomposition-based method is introduced to estimate the channel parameters. After the channel parameters in each AP are available, a nonlinear weighted least-square problem is proposed to recover the location, heading and velocity of the vehicle accurately.

2 System Model

We consider an uplink V2I mmWave OFDM system, where each access point (AP) is equipped with a uniform lin-

ear array (ULA) of N_r antennas and the vehicle is equipped with a ULA with N_t antennas. The system is assumed to operate at a carrier frequency f_c and the total number of OFDM tones (subcarriers) is \bar{Q} . The q -th subcarrier shift is $f_q = \frac{qf_s}{\bar{Q}}$,

where f_s is the sampling rate. The duration time of an OFDM symbol is set to T_{sym} . The vehicle is moving at a certain speed, and the relative motion between the AP and the vehicle gives rise to the Doppler effect, which in turn leads to time-varying channels.

2.1 Time-Varying Channel Model

Due to the sparse scattering characteristic of mmWave channels, we adopt a geometric wideband mmWave channel model to characterize the channel between the AP and the vehicle^[22]. Specifically, considering the Doppler shift caused by the vehicle's mobility, the frequency-domain mmWave channel associated with the q -th subcarrier at the t -th time instant can be expressed as follows^[15, 23].

$$\mathbf{H}_q(t) = \sum_{l=1}^L \beta_{l,l} \mathbf{a}_R(\phi_l) \mathbf{a}_T^H(\theta_l) e^{-j2\pi f_q \tau_l} e^{j2\pi \nu_l t}, \quad (1)$$

where L represents the number of signal paths, $\beta_{l,l}$, θ_l , ϕ_l , τ_l and ν_l denote the complex path gain, AoD/AoA, time delay, and Doppler shift of the l -th path, respectively. The Doppler shift can be calculated as $\nu_l = v_l f_c / c$, where v_l is the radial velocity (i.e. the component of velocity along the line of sight to the observer) of the l -th path, and c represents the speed of light. Here we assume the path gain $\beta_{l,l}$ remains unaltered during one OFDM frame, where the frame structure will be elaborated later. Also, we assume that the angle parameters such as AoAs and AoDs remain unchanged within the frame, as these parameters depend only on the relative positions of the AP, the vehicle, and the scatterers^[2]. The steering vectors of the vehicle and the AP are represented by $\mathbf{a}_T(\theta) \in \mathbb{C}^{N_t}$ and $\mathbf{a}_R(\phi) \in \mathbb{C}^{N_r}$, which are given as

$$\mathbf{a}_T(\theta) \triangleq \frac{1}{\sqrt{N_t}} \left[1, e^{j\frac{2\pi}{\lambda_c} d \sin(\theta)}, \dots, e^{j\frac{2\pi}{\lambda_c} d(N_t-1) \sin(\theta)} \right]^T, \quad (2)$$

$$\mathbf{a}_R(\phi) \triangleq \frac{1}{\sqrt{N_r}} \left[1, e^{j\frac{2\pi}{\lambda_c} d \sin(\phi)}, \dots, e^{j\frac{2\pi}{\lambda_c} d(N_r-1) \sin(\phi)} \right]^T, \quad (3)$$

where d denotes the distance between two adjacent antenna elements, and typically d is set to be half of the signal wavelength.

2.2 Uplink Transmission and Signal Model

We assume that hybrid analog and digital beamforming structures are employed by both the vehicle and the AP. Specifically, the vehicle and the AP are respectively equipped

with $M_l \leq N_l$ and $M_r \leq N_r$ radio frequency (RF) chains. At each time instant, the pilot symbol of each subcarrier $s_q(t)$ is first precoded by a baseband precoding vector $\mathbf{f}_{D,q}(t) \in \mathbb{C}^{M_l}$. Then the symbol blocks are converted to a time domain by M_l \bar{Q} -point inverse discrete Fourier transforms (IDFTs). After that, the cyclic prefix is added and then followed by an analog RF beamformer $\mathbf{F}_A(t) \in \mathbb{C}^{N_l \times M_l}$, which is common for all subcarriers. Finally, the signal transmitted at the q -th subcarrier can be written as:

$$\mathbf{x}_q(t) = \mathbf{F}_A(t) \mathbf{f}_{D,q}(t) s_q(t) \triangleq \mathbf{f}_q(t) s_q(t), \quad (4)$$

where $\mathbf{f}_q(t) \triangleq \mathbf{F}_A(t) \mathbf{f}_{D,q}(t)$ denotes the hybrid precoding vector.

At each AP, the received signal is first combined with an RF combiner $\mathbf{W}_A(t) \in \mathbb{C}^{N_r \times M_r}$, which is common for all subcarriers. After the cyclic prefix is removed, the symbols are transformed to the frequency domain by M_r \bar{Q} -point DFTs and then the symbols associated with the q -th subcarrier are combined by a digital baseband combining matrix $\mathbf{W}_{D,q}(t) \in \mathbb{C}^{M_r \times M}$, where $M \leq M_r$. With the assumption of perfect time synchronization, the received signal at the q -th subcarrier can finally be written as:

$$\mathbf{y}_q(t) = \mathbf{W}_{D,q}^H(t) \mathbf{W}_A^H(t) (\mathbf{H}_q(t) \mathbf{x}_q(t) + \mathbf{n}_q(t)) \triangleq \mathbf{W}_q^H(t) \mathbf{H}_q(t) \mathbf{f}_q(t) s_q(t) + \mathbf{W}_q^H(t) \mathbf{n}_q(t), \quad (5)$$

where $\mathbf{W}_q(t) \triangleq \mathbf{W}_A(t) \mathbf{W}_{D,q}(t)$ denotes the hybrid combining matrix, and $\mathbf{n}_q(t) \in \mathbb{C}^M, \sim \mathcal{CN}(0, \sigma_n^2)$ is the additive white Gaussian noise.

Our objective is to estimate the channel parameters including the complex gain, AoA, AoD, time delay and the Doppler shift for each path. After the channel parameters are estimated, the obtained channel state information is further used for estimating the location, speed and heading of the target vehicle. In the following section, we propose a novel training protocol that allows to express the received signal as a fourth-order tensor that admits a CPD.

3 Proposed Approach

3.1 CP Formulation

To facilitate the algorithmic development, we first propose a new frame structure, where each frame is divided into K_f subframes, and each subframe consists of P OFDM symbols. The first K subframes are used for channel estimation, and the rest $K_f - K$ subframes are used for data transmission. For each frame, the frequency-domain channel associated with the q -th subcarrier at a certain time, e.g., at the p -th symbol of the $(k+1)$ -th subframe, can be expressed as:

$$\mathbf{H}_q[(kP+p)T_{\text{sym}}] = \sum_{l=1}^L \beta_l \mathbf{a}_R(\phi_l) \mathbf{a}_T^H(\theta_l) e^{-j2\pi f_c \tau_l} e^{j2\pi \nu_l (kP+p)T_{\text{sym}}}. \quad (6)$$

For notational convenience, $\mathbf{H}_q[(kP+p)T_{\text{sym}}]$ is also denoted by $\mathbf{H}_q[k,p]$. Similarly, we use $\mathbf{F}_A[k,p]$, $\mathbf{f}_{D,q}[k,p]$, and $s_q[k,p]$ to respectively represent $\mathbf{F}_A[(kP+p)T_{\text{sym}}]$, $\mathbf{f}_{D,q}[(kP+p)T_{\text{sym}}]$, and $s_q[(kP+p)T_{\text{sym}}]$.

In the channel estimation stage, we suppose $\mathbf{F}_A[k,p] = \mathbf{F}_A[p]$, $\mathbf{f}_{D,q}[k,p] = \mathbf{f}_D[p]$ and $s_q[k,p] = s[p] = 1$. Thus, we have:

$$\mathbf{x}_q[k,p] = \mathbf{f}[p]. \quad (7)$$

Similarly, we suppose $\mathbf{W}_A[k,p] = \mathbf{W}_A[p]$, $\mathbf{W}_{D,q}[k,p] = \mathbf{W}_D[p]$, and let $\mathbf{W} = \mathbf{W}[p] \triangleq \mathbf{W}_A[p] \mathbf{W}_D[p]$. Consequently, the received signal at the q -th symbol of the k -th subframe can be expressed as:

$$\mathbf{y}_q[k,p] = \mathbf{W}^H \mathbf{H}_q[k,p] \mathbf{f}[p] + \mathbf{W}^H \mathbf{n}_q[k,p]. \quad (8)$$

We define

$$\mathbf{H}_{q,l}[k] \triangleq \beta_l \mathbf{a}_R(\phi_l) \mathbf{a}_T^H(\theta_l) e^{-j2\pi f_c \tau_l} e^{j2\pi \nu_l k P T_{\text{sym}}}. \quad (9)$$

We can express $\mathbf{H}_q[k,p]$ as:

$$\mathbf{H}_q[k,p] = \sum_{l=1}^L \mathbf{H}_{q,l}[k] e^{j2\pi \nu_l p T_{\text{sym}}}. \quad (10)$$

For each subcarrier, we collect signals received at each subframe and define $\mathbf{Y}_{k,q} \triangleq [\mathbf{y}_q[k,1] \cdots \mathbf{y}_q[k,P]] \in \mathbb{C}^{M \times P}$. We can express $\mathbf{Y}_{k,q}$ as:

$$\mathbf{Y}_{k,q} = \sum_{l=1}^L \mathbf{W}^H \mathbf{H}_{q,l}[k] \mathbf{F} \mathbf{X}_{\nu_l} + \mathbf{N}_{k,q}, \quad (11)$$

where $\mathbf{F} \triangleq [\mathbf{f}[1] \cdots \mathbf{f}[P]] \in \mathbb{C}^{N_l \times P}$, $\mathbf{X}_{\nu_l} \triangleq \text{diag}(\tilde{\mathbf{g}}(\nu_l))$, and

$$\tilde{\mathbf{g}}(\nu_l) \triangleq [e^{j2\pi \nu_l T_{\text{sym}}} \cdots e^{j2\pi \nu_l P T_{\text{sym}}}]^T \in \mathbb{C}^P. \quad (12)$$

Substituting Eq. (9) into Eq. (11), we obtain:

$$\begin{aligned} \mathbf{Y}_{k,q} &= \sum_{l=1}^L \beta_l e^{-j2\pi f_c \tau_l} e^{j2\pi \nu_l k P T_{\text{sym}}} \mathbf{W}^H \mathbf{a}_R(\phi_l) \mathbf{a}_T^H(\theta_l) \mathbf{F} \mathbf{X}_{\nu_l} + \mathbf{N}_{k,q} = \\ &= \sum_{l=1}^L \beta_l e^{-j2\pi f_c \tau_l} \mathbf{g}_k(\nu_l) \mathbf{W}^H \mathbf{a}_R(\phi_l) \mathbf{a}_T^H(\theta_l) \mathbf{F} \mathbf{X}_{\nu_l} + \mathbf{N}_{k,q} = \\ &= \sum_{l=1}^L \beta_l e^{-j2\pi f_c \tau_l} \mathbf{g}_k(\nu_l) \tilde{\mathbf{a}}_R(\phi_l) \tilde{\mathbf{a}}_T(\theta_l, \nu_l) + \mathbf{N}_{k,q}, \end{aligned} \quad (13)$$

where $\tilde{\mathbf{a}}_T(\theta_l, \nu_l) \triangleq \mathbf{X}_{\nu_l}^H \mathbf{F}^H \mathbf{a}_T(\theta_l) \in \mathbb{C}^P$, $\mathbf{g}_k(\nu_l) \triangleq e^{j2\pi \nu_l k P T_{\text{sym}}}$ and $\tilde{\mathbf{a}}_R(\phi_l) \triangleq \mathbf{W}^H \mathbf{a}_R(\phi_l) \in \mathbb{C}^M$.

For each subcarrier, the received signal collected from all K subframes can naturally be organized as a third-order tensor $\mathcal{Y}_q \in \mathbb{C}^{M \times P \times K}$. Note that each slice of the tensor \mathcal{Y}_q , $\mathbf{Y}_{k,q}$, is a weighted sum of a common set of rank-one outer products. Therefore, the tensor \mathcal{Y}_q admits a CP decomposition

that decomposes a tensor into a sum of rank-one component tensors, i.e.,

$$\mathcal{Y}_q = \sum_{l=1}^L \beta_l e^{-j2\pi f_l \tau_l} \tilde{\mathbf{a}}_R(\phi_l) \circ \tilde{\mathbf{a}}_T(\theta_l, \nu_l) \circ \mathbf{g}(\nu_l) + \mathcal{N}_q, \quad (14)$$

where $\mathbf{g}(\nu_l) \triangleq [e^{j2\pi\nu_l P T_{\text{sym}}} \dots e^{j2\pi\nu_l K P T_{\text{sym}}}]^T \in \mathbb{C}^K$. Furthermore, the received signal associated with all Q subcarriers can be constructed as a fourth-order tensor $\mathcal{Y} \in \mathbb{C}^{M \times P \times K \times Q}$, which also admits a CP decomposition as follows.

$$\mathcal{Y} = \sum_{l=1}^L \tilde{\mathbf{a}}_R(\phi_l) \circ \tilde{\mathbf{a}}_T(\theta_l, \nu_l) \circ \mathbf{g}(\nu_l) \circ \beta_l \mathbf{f}(\tau_l) + \mathcal{N}, \quad (15)$$

where $\mathbf{f}(\tau_l) \triangleq [e^{-j2\pi f_l \tau_l} \dots e^{-j2\pi f_l Q \tau_l}]^T \in \mathbb{C}^Q$. The four modes of the tensor $\mathcal{Y} \in \mathbb{C}^{M \times P \times K \times Q}$ stand for the received data stream, the OFDM symbol, the subframe and the subcarrier, respectively.

Due to the sparse scattering characteristics of mmWave channels, the CP rank of the fourth-order tensor, equivalent to the number of signal paths, is small. Therefore, it is expected that the CPD of \mathcal{Y} is unique for moderate values of M , P , K , and Q . Since the training overhead is equal to PKQ , it means that only a small amount of training overhead is needed to uniquely obtain the factor matrices of the tensor \mathcal{Y} . After the factor matrices are obtained, the channel parameters can be readily extracted. Before proceeding, we define the four factor matrices as:

$$\begin{aligned} \mathbf{A} &\triangleq [\tilde{\mathbf{a}}_R(\phi_1), \dots, \tilde{\mathbf{a}}_R(\phi_L)] \in \mathbb{C}^{M \times L}, \\ \mathbf{B} &\triangleq [\tilde{\mathbf{a}}_T(\theta_1, \nu_1), \dots, \tilde{\mathbf{a}}_T(\theta_L, \nu_L)] \in \mathbb{C}^{P \times L}, \\ \mathbf{C} &\triangleq [\mathbf{g}(\nu_1), \dots, \mathbf{g}(\nu_L)] \in \mathbb{C}^{K \times L}, \\ \mathbf{D} &\triangleq [\beta_1 \mathbf{f}(\tau_1), \dots, \beta_L \mathbf{f}(\tau_L)] \in \mathbb{C}^{Q \times L}. \end{aligned} \quad (16)$$

3.2 CP Decomposition

We commence with the number of paths which is known or has been estimated a priori. The CP decomposition of \mathcal{Y} can be accomplished by solving the following optimization problem.

$$\min_{\hat{\mathbf{A}}, \hat{\mathbf{B}}, \hat{\mathbf{C}}, \hat{\mathbf{D}}} \left\| \mathcal{Y} - \sum_{l=1}^L \hat{\mathbf{a}}_l \circ \hat{\mathbf{b}}_l \circ \hat{\mathbf{c}}_l \circ \hat{\mathbf{d}}_l \right\|_F^2, \quad (17)$$

where $\hat{\mathbf{A}} = [\hat{\mathbf{a}}_1, \dots, \hat{\mathbf{a}}_L]$, $\hat{\mathbf{B}} = [\hat{\mathbf{b}}_1, \dots, \hat{\mathbf{b}}_L]$, $\hat{\mathbf{C}} = [\hat{\mathbf{c}}_1, \dots, \hat{\mathbf{c}}_L]$, $\hat{\mathbf{D}} = [\hat{\mathbf{d}}_1, \dots, \hat{\mathbf{d}}_L]$ and $\| \cdot \|_F$ denotes the Frobenius norm. The above optimization problem can be readily solved by an alternating least squares (ALS) procedure. Specifically, ALS alternatively minimizes the data fitting error with respect to one of the factor matrices, with the other three factor matrices fixed. The t -th iteration can proceed as

$$\begin{aligned} \hat{\mathbf{A}}^{(t+1)} &= \arg \min_{\hat{\mathbf{A}}} \left\| \mathcal{Y}_{(1)} - \hat{\mathbf{A}} \left(\hat{\mathbf{D}}^{(t-1)} \circ \hat{\mathbf{C}}^{(t-1)} \circ \hat{\mathbf{B}}^{(t-1)} \right)^T \right\|_F^2, \\ \hat{\mathbf{B}}^{(t+1)} &= \arg \min_{\hat{\mathbf{B}}} \left\| \mathcal{Y}_{(2)} - \hat{\mathbf{B}} \left(\hat{\mathbf{D}}^{(t)} \circ \hat{\mathbf{C}}^{(t)} \circ \hat{\mathbf{A}}^{(t)} \right)^T \right\|_F^2, \\ \hat{\mathbf{C}}^{(t+1)} &= \arg \min_{\hat{\mathbf{C}}} \left\| \mathcal{Y}_{(3)} - \hat{\mathbf{C}} \left(\hat{\mathbf{D}}^{(t)} \circ \hat{\mathbf{B}}^{(t)} \circ \hat{\mathbf{A}}^{(t)} \right)^T \right\|_F^2, \\ \hat{\mathbf{D}}^{(t+1)} &= \arg \min_{\hat{\mathbf{D}}} \left\| \mathcal{Y}_{(4)} - \hat{\mathbf{D}} \left(\hat{\mathbf{C}}^{(t)} \circ \hat{\mathbf{B}}^{(t)} \circ \hat{\mathbf{A}}^{(t)} \right)^T \right\|_F^2, \end{aligned} \quad (18)$$

where $\mathcal{Y}_{(n)}$ denotes the mode- n unfolding of \mathcal{Y} . Note the above least squares problems admit closed-form solutions, which are given by $\hat{\mathbf{A}}^{(t+1)} = \mathcal{Y}_{(1)} \left(\left(\hat{\mathbf{D}}^{(t-1)} \circ \hat{\mathbf{C}}^{(t-1)} \circ \hat{\mathbf{B}}^{(t-1)} \right)^T \right)^\dagger$, $\hat{\mathbf{B}}^{(t+1)} = \mathcal{Y}_{(2)} \left(\left(\hat{\mathbf{D}}^{(t)} \circ \hat{\mathbf{C}}^{(t)} \circ \hat{\mathbf{A}}^{(t)} \right)^T \right)^\dagger$, $\hat{\mathbf{C}}^{(t+1)} = \mathcal{Y}_{(3)} \left(\left(\hat{\mathbf{D}}^{(t)} \circ \hat{\mathbf{B}}^{(t)} \circ \hat{\mathbf{A}}^{(t)} \right)^T \right)^\dagger$, and $\hat{\mathbf{D}}^{(t+1)} = \mathcal{Y}_{(4)} \left(\left(\hat{\mathbf{C}}^{(t)} \circ \hat{\mathbf{B}}^{(t)} \circ \hat{\mathbf{A}}^{(t)} \right)^T \right)^\dagger$, respectively. The ALS iteration can proceed until the objective value of Eq. (17) is below a predefined threshold. If the knowledge of the number of paths, L , is unavailable, we adopt a multi-dimensional minimum description length (MDL) criterion to estimate the rank of the tensor^[24-25].

Without loss of generality, for an N -way tensor \mathcal{Y} with rank- R corrupted by zero-mean circularly symmetric complex Gaussian (ZMCSCG) noise, we suppose that its CP decomposition is:

$$\mathcal{Y} = \sum_{r=1}^R \mathbf{a}_r^{(1)} \circ \mathbf{a}_r^{(2)} \circ \dots \circ \mathbf{a}_r^{(N)}. \quad (19)$$

Let M_n be the number of rows of the n -th factor matrix of \mathcal{Y} and the associated factor matrices are defined as $\{\mathbf{A}^{(n)}\}_{n=1}^N$ with $\mathbf{A}^{(n)} \in \mathbb{C}^{M_n \times R}$. Let $\tilde{M} \triangleq \prod_{n=1}^N M_n$. Then for the n -mode unfolding of \mathcal{Y} , we compute the sample covariance matrix as:

$$\hat{\mathbf{R}}_{yy}^{(n)} = \frac{M_n}{\tilde{M}} [\mathcal{Y}_{(n)}][\mathcal{Y}_{(n)}]^H \in \mathbb{C}^{M_n \times M_n}. \quad (20)$$

Define $\lambda_j^{(n)}$ as the j -th eigenvalue of the n -th sample covariance matrix $\hat{\mathbf{R}}_{yy}^{(n)}$, and we assume the M_n eigenvalues of $\hat{\mathbf{R}}_{yy}^{(n)}$ are arranged in a descending order:

$$\lambda_1^{(n)} > \lambda_2^{(n)} > \dots > \lambda_{M_n}^{(n)}. \quad (21)$$

The estimation of the matrix rank of $\mathcal{Y}_{(n)}$ can be given by the MDL criterion as

$\hat{R}^{(n)} = \arg \min_{\ell \in \{0, \dots, M_n - 1\}} \text{MDL}^{(n)}(\ell)$, where

$$\text{MDL}^{(n)}(\ell) = \frac{\ell}{2} (2M_n - \ell) \log(\bar{M}^{(n)}) - \bar{M}^{(n)} (M_n - \ell) \log \left(\frac{\left(\prod_{j=\ell+1}^{M_n} \lambda_j^{(n)} \right)^{\frac{1}{M_n - \ell}}}{\frac{1}{M_n - \ell} \sum_{j=\ell+1}^{M_n} \lambda_j^{(n)}}} \right), \quad (22)$$

in which $\bar{M}^{(n)} = \prod_{i=1, i \neq n}^N M_i$. Finally, the rank of the tensor can be estimated as $\hat{R} = \min \{ \hat{R}^{(n)} \}_{n=1}^N$.

3.3 Estimation of Channel Parameters

We discuss how to estimate the parameters of the time-varying mmWave channel based on the estimated factor matrices $\{\hat{\mathbf{A}}, \hat{\mathbf{B}}, \hat{\mathbf{C}}, \hat{\mathbf{D}}\}$. Note that the CP decomposition is unique up to scaling and permutation ambiguity under a mild condition, as is detailed in the next subsection. More precisely, the relationship between the estimated and true factor matrices is established as follows:

$$\begin{aligned} \hat{\mathbf{A}} &= \mathbf{A} \mathbf{\Lambda}_1 \mathbf{\Pi} + \mathbf{E}_1, \\ \hat{\mathbf{B}} &= \mathbf{B} \mathbf{\Lambda}_2 \mathbf{\Pi} + \mathbf{E}_2, \\ \hat{\mathbf{C}} &= \mathbf{C} \mathbf{\Lambda}_3 \mathbf{\Pi} + \mathbf{E}_3, \\ \hat{\mathbf{D}} &= \mathbf{D} \mathbf{\Lambda}_4 \mathbf{\Pi} + \mathbf{E}_4, \end{aligned} \quad (23)$$

where $\{\mathbf{\Lambda}_1, \mathbf{\Lambda}_2, \mathbf{\Lambda}_3, \mathbf{\Lambda}_4\}$ are unknown nonsingular diagonal matrices that satisfy $\mathbf{\Lambda}_1 \mathbf{\Lambda}_2 \mathbf{\Lambda}_3 \mathbf{\Lambda}_4 = \mathbf{I}$, $\mathbf{\Pi}$ is an unknown permutation matrix, and $\mathbf{E}_1, \mathbf{E}_2, \mathbf{E}_3$, and \mathbf{E}_4 denote the estimation errors associated with the four estimated factor matrices, respectively.

The permutation matrix $\mathbf{\Pi}$ can be ignored as it is common to all factor matrices. Note that the l -th column of \mathbf{A} and \mathbf{C} is determined by $\hat{\phi}_l$ and $\hat{\nu}_l$, respectively. Hence the AoA and the Doppler shift can be estimated via a correlation-based method:

$$\hat{\phi}_l = \arg \max_{\phi_l} \frac{|\hat{\mathbf{a}}_l^H \tilde{\mathbf{a}}_R(\phi_l)|}{\|\hat{\mathbf{a}}_l\|_2 \|\tilde{\mathbf{a}}_R(\phi_l)\|_2}, \quad (24)$$

$$\hat{\nu}_l = \arg \max_{\nu_l} \frac{|\hat{\mathbf{c}}_l^H \mathbf{g}(\nu_l)|}{\|\hat{\mathbf{c}}_l\|_2 \|\mathbf{g}(\nu_l)\|_2}. \quad (25)$$

The l -th column of \mathbf{B} is characterized by both $\hat{\theta}_l$ and $\hat{\nu}_l$. After the Doppler shift is estimated, we define $\tilde{\mathbf{C}} \in \mathbb{C}^{P \times L}$ with $[\tilde{\mathbf{C}}]_{p,l} = e^{j2\pi p T \nu_l}$, and $\tilde{\mathbf{B}} \in \mathbb{C}^{P \times L}$ with $[\tilde{\mathbf{B}}]_{p,l} = [\hat{\mathbf{B}}]_{p,l} / [\tilde{\mathbf{C}}]_{p,l}$.

Defining $\check{\mathbf{a}}_T(\theta_l) \triangleq \mathbf{F}^H \mathbf{a}_T(\theta_l) \in \mathbb{C}^P$, we can estimate the AoD as:

$$\hat{\theta}_l = \arg \max_{\theta_l} \frac{|\check{\mathbf{b}}_l^H \check{\mathbf{a}}_T(\theta_l)|}{\|\check{\mathbf{b}}_l\|_2 \|\check{\mathbf{a}}_T(\theta_l)\|_2}, \quad (26)$$

in which $\check{\mathbf{b}}_l$ is the l -th column of $\tilde{\mathbf{B}}$. Also, we note that the l -th column of \mathbf{D} is $\beta_l \mathbf{f}(\tau_l)$. Hence the time delay τ_l can be estimated via

$$\hat{\tau}_l = \arg \max_{\tau_l} \frac{|\hat{\mathbf{d}}_l^H \mathbf{f}(\tau_l)|}{\|\hat{\mathbf{d}}_l\|_2 \|\mathbf{f}(\tau_l)\|_2}, \quad (27)$$

where $\hat{\mathbf{d}}_l$ denotes the l -th column of $\hat{\mathbf{D}}$.

Finally, we try to recover the complex path gain, given the estimated AoA, AoD, time delay and Doppler shift. We define the reconstructed factor matrices as follows.

$$\begin{aligned} \tilde{\mathbf{A}} &\triangleq [\tilde{\mathbf{a}}_R(\hat{\phi}_1), \dots, \tilde{\mathbf{a}}_R(\hat{\phi}_L)] \in \mathbb{C}^{M \times L}, \\ \tilde{\mathbf{B}} &\triangleq [\tilde{\mathbf{a}}_T(\hat{\theta}_1, \hat{\nu}_1), \dots, \tilde{\mathbf{a}}_T(\hat{\theta}_L, \hat{\nu}_L)] \in \mathbb{C}^{P \times L}, \\ \tilde{\mathbf{C}} &\triangleq [\mathbf{g}(\hat{\nu}_1), \dots, \mathbf{g}(\hat{\nu}_L)] \in \mathbb{C}^{K \times L}, \\ \tilde{\mathbf{D}} &\triangleq [\mathbf{f}(\hat{\tau}_1), \dots, \mathbf{f}(\hat{\tau}_L)] \in \mathbb{C}^{Q \times L}. \end{aligned} \quad (28)$$

Note that the reconstructed factor matrices share the same permutation ambiguity $\mathbf{\Pi}$, and $\tilde{\mathbf{D}}$ does not include the complex path gains. With the reconstructed $\tilde{\mathbf{A}}, \tilde{\mathbf{B}}, \tilde{\mathbf{C}}$, we can obtain an estimate of the true factor matrix \mathbf{D} by resorting to the mode-4 unfolding of $\mathcal{Y}_{(4)}$, i.e.

$$\check{\mathbf{D}} = \arg \min_{\check{\mathbf{D}}} \left\| \mathcal{Y}_{(4)} - \check{\mathbf{D}} (\tilde{\mathbf{C}} \circ \tilde{\mathbf{B}} \circ \tilde{\mathbf{A}})^T \right\|_F^2. \quad (29)$$

Define $\check{\mathbf{Z}}_\beta = \text{diag}(\beta_1, \dots, \beta_L)$. Theoretically we have

$$\hat{\check{\mathbf{Z}}}_\beta = \arg \min_{\check{\mathbf{Z}}_\beta} \left\| \check{\mathbf{D}} - \tilde{\mathbf{D}} \hat{\check{\mathbf{Z}}}_\beta \right\|_F^2. \quad (30)$$

Thus the complex path gains can be estimated via a least squares (LS) method

$$\hat{\beta}_l = [\tilde{\mathbf{D}}^\dagger \check{\mathbf{D}}]_{l,l}. \quad (31)$$

3.4 Uniqueness Condition and Sample Complexity

Clearly, the uniqueness of the CP decomposition is essential to the success of recovering channel parameters. In this subsection, we analyze the conditions that ensure the uniqueness of the CPD for our problem. The uniqueness conditions also shed light on the sample complexity (i.e. training overhead) required by the proposed algorithm.

A well-known condition for the uniqueness of CPD is

Kruskal's condition. Specifically, let k_X denote the k -rank of a matrix X , which is defined as the largest value of k_X so that every subset of k_X columns of the matrix X is linearly independent. We then have the following theorem concerning the uniqueness of CP decomposition for the N -th-order tensor, which is reported in Ref. [26].

Theorem 1: Let χ be an N -way tensor with rank- R and suppose that its CP decomposition is:

$$\chi = \sum_{r=1}^R \mathbf{a}_r^{(1)} \circ \mathbf{a}_r^{(2)} \circ \dots \circ \mathbf{a}_r^{(N)}. \quad (32)$$

Then a sufficient condition for the uniqueness is

$$\sum_{n=1}^N k_{A^{(n)}} \geq 2R + (N - 1). \quad (33)$$

Note that Kruskal's condition cannot hold, when $R = 1$. However, in that case, the uniqueness has been proved by Harshman. Kruskal's sufficient condition is also necessary for $R = 2$ and $R = 3$, but not for $R > 3$.

From the above theorem, we know that if

$$k_A + k_B + k_C + k_D \geq 2L + 3, \quad (34)$$

then the CP decomposition of \mathcal{Y} is unique. We first examine the k -rank of $\mathbf{D} = [\mathbf{f}(\tau_1), \dots, \mathbf{f}(\tau_L)] \mathbf{Z}_\beta$, where $\mathbf{f}(\tau_l)$ has a Vandermonde structure. Obviously, \mathbf{D} is a columnwise-scaled Vandermonde matrix, and its k -rank is thus given by $k_D = \min\{Q, L\}$.

Next, we examine the k -rank of \mathbf{A} . Note that

$$\mathbf{A} = \mathbf{W}^H [\mathbf{a}_R(\phi_1), \dots, \mathbf{a}_R(\phi_L)] \triangleq \mathbf{W}^H \mathbf{A}_R, \quad (35)$$

where $\mathbf{A}_R \in \mathbb{C}^{N \times L}$ is a Vandermonde matrix under the ULA consideration. It was proved in Ref. [11] that for a randomly generated \mathbf{W} , the k -rank of \mathbf{A} is $k_A = \min\{M, L\}$.

We now study the k -rank of \mathbf{B} . The factor matrix \mathbf{B} is expressed as:

$$\mathbf{B} = \mathbf{G} * (\mathbf{F}^H [\mathbf{a}_T(\theta_1), \dots, \mathbf{a}_T(\theta_L)]) \triangleq \mathbf{G} * (\mathbf{F}^H \mathbf{A}_T), \quad (36)$$

where $\mathbf{G} \in \mathbb{C}^{P \times L}$ with $[\mathbf{G}]_{p,l} = e^{j2\pi p T_{\text{syn}} \nu_l}$, and $*$ denotes the Hadamard product. Note \mathbf{G} has a Vandermonde structure and its l -th column is characterized by the Doppler shift of the l -th path. For a randomly generated $\mathbf{F} \in \mathbb{C}^{N_l \times P}$ with each of its elements uniformly chosen from a unit circle, we define $b_{p,l} \triangleq [\mathbf{G}]_{p,l} \mathbf{f}_p^H \mathbf{a}_T(\theta_l)$ as the (p, l) -th entry of \mathbf{B} , where \mathbf{f}_p denotes the p -th column of \mathbf{F} . It can be verified that $\mathbb{E}[b_{p,l}] = 0, \forall p, l$ and

$$\mathbb{E}[b_{p_1, l_1}^H b_{p_2, l_2}] = \begin{cases} 0, & p_1 \neq p_2, \\ \frac{e^{j2\pi T_{\text{syn}} p_1 (\nu_{l_2} - \nu_{l_1})}}{N_l^2} \mathbf{a}_T^H(\theta_{l_1}) \mathbf{a}_T(\theta_{l_2}), & p_1 = p_2. \end{cases} \quad (37)$$

According to the asymptotic orthogonality for ULA^[27], $\mathbf{a}_T^H(\theta_{l_1}) \mathbf{a}_T(\theta_{l_2})/N_l$ converges to zero as $N_l \rightarrow \infty$ with $\theta_{l_1} \neq \theta_{l_2}$. Thus, we can see that the elements of \mathbf{B} are uncorrelated with each other since different paths have distinct AoDs. As a result, the k -rank of \mathbf{B} is given as $k_B = \min\{P, L\}$.

As for k_C , it can be easily verified that $k_C = 1$ when the vehicle is stationary. Moreover, \mathbf{C} is a Vandermonde matrix for non-stationary vehicles, in which case we have $k_C = \min\{K, L\}$.

Finally, based on the above analysis, the Kruskal's condition is equivalent to

$$\min\{M, L\} + \min\{Q, L\} + \min\{P, L\} + \min\{K, L\} \geq 2L + 3. \quad (38)$$

For a small L , we can reasonably assume that the number of subcarriers is greater than L , say, $Q \geq L$. Also, if we assume M , the dimension of the combining matrix $\mathbf{W}_{D,q}(t)$, is greater than 2, that is $M \geq 2$, we only need to ensure $\min\{P, L\} + \min\{K, L\} \geq L + 1$. Such a condition can be easily satisfied by setting either $K = 1, P \geq L$ or $P = 1, K \geq L$.

Note that the training overhead required by the proposed method is PKQ . From the above discussion, it is easy to know that the amount of training overhead is in the order of $\mathcal{O}(L^2)$. Due to the sparse scattering characteristics of mmWave channels, L is usually small. Hence the proposed method can achieve reliable channel estimates with a moderate amount of training overhead.

4 Vehicle Sensing Based on Channel Estimates

In V2I systems, based on the estimated channel parameters, multiple APs can collaborate to localize a target vehicle and estimate its related kinematic parameters such as the heading and speed of the vehicle. These estimated positions and kinematic parameters can be used to assist the communication between the vehicle and APs, such as beam switching and beam tracking. On the other hand, these APs can construct a real-time traffic map based on the positions and kinematic parameters of different vehicles, which can be used to give driving suggestions to vehicles, such as traffic jams ahead, vehicle formation, follow-up, and lane change, so that the traffic efficiency is enhanced^[28].

For simplicity, we consider a two-dimensional Cartesian coordinate system (CCS) as illustrated in Fig. 1, where the orientation of each AP's antenna array is assumed to be parallel with the y -axis. The locations of the n -th AP and the ve-

hicle are respectively denoted as

$$\begin{aligned} \mathbf{p}_{\text{AP}}^n &= [x_{\text{AP}}^n, y_{\text{AP}}^n]^T \in \mathbb{R}^2, \\ \mathbf{p}_v &= [x_v, y_v]^T \in \mathbb{R}^2, \end{aligned} \quad (39)$$

where \mathbf{p}_{AP}^n is known while \mathbf{p}_v is to be estimated. In addition, there is an unknown vehicle heading, namely the orientation of the vehicle's antenna array, which is denoted by $\alpha \in [0, \frac{\pi}{2})$, and the speed of the vehicle in this direction is denoted as v .

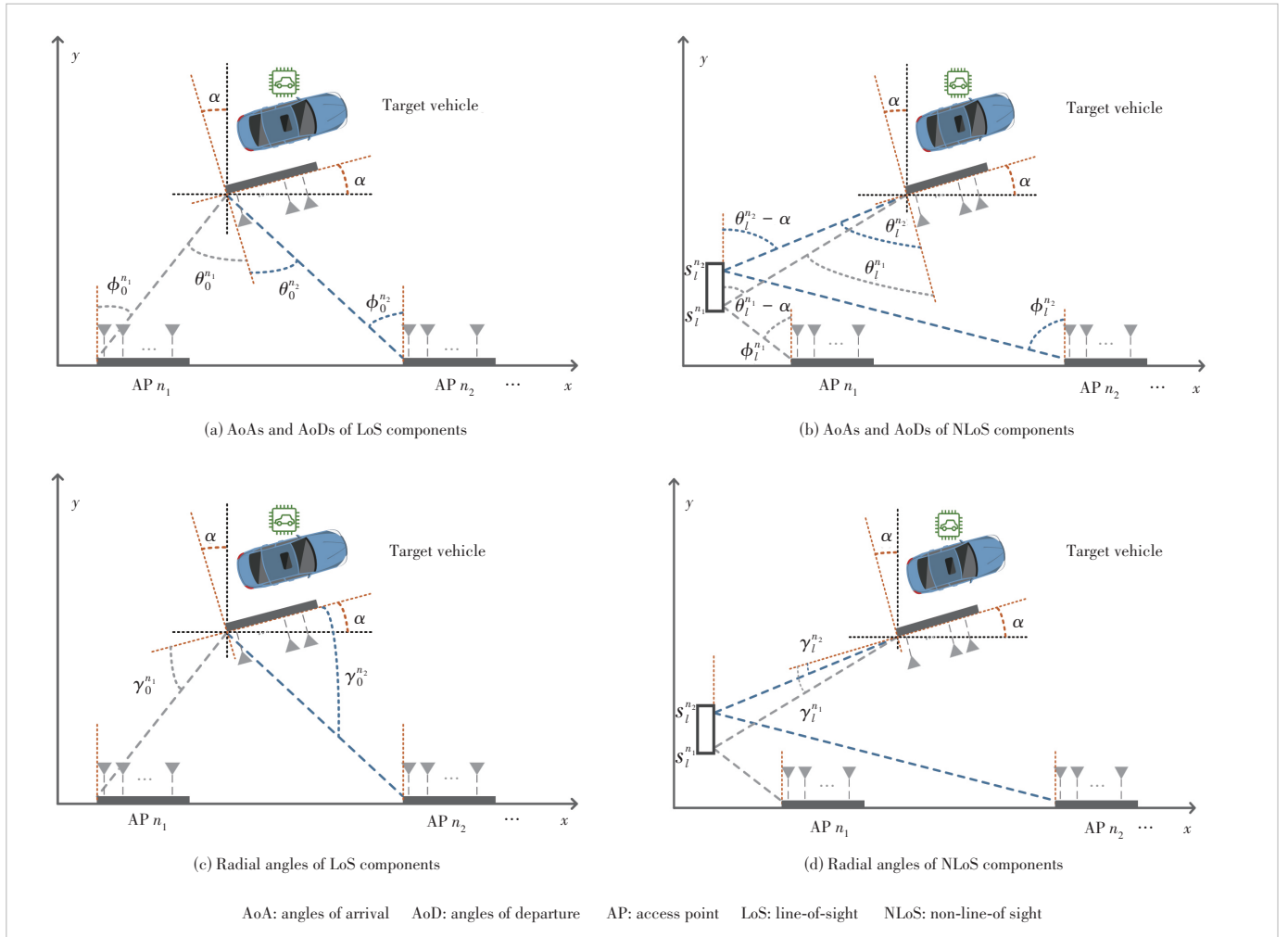
For each AP, like the n -th AP, we assume there exists a LOS path and $L_n - 1$ non-line-of sight (NLOS) paths. The l -th ($l > 0$) NLOS path is a result of a scatterer at an unknown location:

$$\mathbf{p}_s^{n,l} = [x_s^{n,l}, y_s^{n,l}]^T \in \mathbb{R}^2. \quad (40)$$

Note that for different APs, different paths may corre-

spond to the same scatterer. For the uplink scenario, from the geometric relationship delineated in Figs. 1(a) and 1(b), the time delay, AoD, and AoA of each path and the positions of the vehicle/AP can be expressed as

$$\begin{aligned} \tau_0^n &= \frac{\|\mathbf{p}_{\text{AP}}^n - \mathbf{p}_v\|_2}{c}, \\ \tau_l^n &= \frac{\|\mathbf{p}_{\text{AP}}^n - \mathbf{p}_s^{n,l}\|_2 + \|\mathbf{p}_v - \mathbf{p}_s^{n,l}\|_2}{c}, \quad l > 0, \\ \phi_0^n &= \arctan\left(\frac{x_v - x_{\text{AP}}^n}{y_v - y_{\text{AP}}^n}\right), \\ \phi_l^n &= \arctan\left(\frac{x_s^{n,l} - x_{\text{AP}}^n}{y_s^{n,l} - y_{\text{AP}}^n}\right), \quad l > 0, \\ \theta_0^n &= \phi_0^n + \alpha, \\ \theta_l^n &= \arctan\left(\frac{x_v - x_s^{n,l}}{y_v - y_s^{n,l}}\right) + \alpha, \quad l > 0, \end{aligned} \quad (41)$$



▲ Figure 1. A schematic for Vehicle-to-Infrastructure (V2I) coordinate systems

where $\phi_l^n \in \left(-\frac{\pi}{2}, \frac{\pi}{2}\right)$, and $\theta_l^n \in \left(-\frac{\pi}{2}, \frac{\pi}{2}\right)$.

To portray the motion relationship between the target vehicle and APs, we define the radial angle $\gamma_l^n \in [0, \frac{\pi}{2}]$, $l \geq 0$, as shown in Figs. 1(c) and 1(d). For the LoS path, the radial angle can be calculated as:

$$\gamma_0^n = \begin{cases} \frac{\pi}{2} + \phi_0^n + \alpha, x_v \leq x_{\text{AP}}^n (\phi_0^n \leq 0); \\ \frac{\pi}{2} - \phi_0^n - \alpha, x_v > x_{\text{AP}}^n (\phi_0^n > 0). \end{cases} \quad (42)$$

For the NLoS path, the radial angle can be calculated as

$$\gamma_l^n = \begin{cases} \frac{\pi}{2} + \phi_l^n + \alpha, x_v \leq x_s^{n,l} (\phi_l^n \leq 0); \\ \frac{\pi}{2} - \phi_l^n - \alpha, x_v > x_s^{n,l} (\phi_l^n > 0). \end{cases} \quad (43)$$

Note that γ_l^n ($l > 0$) is actually the radial angle between the target vehicle and the scatterer s_l^n , so that the radial velocity between the target vehicle and the scatterer s_l^n can be regarded as the radial velocity between the target vehicle and the n -th AP under the assumption that all scatterers are static or quasi-static.

According to the kinematic relation between the vehicle and the n -th AP, the radial velocity of the target vehicle concerning the n -th AP can be expressed as:

$$v_l^n = \begin{cases} v \cos \gamma_l^n, \text{ toward AP movement;} \\ -v \cos \gamma_l^n, \text{ reverse AP movement,} \end{cases} \quad (44)$$

where $l \geq 0$. Obviously, based on achieving super-resolution channel estimation, highly accurate target vehicle localization and motion state (including heading and velocity) can be perceived via channel parameters.

4.1 Case of Single AP

For the proposed V2I mmWave MIMO OFDM system, after the channel estimation stage, we can reap the channel parameters from the target vehicle to all APs so that the location and motion of the target vehicle can be perceived through the geometric relationship. We define $\{\hat{\theta}_l^n, \hat{\phi}_l^n, \hat{\beta}_l^n, \hat{\tau}_l^n, \hat{\nu}_l^n\}_{l=0}^{L_n-1}$ as the estimated channel path parameters from the vehicle to the n -th AP, where $l = 0$ means the LoS components of the n -th link. The vehicle's position and heading can be consequently given as

$$\begin{aligned} \hat{p}_v^n &= p_{\text{AP}}^n + \hat{\tau}_0^n c [\sin \hat{\phi}_0^n, \cos \hat{\phi}_0^n]^T, \\ \hat{\alpha}^n &= \hat{\theta}_0^n - \hat{\phi}_0^n, \end{aligned} \quad (45)$$

and then the first-order reflection s_l^n can be reasonably acquired by the intersection of the straight lines that respec-

tively start from the AP's and vehicle's location, i.e.

$$\begin{aligned} \hat{x}_s^{n,l} &= x_{\text{AP}}^n + (y_s^{n,l} - y_{\text{AP}}^n) \tan \hat{\phi}_l^n, \quad l > 0, \\ \hat{y}_s^{n,l} &= \frac{x_{\text{AP}}^n - \hat{x}_v + y_v \tan(\hat{\theta}_l^n - \hat{\alpha}) - y_{\text{AP}}^n \tan \hat{\phi}_l^n}{\tan(\hat{\theta}_l^n - \hat{\alpha}) - \tan \hat{\phi}_l^n}, \quad l > 0. \end{aligned} \quad (46)$$

Next, the radial degree between the vehicle and the n -th anchor can be calculated as:

$$\hat{\gamma}_0^n = \begin{cases} \frac{\pi}{2} + \hat{\phi}_0^n + \hat{\alpha}, \hat{x}_v^n \leq x_{\text{AP}}^n; \\ \frac{\pi}{2} - \hat{\phi}_0^n - \hat{\alpha}, \hat{x}_v^n > x_{\text{AP}}^n. \end{cases} \quad (47)$$

and the estimated vehicle velocity at the n -th AP is:

$$\hat{v}^n = \frac{\hat{\nu}_0^n}{\cos \hat{\gamma}_0^n}, \quad (48)$$

where $\hat{\nu}_0^n = \hat{\nu}_0^n c/f_c$, and $\hat{\nu}_0^n$ is the estimated Doppler shift from the LoS component. Moreover, it can be inferred the target vehicle moves toward the n -th AP if $\hat{\nu}^n > 0$ and vice versa.

4.2 Case of Multi-APs

For the case of multi-APs, we have the estimated time-varying channel parameters as $\{\hat{\theta}_l^n, \hat{\phi}_l^n, \hat{\beta}_l^n, \hat{\tau}_l^n, \hat{\nu}_l^n\}_{l=0, n=1}^{L_n-1, N}$. For a LoS path, the location of targets is determined only by the path delay and AoA with respect to the related AP, hence we develop the estimation of the vehicle's location from the estimated path delays and AoAs of all LoS paths between the vehicle and APs. For simplicity, we ignore the subscript of the LoS path, and define the mapping as follows.

$$\boldsymbol{\eta}^n(p_v) \triangleq \left[\arctan \left(\frac{x_v - x_{\text{AP}}^n}{y_v - y_{\text{AP}}^n} \right), \frac{\|p_{\text{AP}}^n - p_v\|_2}{c} \right]^T. \quad (49)$$

For the n -th AP, $n = 1, \dots, N$, we have

$$\hat{\boldsymbol{\eta}}^n = \boldsymbol{\eta}^n(p_v) + \boldsymbol{\omega}^n, \quad (50)$$

where $\hat{\boldsymbol{\eta}}^n = [\hat{\phi}^n, \hat{\tau}^n]^T$, and $\boldsymbol{\omega}^n$ is the measurement error. Without loss of generality, we assume $\boldsymbol{\omega} \triangleq [[\boldsymbol{\omega}^1]^T, \dots, [\boldsymbol{\omega}^N]^T]^T$ is distributed with mean zero and covariance $\boldsymbol{\Sigma}_\omega$. Define $\boldsymbol{\eta}(p_v) \triangleq [[\boldsymbol{\eta}^1(p_v)]^T, \dots, [\boldsymbol{\eta}^N(p_v)]^T]^T \in \mathbb{R}^{2N}$, $\hat{\boldsymbol{\eta}} \triangleq [[\hat{\boldsymbol{\eta}}^1]^T, \dots, [\hat{\boldsymbol{\eta}}^N]^T]^T \in \mathbb{R}^{2N}$, and the estimation of the target location from multi-APs can be formulized as the following nonlinear weighted least-square (WLS) problem, i.e.

$$\begin{aligned} \hat{p} &= \arg \min_p [\hat{\boldsymbol{\eta}} - \boldsymbol{\eta}(p)]^T \mathbf{R} [\hat{\boldsymbol{\eta}} - \boldsymbol{\eta}(p)] \\ \text{s.t. } & p \in \mathcal{D}_v, \end{aligned} \quad (51)$$

where \mathcal{D}_v denotes the location range of the target vehicle and \mathbf{R} can be chosen as $\mathbf{R} = \mathbf{I}$ or $\mathbf{R} = \Sigma_{\omega}^{[29]}$.

Next, we develop the Gauss-Newton method to iteratively solve Problem (51), which approximates the mapping $\boldsymbol{\eta}(\mathbf{p})$ by the first-order Taylor-series expansion at a given point $\mathbf{p}^{(0)}$ as:

$$\begin{aligned} \boldsymbol{\eta}(\mathbf{p}) &\approx \boldsymbol{\eta}(\mathbf{p}^{(0)}) + \mathbf{J}(\mathbf{p}^{(0)})(\mathbf{p} - \mathbf{p}^{(0)}), \\ \mathbf{J}(\mathbf{p}^{(0)}) &= \left. \frac{\partial \boldsymbol{\eta}(\mathbf{p})}{\partial \mathbf{p}} \right|_{\mathbf{p}=\mathbf{p}^{(0)}}. \end{aligned} \quad (52)$$

The nonlinear WLS Problem (51) can be converted to

$$\begin{aligned} \hat{\mathbf{p}} &= \arg \min_{\mathbf{p}} \left[\hat{\boldsymbol{\eta}} - \boldsymbol{\eta}(\mathbf{p}^{(0)}) - \mathbf{J}(\mathbf{p}^{(0)})(\mathbf{p} - \mathbf{p}^{(0)}) \right]^T \mathbf{R} \times \\ &\quad \left[\hat{\boldsymbol{\eta}} - \boldsymbol{\eta}(\mathbf{p}^{(0)}) - \mathbf{J}(\mathbf{p}^{(0)})(\mathbf{p} - \mathbf{p}^{(0)}) \right] \\ \text{s.t. } &\mathbf{p} \in \mathcal{D}_v, \end{aligned} \quad (53)$$

and the estimate of \mathbf{p}_v at the $(t+1)$ -th iteration can be obtained by

$$\hat{\mathbf{p}}^{(t+1)} = \hat{\mathbf{p}}^{(t)} + \left(\mathbf{J}^T(\mathbf{p}^{(t)}) \mathbf{R} \mathbf{J}(\mathbf{p}^{(t)}) \right)^{-1} \mathbf{J}^T(\mathbf{p}^{(t)}) \boldsymbol{\Delta}(\mathbf{p}^{(t)}), \quad (54)$$

where $\boldsymbol{\Delta}(\mathbf{p}^{(t)}) = (\hat{\boldsymbol{\eta}} - \boldsymbol{\eta}(\mathbf{p}^{(t)}))$. The above iteration can proceed until the convergence condition $\|\boldsymbol{\Delta}(\mathbf{p}^{(t)})\| < \varepsilon$ is met, where ε is a predefined stopping threshold. Moreover, we can project the finally iterated result to \mathcal{D}_v and make a significant location estimation of the target vehicle.

Defining $\hat{\mathbf{p}}_v = [\hat{x}_v, \hat{y}_v]^T$ as the estimate of the vehicle's location by Eq. (53), we then discuss how to obtain the vehicle's heading α and velocity v . Specifically, we first reconstruct the observation of AoD at all APs as:

$$\tilde{\phi}^n = \arctan \left(\frac{\hat{x}_v - x_{\text{AP}}^n}{\hat{y}_v - y_{\text{AP}}^n} \right), \quad n = 1, \dots, N, \quad (55)$$

with which we have a series of remodeled heading as

$$\tilde{\alpha}^n = \hat{\theta}^n - \tilde{\phi}^n, \quad n = 1, \dots, N. \quad (56)$$

Let $\tilde{\boldsymbol{\eta}}_{\alpha} \triangleq [\tilde{\alpha}^1, \dots, \tilde{\alpha}^N]^T$, and an LS estimator of α can be given as

$$\begin{aligned} \hat{\alpha} &= \arg \min_{\alpha} \left\| \tilde{\boldsymbol{\eta}}_{\alpha} - \boldsymbol{\eta}_{\alpha} \right\|_2^2 \\ \text{s.t. } &\boldsymbol{\eta}_{\alpha} = \mathbf{1} \cdot \alpha \\ &\alpha \in \mathcal{D}_{\alpha}, \end{aligned} \quad (57)$$

where \mathcal{D}_{α} denotes the angle range of the vehicle's heading.

The LS solution can be easily obtained as $\hat{\alpha} = \frac{1}{N} \sum_{n=1}^N \tilde{\alpha}^n$.

Furthermore, we have a similar way to remodel the obser-

vation of radial angles at all APs as:

$$\tilde{\gamma}^n = \begin{cases} \frac{\pi}{2} + \tilde{\phi}^n + \hat{\alpha}, & \hat{x}_v \leq x_{\text{AP}}^n; \\ \frac{\pi}{2} - \tilde{\phi}^n - \hat{\alpha}, & \hat{x}_v > x_{\text{AP}}^n, \end{cases} \quad (58)$$

with which we have $\tilde{v}^n = \frac{\hat{v}^n \cdot c}{\cos \tilde{\gamma}^n \cdot f_c}$, where \hat{v}^n is the estimated Doppler shift from the LoS component of the channel between the n -th AP and the vehicle. Let $\tilde{\boldsymbol{\eta}}_v \triangleq [|\tilde{v}^1|, \dots, |\tilde{v}^N|]^T$, and an LS estimator of v can be given as

$$\begin{aligned} \hat{v} &= \arg \min_v \left\| \tilde{\boldsymbol{\eta}}_v - \boldsymbol{\eta}_v \right\|_2^2 \\ \text{s.t. } &\boldsymbol{\eta}_v = \mathbf{1} \cdot v \\ &v \in \mathcal{D}_v, \end{aligned} \quad (59)$$

where \mathcal{D}_v denotes the velocity range of the vehicle. The LS solution can be easily obtained as $\hat{v} = \frac{1}{N} \sum_{n=1}^N |\tilde{v}^n|$.

5 Simulation Results

In this section, we carry out experiments to illustrate the performance of our proposed method. In simulations, the AP is located at $\mathbf{p}_{\text{AP}} = [21, 0]^T$. The vehicle is located at $\mathbf{p}_v = [43, 8]^T$ and moving with a heading $\alpha = \frac{\pi}{12}$ and a radial velocity $v = 40$ km/h toward the AP. The number of paths $L = 3$ and we consider a distance-dependent path loss. For the LoS path ($l = 0$), $\beta_0 \sim CN(0, 10^{-0.1\kappa})$, and $\kappa = a + 10b \log_{10}(D) + \xi$, in which D denotes the distance between the vehicle and the AP, and $\xi \sim N(0, \sigma_{\xi}^2)$. The values of a, b, σ_{ξ} are set to be $a = 61.4$ dB, $b = 2$ dB and $\sigma_{\xi} = 5.8$ dB as suggested by LoS real-world channel measurement^[30]. For the NLoS path ($l > 0$), the complex path gain is $\beta_l \sim CN(0, 10^{-0.1(\kappa + \mu)})$, and μ is the Rician factor^[31-32]. The carrier frequency is 28 GHz unless otherwise stated. There are $N_t = 32$ antennas at the vehicle (transmitter), $N_r = 64$ antennas and $M_r = 6$ RF chains at each AP. The total number of subcarriers is $\bar{Q} = 100$, out of which $Q = 10$ subcarriers are selected for training, and the sampling rate is set to $f_s = 100$ MHz. The number of subframes for training is set to $K = 3$, and the number of symbols in one subframe is set to $P = 10$. The beamforming matrices \mathbf{F} and \mathbf{W} are randomly generated with their entries uniformly chosen from a unit circle. The signal-to-noise ratio (SNR) is defined as:

$$\text{SNR} = \frac{\left\| \mathbf{y} - \mathcal{N} \right\|_F^2}{\left\| \mathcal{N} \right\|_F^2}, \quad (60)$$

where \mathcal{Y} and \mathcal{N} denote the received signal and the additive noise. The performance of our proposed method is evaluated by the mean square error (MSE), which is defined as

$$\text{MSE}(\mathbf{s}) = \sum_{l=1}^L |\mathbf{s}_l - \hat{\mathbf{s}}_l|^2, \quad (61)$$

where $\mathbf{s}_l \in \{\theta_l, \phi_l, \tau_l, \nu_l, \beta_l\}$ and the MSE is calculated separately to examine the estimation accuracy for each parameter. We also leverage the Cramer-Rao bound (CRB) results for a baseline of the estimates of channel parameters. The CRB is a lower bound on the variance of any biased estimator^[33]. It provides a benchmark for evaluating the performance of our proposed method.

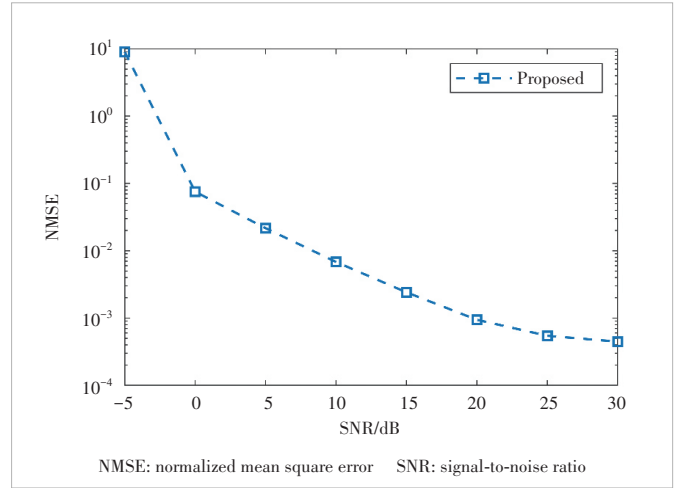
The performance of our proposed method as a function of SNR is depicted in Fig. 2. It can be observed that the CRBs of all five parameters decrease exponentially against the increased SNR. In addition, the MSEs of our proposed method converge to their lower bound while the SNR is increasing, which validates the efficacy of the proposed method for channel estimation. Specifically, the MSEs of AoA, AoD, Doppler shift and time delay are relatively close to its CRB, while the gap between the MSE and CRB of path gain is relatively wider, which may be subject to accumulated estimation errors.

In Fig. 3, we show the normalized mean square error

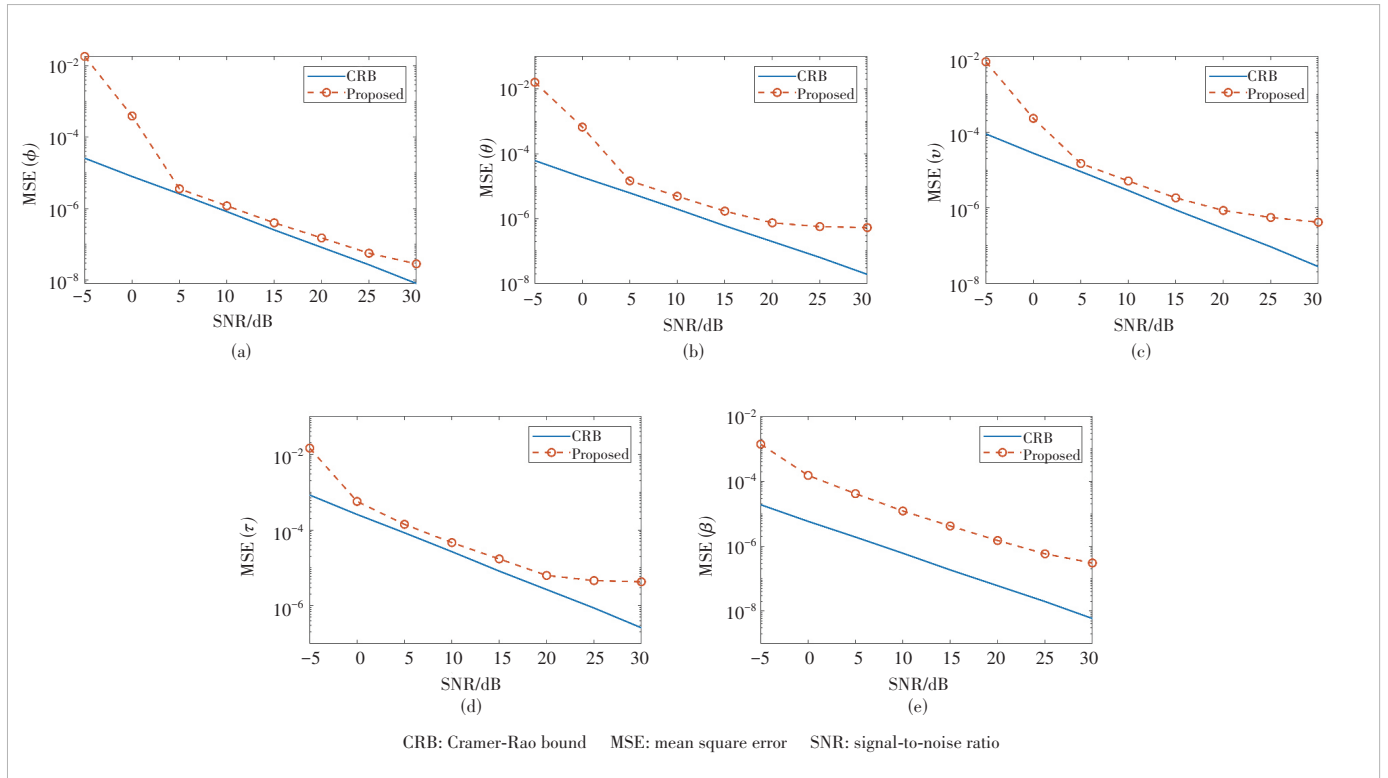
(NMSE) result for our proposed method as a function of SNR, in which the NMSE is defined by:

$$\text{NMSE} = \frac{\sum_{q=1}^Q \|\mathbf{H}_q - \hat{\mathbf{H}}_q\|_F^2}{\sum_{q=1}^Q \|\mathbf{H}_q\|_F^2}, \quad (62)$$

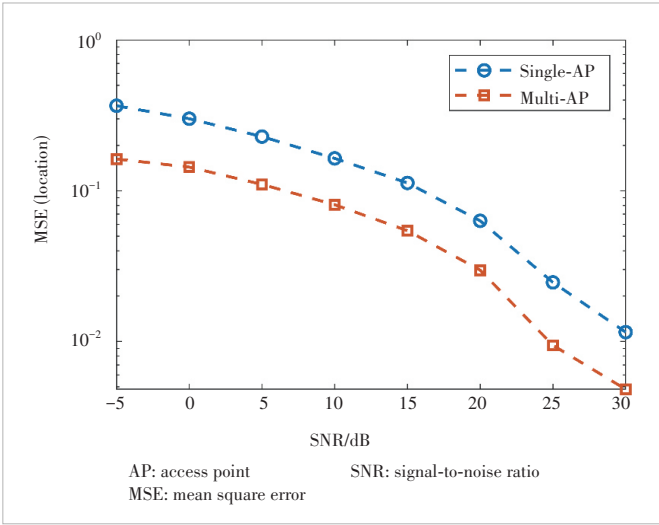
where \mathbf{H}_q denotes the frequency-domain channel matrix as-



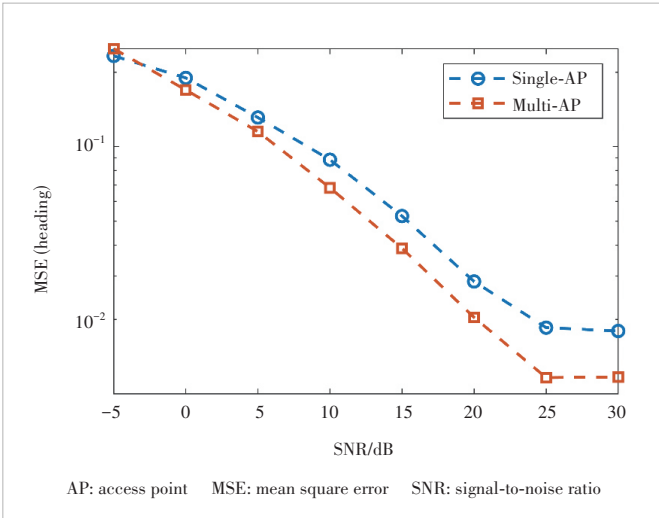
▲ Figure 3. Channel estimation performance versus SNR



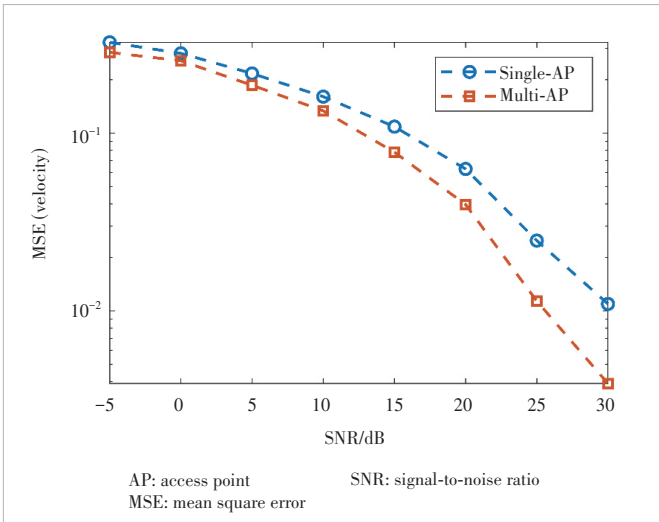
▲ Figure 2. MSEs and CRBs associated with different parameters versus SNR



▲ Figure 4. MSEs of vehicle's location versus SNR



▲ Figure 5. MSEs of vehicle's heading versus SNR



▲ Figure 6. MSEs of vehicle's velocity versus SNR

sociated with the q -th subcarrier, and \hat{H}_q is its estimate. Thanks to accurate channel parameter estimation, the proposed method can deliver a relatively accurate channel estimate as long as the SNR is above 0 dB.

Based on the estimation of channel parameters, the location, heading and velocity of the vehicle can be recovered from the geometric relationship as well as the motion relationship between the vehicle and each AP. To fully illustrate sensing performance, we compare the sensing performance of two cases namely single-AP and multi-AP for the V2I system. Specifically, we consider AP1 is located at $p_{AP}^1 = [21, 0]^T$ and AP2 is located at $p_{AP}^2 = [82, 0]^T$. The vehicle is located at $p_v = [58, 12]^T$ and moving with a heading $\alpha = \frac{\pi}{12}$ and a radial velocity $v = 50$ km/h toward AP2. The sensing performance of the two cases is plotted in Figs. 4, 5 and 6, from which we can observe that the sensing performance of the multi-AP case outperforms that of the single-AP case. The performance improvement can be intuitively explained. Because the vehicle is closer to AP2, the channel link between vehicle-AP2 is stronger than vehicle-AP1, which yields more accurate channel parameter estimation. In particular, the wider performance gap in estimating the vehicle's location between the multi-AP case and the single-AP case is caused by the accumulation of errors, as the location estimation is based on both AoA and time delay estimates.

6 Conclusions

In this paper, a CP decomposition-based method is proposed for high-accuracy channel estimation as well as sensing in mmWave MIMO-OFDM V2I Systems. To characterize the Doppler shift due to the vehicle's mobility, a time-varying frequency-domain mmWave channel is derived, a novel frame structure is introduced and a CP decomposition-based channel estimator is proposed. Utilizing the estimates of channel parameters in multi-APs, a nonlinear weighted least-square problem is proposed to accurately recover the location, heading and velocity of the vehicle. Simulation results are carried out to illustrate the effectiveness of the proposed method in performing communication and sensing in mmWave MIMO-OFDM V2I Systems.

Acknowledgement:

We would like to thank Prof. FANG Jun who led our team and helped revise this paper.

References

[1] RAPPAPORT T S, MURDOCK J N, GUTIERREZ F. State of the art in 60-GHz integrated circuits and systems for wireless communications [J]. Proceedings of the IEEE, 2011, 99(8): 1390 - 1436. DOI: 10.1109/JPROC.2011.2143650

- [2] RANGAN S, RAPPAPORT T S, ERKIP E. Millimeter-wave cellular wireless networks: Potentials and challenges [J]. *Proceedings of the IEEE*, 2014, 102(3): 366 – 385. DOI: 10.1109/JPROC.2014.2299397
- [3] GHOSH A, THOMAS T A, CUDAK M C, et al. Millimeter-wave enhanced local area systems: a high-data-rate approach for future wireless networks [J]. *IEEE journal on selected areas in communications*, 2014, 32(6): 1152 – 1163. DOI: 10.1109/JSAC.2014.2328111
- [4] YANG G, XIAO M, GROSS J, et al. Delay and backlog analysis for 60 GHz wireless networks [C]//*Proceedings of IEEE Global Communications Conference (GLOBECOM)*. IEEE, 2016: 1 – 7. DOI: 10.1109/GLOCOM.2016.7841725
- [5] SWINDLEHURST A L, AYANOGLU E, HEYDARI P, et al. Millimeter-wave massive MIMO: the next wireless revolution? [J]. *IEEE communications magazine*, 2014, 52(9): 56 – 62. DOI: 10.1109/MCOM.2014.6894453
- [6] ALKHATEEB A, EL AYACH O, LEUS G, et al. Channel estimation and hybrid precoding for millimeter wave cellular systems [J]. *IEEE journal of selected topics in signal processing*, 2014, 8(5): 831 – 846. DOI: 10.1109/JSTSP.2014.2334278
- [7] ALKHATEEB A, LEUS G, HEATH R W. Compressed sensing based multi-user millimeter wave systems: how many measurements are needed? [C]//*IEEE International Conference on Acoustics, Speech and Signal Processing (ICASSP)*. IEEE, 2015: 2909 – 2913. DOI: 10.1109/ICASSP.2015.7178503
- [8] ZHAO L, NG D W K, YUAN J H. Multi-user precoding and channel estimation for hybrid millimeter wave systems [J]. *IEEE journal on selected areas in communications*, 2017, 35(7): 1576 – 1590. DOI: 10.1109/JSAC.2017.2699378
- [9] VENUGOPAL K, ALKHATEEB A, GONZÁLEZ PRELCIC N, et al. Channel estimation for hybrid architecture-based wideband millimeter wave systems [J]. *IEEE journal on selected areas in communications*, 2017, 35(9): 1996 – 2009. DOI: 10.1109/JSAC.2017.2720856
- [10] ZHOU Z, FANG J, YANG L X, et al. Channel estimation for millimeter-wave multiuser MIMO systems via PARAFAC decomposition [J]. *IEEE transactions on wireless communications*, 2016, 15(11): 7501 – 7516. DOI: 10.1109/TWC.2016.2604259
- [11] ZHOU Z, FANG J, YANG L X, et al. Low-rank tensor decomposition-aided channel estimation for millimeter wave MIMO-OFDM systems [J]. *IEEE journal on selected areas in communications*, 2017, 35(7): 1524 – 1538. DOI: 10.1109/JSAC.2017.2699338
- [12] SONG H, FANG X M, FANG Y G. Millimeter-wave network architectures for future high-speed railway communications: Challenges and solutions [J]. *IEEE wireless communications*, 2016, 23(6): 114 – 122. DOI: 10.1109/MWC.2016.1500255WC
- [13] XIAO Z Y, XIA P F, XIA X G. Enabling UAV cellular with millimeter-wave communication: potentials and approaches [J]. *IEEE communications magazine*, 2016, 54(5): 66 – 73. DOI: 10.1109/MCOM.2016.7470937
- [14] CHOI J, VA V, GONZALEZ-PRELCIC N, et al. Millimeter-wave vehicular communication to support massive automotive sensing [J]. *IEEE communications magazine*, 2016, 54(12): 160 – 167. DOI: 10.1109/MCOM.2016.1600071CM
- [15] QIN Q B, GUI L, CHENG P, et al. Time-varying channel estimation for millimeter wave multiuser MIMO systems [J]. *IEEE transactions on vehicular technology*, 2018, 67(10): 9435 – 9448. DOI: 10.1109/TVT.2018.2854735
- [16] CHENG L, YUE G R, YU D Z, et al. Millimeter wave time-varying channel estimation via exploiting block-sparse and low-rank structures [J]. *IEEE access*, 2019, 7: 123355 – 123366. DOI: 10.1109/ACCESS.2019.2937628
- [17] SANCHIS P, MARTINEZ J M, HERRERA J, et al. A novel simultaneous tracking and direction of arrival estimation algorithm for beam-switched base station antennas in millimeter-wave wireless broadband access networks [C]//*IEEE Antennas and Propagation Society International Symposium*. IEEE, 2002: 594 – 597. DOI: 10.1109/APS.2002.1016415
- [18] DENG H, SAYEED A. Mm-wave MIMO channel modeling and user localization using sparse beamspace signatures [C]//*The 15th International Workshop on Signal Processing Advances in Wireless Communications (SPAWC)*. IEEE, 2014: 130 – 134. DOI: 10.1109/SPAWC.2014.6941331
- [19] VARI M, CASSIOLI D. mmWaves RSSI indoor network localization [C]//*IEEE International Conference on Communications Workshops (ICC)*. IEEE, 2014: 127 – 132. DOI: 10.1109/ICCW.2014.6881184
- [20] HU A Z, LV T J, GAO H, et al. An ESPRIT-based approach for 2-D localization of incoherently distributed sources in massive MIMO systems [J]. *IEEE journal of selected topics in signal processing*, 2014, 8(5): 996 – 1011. DOI: 10.1109/JSTSP.2014.2313409
- [21] GUERRA A, GUIDI F, DARDARI D. Position and orientation error bound for wideband massive antenna arrays [C]//*IEEE International Conference on Communication Workshop (ICCW)*. IEEE, 2015: 853 – 858. DOI: 10.1109/ICCW.2015.7247282
- [22] ALKHATEEB A, HEATH R W. Frequency selective hybrid precoding for limited feedback millimeter wave systems [J]. *IEEE transactions on communications*, 2016, 64(5): 1801 – 1818. DOI: 10.1109/TCOMM.2016.2549517
- [23] BAJWA W U, HAUPT J, SAYEED A M, et al. Compressed channel sensing: A new approach to estimating sparse multipath channels [J]. *Proceedings of the IEEE*, 2010, 98(6): 1058 – 1076. DOI: 10.1109/JPROC.2010.2042415
- [24] DA COSTA J P C L, ROEMER F, HAARDT M, et al. Multi-dimensional model order selection [J]. *EURASIP journal on advances in signal processing*, 2011, 2011(1): 26. DOI: 10.1186/1687-6180-2011-26
- [25] LIN Y X, JIN S, MATTHAIU M, et al. Tensor-based channel estimation for millimeter wave MIMO-OFDM with dual-wideband effects [J]. *IEEE transactions on communications*, 2020, 68(7): 4218 – 4232. DOI: 10.1109/TCOMM.2020.2983673
- [26] KRUSKAL J B. Three-way arrays: Rank and uniqueness of trilinear decompositions, with application to arithmetic complexity and statistics [J]. *Linear algebra and its applications*, 1977, 18(2): 95 – 138. DOI: 10.1016/0024-3795(77)90069-6
- [27] CHEN J H. When does asymptotic orthogonality exist for very large arrays? [C]//*IEEE Global Communications Conference (GLOBECOM)*. IEEE, 2013: 4146 – 4150. DOI: 10.1109/GLOCOM.2013.6831723
- [28] YANG Y, HUA K. Emerging technologies for 5G-enabled vehicular networks [J]. *IEEE access*, 2019, 7: 181117 – 181141. DOI: 10.1109/ACCESS.2019.2954466
- [29] LI Q, LAN J, ZHANG L, et al. Augmented nonlinear least squares estimation with applications to localization [J]. *IEEE transactions on aerospace and electronic systems*, 2022, 58(2): 1042 – 1054. DOI: 10.1109/TAES.2021.3115566
- [30] AKDENIZ M R, LIU Y P, SAMIMI M K, et al. Millimeter wave channel modeling and cellular capacity evaluation [J]. *IEEE journal on selected areas in communications*, 2014, 32(6): 1164 – 1179. DOI: 10.1109/JSAC.2014.2328154
- [31] YING K K, GAO Z, LYU S X, et al. GMD-based hybrid beamforming for large reconfigurable intelligent surface assisted millimeter-wave massive MIMO [J]. *IEEE access*, 2020, 8: 19530 – 19539. DOI: 10.1109/ACCESS.2020.2968456
- [32] SAMIMI M K, MACCARTNEY G R, SUN S, et al. 28 GHz millimeter-wave ultrawideband small-scale fading models in wireless channels [C]//*Proceedings of IEEE 83rd Vehicular Technology Conference (VTC Spring)*. IEEE, 2016: 1 – 6. DOI: 10.1109/VTC-Spring.2016.7503970
- [33] KAY S M. *Fundamentals of statistical signal processing* [M]. Englewood Cliffs, NJ: Prentice-Hall PTR, 1993

Biographies

WANG Jilin (jilinwang@std.uestc.edu.cn) has been working toward his PhD degree with National Key Laboratory of Wireless Communications, University of Electronic Science and Technology of China (UESTC) since 2021. His current research interests include compressed sensing and millimeter-wave communication.

ZENG Xianlong received his BS degree from University of Electronic Science and Technology of China (UESTC) in 2018. He has been working toward his MS degree with National Key Laboratory of Wireless Communications, UESTC since 2022. His current research interests include integrated sensing and communication (ISAC).

YANG Yonghui received his BS degree in information countermeasure techniques and MS degree in electronic information engineering from Xidian University, China in 2006 and 2010, respectively. Since 2010, he has been with ZTE Corporation, where his research interests focus on wireless communications. His current research interests include 5G and 6G technology, and

millimeter-wave and terahertz communication.

PENG Lin received his BS degree in information engineering and MS degree in electromagnetic field and microwave techniques from Nanjing University of Science and Technology, China in 2004 and 2006, respectively. Since 2006, he has been with ZTE Corporation, where he focuses on the research of wireless communications. His current research interests include beyond 5G and 6G technology, millimeter-wave and terahertz communications and intelligent reflecting surface for wireless applications.

LI Lingxiang received her BS degree from Central South University, China in 2010, and her PhD degree from University of Electronic Science and Technology of China (UESTC) in 2017, all in electrical engineering. She was a visiting PhD student under supervision of Prof. Athina P. PETROPULU at Rutgers, The State University of New Jersey, USA during 2015 – 2016. Dr. LI is now an associate professor with the National Key Lab of Science and Technology on Communications, UESTC. Her research interests include THz communications and Integrated Sensing and Communications (ISAC).

Sensing and Communication Integrated Fast Neighbor Discovery for UAV Networks



WEI Zhiqing, ZHANG Yongji, JI Danna, LI Chenfei

(Beijing University of Posts and Telecommunications, Beijing 100876, China)

DOI: 10.12142/ZTECOM.202403009

<https://kns.cnki.net/kcms/detail/34.1294.TN.20240921.1450.002.html>, published online September 23, 2024

Manuscript received: 2024-08-06

Abstract: In unmanned aerial vehicle (UAV) networks, the high mobility of nodes leads to frequent changes in network topology, which brings challenges to the neighbor discovery (ND) for UAV networks. Integrated sensing and communication (ISAC), as an emerging technology in 6G mobile networks, has shown great potential in improving communication performance with the assistance of sensing information. ISAC obtains the prior information about node distribution, reducing the ND time. However, the prior information obtained through ISAC may be imperfect. Hence, an ND algorithm based on reinforcement learning is proposed. The learning automaton (LA) is applied to interact with the environment and continuously adjust the probability of selecting beams to accelerate the convergence speed of ND algorithms. Besides, an efficient ND algorithm in the neighbor maintenance phase is designed, which applies the Kalman filter to predict node movement. Simulation results show that the LA-based ND algorithm reduces the ND time by up to 32% compared with the Scan-Based Algorithm (SBA), which proves the efficiency of the proposed ND algorithms.

Keywords: unmanned aerial vehicle networks; neighbor discovery; integrated sensing and communication; reinforcement learning; Kalman filter

Citation (Format 1): WEI Z Q, ZHANG Y J, JI D N, et al. Sensing and communication integrated fast neighbor discovery for UAV networks [J]. *ZTE Communications*, 2024, 22(3): 69 – 82. DOI: 10.12142/ZTECOM.202403009

Citation (Format 2): Z. Q. Wei, Y. J. Zhang, D. N. Ji, et al., “Sensing and communication integrated fast neighbor discovery for UAV networks,” *ZTE Communications*, vol. 22, no. 3, pp. 69 – 82, Sept. 2024. doi: 10.12142/ZTECOM.202403009.

1 Introduction

Recently, integrated sensing and communication (ISAC), which improves hardware and spectrum efficiency, has attracted wide attention in both academia and industry. For unmanned aerial vehicle (UAV) networks, ISAC can save limited space and power, minimize the payload, and increase the endurance of UAVs. Therefore, ISAC-driven UAV networking becomes vital to achieve better performance of UAV networking, especially for neighbor discovery (ND). Obtaining the prior knowledge through ISAC can speed up neighbor discovery. The estimated number and directions of neighbors can be obtained through ISAC to avoid invalid transmission in advance. Based on the prior knowledge, the scan-based algorithm (SBA) is used for neighbor discovery^[1-2]. In Ref. [3], LIU et al. used the sensing information obtained by a double-sided phased array radar to assist neighbor

discovery and proposed a new algorithm that applies two beams to transmit and receive independently or simultaneously. In Ref. [4], based on the accuracy of the prior knowledge and the response mechanism, WEI et al. proposed four radar-assisted ND algorithms, including Reply and Non-Stop (RnS), Non-Reply and Non-Stop (nRnS), Reply and Stop (RS), and Non-Reply and Stop (nRS). In Ref. [5], a 79-GHz millimeter-wave radar was used to detect the location and mobility of neighbors and the identity information of neighbors via 5.9-GHz broadcasting was obtained. The UAV node identifies its neighbors by combining the information obtained from the two frequency bands.

Besides ISAC-based ND algorithms, there are other methods to acquire prior knowledge. In Ref. [6], KHAMLIHI et al. applied energy detectors to distinguish whether the receiving node was in a collision state or an idle state. If the receiving node is in the collision state, it will switch to the collision-resolving listening mode and the transmitting node will switch to the collision-resolving re-transmitting mode until the receiving node successfully receives the data packets transmitted by at least two transmitting nodes. GAO et al. proposed an anti-collision ND protocol that avoids beacon collisions through carrier sensing^[7]. The node can decide whether to send a bea-

This work was supported in part by the Fundamental Research Funds for the Central Universities under Grant No. 2024ZCJH01, in part by the National Natural Science Foundation of China (NSFC) under Grant No. 62271081, and in part by the National Key Research and Development Program of China under Grant No. 2020YFA0711302.

con according to the prior knowledge of the channel state obtained by carrier sensing, which can effectively avoid collisions. SUN et al. proposed an ND protocol based on pre-handshake^[8]. The pre-handshake is carried out by adding small sub-slots before the ordinary time slots, which allows nodes to learn the activities of their neighbors in advance to reduce collisions. In Ref. [9], a dual-band system was applied, where one frequency band was used to obtain prior knowledge about neighbors, and the other frequency band was used for neighbor discovery. The paper also discussed how to maximize the efficiency of neighbor discovery in the presence of prior knowledge. Except for applying prior knowledge to improve the performance of algorithms, some researchers consider introducing reinforcement learning algorithms to find an optimal ND strategy by interacting with the environment^[10-11]. Optimizing the classical ND algorithms by dynamically adjusting the parameters are also considered^[12-13]. However, these algorithms are all direct ND algorithms. As the number of nodes increases, some researchers have focused on ND algorithms based on gossip, in which nodes can indirectly discover neighbors by exchanging neighbor lists with their neighbors^[14].

The above studies still have several limitations: 1) When they apply prior knowledge to improve neighbor discovery, they ideally assume that the sense information is perfect. However, ISAC may make the radar detection range smaller than the communication range and lead to the problem of incomplete prior knowledge obtained by nodes; 2) only the initialization phase of the neighbor discovery is studied in the above papers. Some temporary events in the neighbor maintenance phase can easily destroy the node connection, such as node failure, energy exhaustion, and power increase. As neighbor discovery is a continuous process, the maintenance phase should be studied with the initialization phase together. In this paper, reinforcement learning is introduced to solve the problem of incomplete prior knowledge. A Kalman filter is applied to predict the movement of nodes in the neighbor maintenance phase, which can speed up neighbor discovery in the maintenance phase. The main contributions of this paper are summarized as follows.

1) We introduce a reinforcement learning algorithm to address the incompleteness of prior information obtained by ISAC, which occurs in the ND problem. The problem is mapped as a multi-agent learning model, and an ND strategy based on learning automata (LA) is proposed. The algorithm estimates whether the neighbor nodes have been completely discovered according to the distribution of nodes and the partial information obtained by detection. We design a linear reward and punishment mechanism for LA. The simulation results show that when the ratio of radar detection range to communication range is set to 0.6, the time efficiency of the algorithm based on LA can be increased by 32%.

2) Due to the high mobility of UAVs, the neighbor list needs to be continuously updated to maintain the constructed

network topology. Unlike the existing ND algorithms that update the entire network, we separate the neighbor maintenance phase from the traditional initialization phase. In the neighbor maintenance phase, an efficient ND algorithm is designed, where the Kalman filter is introduced based on the prior knowledge obtained in the initialization phase. The switching mechanism between the initialization phase and the maintenance phase is also designed. When an error occurs in node prediction or the duration of the neighbor maintenance phase is greater than a threshold, the maintenance phase will be switched to the initialization phase to ensure the accuracy of the network topology. The simulation results prove that the networking efficiency with this algorithm is much higher than that of traditional neighbor discovery.

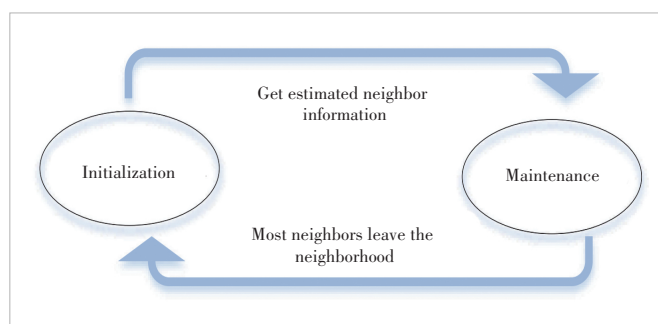
The rest of this paper is organized as follows. In Section 2, the system model and assumptions are described. In Section 3, considering the gap between the radar detection range and communication range, we introduce the reinforcement learning algorithm and design the learning strategy. The upper and lower bounds of time slots required to discover all neighbors are derived in the algorithm. Moreover, the impact of parameter settings on the performance is simulated and analyzed in two-dimensional and three-dimensional UAV networks. In Section 4, the Kalman filter is introduced, which greatly improves the efficiency of neighbor discovery through predictions. In Section 5, the algorithms proposed in Sections 3 and 4 are simulated and analyzed. Section 6 concludes this paper.

2 System Model and Assumptions

2.1 System Model

In UAV networks, neighbor discovery needs to be carried out periodically due to the mobility of nodes and its possible failure. Neighbor discovery can be divided into two procedures: the initialization and maintenance phases^[15]. Previous works performed these two phases with the same scheme^[6, 16-20]. Considering the mobility of nodes and the highly dynamic topology of UAV networks, we use different strategies for the two phases and design their switching mechanism. Fig. 1 shows the transformation of the two phases.

Initialization phase is a traditional stage for neighbor dis-



▲ Figure 1. Two-stage conversion of neighbor discovery

covery. In this stage, we introduce LA for the neighbor discovery. Nodes are regarded as agents with learning ability, and automatic learning machines are applied to change policies to speed up the discovery process. More detailed information is introduced in Section 3.

Maintenance phase refers to the stage in which the topology needs to be updated due to possible failures, which adapts to the highly dynamic topology due to the mobility of UAVs. At this stage, nodes need a more efficient scheme to cope with the rapid changes in topology with limited energy. In Section 4, a neighbor maintenance method based on the Kalman filter is proposed to accelerate the construction of network topology by using the speed and location of the neighbors.

2.2 Neighbor Discovery Assumptions

Undirected graphs $G = (V, E)$ are here used to describe the neighbors of nodes in the network, where $V = (V_1, V_2, \dots, V_N)$ is the set of nodes distributed uniformly and randomly and E is the set of link edges. A link edge $(i, j) \in E$ represents that two nodes (i, j) are one-hop neighbors of each other. Each node is equipped with a directional antenna. For a two-dimensional model, the neighborhood of a node is a circle with radius R_s . The antenna width is α and the neighborhood can be divided into $k = 2\pi/\alpha$ non-overlapping beams. For a three-dimensional model, its neighborhood is a sphere with a radius R_s . The vertical and horizontal widths of a beam of the antenna are both α , and the neighborhood can be divided into $k = 2\pi^2/\alpha^2$ non-overlapping beams. Moreover, the following definitions and assumptions are made.

1) Identification: All nodes are distinguished by unique identification (ID), which can be a media access control (MAC) address.

2) Resource: All nodes will transmit messages on the same frequency band with the same power.

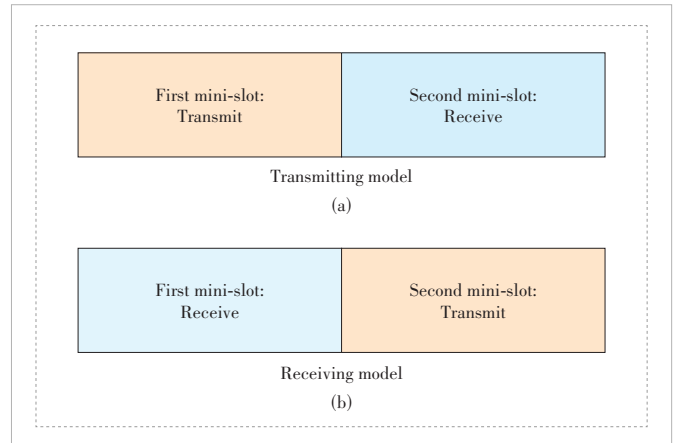
3) Time slot division: The network adopts the synchronous time slot division model^[21], which divides time into time slots of the same length. The algorithm proposed in this paper is based on a two-way handshake mechanism. Therefore, each time slot is divided into two mini-slots, as shown in Fig. 2. In the second mini-slot, after receiving the Hello packet, the receiving node replies with an acknowledgment packet (ACKP) with probability 1.

4) Half-duplex: The nodes work in the half-duplex mode^[22]. A node will be in a transmitting or receiving state at any time slot. In this paper, a node has three modes: transmit (T), receive (R), and idle (I)^[23]. Unlike being in the active states (T/R), nodes in the idle state save power consumption^[24].

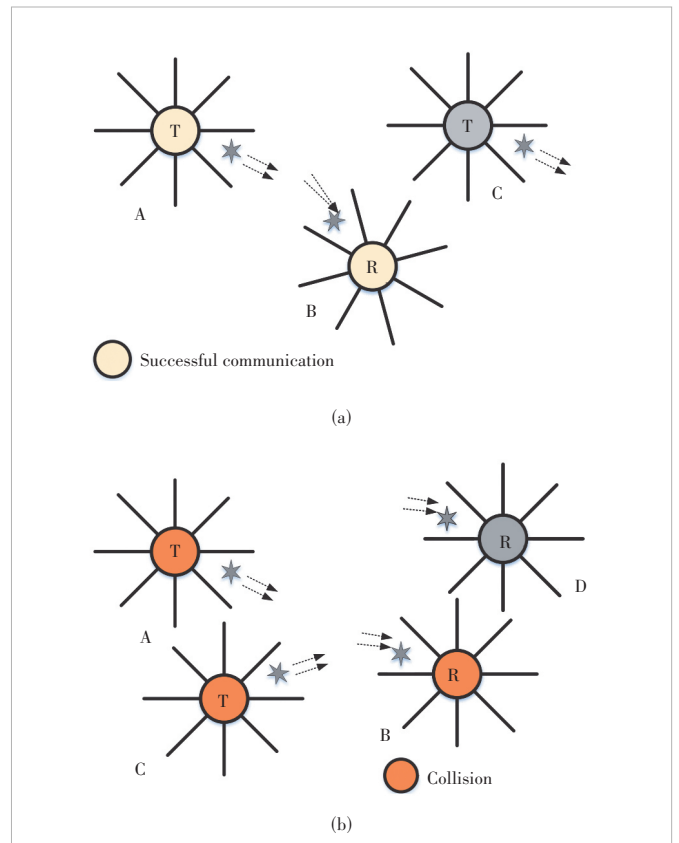
5) Successful communication: Nodes A and B are neighbors to each other only when they are within the one-hop communication range of each other. As shown in Fig. 3(a), successful communication between a pair of nodes requires that antennas are in a complementary state (one node transmits and the other receives) and point to each other at the same time. It is

supposed that the transmitting direction of node A is θ' and the receiving direction of node B is θ'' . For the directional transmission and directional reception mode, the following conditions must be met for successful communication: a) The antenna patterns of the two nodes are complementary; b) the direction meets $\theta' = (\theta'' + \pi) \bmod 2\pi$; c) no collision occurs during the interaction.

6) Collision: When a node receives two or more Hello packets, a data packet conflict has occurred. As shown in Fig. 3(b),



▲ Figure 2. Time slot division



▲ Figure 3. Successful communication and data packet collision

a collision will occur when two nodes send signals to one node at the same time.

7) ISAC: Each node is equipped with a set of transceivers to send and receive ISAC signals. A node transmits the ISAC signal that has detection capabilities and carries the Hello packet. The receiver can process the echo signals and the communication data packets.

8) Neighbor information: Each node maintains an antenna beam number list (ABNL) and a neighbor information list (NIL). Maintained by node $i, \forall i \in N$, the ABNL is denoted as $i, \forall i \in N, \xi_i^k \in \{0, 1\}$, where ξ_i^k denotes the existence of node i in the k -th beam direction according to the result of radar detection. If the radar detects that there are neighbors in the k -th beam, ξ_i^k is marked as 1. Otherwise, it is marked as 0. Maintained by node $j, \forall j \in N$, the NIL is expressed as $I_j = \{I_1, I_2, \dots, I_N\}$, which maintains the information of one-hop neighbors.

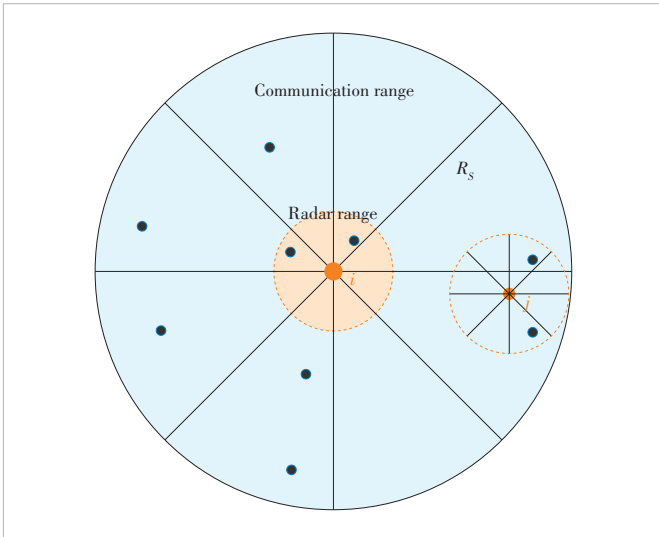
With an ISAC signal, the radar detection range is smaller than the communication range; $\eta = R_r/R_c$ is the ratio of radar detection range to communication range. As shown in Fig. 4, nodes can only detect part of neighborhood information^[25].

The ND algorithm uses LA to solve this problem. The ND process is modeled as autonomous learning. Nodes are regarded as agents, and the neighborhood is regarded as the environment to be learned. Based on the prior knowledge obtained by each time slot, the node optimizes the behavior of selecting the beam in the ND algorithm^[25].

3 Neighbor Discovery Algorithm Based on Learning Automata

3.1 Learning Automata Node

In a non-stationary environment, the reward distribution is



▲ Figure 4. Communication and radar detection range

related to time. So the learning goal of LA is to adjust behavior based on each time slot^[26]. This paper is based on a non-stationary environment and applies a finite state automaton (FSA) to model neighbor discovery.

In each time slot, LA selects an action and receives an enhanced signal β_i from the environment. β_i describes whether the selected action is beneficial or unfavorable. LA observes the input signal and updates the action probability distribution vector P_i to enable a higher probability of successful neighbor discovery in the next time slot. Moreover, in the LA model, there are the following definitions.

Antenna mode $M_i = \{T, R\}$: In each time slot, LA_i independently selects the transmission mode (T) with probability p_t and selects the reception mode (R) with probability $p_r = 1 - p_t$.

Action space $A_i = \{a_1, a_2, \dots, a_k\}$: Action $a_k = 1$ means that LA_i transmits or receives in beam k .

Action probability distribution vector $P_i = \{p_i^1, p_i^2, \dots, p_i^k\}$: p_i^m is the probability that LA_i selects beam m . In each time slot, LA_i selects a beam according to P_i .

Reinforcement signal $\beta_i(t)$: The reinforcement signal $\beta_i(t) \in \{0, 1\}$ is obtained by LA_i in time slot t .

Probability update: The action probability distribution vector is updated to $P_i(t+1)$ according to $\beta_i(t)$ in time slot t .

3.2 Probability Update Strategy

According to the range of radar detection and communication, neighbors are divided into two categories, including the nodes both in the radar detection range and communication range, and the nodes in the communication range and outside the radar detection range. Two lists are defined to describe these two types of neighbors: the radar neighbor list (RNL) and communication neighbor list (CNL). The RNL of node i is a matrix $R_{N \times K}^i$ with dimension $N \times K$, which records the neighbors in the RNL of node i . For example, if node f exists in the RNL of node i , the f -th row of matrix $R_{N \times K}^i$, namely vector $R_{f \times K}^i$, represents the discovery of node f in the beams of node i . When node f is in beam g with $g \in \{1, 2, \dots, K\}$, $R_{f \times K}^i$ is

$$R_{f \times K}^i = \begin{bmatrix} 0 & 0 & 1 & \dots & 0 \end{bmatrix}_{1 \times K}. \quad (1)$$

CNL of node i is denoted by $C_{N \times K}^i$ and $R_{N \times K}^i \in C_{N \times K}^i$. The vector $R_{1 \times K}^i = [r_{11} \ \dots \ r_{1K}]$ is the number of neighbors detected by node i in the second mini-slot. The radar can detect the number and the position of nodes in the current beam^[4].

LA_i optimizes the action selection by updating the action probability distribution vector P_i ^[27]. The update strategy is as follows.

Environmental interaction: At time slot t , LA_i selects an action a_m , calculates the environmental feedback information, gives an enhanced signal $\beta_i(t)$, and updates it to $P_i(t+1)$ according to Eqs. (3) or (4). When the radar detects the same beam multiple times, the inaccurate detection in the previous

time slot can be corrected by updating matrix $\mathbf{R}_{1 \times K}^i$.

Reward and punishment signal β_i^k : When LA_i selects beam k and the transmission mode, the ISAC signal is transmitted in the first mini-slot. In the second mini-slot, LA_i updates $\mathbf{C}_{N \times K}^i$ and $\mathbf{R}_{N \times K}^i$ according to radar detection and the communication result. If there are potential neighbors in beam k , assign $\beta_i^k = 0$. For example, if a neighbor is in beam k in RNL and the ACK packet is not received in the second mini-slot, there is a potential neighbor in beam k and should be rewarded. If there are no potential neighbors in beam k , assign $\beta_i^k = 1$.

In UAV networks, the number of neighbors in each beam is mostly 0 and 1^[4]. In a beam, when a node appears in the radar detection range, the probability of other nodes appearing in the communication range outside the radar detection range is small. $\mathbf{P}_{\text{pte}}^i$ is the probability that there are still neighbors for node i in beam m when all the nodes in the radar detection range are discovered, with expression as follows.

$$\mathbf{P}_{\text{pte}}^i = \mathbf{P}_{\text{pte}}^i(N_1^R) + \mathbf{P}_{\text{pte}}^i(N_2^R) + \dots = \frac{P_{B_2} + \dots + P_{B_m}}{P_{B_1} + P_{B_2} + \dots + P_{B_m}} + \frac{P_{B_3} + \dots + P_{B_m}}{P_{B_2} + \dots + P_{B_m}} + \dots, \quad (2)$$

where $\mathbf{P}_{\text{pte}}^i(N_1^R)$ represents the probability that the sum of the m -th column of $\mathbf{C}_{N \times K}^i - \mathbf{R}_{N \times K}^i$ is greater than 1 when $r_{1m} = 1$, and $\mathbf{P}_{\text{pte}}^i(N_2^R)$ represents the probability that the sum of the m -th column of $\mathbf{C}_{N \times K}^i - \mathbf{R}_{N \times K}^i$ is greater than 1 when $r_{1m} = 2$.

According to the reinforcement signal, the update of the ac-

tion probability distribution vector is divided into the following two cases.

When $\beta_i^k = 0$,

$$\mathbf{P}_i^k(t+1) = \begin{cases} \mathbf{P}_i^k(t) + \phi(\cdot)(1 - \mathbf{P}_i^k(t)), a_i(t) = a_i \\ (1 - \phi(\cdot))\mathbf{P}_i^k(t), a_i(t) \neq a_i \end{cases}, \quad (3)$$

where $\phi(\cdot)$ is a function of the number of potential neighbors.

$$\phi(\cdot) = \begin{cases} \gamma_1 n_i(t), n_i = 1 \\ \gamma_2 n_i(t), n_i > 1, \end{cases} \quad (4)$$

where γ_1 represents the reward coefficient of a single potential neighbor, γ_2 represents the reward coefficient of multiple potential neighbors, and $n_i(t)$ represents the number of potential neighbors.

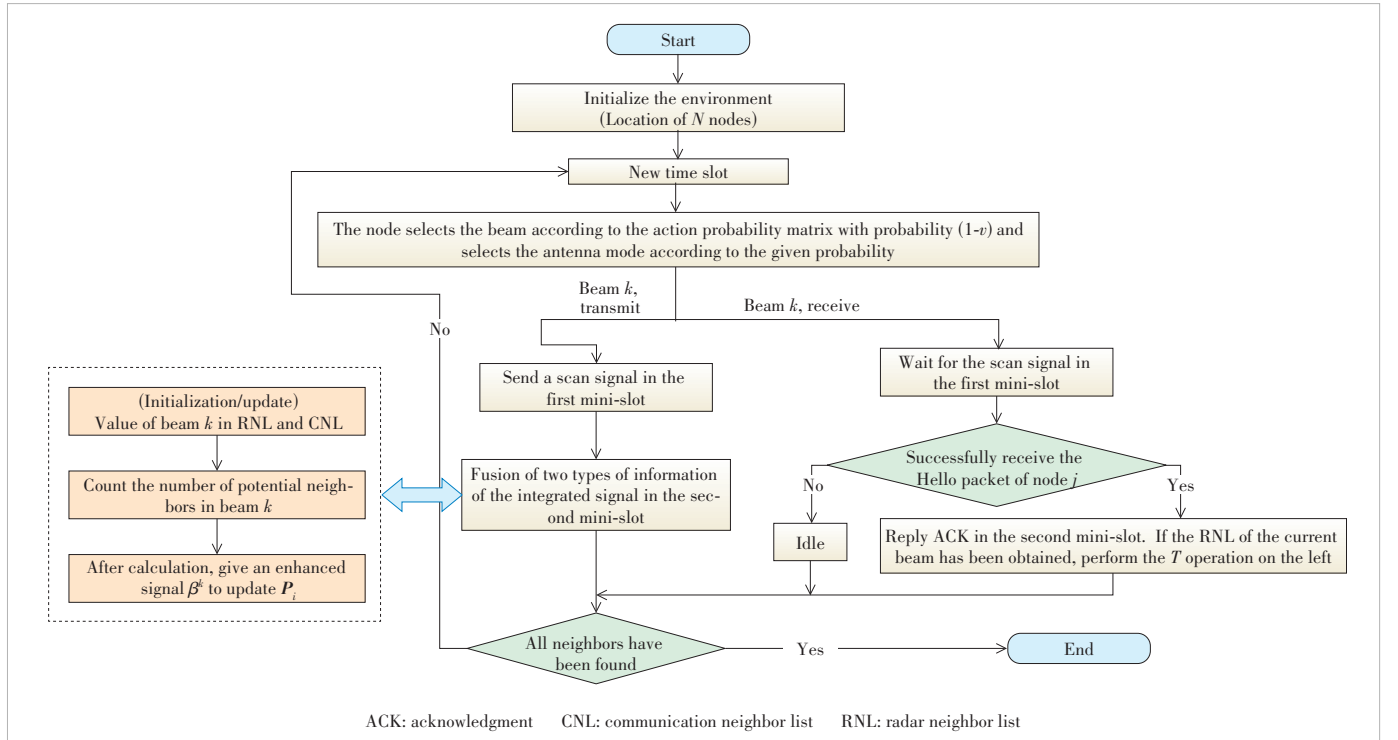
When $\beta_i^k = 1$,

$$\mathbf{P}_i^k(t+1) = \begin{cases} (1 - \mu)\mathbf{P}_i^k(t), a_i(t) = a_i \\ \frac{\mu}{K-1} + (1 - \mu)\mathbf{P}_i^k(t), a_i(t) \neq a_i, \end{cases} \quad (5)$$

where μ is the penalty coefficient.

3.3 ND Process

The ND algorithm based on LA is depicted as follows, and its flow chart is shown in Fig. 5.



▲ Figure 5. Flow chart of the ND algorithm

When neighbor discovery starts, LA_i initializes its action probability distribution vector $\mathbf{P}_i(t=0)$, $\mathbf{P}_i^k = 1/K$, $\forall i \in N$, and assigns matrices $\mathbf{R}_{1 \times K}^i$, $\mathbf{R}_{N \times K}^i$, and $\mathbf{C}_{N \times K}^i$ to zero.

Repeat the following steps for each time slot.

LA_i randomly selects a_k with probability ν or selects a_k according to the action probability distribution vector \mathbf{P}_i with probability $1 - \nu$.

In the second mini-slot, when $M_i = T$, update $\mathbf{R}_{N \times K}^i$ according to radar detection, update $\mathbf{C}_{N \times K}^i$ according to the communication result, and update \mathbf{P}_i according to the reinforcement signal. When $M_i = R$, update $\mathbf{C}_{N \times K}^i$ according to the communication result in the first mini-slot. If the Hello packet is received, it will reply with an ACK packet, otherwise it will be in the idle state.

3.4 Time Convergence Upper and Lower Bound Analysis

In the learning-based ND scheme, the action probability distribution vector changes with time. This section gives the probability update strategy when $\eta = 1$. When the current beam k does not receive an echo, let $\mu = 1$ in Eq. (5), otherwise no update is made.

3.4.1 Discovery Probability Analysis

The ND process can be described as a Bernoulli experiment in all beams^[12].

It takes J frames for a node u to find its neighbor v with probability P_v^u . K is the number of beams. In the two-dimensional model, the node density is $\sigma = N/\pi R_s^2$. In the three-dimensional model, the node density is $\sigma = 3N/4\pi R_s^3$. The average number of beams is $m = N/K$. The probability that any node is transmitting in any time slot is p_t .

After time slot t , the number of neighbors discovered by node u is $\chi(t)$; $(i+1)_{\text{th}}$ means the direction in which the beam is likely to point from $\chi(t) = i$ to $\chi(t) = i+1$. Suppose there are a total of m_j neighbors of node u in beam j . $X = p_t/K$ represents the probability that m_j (including v) neighbors in beam j each send to node u . $X_j = p_r/K$ represents the probability of node u receiving in beam j .

Lemma 1: The probability of finding a specific neighbor when there is a collision is

$$P_{ro} = XX_j(1-X)^{m_j-1}. \quad (6)$$

Based on Lemma 1, in the two-way handshake, if node u discovers its neighbor v in time slot t , the antenna beams of u and v need to point to each other with probability $1/K^2$. The antenna patterns of (u, v) are complementary to each other, which is (T, R) or (R, T) with probability $2 \times p_t \times (1 - p_t)$. In addition, the other $N-1$ neighbors must not interfere with the ND process. When other neighbors select the transmitting mode, the probability of aligning with the receiving node is $1/K^2$ and the non-interference probability is $(1 - 1/K^2)$. When other neighbors select the receiving mode, it does not send an

ACK packet in the second mini-slot^[25]. Therefore, the probability of finding any neighbor is

$$P_{\text{suc}}^{u-v} = 2 \frac{1}{K^2} p_t (1 - p_t) \cdot \left(\left(1 - \frac{1}{K^2} \right) p_t + \left(1 - \frac{1}{K^2} p_t \right) (1 - p_t) \right)^{N-1}, \quad (7)$$

where $K=1$ means the antenna is omni-directional. $P_{\text{suc}}^{u-v} \approx 2p_t(1-p_t)^{2N-1}$ and the best transmission probability is $p_t^{\text{opt}} = 1/(2N)$ ^[25]. When the beam width is small, the optimal value can be set as $p_t^{\text{opt}} = 0.5$ through simulation.

3.4.2 Analysis of Upper and Lower Bounds of Time Slot Mean

When K is a constant, the probability of node u finding any neighbor v in a time slot is a function of N and p_t , which can be expressed as $F_p^{u-v}(N, p_t)$. In ISAC, the central node can update the antenna beam list with the information obtained by radar detection. Because of that, K also affects the probability of success and function $F_p^{u-v}(N, p_t)$ is rewritten as $F_p^{u-v}(N, p_t, K)$. P_{sud}^{u-v} in $E_u^{\text{all}}(N-1)$ ^[28] is changing. The expectation number of slots required for node u to find a new neighbor E_1 ^[28] is also changing. As the neighbor discovery progresses, K gradually becomes smaller and the discovery probability becomes larger.

$$E_i^{\text{all}}(N-1) = \sum_{i=1}^{N-1} \frac{1}{(N-i)P_{\text{sud}}^{u-v}}, \quad (8)$$

$$E_1 = \frac{1}{(N-1)P_{\text{sud}}^{u-v}}. \quad (9)$$

The range of the beams that can be selected for any node i is $x \in [K - N_0^E, K]$. The average number of empty beams is $N_0^E = N(K, N, 0)$, where N is the number of neighbors and K is the number of beams.

The second type of Stirling number $S_2(n, m)$ represents the number of schemes in which n different elements are divided into m sets. According to the principle of tolerance and exclusion, we can get

$$S_2(n, m) = \frac{1}{m!} \sum_{k=0}^m (-1)^2 \binom{m}{k} (m-k)^n. \quad (10)$$

The second type of Stirling recurrence formula is

$$S_2(n, m) = m \cdot S_2(n-1, m) + S_2(n-1, m-1), \quad 1 \leq m \leq n-1. \quad (11)$$

The boundary conditions are

$$\begin{cases} S_2(n, n) = 1, & n \geq 0 \\ S_2(n, 0) = 0, & n \geq 1. \end{cases} \quad (12)$$

We bring $S_2(n, n) = 1$ into Eq. (11) to get

$$\sum_{k=0}^m (-1)^k \binom{m}{k} (m-k)^n = m! \quad (13)$$

When $N \leq K$, N_0^E is expressed as

$$N(K, N, 0) = \sum_{h=0}^{K-1} h \times C_K^h (K-h)! \times S_2(N, K-h) / K^N \quad (14)$$

$$N \geq K,$$

where C_K^h represents the selection of $h \in [K-N, K-1]$ from K beams as empty beams, the fraction means putting the remaining N neighbors into $K-h$ beams and ensuring that no beam is empty, and K^N means the number of schemes in which N neighbors are put into K beams.

When $N > K$, the range of the empty beam is $[1, K-1]$ and N_0^E is

$$N(K, N, 0) = \sum_{h=K-N}^{K-1} h \times \binom{K}{h} E_{K-h}(N) / K^N, \quad N < K, \quad (15)$$

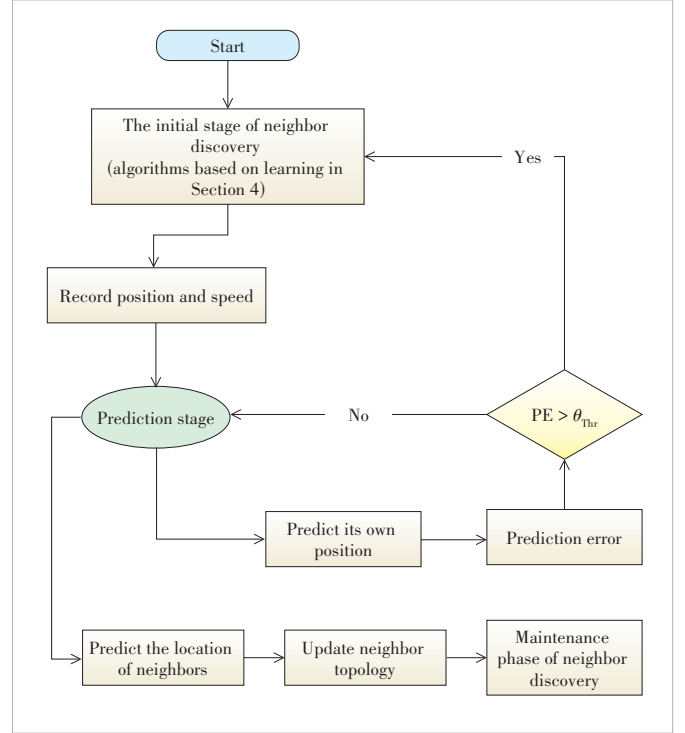
where

$$E_m(j) = \begin{cases} m^j - \sum_{l=1}^{m-1} \binom{m}{l} E_{m-l}(j), & j \geq m \\ 0, & j < m. \end{cases} \quad (16)$$

According to the algorithm, once the node finds that the beam is empty, it does not send Hello messages to the beam afterwards. Therefore, K in Eq. (7) is changing. At the beginning of neighbor discovery, when the central node randomly selects in each slot, the probability of finding an empty beam is the largest, which is $P_{\text{dis},0} = N_0^E / K$. When an empty beam is found, the probability of finding a new empty beam is $P_{\text{dis},1} = (N_0^E - 1) / (K - 1)$. By analogy, the probability of finding the last empty beam is $P_{\text{dis},N_0^E} = 1 / (K - N_0^E + 1)$.

We construct function $f(t, P_{\text{dis}}) = (1 - P_{\text{dis}})^{t-1} P_{\text{dis}}$ to represent the probability of beam quality change in t time slots, where P_{dis} represents the probability of selecting an empty beam in the current time slot. When the beam is fixed at $x = K - N_0^E$, the velocity reaches its peak. When $x = K$, the time is the longest. As shown in Fig. 6, we can give more precise upper and lower bounds according to the characteristics of the discovery process.

It can be seen intuitively from Eq. (17) that $E_i^{\text{all}}(N)$ and P_{sud}^{u-v} are inversely proportional, so the lower bound of $E_i^{\text{all}}(N)$ is the upper bound of P_{sud}^{u-v} . The average value of the empty beam is rounded to $N_{\text{ceil}} = \lceil N_0^E \rceil$. Then in this time slot, time T_x^{dis} for each beam x is set to be the same and the average time $E_i^{\text{all}}(N)$ is obtained. P_{sud} is revised as



▲ Figure 6. Flow chart of neighbor discovery based on Kalman filter

$$P_{\text{upper}}^{u-v} = \frac{1}{N_0^E + 1} \sum_{x=K-N_0^E}^K \frac{1}{2x^2} \left(\left(1 - \frac{1}{x^2}\right) \times \frac{1}{2} + \left(1 - \frac{1}{2x^2}\right) \times \frac{1}{2} \right)^{N-1} \quad (17)$$

The mathematical upper bound of the neighbor discover time $E_i^{\text{all}}(N)$ is the lower bound of P_{sud}^{u-v} . The number of possible empty beams in the entire ND process of a node is N_0^E . When K in P_{sud}^{u-v} is unchanged, the time is the longest, which is the upper bound of the time. In this section, to get an accurate upper bound, in any time slot, set time T_x^{dis} of these $(N_0^E - 2)$ beams appearing to be the same. It is equivalent to dividing the time of the larger discovery probability to the smaller discovery probability, so as to obtain the upper bound of the time of neighbor discovery. P_{sud} can be expressed as

$$P_{\text{lower}}^{u-v} = \frac{1}{N_0^E - 2} \sum_{x=K-N_0^E+1}^K \frac{1}{2x^2} \left(\left(1 - \frac{1}{x^2}\right) \times \frac{1}{2} + \left(1 - \frac{1}{2x^2}\right) \times \frac{1}{2} \right)^{N-1} \quad (18)$$

4 Neighbor Maintenance Method Based on Kalman Filter

4.1 Flight Model of UAV

The initial speed and direction of a UAV are initialized

with a random pattern^[29]. In a two-dimensional scene, the physical movement of the UAV is represented as vector $X_k = [x \ V_x \ y \ V_y]$. In a three-dimensional scene, it can be represented as $X_k = [x \ V_x \ y \ V_y \ z \ V_z]$. Fig. 7 shows the movement of two UAVs. The two-dimensional scene is a flat circle, and the three-dimensional scene is a cross-cut circle. Both of them have a radius of R_s .

The predefined time interval is T_{th} (PTI)^[30], which represents the time when B leaves the one-hop communication range of A.

$$T_{th} = \frac{2R_s}{E[V']}, \quad (19)$$

where $E[V']$ represents the average value of relative speed.

In Fig. 7, V_1 and V_2 obey the uniform distribution on $[L_1, L_2]$ and θ_1 and θ_2 obey the uniform distribution on $[0, \pi]$. They satisfy $V' = V_1 \cos \theta_1 + V_2 \cos \theta_2$. The expression of the probability density function of V_1 is

$$f(V_1) = \begin{cases} \frac{1}{(L_2 - L_1)} & L_1 \leq V_1 \leq L_2 \\ 0 & \text{others} \end{cases}. \quad (20)$$

The function $f(D)$ is the probability density of $D = \cos \theta_1$, and its expression is

$$f(D) = \begin{cases} \frac{2}{\pi \sqrt{1 - D^2}} & 0 \leq D \leq 1 \\ 0 & \text{others} \end{cases}. \quad (21)$$

V_1 and D are distributed independently, so the joint probability density function is the product of the two, denoted as

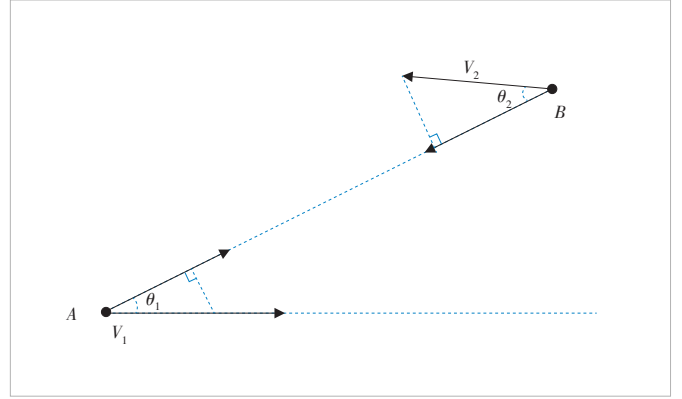
$$f(V_1, D) = \begin{cases} \frac{2}{\pi(L_2 - L_1) \sqrt{1 - D^2}} & 0 \leq D \leq 1, L_1 < V_1 < L_2 \\ 0 & \text{others} \end{cases}. \quad (22)$$

Given that $E[V'] = 2E[V]$, V_1 and θ_1 are taken as examples to find $E[V]$, and the process is

$$E[V] = \int_{L_1}^{L_2} \int_0^1 V_1 D f(V_1, D) dV_1 dD = \int_{L_1}^{L_2} \int_0^1 V_1 D \frac{2}{\pi(L_2 - L_1) \sqrt{1 - D^2}} dV_1 dD = \frac{(L_2 + L_1)}{\pi}. \quad (23)$$

We put the result of Eq. (23) into Eq. (19) to get

$$T_{th} = \frac{\pi R_s}{(L_2 + L_1)}. \quad (24)$$



▲ Figure 7. Relative movement of two nodes

4.2 Kalman Filter Model

The Kalman filter estimates the value of variables based on observations, noise and errors, which is more accurate than the estimation based on observations^[29].

We assume that each UAV saves $N + 1$ quadruples $\langle \text{ID} \ V \ P \ T_k \rangle$, where V and P represent the speed and position of the UAV respectively, and T_k is the timestamp. The state is represented as $X_k = [V_{T_k} \ P_{T_k}]$.

$$X_{k+1} = A_k X_k + w_k, \quad (25)$$

$$Z_k = H_k X_k + v_k. \quad (26)$$

In Eq. (25), X_k is the real state at time k , X_{k+1} is the predicted state, and A_k is the 4×4 state transition matrix. That is $X_k \xrightarrow{A_k} X_{k+1}$, where Δt can be set according to actual conditions. The process noise w_k obeys Gaussian distribution of $N(0, Q)$. In Eq. (26), Z_k represents the estimated position vector, H_k is the observation matrix, and observation noise v_k obeys the Gaussian distribution of $N(0, R)$.

Covariance Q and R can be obtained through empirical analysis, and the settings in this section are as

$$Q = 0.01 \times E_{4 \times 4}, \quad (27)$$

$$R = 10 \times E_{2 \times 2}, \quad (28)$$

$$A_k = \begin{bmatrix} 1 & \Delta t & 0 & 0 \\ 0 & 1 & 0 & 0 \\ 0 & 0 & 1 & \Delta t \\ 0 & 0 & 0 & 1 \end{bmatrix}, \quad (29)$$

$$H_k = \begin{bmatrix} 1 & 0 & 0 & 0 \\ 0 & 0 & 1 & 0 \end{bmatrix}. \quad (30)$$

At the prediction stage^[29], the state value \hat{X}'_k at the next moment is estimated according to

$$\hat{X}'_k = A_{k-1} \hat{X}_{k-1}. \quad (31)$$

1) Prediction and estimation

The covariance matrix P'_k is predicted and estimated according to

$$P'_k = A_k P_{k-1} A_k^T + Q_{k-1}. \quad (32)$$

2) Stage update^[29]

The optimal Kalman gain is calculated by

$$K_k = P'_k H^T (H_k P'_k H^T + R)^{-1}. \quad (33)$$

The estimated state \hat{X}'_k is updated by

$$\hat{X}'_k = \hat{X}'_k + K_k (Z_k - H_k \hat{X}'_k). \quad (34)$$

The estimated covariance matrix P_k is updated by

$$P_k = (I - K_k H_k) P'_k. \quad (35)$$

\hat{X}'_k is then used to predict the next moment, so that the prediction is more accurate^[30].

3) Error forecast

In order to measure the effect of Kalman filtering, position error (PE) is

$$PE = \sqrt{\left[(y'_i - y_i)^2 + (x'_i - x_i)^2 \right]}, \quad (36)$$

where (x_i, y_i) is the true value and (x'_i, y'_i) is the predicted value.

The right-angled side R_l conforms to the uniform distribution $R_l \sim U[0, R_s \cos(\alpha/2)]$, and the mathematical expectation is

$$E_{R_b} = R_s \cos(\alpha/2) / 2, \quad (37)$$

where the value of the bottom R_b is the error threshold $\theta_{Thr} = 2E_{R_b} \times \tan(\alpha/2)$.

4.3 Switching Mechanism Between Initialization and Maintenance Phases

In the maintenance phase, after the node gets a highly accurate topology, a stop mechanism is joined^[4]. The difference between the maintenance and stop mechanisms^[4] is that the beam selection probability changes with the number of undiscovered neighbors.

The size of the Hello packet can be changed according to the needs of the protocol. For example, node ID (4 B), node lo-

cation (usually two integers, 8 B), speed (1 B) and direction (1 B) can be added and deleted as needed^[30]. In the initialization phase, the Hello packet contains ID, speed, and location information. In the maintenance phase, to reduce the data overhead, neighbor information can be obtained through prediction, and the Hello packet only contains the ID.

Next, the outgoing and incoming of UAVs are explored during the maintenance period of neighbor discovery^[31].

UAV i calculates the distance R_{i-j} from neighbor j . When $R_{i-j} > R_s$, the UAV determines that the neighbor has left and no longer sends Hello packets, which can reduce bandwidth consumption^[31].

In each time slot, UAV predicts its own position. When $PE > \theta_{Thr}$, it will switch to the initial stage of neighbor discovery. When the neighbor maintenance phase continues to be greater than the predefined time interval (PTI), even if $PE < \theta_{Thr}$, it will also switch to the initial phase. In addition, to prevent the emergence of extreme situations, a random scan factor P_{arbit} is added to optimize the algorithm. All directions are arbitrarily selected with a small probability, which trades discovery time for accuracy. The parameters θ_{Thr} , PTI and P_{arbit} all have an impact on the protocol performance. If the random scan factor P_{arbit} is too small, the neighbors that accidentally enter will not be discovered. If P_{arbit} is too large, the discovery time of the neighbor maintenance phase is prolonged. These parameters need to be set according to the actual scene^[30]. The distance prediction error threshold θ_{Thr} and the time interval threshold T_{th} will have an impact on the performance of the two-phase handover. First of all, if θ_{Thr} is too large, the predicted topology in the maintenance phase is not accurate enough, which prolongs the discovery time of the maintenance phase. If θ_{Thr} is too small, it will enter the initial stage too frequently, which will increase data overhead. Secondly, if θ_{Thr} is too large, the UAV may still not enter the initialization phase, but the actual topology has changed, which will also increase the average discovery time. If T_{th} is too small, it will frequently enter the initial phase and increase data overhead.

5 Simulation Results and Analysis

5.1 Neighbor Discovery Algorithm Based on Learning Automata

Discovery time $E_i^{all}(t)$ and speed $V_i^{all}(t)$ are used as measurement standards. Some studies use neighbor convergence of 70%^[11] as indicators to measure the algorithm performance. However, the algorithm based on purely directional Completely Random Algorithms (CRA) has a long tail problem^[11]. In this section, to fully see the effect of the algorithm, 100% convergence of the nodes in the network is used as the criterion.

Each parameter influences the performance of the algorithm. Function $E_i^{all}(t) = f(N, K, \eta, \varpi, \nu)$ represents the discovery time of the algorithm based on the LA, where N is the

network size, K is the number of beams, η is the radar communication ratio, and $\varpi = \{\gamma_1, \gamma_2, \mu\}$ and ν are the reward and punishment factors. In order to eliminate the influence of ν , we set $\nu = 0.01$. Next, the controlled variable methods are used to perform multiple simulations and the average value is taken. In order to better analyze the influence of the parameters, Table 1 shows the parameter values obtained through multiple simulation observations.

Fig. 8 illustrates the relationship between the radar communication ratio η and the convergence time $E_i^{\text{all}}(t)$. When $K = 36$, for the same topology size N , the larger the value of η , the smaller the time. The reason is that the larger η is, the more accurate the information obtained by the node in each time slot is. The action probability distribution obtained by iteration A can maximize the success rate of neighbor discovery in each slot. For $N = 30$, compared with classic CRA, when $\eta = \{\eta_1, \eta_2, \eta_3, \eta_5\}$, the efficiency increases by 13.5%, 30.9%, 57.9%, and 65.2%, respectively.

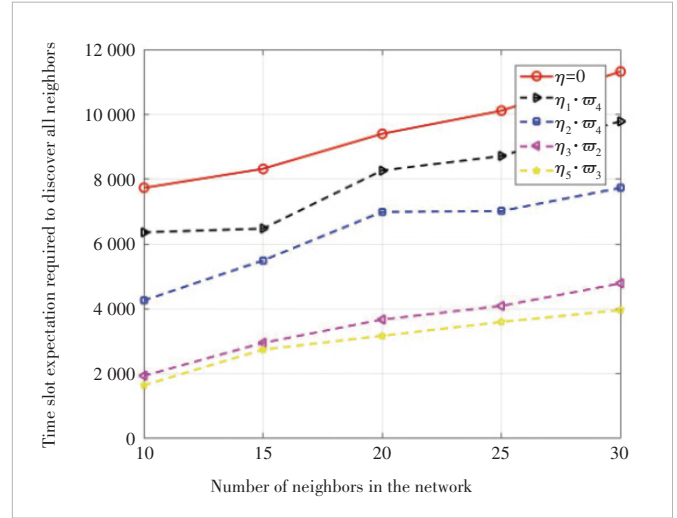
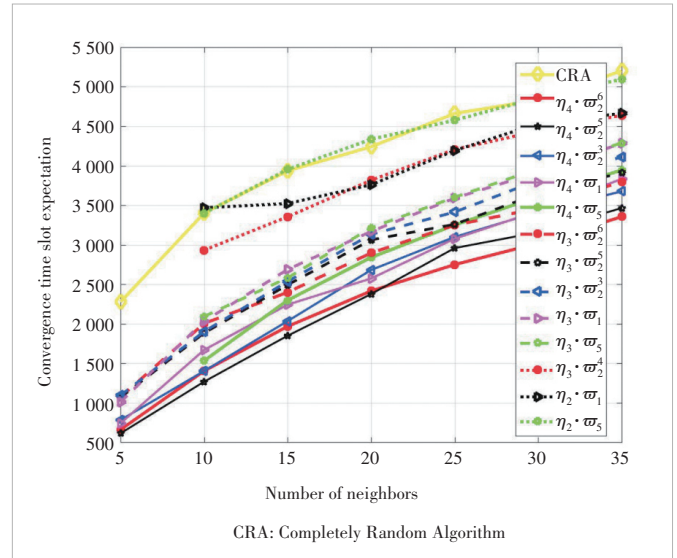
Fig. 9 shows the effect of the reward and punishment factor ϖ on $E_i^{\text{all}}(t)$ and the velocity when N and $K = 24$ are fixed. Given $\gamma_1, \gamma_2, \mu \in [0, 1]$, the simulation parameters cannot be enumerated due to the complex and diverse combinations of parameters. When $\mu/\gamma_1 = 2$, let the set $\varpi_2 = \{\varpi_2^6, \varpi_2^5, \varpi_2^4, \varpi_2^3\}$, $\gamma_1 = 0.1, \mu = 0.2, \gamma_2 = 0.6$ in ϖ_2^6 , etc. Comparing the curves longitudinally, it can be seen that the optimal values of ϖ_{opt} are different in different scenarios. The simulation results also show that the algorithm can maintain a better performance effect than the classic ND algorithm in actual scenarios.

Fig. 10 shows the influence of the beam change on time $E_i^{\text{all}}(t)$ when $N = 10$. For the ISAC signal that shares the waveform, its power is both the communication power and the radar power. Under normal circumstances, the radar signal has two path losses, while the communication has only one path loss. Without tuning parameters, the detection range of radar is generally about half of that of communication^[32]. It is more practical to set η to 0.5 and 0.6. Set $\varpi_{\text{opt}} = \varpi_2^4$. Next, the first three sets of data in the histogram are analyzed. When $K = 36$, the data are (8 166, 6 099, 5 558). When $K = 10$, the data are (692.4, 591.2, 560.4). It can be calculated that compared with CRA, the narrower the beam, the more obvious the efficiency improvement. When the number of neighbors is fixed, the narrow beam means that probability P_{plen}^i is small, and the probability of learning correct is high.

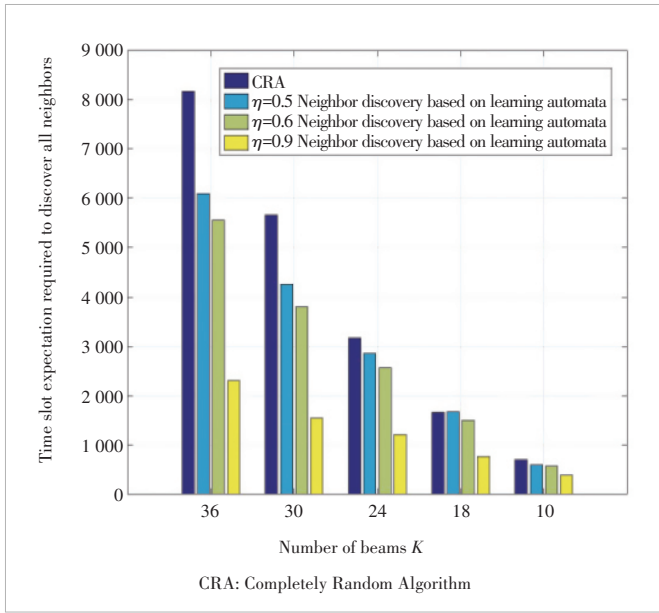
Convergence (discovery) rate $V_i^{\text{all}}(t)$ is quantitatively analyzed from a computational perspective here. When the number of beams is $K = 36$ and the number of neighbors is $N = 25$, a different η is set, and the reward and punishment factor is set to $\varpi_{\text{opt}} = \varpi_2^6$. Then the success rate of neighbor discovery is observed under different time slot consumption (the ratio of successfully discovered neighbors to all neighbors). Reciprocal k' of the slope of the curve is used to repre-

Table 1. Parameter value setting

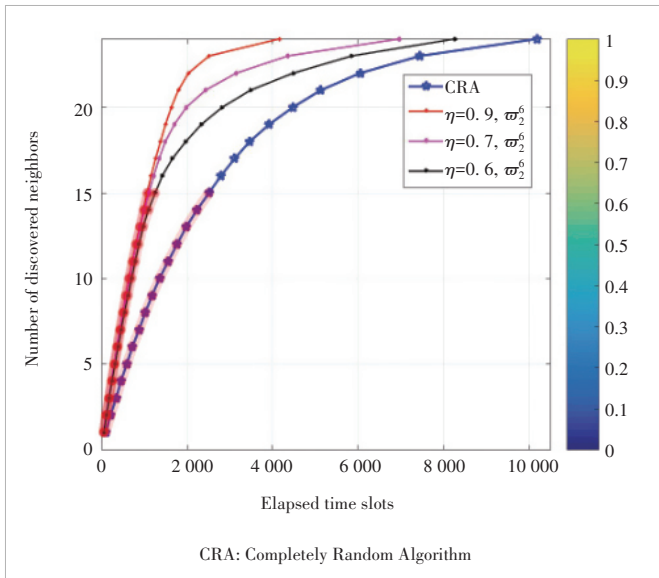
η	ϖ
$\eta_1 = 0.3$	$\varpi_1 = (0.2, 0.3, 0.2)$
$\eta_2 = 0.5$	$\varpi_2 = (0.1, 0.4, 0.1)$
$\eta_3 = 0.7$	$\varpi_3 = (0.1, 0.2, 0.05)$
$\eta_4 = 0.8$	$\varpi_4 = (0.1, 0.2, 0.1)$
$\eta_5 = 0.9$	$\varpi_5 = (0.1, 0.3, 0.2)$


Figure 8. The relationship between network size and time slot expectations

Figure 9. Relationship between the coverage time slot expectation and the number of beams

sent $V_i^{\text{all}}(t)$. The highlighted part in Fig. 11 is the time period when the central node discovers 62.5% of neighbors. The rate of the learning-based algorithm is $k'_{\text{Learn}} = 78.9$ (slot/a new neighbor). The rate of the traditional CRA is $k'_{\text{class}} = 192.3$ (slot/a new neighbor). The discovery rate is in-



▲ Figure 10. Trends of neighbors discovered in different algorithms over time



▲ Figure 11. Comparison of discovery efficiency in the same node density network

creased by about 60%. In addition, the discovery of the last neighbor takes time slots respectively. That is to say, the algorithm in Section 3 improves the convergence speed, but there is still a long tail problem.

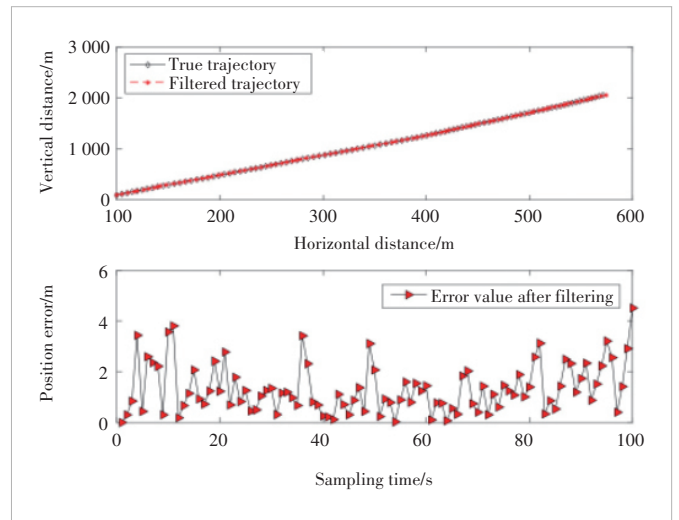
5.2 Neighbor Maintenance Methods Based on Kalman Filter

1) Analysis of forecast errors: Fig. 12 shows the PE at different prediction moments. In the simulation, the horizontal velocity is 5 m/s, the vertical velocity is 20 m/s, and the prediction period is 1 s^[33]. From a numerical point of view, the error

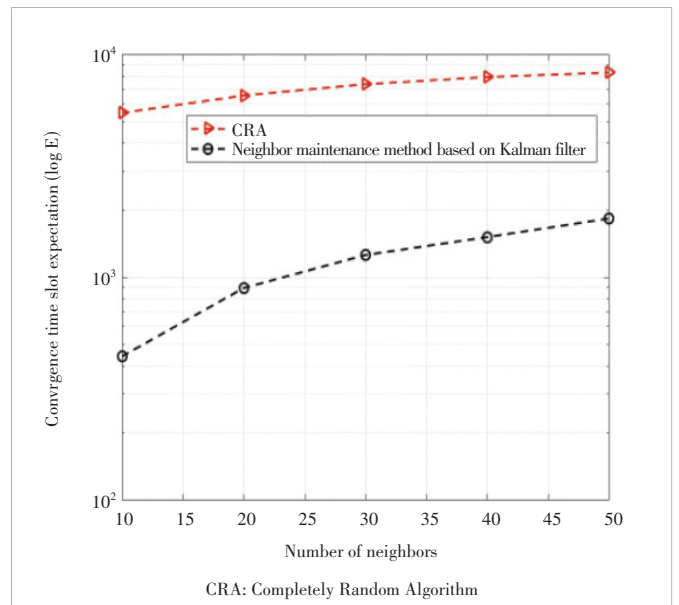
is about 5 m, which shows that the prediction result based on the Kalman filter has a higher accuracy rate. The specific reason is that the filtering model predicts by the estimated \hat{X}_k at the next moment. If we consider the influence of actual noise, the prediction will be more accurate.

2) Analysis of discovery efficiency: In Fig. 13, $N \in [10, 50]$ nodes are randomly scattered in an area of 2 km \times 2 km. The number of beams is 30. Comparing the two curves, the algorithm in Section 4 can greatly reduce the network delay.

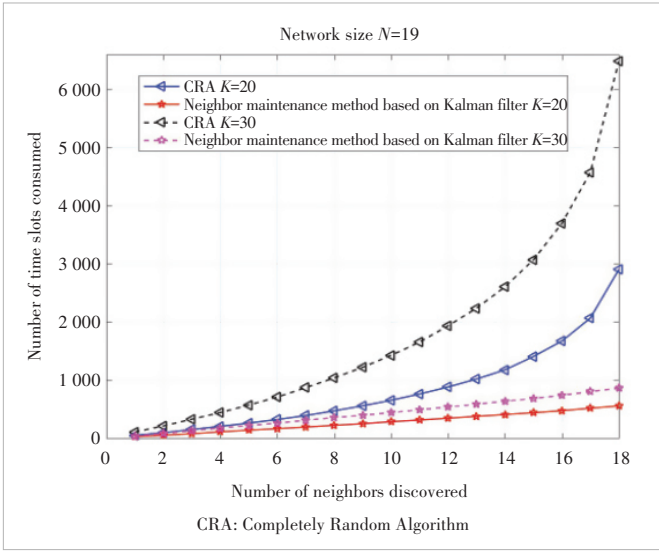
The following part studies the ND convergence process of any node i . In Fig. 14, the topology size is fixed at 19, and K is fixed at 30 and 20. The meaning of the ordinate is time interval $E_i^1(t)$ between the discovery of two new neighbors. Ana-



▲ Figure 12. Position error after Kalman filtering



▲ Figure 13. Comparison of convergence time of different algorithms in different network sizes



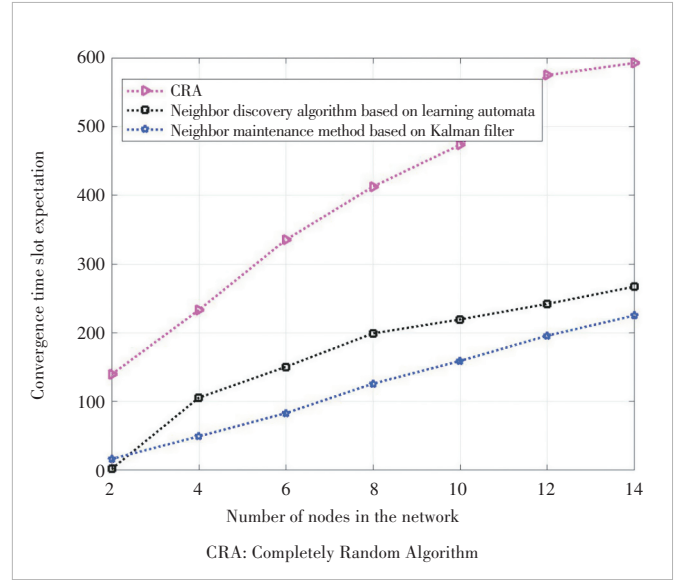
▲ Figure 14. Comparison of discovery efficiency in the same node density network

lyze the “★” and “△” curves longitudinally from the slope of the curve. The filtering-based algorithm represented by the “★” curve maintains a high ND rate throughout the process. The curve can be fitted to a straight line, which means that the long tail problem of neighbor discovery is overcome. In $K = 30$, when the filtering-based algorithm converges to 100%, the CRA algorithm only converges about 37%. Figs. 13 and 14 show that adding the filtering model not only increases the discovery speed but also shortens the time. The reason is that before the ND phase starts, the node has predicted a topology through the Kalman filter model as prior knowledge. Based on this prior knowledge, nodes can scan the targeted to shorten the discovery time.

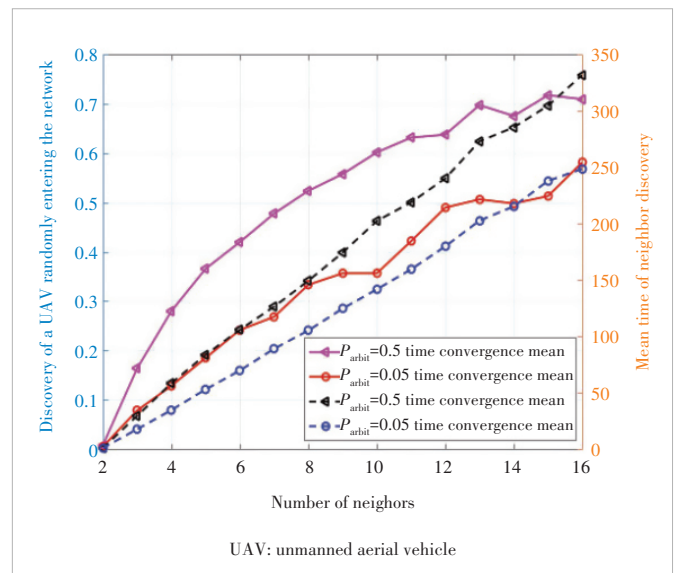
3) Impact of mobility: In a three-dimensional scene, the UAV applies a phased array antenna to scan the entire sphere. To simplify the performance research of the proposed algorithm, a scene where a single UAV is in the center and other UAVs are uniformly and randomly distributed is observed. The following part studies probability P_{dis}^x of any UAV being discovered after entering the network topology in the neighbor maintenance phase.

Fig. 15 is the comparison of the three neighbor discovery strategies. For example, when $N = 8$, compared with CRA, the efficiency of filtering-based algorithms is increased by 69.6%, and compared with learning-based algorithms by 36.9%. In addition, from the perspective of slope, $k_{KF} < k_{LA} < k_{CRA}$, the node sensitivity is overcome to a certain extent. Compared with the classic CRA, the algorithm proposed in Section 4 avoids the invalid scanning of blank areas and reduces the time. Compared with the LA scheme based on time slots to obtain prior knowledge, the algorithm in Section 3 obtains all prior knowledge before the neighbor discovery starts, which can improve the timeliness. In addition, because the nodes

(beams) that have been discovered no longer occupy communication resources, the sensitivity of the nodes is overcome to a certain extent. In Fig. 16, the left and right ordinates are P_{dis}^x and $E_i^{all}(t)$ respectively. It can be seen that under the same UAV density, P_{dis}^x and $E_i^{all}(t)$ increase with the increase of P_{arbit} . The reason is that the increase of the random factor P_{arbit} (in a mobile scene, an optimization factor that increases the probability that a random UAV enters the network topology is found) increases the scanning probability of other beams, which increases the probability of random UAVs discovery chances. At the same time, it also increases the prob-



▲ Figure 15. Comparison of convergence time of different neighbor discovery strategies



▲ Figure 16. Probability of discovery and the average time slot for different numbers of neighbors

ability of invalid scanning, which in turn increases the time of the entire network topology construction.

6 Conclusions

This paper proposes the sensing and communication integrated intelligent ND algorithms for UAV networks. Reinforcement learning is introduced to solve the problem that the radar detection range is not equal to the communication range in the integration. Simulation results show that the algorithm based on LA can increase the time efficiency by up to 32% compared with the classic scan-based algorithm, when the radar communication ratio $\eta = 0.6$. This paper also considers the high mobility of UAVs and designs an efficient neighbor maintenance algorithm that predicts the node motion through the Kalman filter. In the current work, we only introduce a relatively simple LA algorithm to solve the problem of neighbor discovery in the UAV network. In the future, more learning algorithms can be introduced in combination with specific scenarios to improve the efficiency of neighbor discovery.

References

- [1] LI J M, PENG L X, YE Y L, et al. A neighbor discovery algorithm in network of radar and communication integrated system [C]//Proc. IEEE 17th International Conference on Computational Science and Engineering. IEEE, 2014: 1142 - 1149. DOI: 10.1109/CSE.2014.224
- [2] JI D N, WEI Z Q, CHEN X, et al. Radar-communication integrated neighbor discovery for wireless ad hoc networks [C]//Proc. 11th International Conference on Wireless Communications and Signal Processing (WCSP). IEEE, 2019: 1 - 5. DOI: 10.1109/WCSP.2019.8927896
- [3] LIU N X, PENG L X, XU R H, et al. Neighbor discovery in wireless network with double-face phased array radar [C]//Proc. 12th International Conference on Mobile Ad-Hoc and Sensor Networks (MSN). IEEE, 2016: 434 - 439. DOI: 10.1109/MSN.2016.080
- [4] WEI Z Q, HAN C Y, QIU C, et al. Radar assisted fast neighbor discovery for wireless ad hoc networks [J]. IEEE access, 2019, 7: 176514 - 176524. DOI: 10.1109/ACCESS.2019.2950277
- [5] HAN Y, EKICI E, KREMO H, et al. Automotive radar and communications sharing of the 79-GHz band [C]//Proc. First ACM International Workshop on Smart, Autonomous, and Connected Vehicular Systems and Services. ACM, 2016: 6 - 13. DOI: 10.1145/2980100.2980106
- [6] EL KHAMLICHI B, NGUYEN D H N, EL ABBADI J, et al. Collision-aware neighbor discovery with directional antennas [C]//Proc. International Conference on Computing, Networking and Communications (ICNC). IEEE, 2018: 220 - 225. DOI: 10.1109/ICNC.2018.8390323
- [7] GAO M J, SHEN R J, MU L H, et al. An anti-collision neighbor discovery protocol for multi-node discovery [C]//Proc. 11th International Conference on Wireless Communications and Signal Processing (WCSP). IEEE, 2019: 1 - 5. DOI: 10.1109/WCSP.2019.8927864
- [8] SUN G B, WU F, GAO X F, et al. Time-efficient protocols for neighbor discovery in wireless ad hoc networks [J]. IEEE transactions on vehicular technology, 2013, 62(6): 2780 - 2791. DOI: 10.1109/TVT.2013.2246204
- [9] BURGHAL D, TEHRANI A S, MOLISCH A F. On expected neighbor discovery time with prior information: modeling, bounds and optimization [J]. IEEE transactions on wireless communications, 2018, 17(1): 339 - 351. DOI: 10.1109/TWC.2017.2766219
- [10] WANG Y H, PENG L X, XU R H, et al. A fast neighbor discovery algorithm based on Q-learning in wireless ad hoc networks with directional antennas [C]//Proc. IEEE 6th International Conference on Computer and Communications (ICCC). IEEE, 2020: 467 - 472. DOI: 10.1109/ICCC51575.2020.9345296
- [11] EL KHAMLICHI B, EL ABBADI J, ROWE N W, et al. Adaptive directional neighbor discovery schemes in wireless networks [C]//Proceedings of International Conference on Computing, Networking and Communications (ICNC). IEEE, 2020: 332 - 337. DOI: 10.1109/ICNC47757.2020.9049819
- [12] BAI W, XU Y H, WANG J L, et al. Cognitive neighbor discovery with directional antennas in self-organizing IoT networks [J]. IEEE Internet of Things journal, 2021, 8(8): 6865 - 6877. DOI: 10.1109/JIOT.2020.3037067
- [13] ZHU L N, GU W Y, YI J J, et al. On mobility-aware and channel-randomness-adaptive optimal neighbor discovery for vehicular networks [J]. IEEE Internet of Things journal, 2021, 8(8): 6828 - 6839. DOI: 10.1109/JIOT.2020.3036251
- [14] KAROWSKI N, WILLIG A, WOLISZ A. Cooperation in neighbor discovery [C]//Proc. Wireless Days. IEEE, 2017: 99 - 106. DOI: 10.1109/WD.2017.7918123
- [15] LUO Y, DANG J, SONG Z X, et al. Compressed sensing algorithm for neighbour discovery in mobile ad hoc networks [J]. IET communications, 2019, 13(12): 1781 - 1786. DOI: 10.1049/iet-com.2018.5127
- [16] ASTUDILLO G, KADOCH M. Neighbor discovery and routing schemes for mobile ad-hoc networks with beamwidth adaptive smart antennas [J]. Telecommunication systems, 2017, 66(1): 17 - 27. DOI: 10.1007/s11235-016-0268-x
- [17] CHEN L, LI Y, VASILAKOS A V. On oblivious neighbor discovery in distributed wireless networks with directional antennas: theoretical foundation and algorithm design [J]. IEEE/ACM transactions on networking, 2017, 25(4): 1982 - 1993. DOI: 10.1109/TNET.2017.2673862
- [18] LIAO Y L, PENG L X, XU R H, et al. Neighbor discovery algorithm with collision avoidance in ad hoc network using directional antenna [C]//Proc. IEEE 6th International Conference on Computer and Communications (ICCC). IEEE, 2020: 458 - 462. DOI: 10.1109/ICCC51575.2020.9344952
- [19] ZHANG Z S. Performance of neighbor discovery algorithms in mobile ad hoc self-configuring networks with directional antennas [C]//Proc IEEE Military Communications Conference (MILCOM 2005). IEEE, 2005: 3162 - 3168. DOI: 10.1109/MILCOM.2005.1606143
- [20] GAMMARANO N, SCHANDY J, STEINFELD L. Q-SAND: a quick neighbor discovery protocol for wireless networks with sectored antennas [C]//Proc. Ninth Argentine Symposium and Conference on Embedded Systems (CASE). IEEE, 2018: 19 - 24
- [21] ZHANG Z S, RYU B, NALLAMOTHU G, et al. Performance of all-directional transmission and reception algorithms in wireless ad hoc networks with directional antennas [C]//Proc. MILCOM 2005 - 2005 IEEE Military Communications Conference. IEEE, 2005: 225 - 230. DOI: 10.1109/MILCOM.2005.1605690
- [22] RUSSELL A, VASUDEVAN S, WANG B, et al. Neighbor discovery in wireless networks with multipacket reception [J]. IEEE transactions on parallel and distributed systems, 2015, 26(7): 1984 - 1998. DOI: 10.1109/TPDS.2014.2321157
- [23] SHEN Z, JIANG H, DONG Q K, et al. Energy-efficient neighbor discovery for the Internet of Things [J]. IEEE Internet of Things journal, 2020, 7(1): 684 - 698. DOI: 10.1109/JIOT.2019.2949922
- [24] SARAEREH O A, KHAN I, LEE B M. An efficient neighbor discovery scheme for mobile WSN [J]. IEEE access, 2019, 7: 4843 - 4855. DOI: 10.1109/ACCESS.2018.2886779
- [25] ZHANG Z S, LI B. Neighbor discovery in mobile ad hoc self-configuring networks with directional antennas: algorithms and comparisons [J]. IEEE transactions on wireless communications, 2008, 7(5): 1540 - 1549. DOI: 10.1109/TWC.2008.05908
- [26] WUNDER M, LITTMAN M L, BABES-VROMAN M. Classes of multia-

- gent Q-learning dynamics with e-greedy exploration [C]//Proc. 27th International Conference on Machine Learning (ICML-10). ICML, 2010: 1167 - 1174
- [27] EL KHAMLI B, NGUYEN D H N, EL ABBADI J, et al. Learning automaton-based neighbor discovery for wireless networks using directional antennas [J]. *IEEE wireless communications letters*, 2019, 8(1): 69 - 72. DOI: 10.1109/lwc.2018.2855120
- [28] LIU L J, PENG L X, XU R H, et al. A neighbor discovery algorithm for flying ad hoc network using directional antennas [C]//Proc. 28th Wireless and Optical Communications Conference (WOCC). IEEE, 2019: 1 - 5. DOI: 10.1109/WOCC.2019.8770698
- [29] XU H, CHO J, LEE S. A predictive and synchronized neighborhood tracking scheme for mobile ad hoc networks [C]//Proc. 7th IEEE International Conference on Computer and Information Technology. IEEE, 2007: 429 - 434. DOI: 10.1109/CIT.2007.33
- [30] LIU C F, ZHANG G, GUO W S, et al. Kalman prediction-based neighbor discovery and its effect on routing protocol in vehicular ad hoc networks [J]. *IEEE transactions on intelligent transportation systems*, 2020, 21(1): 159 - 169. DOI: 10.1109/TITS.2018.2889923
- [31] ZHOU L, WANG H H, GUIZANI M. How mobility impacts video streaming over multi-hop wireless networks? [J]. *IEEE transactions on communications*, 2012, 60(7): 2017 - 2028. DOI: 10.1109/TCOMM.2012.051712.110165
- [32] MA H, WEI Z Q, CHEN X, et al. Performance analysis of joint radar and communication enabled vehicular ad hoc network [C]//Proc. IEEE/CIC International Conference on Communications in China (ICCC). IEEE, 2019: 887 - 892. DOI: 10.1109/ICCCChina.2019.8855937
- [33] OOMMEN B J, THATHACHAR M A L. Multiaction learning automata possessing ergodicity of the mean [J]. *Information sciences*, 1985, 35(3): 183 - 198. DOI: 10.1016/0020-0255(85)90049-0

Biographies

WEI Zhiqing (weizhiqing@bupt.edu.cn) received his BE and PhD degrees from Beijing University of Posts and Telecommunications (BUPT), China in 2010 and 2015, respectively. He is an associate professor with BUPT. He has authored one book, three book chapters, and more than 50 papers. His research interest is the performance analysis and optimization of intelligent machine networks. He was granted the Exemplary Reviewer of *IEEE Wireless Communications Letters* in 2017, the Best Paper Award of WCSP 2018. He was the Registration Co-Chair of IEEE/CIC ICC 2018 and the Publication Co-Chairs of IEEE/CIC ICC 2019 and IEEE/CIC ICC 2020.

ZHANG Yongji is an undergraduate student studying at the School of Information and Communication Engineering, Beijing University of Posts and Telecommunications (BUPT), China. His research interests include integrated perception, communication, computing, machine learning, etc.

JI Danna received her BE degree from University of Science and Technology Beijing (USTB), China and ME degree from the School of Information and Communication Engineering, Beijing University of Posts and Telecommunications (BUPT), China. Her research interests include wireless communication networking, joint radar and communication, etc.

LI Chenfei received her BE degree from Nankai University (NKU), China in 2021 and master's degree from Beijing University of Posts and Telecommunications (BUPT), China in 2024. Her research interests include integrated sensing and communication neighbor discovery and positioning.



A Survey on Task Scheduling of CPU-GPU Heterogeneous Cluster

ZHOU Yiheng¹, ZENG Wei², ZHENG Qingfang^{3,4},
LIU Zhilong^{3,4}, CHEN Jianping²

(1. University of Shanghai for Science and Technology, Shanghai 200093, China;

2. National Key Laboratory for Multimedia Information Processing, School of Computer Science, Peking University, Beijing 100871, China;

3. State Key Laboratory of Mobile Network and Mobile Multimedia Technology, Shenzhen 518055, China;

4. ZTE Corporation, Shenzhen 518057, China)

DOI: 10.12142/ZTECOM.202403010

<https://kns.cnki.net/kcms/detail/34.1294.TN.20240724.1705.003.html>,
published online July 29, 2024

Manuscript received: 2024-04-07

Abstract: This paper reviews task scheduling frameworks, methods, and evaluation metrics of central processing unit-graphics processing unit (CPU-GPU) heterogeneous clusters. Task scheduling of CPU-GPU heterogeneous clusters can be carried out on the system level, node-level, and device level. Most task-scheduling technologies are heuristic based on the experts' experience, while some technologies are based on statistic methods using machine learning, deep learning, or reinforcement learning. Many metrics have been adopted to evaluate and compare different task scheduling technologies that try to optimize different goals of task scheduling. Although statistic task scheduling has reached fewer research achievements than heuristic task scheduling, the statistic task scheduling still has significant research potential.

Keywords: CPU-GPU heterogeneous cluster; task scheduling; heuristic task scheduling; statistic task scheduling; parallelization

Citation (Format 1): ZHOU Y H, ZENG W, ZHENG Q F, et al. A survey on task scheduling of CPU-GPU heterogeneous cluster [J]. *ZTE Communications*, 2024, 22(3): 83 – 90. DOI: 10.12142/ZTECOM.202403010

Citation (Format 2): Y. H. Zhou, W. Zeng, Q. F. Zheng, et al., "A survey on task scheduling of CPU-GPU heterogeneous cluster," *ZTE Communications*, vol. 22, no. 3, pp. 83 – 90, Sept. 2024. doi: 10.12142/ZTECOM.202403010.

1 Introduction

Cloud computing platforms have become fundamental information infrastructures in modern society^[1]. A large number of computing servers in one cluster are connected by high-speed communication networks and provide high concurrency for users' remote accesses. central processing unit (CPU) and graphics processing unit (GPU) servers are dominantly used as core computing resources and virtualized into different computing resource pools to cater to various services. Computing tasks are calculated in the servers and provide various services at the Infrastructure as a Service (IaaS), Platform as a Service (PaaS), and Software as a Service (SaaS) levels^[2]. Tasks running on suitable servers can save cost and finish computing as soon as possible. Such task assignment is an important technology called task scheduling^[3]. Bad task scheduling will waste computing resources, cost more, and lead to a bad user experience^[4].

CPU servers are generally dominant in cloud platforms due

to their universal computing architecture. However, with the rapid development of artificial intelligence (AI) technologies, the GPU has been more and more widely used in heterogeneous clusters. Cluster heterogeneity is heterogeneous among computing servers, and between CPU and GPU within a server. In most cases, one cluster may have both the CPU server and the GPU server simultaneously. Consequently, task scheduling in CPU-GPU heterogeneous clusters is more complex and different^[5].

Good task scheduling should have the following characteristics:

- Maximizing clusters' system goals, e.g. throughput, energy cost, Quality of Service (QoS), etc;
- Balancing networks and storage with computing, and preventing network jams, long-time idleness, hot end, and so on;
- Assigning tasks to the best-matched CPUs or GPUs as far as possible.

2 Framework of Task Scheduling for Clusters

Task scheduling in cloud environments is a hot issue because of the prevalence of cloud computing. ARUNARANI et al. presented a comprehensive literature survey of task scheduling strategies and the associated metrics suitable for cloud

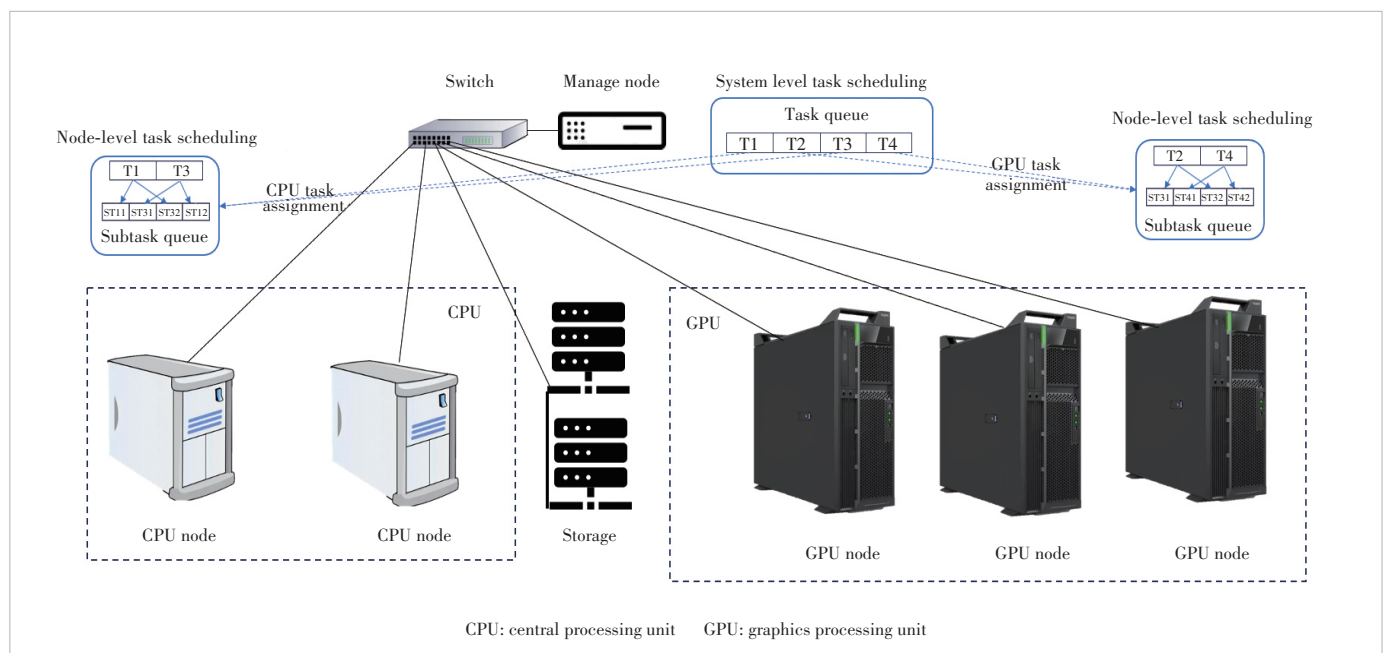
This work is supported by ZTE-University-Institute Fund Project under Grant No. IA20230629009.

computing environments^[3], in which the methods, applications, and parameter-based measures utilized for task scheduling are discussed. QoS, ant colony optimization, particle swarm optimization, genetic algorithms, multi-processors, fuzzy algorithms, clustering, deadline constraints, and cost-based algorithms were summarized and analyzed. As mentioned by the survey, from 2003 to 2018, a large number of studies on different techniques to solve scheduling problems were conducted. YANG et al. reviewed task scheduling algorithms for cloud computing^[6]. They divided scheduling algorithms into single-objective optimization algorithms and multi-objective task scheduling algorithms. They also analyzed the representative algorithms of each method, and compared and summarized the advantages and disadvantages of different algorithms. The authors in Ref. [7] categorized scheduling methods into traditional scheduling strategies, heuristic-based intelligent algorithms, emerging swarm intelligence algorithms, and hybrid algorithms, which accomplished a review of nature-inspired optimization techniques for scheduling tasks in cloud computing. SINGH et al. reviewed the meta-heuristics techniques for scheduling tasks in cloud computing^[4], and presented the taxonomy and comparative review of these algorithms. Methodical analysis was presented based on swarm intelligence and bio-inspired techniques^[4]. Since multi-objective optimization can deal with multiple conflicting goals, HOSSEINZADEH et al. presented a comprehensive survey and overview of the multi-objective scheduling approaches designed for various cloud computing environments^[8]. They classified the scheduling schemes into different types such as reducing execution cost, reducing makespan, re-

ducing SLA violation, and meeting deadlines, regarding applied multi-objective optimization algorithms. PRITY et al. provided a review of nature-inspired optimization techniques for scheduling tasks^[9]. A novel classification taxonomy and comparative review of these techniques were presented. JAWADE et al. gave a compact analytical survey on task scheduling^[10], which vividly explained different approaches utilized for task scheduling in diverse works.

Since AI has played an increasingly significant role, clusters with GPU become common and important. Amazon AWS, Microsoft Azure, Ali Cloud, Huawei Cloud, Baidu Cloud, and so forth, provide GPU computing services in their clouds. The hardware in such clouds is the CPU-GPU cluster. Tasks and devices in the CPU-GPU cluster are heterogeneous. PRADHAN et al. compared and described various task scheduling methods in heterogeneous cloud environments^[5]. They categorized scheduling algorithms into heuristics and hybrid methods. Heuristics algorithms were categorized into static and dynamic scheduling. Dynamic scheduling was then categorized into online and batch modes.

In general, task scheduling has two stages. System-level task scheduling is carried out in the first stage, whose goal is to optimize system performance, such as load balance, total computing efficiency, power consumption, system response, and temperature constraints. After tasks are assigned to nodes, task scheduling is carried out within the nodes in the second stage, whose goal is to optimize computing node performance, such as makespan, node computing efficiency, and node temperature. Fig. 1 shows the two-stage task scheduling framework.



▲ Figure 1. Two-stage task scheduling framework

3 Task Scheduling of CPU-GPU Heterogeneous Cluster

Compared with CPU clusters, the CPU-GPU cluster shows more heterogeneity in terms of architecture and task types. The task scheduling framework for CPU-GPU heterogeneous cluster is shown in Fig. 2.

In node-level task scheduling, tasks could be classified as CPU tasks and GPU tasks depending on the type of device used. In node inner task scheduling, GPU tasks can be assigned to different GPU devices since there are multiple GPUs in the node. Based on different strategies and methodologies, the task scheduling for the CPU-GPU heterogeneous clusters still can follow heuristic methods and statistic methods partition.

3.1 Heuristic Methods

Heuristic task scheduling relies on human-designed models to strategies and performs task assignments^[11-31]. Task assignments follow human-defined rules and are implemented by mathematical models and algorithms.

Early task scheduling was still based on the Hadoop framework^[11]. The hybrid map method minimized the overall MapReduce job execution time by using profiles collected from dynamic monitoring of the map task behavior.

Later, energy consumption was taken into consideration in task scheduling that focused on system-level energy optimization^[12]. The coarse-grained and fine-grained strategies of the Waterfall model were migrated into the scheme. The energy efficiency problem was translated into static power consumption loss and resource utilization problems. According to the heterogeneity of the tasks and task types, buddy allocation was proposed to improve energy efficiency. HUO et al. abstracted computing resources into many identical virtual CPUs and formulated the scheduling problem into an optimization problem with integer variables and nonlinear constraints^[12]. The energy

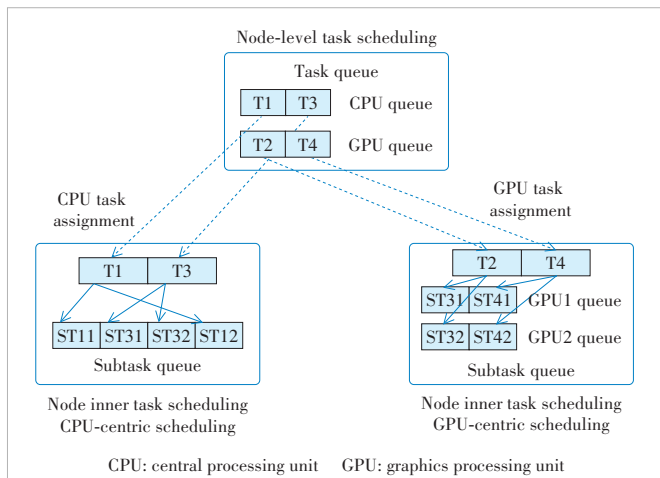
consumption minimization problem was formulated as an integer nonlinear programming problem, necessitating the determination of both a task assignment plan and a tailored resource allocation plan.

Similar to energy consumption, temperature becomes an optimized goal of task scheduling, especially for big clusters. Temperature, reliability, and computing performance were taken into account to reduce node performance differences and improve throughput per unit time in clusters^[13]. Temperature heat islands caused by slow nodes could be prevented by optimizing scheduling. CAO and WANG proposed a novel task-scheduling model for GPU clusters with temperature limitations^[14]. GPU and temperature were both considered during task scheduling. A state matrix was designed to monitor the GPU cluster and provide status information for the scheduler. Compared with the benchmark scheduling model, the loss of scheduling performance is more acceptable.

In order to deal with the problem of unbalanced workload, task classification and packing were both used to match CPU and GPU loads^[15]. Tasks were classified into six classes according to parallelism degrees and workloads, and then assigned to minimize the execution time^[16]. The approach is forming a good match between the task distribution and the architecture of the heterogeneous cluster through the task classifications and combinations. Besides task classification, CHEN et al. proposed a multi-granularity partition approach to synchronizing data flow graphs and task partition on CPU and GPU tasks^[17]. This method can satisfy load balancing and improve the utilization rate of the cluster. CI et al. designed an adaptive scheduling strategy to alleviate imbalance and under-utilization^[18], which logically treated all GPUs in the cluster as a whole. Every cluster node maintains a local information table of all GPUs. Once a GPU call request is received, a node will select a GPU to run the task adaptively based on this table. This strategy could significantly improve the GPU utilization rate and reduce mean waiting time.

Some task scheduling strategies focus on makespan optimization. This can maximize the parallel degree between CPUs and GPUs. Ref. [19] presented a scheduling algorithm using a generic methodology. The main idea of the approach is to determine an adequate partition of the set of tasks on the CPUs and the GPUs using a dual approximation scheme. ZHU et al. separated data into different data splits first, and then the scheduler assigned tasks to the CPU or GPU according to their computing resources^[20]. In this case, the data size becomes a measure of processing time.

Different types of tasks may be dominant in different clusters, and task-type-oriented scheduling strategies are then designed. A parallel version of the min-min heuristic method, which is an advanced parallel cellular genetic algorithm (CGA), was proposed for large instances of tasks in a cluster^[21]. For short tasks, SHAO et al. implemented a container-based batch computing system, which accepted and executed



▲ Figure 2. Task scheduling framework for CPU-GPU heterogeneous cluster

users' jobs through container images and specified configurations^[22]. A shortest-job-first-based scheduling policy was used to ensure the priority of the short tasks and to prevent long tasks from starving. For gaming tasks, ZHANG et al. proposed a fine-grained scheduling framework that decomposed game workloads into small and independent render tasks and dispatched the small tasks to different machines^[23]. The scheduling objective was to maximize a utility function. If all resources are fully used by games, the utility function achieves its maximum value. The proposed approach requires only 26.4% of the servers compared with packing algorithms. Since task scheduling strategies based on artificial intelligence become more and more prevalent in clusters, efficient machine learning task scheduling has attracted increasing research interests^[24-28]. CHEN et al. focused on convolutional neural networks (CNN)-based task scheduling^[24]. The scheduling strategy leverages an analytical prediction model to optimize the allocation of computing resources for impending tasks, thereby enhancing system efficiency and prioritizing user satisfaction. To improve performance and reduce energy consumption, CHEN et al. proposed a prediction method to predict the completion time and energy consumption of deep training tasks first, and then used the GPU allocation strategy algorithm that depended on the prediction of completion time and energy consumption to assign tasks^[25]. For more time-consuming training tasks, HAN et al. proposed a method to eliminate network contention by jointly optimizing network topology and communication patterns in distributed training^[26]. CHEN et al. proposed a training-inference joint scheduling framework, called DeepBoot, to support training tasks and utilize the idle GPUs in the inference cluster^[27]. DeepBoot could overcome the unbalanced GPU utilization stemming from the periodic difference in training and inference workload. CHEN et al. proposed a QoS-aware scheduling framework for a deep learning R&D platform^[28]. The framework provides lightweight offline profiling and online dynamic scheduling on GPU clusters. Using the lightweight offline profiler, the framework could provide a prediction model according to the domain-specific information of deep learning tasks derived from a comprehensive characterization.

Some research focuses on the methodology of scheduling algorithms^[29-31]. ZHANG and WU presented the weighted system-level scheduling algorithm (WSLSA) which involved the weights of the processor^[29]. Due to the doubly linked list data structure for system-level tasks, the algorithm could assign and remove a task in a single direction (denoted by WSLSA-S) from the task list or it could also assign and remove a task in both directions (denoted by WSLSA-B) from the task list. ITURRIAGA et al. presented a parallel implementation on CPU/GPU of two variants of a stochastic local search method to efficiently solve the scheduling problem in heterogeneous computing systems^[30]. Both methods are based on a set of simple operators to keep the computational com-

plexity as low as possible. A two-level dynamic scheduling algorithm of CPU and GPU cooperative computing in heterogeneous clusters was proposed^[31]. The algorithm could dynamically distribute data according to each node's computing capability and schedule tasks dynamically between the CPU and GPU in the node.

3.2 Statistic Methods

Different from heuristic task scheduling, statistic methods learn scheduling strategies from clusters of system data. The system data include CPU utilization information, GPU utilization information, host memory utilization information, GPU memory utilization information, node uplink traffic rate, node downlink traffic rate, global load throughput of GPU, global store throughput of GPU, etc. With the burgeoning development of AI, deep reinforcement learning and deep neural networks are employed in tasking scheduling^[32-35].

By using the deep Q-network, the two-stage scheduling model was adopted to learn to perform the current optimal scheduling actions online according to the runtime status of cluster environments, the characteristics of video tasks, and the dependencies between video tasks^[32]. The interference-aware workload parallelization (IAWP) method assigns subtasks with dependencies to the appropriate computing units, taking the interference of subtasks on the GPU by using neural collaborative filtering into account^[33]. To make the learning of neural networks more efficient, pre-training is adopted in the two-stage scheduler. The transfer learning technology is used to efficiently rebuild the task scheduling model referring to the existing model.

Since prediction-based schedulers are limited in terms of their prediction accuracy and offline-profiling overhead, the Q-learning framework was designed to model the R&D scenarios and was proposed to build a series of implementations including state space, action space, reward function, and update scheme for task scheduling^[34]. The learning agent could learn from the feedback on task performance independently and continuously to adjust online task scheduling decisions. The Q-learning-based scheduler significantly improves the task average normalized throughput and makespan. Moreover, the proposed scheduler is more suitable for long-term deep-learning R&D scenarios.

The deep network can be used to produce task scheduling strategy candidates first^[35]. A set of feasible solutions is then generated through cross-variance and other operations. The optimal solutions are screened out and stored in the empirical buffer area. Finally, the neural network parameters are optimized through the empirical buffer samples.

Compared with heuristic task scheduling methods, statistic methods have demonstrated fewer achievements. This is because task scheduling is dynamic and non-deterministic polynomial (NP)-hard. It is not easy to obtain a suitable deep network to efficiently describe all behaviors of task scheduling.

Along with the evolution of machine learning technologies, more and more algorithms will emerge and provide better performance.

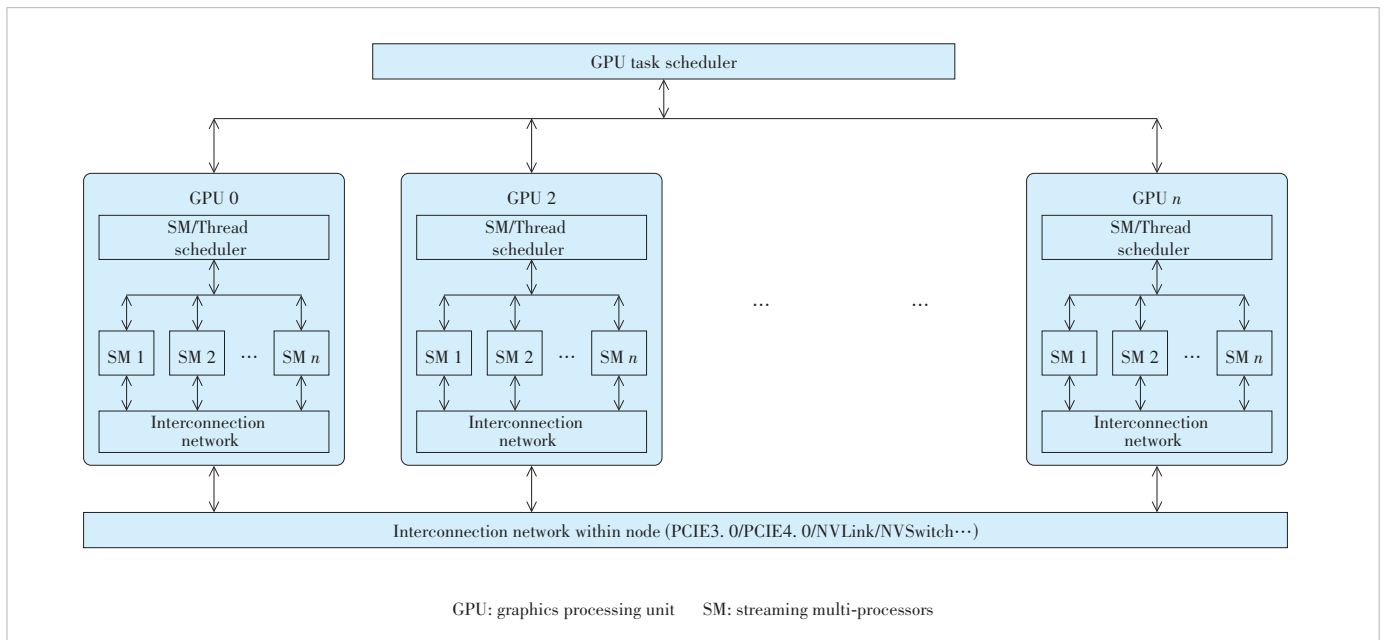
4 Task Scheduling of GPU

Modern GPU computing allows application programmers to exploit parallelism using new parallel programming languages such as CUDA and OpenCL and a growing set of familiar programming tools, leveraging the substantial investment in parallelism that high-resolution real-time graphics require and AI applications^[36]. Different from the CPU, the GPU cannot be partitioned into arbitrary virtual GPUs with cores. GPUs also cannot compute without cooperation with the CPU. Therefore, GPUs show different characteristics of computing. GPUs offer the capability to handle multiple tasks at the process level, that is, multiple processes can run on one GPU. However, frequent process switching may destroy the hardware pipeline of GPUs. Usually, a server may have several GPUs. Different GPUs are treated as different devices although such GPUs are connected by high-speed interconnection networks. As a result, tasks can be scheduled among GPUs and processed within a GPU server, which is device-level task scheduling. The task scheduling framework of GPU is shown in Fig. 3.

Most research focuses on task scheduling within GPU^[37-45]. The goal of task scheduling within GPU is to exploit the throughput of the GPU kernel and give the best separation of SM or threads. In the early stage, AUGONNET et al. presented StarPU, a runtime system that efficiently exploited heterogeneous multicore architectures^[37]. StarPU provides a uniform execution model and a high-level framework to design scheduling policies. StarPU permits dynamically selecting the

strategies at runtime, thus letting the programmer try and choose the most efficient strategy. This makes it possible to benefit the scheduling without setting restrictions or making excessive assumptions. Later, ZHONG and HE proposed Kernelet, a runtime system that improved the throughput of concurrent kernel executions on the GPU^[38]. Kernelet embraces transparent memory management, PCIe data transfer techniques, and dynamic slicing and scheduling techniques for kernel executions. A novel Markov chain-based performance model to guide the scheduling decision was proposed in Kernelet. Recently, ZOU et al. proposed RTGPU that combined fine-grain GPU partitioning on the system side with a novel scheduling algorithm on the theory side^[39]. RTGPU leverages a precise timing model of the GPU applications with the persistent threads technique and improves fine-grained utilization through interleaved execution. The RTGPU real-time scheduling algorithm can provide real-time guarantees of meeting deadlines for GPU tasks with better scheduling ability.

Besides the scheduling framework, some research focuses on scheduling strategies^[40-41]. LOPEZ-ALBELDA et al. employed a scheduling theory to build a model that took into account the device capabilities, workload characteristics, constraints, and objective functions^[40]. The heuristic called NEH-GPU, which combines an existing heuristic with a GPU task execution model, has been developed. HUANG et al. proposed a dynamic GPU task balance scheduling called the coefficient of balance and equipment history ratio value (CB-HRV) task scheduling^[41], which was developed to reduce system energy consumption during task execution by allocating tasks based on workload balance, thereby improving GPU en-



▲ Figure 3. Task scheduling framework of GPU

ergy usage. The CB-HRV algorithm is more balanced, and it allows the computing device to be utilized more reasonably and efficiently.

For special types of tasks, an efficient task scheduling frame was designed^[42-44]. LI et al. proposed a two-level scheduling strategy to distribute irregular tasks and enable resource sharing on GPUs, by managing tasks and threads hierarchically^[42]. The framework manages both tasks and threads in the two levels to allow for helpful resource sharing. KWON et al. proposed Nimble, a deep-learning execution engine that runs GPU tasks in parallel with minimal scheduling overhead^[43]. Nimble introduces a technique called ahead-of-time (AoT) scheduling, which pre-runs the given neural network once according to the generated stream mapping and records all the GPU tasks as an execution trace. AoT scheduling also intercepts memory allocation/free requests from the base framework and reserves the GPU memory allocated in the pre-run. At the end of the AoT scheduling, Nimble packs the execution trace and reserves the memory into a task schedule. CHEN et al. presented Atos, a task-parallel GPU dynamic scheduling framework that was especially targeted at dynamic irregular applications^[44]. Atos exposes additional concurrency by supporting task-parallel formulations of applications with relaxed dependencies, achieving higher GPU utilization. Atos also offers implicit task-parallel load balancing in addition to data-parallel load balancing, providing users the flexibility to balance between them to achieve optimal performance.

However, there is a relative scarcity of research on task scheduling for multi-GPU systems. TANG et al. proposed AEML, an acceleration engine for multi-GPU load-balancing in distributed heterogeneous environments^[45]. AEML could effectively integrate GPUs into the distributed processing framework and achieve good load balance among multiple heterogeneous GPUs. To achieve the best load-balancing among multiple heterogeneous GPUs, the AEML model utilizes four techniques: a fine-grained task mapping mechanism, a device resource unified management scheme, a novel resource-aware GPU task scheduling strategy, and a feedback-based stream adjustment scheme.

5 Evaluation

The goal of task scheduling is to exploit all potential parallelism of heterogeneous clusters composed of multi-CPU and multi-GPUs. Some metrics are adopted to evaluate and compare different methods, such as makespan, load balance, resource utilization, energy, speedup and QoS^[46-47]. The scheduling methods will optimize several metrics simultaneously. We summarize the motioned scheduling technologies in Table 1.

From Table 1, it can be clearly seen that most algorithms focus on makespan and resource utilization. This is because that makespan is very important for cluster users' feeling. Resource utilization optimization can improve cluster system effi-

▼Table 1. Summary of scheduling technologies based on evaluation metrics

Task Scheduling Technology	Evaluation Metrics					
	Speed-up	Energy	Load balance	Makespan	Resource utilization	QoS
Hybrid map ^[11]	✓					
Energy efficient task scheduling ^[12]		✓				
Energy-minimized scheduling ^[13]		✓				
Task scheduling with temperature constraint ^[14-15]		✓				
PTA&WSLSA ^[16]			✓			
Multi-granularity partition ^[17]			✓			
Adaptive and transparent task scheduling ^[18]			✓			
Dual approximation technique ^[19]				✓		
Data partition ^[20]				✓		
Large instance scheduling ^[21]	✓					
Short task scheduling ^[22]				✓		
Fine-grained scheduling ^[23]					✓	
CNN-based task scheduling ^[24]				✓	✓	
GAS ^[25]		✓		✓		✓
Isolated scheduling ^[26]	✓				✓	✓
DeepBoot ^[27]					✓	
QoS guarantee scheduling ^[28]						✓
Greedy heuristics ^[29]			✓			
Local serach ^[30]				✓	✓	
CPU and GPU cooperative scheduling ^[31]					✓	
Learning driven scheduling ^[32-33]				✓	✓	
Q-learning ^[34]				✓		
Dynamic priority task scheduling ^[35]				✓		✓
StarPU ^[37]					✓	
Kernelet ^[38]	✓				✓	
RTGPU ^[39]					✓	
Heuristics for concurrent task scheduling ^[40]				✓	✓	
Task balance scheduling ^[41]		✓				
Two-level task Scheduling ^[42]	✓					
Nimble ^[43]	✓					
Atos ^[44]	✓					
AEML ^[45]			✓		✓	

CNN: convolutional neural network
CPU: central processing unit
GAS: GPU allocation strategy
GPU: graphics processing unit

PTA: packing task algorithm
QoS: Quality of Service
WSLSA: weighted system-level scheduling algorithm

ciency, which is the main purpose of task scheduling technologies. Energy-based task scheduling is mainly designed for GPU clusters since GPUs are highly energy-consuming. Heuristic methods are dominant since statistic-based approaches require running data from the real clusters which are hard to collect. However, learning-based scheduling can provide more intelligent scheduling strategies and will attract more attention in future research.

6 Conclusions

Task scheduling is a long-term hot research topic in companies with cloud computing and AI's flourishing. Most task scheduling strategies are heuristic and based on experts' experience. Statistic strategies have attracted researchers' interest recently. Different from task scheduling of CPU clusters, task scheduling of CPU-GPU clusters is more complex due to heterogeneous system composition. Task-oriented scheduling focuses on short tasks, gaming tasks, deep learning tasks, etc. This paper also reviews task scheduling strategies within GPU. This is because GPU has process-level parallel ability and incompatible tasks will decrease GPU's workflow and parallelism.

This paper describes a task scheduling framework for CPU-GPU heterogeneous clusters and a task scheduling framework for GPU servers with multiple GPUs. From the two frameworks, we can clearly see that task scheduling can be separated into the system level, the node level, and the device level. Although research achievements in statistic task scheduling are less than heuristic task scheduling, statistic task scheduling is still a highly potential technology.

References

- [1] BOHN R B, MESSINA J, LIU F, et al. NIST cloud computing reference architecture [C]//IEEE World Congress on Services. IEEE, 2011: 594 - 596. DOI: 10.1109/SERVICES.2011.105
- [2] CAITHNESS N, DRESCHER M, WALLOM D. Can functional characteristics usefully define the cloud computing landscape and is the current reference model correct? [J]. Journal of cloud computing, 2017, 6(1): 10. DOI: 10.1186/s13677-017-0084-1
- [3] ARUNARANI A, MANJULA D, SUGUMARAN V. Task scheduling techniques in cloud computing: a literature survey [J]. Future generation computer systems, 2019, 91: 407 - 415. DOI: 10.1016/j.future.2018.09.014
- [4] SINGH P, DUTTA M, AGGARWAL N. A review of task scheduling based on meta-heuristics approach in cloud computing [J]. Knowledge and information systems, 2017, 52(1): 1 - 51. DOI: 10.1007/s10115-017-1044-2
- [5] PRADHAN R, SATAPATHY S C. Advances in intelligent systems and computing: task scheduling in heterogeneous cloud environment—a Survey [M]. Singapore: Springer, 2020
- [6] YANG G, ZHAO X, HUANG J. Survey on task scheduling algorithms for cloud computing [J]. Computer systems and applications, 2020, 29(3): 11 - 19. DOI: 10.15888/j.enki.csa.007261
- [7] WANG H, WANG H H. Survey on task scheduling in cloud computing environment [C]//The 7th International Conference on Intelligent Informatics and Biomedical Science. IEEE, 2022: 286 - 291. DOI: 10.1109/ICIIBMS55689.2022.9971622
- [8] HOSSEINZADEH M, GHAFOR M Y, HAMA H K, et al. Multi-objective task and workflow scheduling approaches in cloud computing: a comprehensive review [J]. Journal of grid computing, 2020, 18(3): 327 - 356. DOI: 10.1007/s10723-020-09533-z
- [9] PRITY F S, GAZI M H, ASLAM UDDIN K M. A review of task scheduling in cloud computing based on nature-inspired optimization algorithm [J]. Cluster computing, 2023, 26(5): 3037 - 3067. DOI: 10.1007/s10586-023-04090-y
- [10] JAWADE P B, SAI KUMAR D, RAMACHANDRAM S. A compact analytical survey on task scheduling in cloud computing environment [J]. International journal of engineering trends and technology, 2021, 69(2): 178 - 187. DOI: 10.14445/22315381/ijett-v69i2p225
- [11] SHIRAHATA K, SATO H, MATSUOKA S. Hybrid map task scheduling for GPU-based heterogeneous clusters [C]//The 2nd International Conference on Cloud Computing Technology and Science. IEEE, 2010: 733 - 740. DOI: 10.1109/CloudCom.2010.55
- [12] HUO H P, SHENG C C, HU X M, et al. An energy efficient task scheduling scheme for heterogeneous GPU-enhanced clusters [C]//International Conference on Systems and Informatics. IEEE, 2012: 623 - 627. DOI: 10.1109/ICSAI.2012.6223074
- [13] HU B, YANG X C, ZHAO M G. Energy-minimized scheduling of intermittent real-time tasks in a CPU-GPU cloud computing platform [J]. IEEE transactions on parallel and distributed systems, 2023, 34(8): 2391 - 2402. DOI: 10.1109/TPDS.2023.3288702
- [14] CAO Y P, WANG H F. A task scheduling scheme for preventing temperature hotspot on GPU heterogeneous cluster [C]//International Conference on Green Informatics. IEEE, 2017: 117 - 121. DOI: 10.1109/ICGI.2017.20
- [15] WANG H F, CAO Y P. Task scheduling of GPU cluster for large-scale data process with temperature constraint [C]//International Conference on Computer Engineering and Networks. CENet, 2020: 110-117.10.1007/978-3-030-14680-1_13
- [16] ZHANG K L, WU B F. Task scheduling for GPU heterogeneous cluster [C]//International Conference on Cluster Computing Workshops. IEEE, 2012: 161 - 169. DOI: 10.1109/ClusterW.2012.20
- [17] CHEN W B, YANG R R, YU J Q. Multi-granularity partition and scheduling for stream programs based on multi-CPU and multi-GPU heterogeneous architectures [J]. Computer engineering & science, 2017, 39(1): 15. DOI: 10.3969/j.issn.1007-130X.2017.01.002
- [18] CI Q Y, LI H R, YANG S W, et al. Adaptive and transparent task scheduling of GPU-powered clusters [J]. Concurrency and computation: Practice and experience, 2022, 34(9): e5793. DOI: 10.1002/cpe.5793
- [19] KEDAD-SIDHOUM S, MONNA F, MOUNIÉ G, et al. Scheduling independent tasks on multi-cores with GPU accelerators [C]//European Conference on Parallel Processing. Berlin, Heidelberg: Springer, 2014: 228-237.10.1007/978-3-642-54420-0_23
- [20] ZHU Z Y, TANG X C, ZHAO Q. A unified schedule policy of distributed machine learning framework for CPU-GPU cluster [J]. Journal of north-western polytechnical university, 2021, 39(3): 529 - 538. DOI: 10.1051/jnwpu/20213930529
- [21] PINEL F, DORRONSORO B, BOUVRY P. Solving very large instances of the scheduling of independent tasks problem on the GPU [J]. Journal of parallel and distributed computing, 2013, 73(1): 101 - 110. DOI: 10.1016/j.jpdc.2012.02.018
- [22] SHAO J L, MA J M, LI Y, et al. GPU scheduling for short tasks in private cloud [C]//IEEE International Conference on Service-Oriented System Engineering. IEEE, 2019: 215 - 2155. DOI: 10.1109/SOSE.2019.00037
- [23] ZHANG W, LIAO X F, LI P, et al. Fine-grained scheduling in cloud gaming on heterogeneous CPU-GPU clusters [J]. IEEE network, 2018, 32(1): 172 - 178. DOI: 10.1109/MNET.2017.1700047
- [24] CHEN Z Y, LUO L, QUAN W, et al. Multiple CNN-based tasks scheduling across shared GPU platform in research and development scenarios [C]//The 20th International Conference on High Performance Computing

- and Communications. IEEE, 2018: 578 – 585. DOI: 10.1109/HPCC/SmartCity/DSS.2018.00107
- [25] CHEN Y W, HAN J C, ZHOU H, et al. GAS: GPU allocation strategy for deep learning training tasks [C]//IEEE Smartworld, Ubiquitous Intelligence & Computing, Scalable Computing & Communications, Digital Twin, Privacy Computing, Metaverse, Autonomous & Trusted Vehicles. IEEE, 2022: 880 – 887. DOI: 10.1109/SmartWorld-UIC-ATC-ScalCom-DigitalTwin-PriComp-Metaverse56740.2022.00133
- [26] HAN X C, JIANG W H, CAO P R, et al. Isolated scheduling for distributed training tasks in GPU clusters [EB/OL]. (2023-8-10)[2023-9-30]. <https://doi.org/10.48550/arXiv.2308.05692>
- [27] CHEN Z Q, ZHAO X K, ZHI C, et al. DeepBoot: dynamic scheduling system for training and inference deep learning tasks in GPU cluster [J]. IEEE transactions on parallel and distributed systems, 2023, 34(9): 2553 – 2567. DOI: 10.1109/TPDS.2023.3293835
- [28] CHEN Z Y, QUAN W, WEN M, et al. Deep learning research and development platform: characterizing and scheduling with QoS guarantees on GPU clusters [J]. IEEE transactions on parallel and distributed systems, 2020, 31(1): 34 – 50. DOI: 10.1109/TPDS.2019.2931558
- [29] ZHANG K L, WU B F. Task scheduling greedy heuristics for GPU heterogeneous cluster involving the weights of the processor [C]//IEEE International Symposium on Parallel & Distributed Processing, Workshops and PhD Forum. IEEE, 2013: 1817 – 1827. DOI: 10.1109/IPDPSW.2013.38
- [30] ITURRIAGA S, NESMACHNOW S, LUNA F, et al. A parallel local search in CPU/GPU for scheduling independent tasks on large heterogeneous computing systems [J]. The journal of supercomputing, 2015, 71(2): 648 – 672. DOI: 10.1007/s11227-014-1315-6
- [31] GAO Y, GU W J, DING Y H, et al. Design and implementation of CPU and GPU cooperative scheduling algorithm with heterogeneous clusters [J]. Computer engineering and design, 2020, 41(2): 10. DOI: CNKI:SUN:SJSJ.0.2020-02-045
- [32] ZHANG H T, TANG B C, GENG X, et al. Learning driven parallelization for large-scale video workload in hybrid CPU-GPU cluster [C]//The 47th International Conference on Parallel Processing. ACM, 2018. DOI: 10.1145/3225058.3225070
- [33] ZHANG H T, GENG X, MA H D. Learning-driven interference-aware workload parallelization for streaming applications in heterogeneous cluster [J]. IEEE transactions on parallel and distributed systems, 2021, 32(1): 1 – 15. DOI: 10.1109/TPDS.2020.3008725
- [34] CHEN Z Y. Research on deep learning task scheduling based on small scale GPU cluster platform [M]. Hunan, China: National University of Defense Technology, 2019
- [35] QI Y F, He X. Dynamic priority task scheduling algorithm based on deep learning [J]. Computer systems and applications, 2023, 32(7): 195 – 201. DOI: 10.15888/j.cnki.csa.009169
- [36] KECKLER S W, DALLY W J, KHAILANY B, et al. GPUs and the future of parallel computing [J]. IEEE micro, 2011, 31(5): 7 – 17. DOI: 10.1109/MM.2011.89
- [37] AUGONNET C, THIBAUT S, NAMYST R, et al. StarPU: a unified platform for task scheduling on heterogeneous multicore architectures [M]//Lecture Notes in Computer Science. Berlin, Germany: Springer, 2009: 863 – 874. DOI: 10.1007/978-3-642-03869-3_80
- [38] ZHONG J L, HE B S. Kernelet: high-throughput GPU kernel executions with dynamic slicing and scheduling [J]. IEEE transactions on parallel and distributed systems, 2014, 25(6): 1522 – 1532. DOI: 10.1109/TPDS.2013.257
- [39] ZOU A, LI J, GILL C D, et al. RTGPU: real-time GPU scheduling of hard deadline parallel tasks with fine-grain utilization [J]. IEEE transactions on parallel and distributed systems, 2023, 34(5): 1450 – 1465. DOI: 10.1109/TPDS.2023.3235439
- [40] LÓPEZ-ALBELDA B, LÁZARO-MUÑOZ A J, GONZÁLEZ-LINARES J M, et al. Heuristics for concurrent task scheduling on GPUs [J]. Concurrency and computation, 2020, 32(20): e5571. DOI: 10.1002/cpe.5571
- [41] HUANG Y H, GUO B, SHEN Y. GPU energy optimization based on task balance scheduling [J]. Journal of systems architecture, 2020, 107: 101808. DOI: 10.1016/j.sysarc.2020.101808
- [42] LI J, LIU L, WU Y, et al. Two-level task scheduling for irregular applications on GPU platform [J]. International journal of parallel programming, 2017, 45(1): 79 – 93. DOI: 10.1007/s10766-015-0387-0
- [43] KWON W, YU G-I, JEONG E, et al. Nimble: lightweight and parallel GPU task scheduling for deep learning [C]//The 34th International Conference on Neural Information Processing Systems. Curran Associates, 2020: 8343 – 8354. DOI: <https://dl.acm.org/doi/10.5555/3495724.3496423>
- [44] CHEN Y X, BROCK B, PORUMBESCU S, et al. Atos: a task-parallel GPU scheduler for graph analytics [C]//The 51st International Conference on Parallel Processing. ACM, 2022. DOI: 10.1145/3545008.3545056
- [45] TANG Z, DU L F, ZHANG X D, et al. AEML: an acceleration engine for multi-GPU load-balancing in distributed heterogeneous environment [J]. IEEE transactions on computers, 2022, 71(6): 1344 – 1357. DOI: 10.1109/TC.2021.3084407
- [46] LIMA J V F, GAUTIER T, DANJEAN V, et al. Design and analysis of scheduling strategies for multi-CPU and multi-GPU architectures [J]. Parallel computing, 2015, 44: 37 – 52. DOI: 10.1016/j.parco.2015.03.001
- [47] ALEBRAHIM S, AHMAD I. Task scheduling for heterogeneous computing systems [J]. The journal of supercomputing, 2017, 73(6): 2313 – 2338. DOI: 10.1007/s11227-016-1917-2

Biographies

ZHOU Yiheng has received his bachelor's degree in robotic engineering from University of Shanghai for Science and Technology, China in 2024. He has been working as a research assistant at Peking University, China since 2023. His research interests include computer vision (detection and pose estimation), robotic arm control, and artificial intelligence (AI computing platform).

ZENG Wei (weizeng@pku.edu.cn) is currently a research professor at the School of Computer Science, Peking University, China. He was a senior researcher at NEC Laboratories, China from 2005 to 2015. He worked as a visiting scholar at Stanford University, USA in 2012. He received his PhD degree in computer science and engineering from Harbin Institute of Technology, China in 2005. His research interests include computer vision (object detection and segmentation), artificial intelligence (AI computing platform), and media analysis (video retrieval). He is the author or coauthor of over 40 refereed journals and conference papers. He was the reviewer of ICCV2023, CVPR2023, ACM MM2022, ICPR2020, BigMM2020, and so forth.

ZHENG Qingfang received his BS degree from Shanghai Jiaotong University, China in 2002 and PhD degree in computer science from the Institute of Computing Technology, Chinese Academy of Sciences in 2008. He is now the chief scientist of cloud video product and deputy director of the Video Technology Committee of ZTE Corporation. His current research interests include video communication, computer vision and artificial intelligence.

LIU Zhilong is currently working with the Video Systems Department, ZTE Corporation as a senior system architecture engineer. He graduated from University of Electronic Science and Technology of China with a master's degree in 2015. His research interests include media transmission, real-time audio and video networks (RTN), and video computing networks.

CHEN Jianping is currently a senior research engineer at the School of Computer Science, Peking University, China. His research interests include media analysis, AI platform, and video retrieval.



Multi-View Image-Based 3D Reconstruction in Indoor Scenes: A Survey

LU Ping^{1,2}, SHI Wenzhe^{1,2}, QIAO Xiuquan³

(1. State Key Laboratory of Mobile Network and Mobile Multimedia Technology, Shenzhen 518055, China;

2. ZTE Corporation, Shenzhen 518057, China;

3. State Key Laboratory of Networking and Switching Technology, Beijing University of Posts and Telecommunications, Beijing 100876, China)

DOI: 10.12142/ZTECOM.202403011

<https://kns.cnki.net/kcms/detail/34.1294.TN.20240912.1012.002.html>,
published online September 12, 2024

Manuscript received: 2023-09-14

Abstract: Three-dimensional reconstruction technology plays an important role in indoor scenes by converting objects and structures in indoor environments into accurate 3D models using multi-view RGB images. It offers a wide range of applications in fields such as virtual reality, augmented reality, indoor navigation, and game development. Existing methods based on multi-view RGB images have made significant progress in 3D reconstruction. These image-based reconstruction methods not only possess good expressive power and generalization performance, but also handle complex geometric shapes and textures effectively. Despite facing challenges such as lighting variations, occlusion, and texture loss in indoor scenes, these challenges can be effectively addressed through deep neural networks, neural implicit surface representations, and other techniques. The technology of indoor 3D reconstruction based on multi-view RGB images has a promising future. It not only provides immersive and interactive virtual experiences but also brings convenience and innovation to indoor navigation, interior design, and virtual tours. As the technology evolves, these image-based reconstruction methods will be further improved to provide higher quality and more accurate solutions to indoor scene reconstruction.

Keywords: 3D reconstruction; MVS; NeRF; neural implicit surface

Citation (Format 1): LU P, SHI W Z, QIAO X Q. Multi-view image-based 3D reconstruction in indoor scenes: a survey [J]. *ZTE Communications*, 2024, 22(3): 91 – 98. DOI: 10.12142/ZTECOM.202403011

Citation (Format 2): P. Lu, W. Z. Shi, and X. Q. Qiao, “Multi-view image-based 3D reconstruction in indoor scenes: a survey,” *ZTE Communications*, vol. 22, no. 3, pp. 91 – 98, Sept. 2024. doi: 10.12142/ZTECOM.202403011.

1 Introduction

Traditional 3D reconstruction techniques play a crucial role in the field of computer vision and encompass commonly used tools and libraries such as ColMap^[1] and OpenMVS^[2]. These techniques estimate the 3D positions of points in a scene through feature extraction and matching, followed by steps like sparse point cloud generation and dense point cloud generation to create dense point clouds and 3D models with high-quality geometry and texture. These traditional 3D reconstruction techniques find widespread applications in various domains, including virtual reality, augmented reality, indoor navigation, building reconstruction, and cultural heritage preservation tasks. They perform well in handling small objects, small-scale scenes, and simple scenes. However, when it comes to indoor scenes containing a large number of textureless or repetitive texture regions, traditional reconstruction methods struggle to extract meaningful features, resulting in significant holes and noise during the reconstruction process.

This limitation restricts their applicability in large-scale and complex scenes.

With the continuous advancement of technology, there is increasing attention on deep learning-based 3D reconstruction techniques for indoor scenes^[3-5]. Compared to traditional 3D reconstruction methods, these techniques leverage the power of deep learning models in processing and analyzing multiple-view RGB images to extract feature representations of the scene, leading to high-quality 3D model reconstruction. Specifically, convolutional neural networks (CNNs), Transformer^[6], and vision Transformers (ViT)^[7] are used to process and analyze multiple-view RGB images. These models extract feature representations of objects in the scene. Through learning and training, these deep learning models gain an understanding of the geometric shapes, texture information, and other visual cues present in the images, encoding them as feature representations. Once the feature representations of objects are obtained, 3D reconstruction will be conducted. This includes estimating the 3D coordinates of points in the scene and performing optimization and refinement to obtain accurate 3D reconstruction results.

In recent years, there has been rapid development in combining neural radiance fields (NeRF)^[8] with neural implicit surface-

This work was supported by ZTE Industry-University-Institute Cooperation Funds under Grant No. HC-CN-20221102002.

based techniques for the 3D reconstruction of indoor scenes. This development is driven by the remarkable success of NeRF^[8] in the field of novel view synthesis. These methods utilize neural network models to learn implicit representation functions of objects, enabling the capture of their geometric shapes and texture information without the explicit representation of 3D geometry. Compared to explicit representations, such as point clouds and voxel grids, these methods offer higher-resolution 3D reconstruction with enhanced expressive power and generalization capabilities. They can handle complex scenes and shape variations by leveraging the flexibility of neural networks in modeling intricate geometric details and capturing rich texture information. By learning implicit representations of objects, these techniques allow for more accurate and detailed reconstructions, even in the presence of challenging factors like occlusions and varying lighting conditions. The implicit nature of the representation enables these methods to generate novel views of the scene from previously unseen viewpoints, contributing to their growing success in the field of indoor scene 3D reconstruction.

In summary, the use of multi-view RGB images for indoor scene 3D reconstruction offers a new approach to achieving low-cost and high-quality reconstructions. It not only reduces equipment requirements and operational complexity but also presents broad application prospects in various fields, including virtual reality, augmented reality, indoor navigation, and game development. However, existing techniques also face several challenges. Traditional methods demonstrate stability in handling small objects, small-scale scenes, and simple scenes but encounter difficulties in dealing with textureless regions and repetitive texture regions in indoor scenes. On the other hand, deep learning-based techniques for indoor scene 3D reconstruction, mostly relying on computationally expensive 3D CNNs^[9] or structures like Transformer^[6], require processing a large volume of image data for large-scale indoor scenes. Additionally, generating high-resolution voxel grids consumes significant storage resources, posing challenges in terms of computational resources and storage space. Furthermore, capturing details and handling variations in complex scenes and shape changes demand more complex and robust deep learning models, along with considerable time and effort for data annotation and model training. Inspired by the tremendous success of NeRF^[8] in the field of novel view synthesis, many techniques combining neural implicit surface-based methods with NeRF have rapidly developed for indoor scene 3D reconstruction. These methods employ neural network models to learn implicit representation functions of objects, enabling the capture of geometric shapes and texture information without explicit representation of 3D geometry. Compared to explicit representation methods, neural implicit surface-based approaches achieve higher-resolution 3D reconstruction, possess stronger expressive power, and can handle complex scenes and shape variations.

Future trends in the development of indoor scene 3D recon-

struction include enhancing the robustness of traditional methods and their adaptability to handle textureless scenes. Efforts will be made to strengthen the research on data utilization efficiency and generalization capabilities in deep learning-based approaches. Additionally, exploring performance improvements of neural implicit surface-based methods in complex scenes will be a focus. As technology evolves and innovates, multi-view-based indoor 3D reconstruction techniques will continue to provide more accurate and realistic ways of generating 3D scene content for various fields. These advancements will enable the creation of highly precise and realistic 3D scenes, benefiting applications in virtual reality, augmented reality, indoor navigation, and game development, among others.

2 Multi-View-Based Indoor 3D Reconstruction

The multi-view-based indoor 3D reconstruction techniques are of significant importance in the field of computer vision. Existing methods can be broadly classified into three categories. The first category is the traditional 3D reconstruction methods based on feature matching, which recovers the 3D structure of the scene by extracting feature points from images and performing feature matching. Methods such as ColMap^[1] and OpenMVS^[2] utilize techniques like feature point matching, camera pose estimation, and triangulation to achieve sparse and dense 3D reconstruction. These methods have shown good results for indoor scenes, but they perform poorly in scenarios with textureless or low-texture regions.

The second category is the deep learning-based 3D reconstruction techniques, which directly learn the 3D representation of the scene from multi-view image data. These methods can extract rich semantic and geometric information from images and achieve end-to-end 3D reconstruction with good generalization. Examples of such methods include Pixel2Mesh^[10], SimpleRecon^[11], and NeuralRecon^[12], which have achieved significant advancements in indoor scene reconstruction and can generate high-quality 3D models.

The third category is the 3D reconstruction techniques based on neural implicit surface representation, where the implicit representation function of the object is learned by neural networks, eliminating the need for explicit representation of 3D geometry. These methods can handle complex scenes and shape variations and generate highly accurate 3D models. Examples of such methods include VolSDF^[13] and NeuS^[14], which have made notable progress in indoor scene reconstruction, enabling high-fidelity geometry and texture reconstruction. By leveraging image data from multiple viewpoints, these methods can reconstruct the 3D structure and texture information of indoor scenes, providing a foundation for applications such as indoor navigation, virtual reality, and augmented reality.

2.1 Stereoscopic Matching-Based 3D Reconstruction Methods

Traditional stereoscopic matching-based 3D reconstruction methods, such as ColMap^[1] and OpenMVS^[2], play a significant

role in indoor 3D reconstruction. ColMap integrates Structure-from-Motion (SfM) and Multi-View Stereo (MVS) technologies, while OpenMVS^[2] focuses specifically on MVS. These tools possess strong capabilities and have become standard tools in both academia and industry for generating high-quality 3D models from multi-view RGB images. However, these traditional methods still face several challenges. They perform poorly in dealing with large areas devoid of textures, which often leads to feature matching failures and consequently impacts reconstruction accuracy. Additionally, these methods require significant computational resources and storage space, especially when handling large-scale scenes, which can be limiting factors. Furthermore, these traditional methods have limitations when dealing with closed and transparent surfaces, as well as scenes with complex textures and fine geometric structures. Therefore, researchers are continuously working to enhance these methods to improve their performance and robustness, particularly in dealing with complex scenes and textureless regions. Future research directions may include better addressing these challenges to enable traditional feature matching methods to be more effective in a wider range of application scenarios.

Fig. 1 shows the workflow of matching-based 3D reconstruction method. These methods typically involve the following detailed procedures and techniques.

2.1.1 Image Acquisition and Feature Extraction

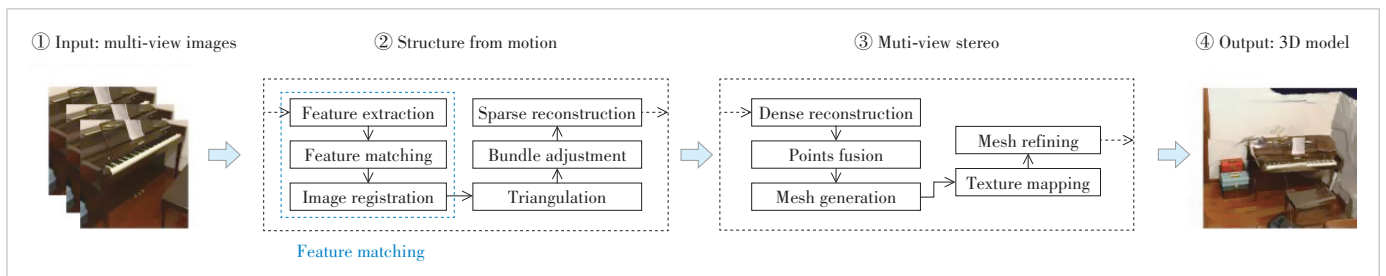
Multiple images are captured from different viewpoints using cameras or a camera system. For each image, feature extraction algorithms (e.g., SIFT^[15], SURF^[16], or ORB^[17]) are used to detect and describe key points and feature descriptors in the images. For example, in ColMap^[1], the input images are preprocessed by converting them to grayscale to reduce computational complexity and improve robustness. Then, histogram equalization is applied to enhance contrast and details. Next, the classic Scale-Invariant Feature Transform (SIFT) algorithm^[15] is used with various optimizations and improvements to extract stable and discriminative key points and compute descriptive feature descriptors. These extracted key points and descriptors are essential input data for subsequent 3D reconstruction tasks. ColMap^[1] also provides features such as GPU acceleration, visualization, and debugging tools to enhance the efficiency and convenience of feature extraction.

2.1.2 Camera Pose Estimation

Camera pose estimation, a crucial step in 3D reconstruction, is used to estimate the position and orientation of cameras in the world coordinate system. Feature matching algorithms (e.g., based on feature descriptors or optical flow) are used to match the feature points between different images. Through geometric verification and filtering of the matched point pairs, the relative camera poses and parameters, i.e., camera pose estimation, can be obtained. For example, OpenMVG^[18] provides a selection of feature extraction algorithms based on specific application requirements. It estimates camera rotation and translation through fundamental matrix estimation and pose recovery. Fundamental matrix estimation calculates the fundamental matrix between two views from the results of feature matching, and then camera rotation and translation can be inferred by solving the fundamental matrix. To further improve reconstruction accuracy and stability, OpenMVG^[18] also offers camera network optimization. By performing bundle adjustment and other global optimization algorithms, the poses of all cameras can be optimized to minimize reprojection errors and maintain consistency. Camera network optimization helps correct errors in feature matching and camera pose estimation, resulting in more accurate reconstruction results.

2.1.3 3D Point Cloud Generation and Reconstruction

3D point cloud generation and sparse/dense reconstruction are key steps in 3D reconstruction, and popular toolkits like ColMap^[1], OpenMVG^[18], and OpenMVS^[2] provide corresponding functionalities. These tools can generate 3D point clouds from multi-view images, converting the feature points in the images into 3D points through feature extraction, feature matching, and camera pose estimation. This process produces a sparse point cloud, representing the geometric structure of the scene with only a small number of key points. Subsequently, dense point cloud generation is performed by interpolating or optimizing to fill the gaps between sparse points, resulting in a denser point cloud with richer details. ColMap^[1] employs various feature extraction and matching algorithms and offers Multi-View Geometry (MVG) and incremental sparse reconstruction algorithms. OpenMVG^[18] focuses more on geometry recovery and camera pose estimation using algorithms such as fundamental matrix estimation and bundle adjustment. OpenMVS^[2] is dedicated to dense reconstruction, utilizing multi-view stereo-



▲ Figure 1. Workflow of matching-based 3D reconstruction methods

scopic matching algorithms to generate a denser point cloud.

Finally, through steps such as triangulation, mesh optimization, and texture mapping, it is possible to generate a 3D mesh model with continuous surfaces and textures. Different mesh generation algorithms and techniques can be selected and optimized according to application requirements to obtain high-quality mesh models.

2.2 Deep Learning-Based 3D Reconstruction Methods

Traditional 3D reconstruction methods based on deep learning, such as SimpleRecon and NeuralRecon, represent the application of deep learning techniques in the field of 3D reconstruction, offering numerous innovations and advantages. These methods harness the powerful capabilities of deep learning, leveraging structures like CNNs to infer depth and geometric information from multi-view RGB images. Approaches like SimpleRecon and NeuralRecon utilize computationally expensive deep learning structures, including 3D CNNs, to model the three-dimensional geometry of scenes, enabling them to produce high-quality 3D reconstruction results. While these methods often require substantial training data and model training time, they excel in handling complex scenes and scenarios with shape variations. Compared to traditional feature-based methods, deep learning-based 3D reconstruction methods exhibit higher levels of automation and robustness. They can overcome some of the limitations of feature-based methods in textureless and repetitive texture regions and can handle more complex scenes and geometric structures. These methods often benefit from related work in deep learning, such as 3D point cloud processing and image semantic segmentation. Despite showing immense potential in 3D reconstruction, deep learning-based methods still face several challenges. Firstly, these methods often require significant computational resources, especially when generating high-resolution voxel grids. Secondly, model training demands substantial computational resources and time, typically relying on a large amount of annotated data. Additionally, these methods may be susceptible to issues like motion blur and discontinuities when dealing with complex scenes, particularly in the presence of dynamic objects or camera motion. Furthermore, compared to traditional methods, these methods may be less sensitive to scene details and textures. Therefore, future research directions may include improving the efficiency and generalization capabilities of models and enhancing their ability to handle complex scenes and dynamic objects. Attention should also be given to self-supervised and unsupervised training methods for deep learning models to reduce reliance on

extensive annotated data.

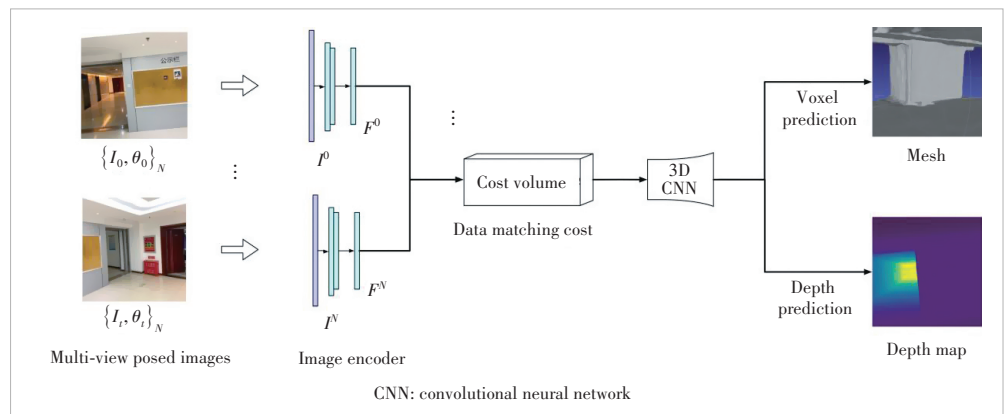
Fig. 2 shows the workflow of convolution-based 3D reconstruction techniques, which mainly consists of feature extraction, cost volume construction, and cost volume regularization. These steps leverage the powerful capabilities of deep learning and convolutional neural networks to achieve accurate reconstruction and depth estimation from images, with wide application prospects in computer vision, robotics, augmented reality, and other fields.

2.2.1 Feature Extraction

Feature extraction is the first step in 3D reconstruction, aiming to extract useful features from input images. CNNs are commonly used as feature extraction networks, with popular network architectures including ResNet^[19] and U-Net^[20]. These networks can extract local and global features from images and provide more representative feature representations for subsequent steps. In the feature extraction process, techniques such as fusing prior information and hierarchical convolution can be used to integrate features from different modalities and scales. For example, SimpleRecon^[11] combines pose, geometry features, and depth image features through convolutional feature extraction, while NeuralRecon^[12] utilizes distance priors obtained from the MVS process to ensure accuracy in texture-rich and edge regions, and normal priors to preserve completeness in texture-lacking regions.

2.2.2 Cost Volume Construction

The cost volume is a key concept in 3D reconstruction and is used to represent the similarity of image matching under different depth hypotheses. The basic idea of cost volume construction is to use a plane sweeping algorithm to project the source images onto parallel planes of a reference camera frustum and compute the similarity among the projected images. This process can be achieved through pairwise image matching and view aggregation. The construction of the cost volume can effectively filter out reliable depth hypotheses and provide a basis for subsequent depth estimation. Since the disparity values are in pixel units, this task becomes a classification problem, where



▲ Figure 2. Overall structure of learning-based methods

each class represents a discretized disparity value. Generally, CNNs can produce more reliable results. For MVS, the methods for generating the cost volume are mainly divided into two categories. For example, MVSNNet^[21] applies variance to all feature vectors to construct the cost volume, while DPSNet^[22] concatenates features pair by pair and averages all N-1 volumes to obtain the final cost volume.

2.2.3 Cost Volume Regularization

The purpose of cost volume regularization is to predict relatively accurate depth values based on aggregated features and smooth and refine the cost volume to generate high-quality depth maps. Common methods for cost volume regularization include 3D CNN-based neural networks, such as those used in Atlas^[23], recurrent neural networks (RNNs) as in DHC-RMVSNet^[24], and a coarse-to-fine aggregation strategy used in NeuralRecon^[12]. Among them, 3D CNN can aggregate local and global features across all dimensions but requires higher computational cost; RNN reduces memory consumption by sequentially processing each depth hypothesis; the coarse-to-fine strategy improves the accuracy and details of the depth map through multiple stages of prediction and refinement.

In summary, the workflow of convolution-based 3D reconstruction includes three key steps: feature extraction, cost volume construction, and cost volume regularization. Through these steps, features can be extracted from input images, cost volumes can be constructed, and depth estimation and reconstruction can be performed using the cost volumes, thereby achieving a complete 3D reconstruction process.

2.3 Neural Implicit Surface-Based 3D Reconstruction Methods

Neural implicit surface-based 3D reconstruction methods (Fig. 3), such as NeuS and nvdiffric, represent cutting-edge technology in the field of 3D reconstruction. These methods, which involve learning the implicit representation of object surfaces through neural networks, have made significant advancements. For instance, NeuS introduces a novel volumetric rendering method by training neural signed distance function (SDF)

representations, achieving high-quality 3D reconstructions. Nvdiffrec adopts the marching tetrahedra algorithm to generate higher-quality mesh models. However, neural implicit surface-based methods still face some challenges, including accurately capturing boundary information in complex scenes, handling dynamic objects and camera motion and enhancing their ability to process details and textures. In the future, the development of these methods may focus on improving the robustness of models, expanding their applicability to a wider range of scenarios and enhancing their ability to handle details and boundary information. These methods have opened up new possibilities in the field of 3D reconstruction and hold potential for future research and applications.

Inspired by the density-based volume rendering algorithm in NeRF^[8], significant progress has been made in combining neural implicit surface representation with volume rendering in 3D reconstruction. Neural implicit surface-based 3D reconstruction methods learn the implicit representation function of objects through neural networks and project the reconstructed models to pixel space through volume rendering for training optimization, ultimately achieving high-quality 3D reconstruction.

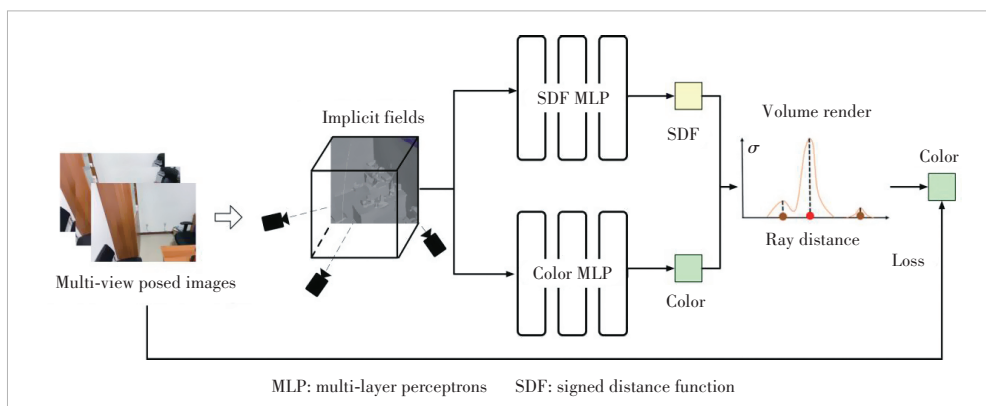
2.3.1 Neural Implicit Surface Representation

Most neural implicit surface representation methods^[13-14] model the surface of the target object or scene using two functions. The first function $f: R^3 \rightarrow R$ converts spatial coordinates into signed distances from the point to the object surface, where the object's surface is represented by the zero level set of SDF, as shown in Eq. (1).

$$S = \{x \in R^3 | f(x) = 0\}. \quad (1)$$

The other function $c: R^3 \times S^2 \rightarrow R^3$ encodes pixel colors related to spatial coordinates and viewing directions. Two multi-layer perceptrons (MLPs) are used to approximate these two functions. A new volume rendering method is developed in NeuS^[14] to train the neural SDF representation. YARIV et al.^[13] improved the geometric representation and reconstruction in neural volume rendering by modeling the volume density as a function of geometry, as arbitrary level set extraction of the density function may lead to low-fidelity reconstruction.

To address the presence of numerous large planar surfaces and weakly textured areas in indoor scenes, some methods also add constraints to the loss function to constrain the training results and produce smoother surface representations. For example, MonoSDF^[25] uses depth and normal maps to constrain



▲ Figure 3. Overview of neural implicit surface-based methods

the reconstruction results and eliminate noise and discontinuities in the reconstructed surface through normal consistency.

2.3.2 Surface Reconstruction

The generated neural implicit field describes the density and color information of each spatial point in the scene. However, to further analyze and visualize the reconstruction results, it is necessary to extract the surface geometry information of objects from the model and convert the continuous object geometry into a discrete voxel representation. Voxel sampling divides the 3D space into a set of small cubic units. By inputting the coordinates of each voxel vertex into an MLP network, the implicit function value of the voxel can be obtained, which records whether it is inside or outside the object and the distance to the object's surface. Specifically, to begin the surface reconstruction process, a three-dimensional grid is first defined within the 3D space. Typically, this grid takes the form of a cube or voxel grid. This grid serves as the basis for point sampling, facilitating the computation of the distance from each point to the object's surface. For each point within this grid, its coordinates are fed into a pre-trained neural network. The neural network then produces an output representing the distance from the point to the object's surface, which is the output of the neural implicit surface function. This distance value is used to determine whether each point is located on the object's surface, with points on the surface generally having a distance of zero or very close to zero. Consequently, the sign of the distance value can be employed to detect points situated on the surface. After identifying the surface points, triangles or other polygons can be generated by connecting these points, thus reconstructing the geometric shape of the object's surface. By traversing the voxel grid and using the implicit function values for interpolation, a continuous geometric surface can be generated. For example, the Marching Cubes^[26] algorithm, based on the idea of isosurface extraction, converts the continuous density field into a discrete 3D grid representation to obtain the surface geometry of the object. Additionally, many studies have employed optimized voxelization methods to generate smoother surface representations, such as using the marching tetrahedra algorithm^[27] instead of the Marching Cubes^[26] algorithm to generate high-quality mesh models in Nvdiffrac^[28].

2.3.3 Texture Rendering

To present more realistic object details and achieve more convincing visual effects, existing neural implicit surface-based reconstruction techniques use various methods to model the color, texture, material, and lighting information on the object's surface. For example, in Nvdiffrac^[28], a coordinate-based network is used to achieve a compact representation of volume textures, and environmental lighting segmentation and an approximate differential formula are introduced to efficiently recover full-frequency lighting. The output triangle mesh, along with spatially varying materials and environmental lighting, can be

directly viewed in any traditional graphics engine. Another example is BakedSDF^[29], which bakes the implicit scene representation into a high-quality triangle mesh and then designs a view-dependent appearance model based on spherical Gaussians. This approach generates models that can be used for real-time view synthesis using accelerated polygon rasterization pipelines on commodity hardware.

The implicit texture generation process using xAtlas^[30] involves several steps as follows:

1) Surface data generation: Initially, the 3D model's surface data, including geometric information but excluding texture information, is generated based on the implicit surface neural radiance field.

2) UV mapping: xAtlas^[30] is then used to perform UV mapping, which associates texture coordinates with the surface of the 3D model. UV mapping is a 2D coordinate system commonly used to map texture images onto the surface of 3D objects. In this step, xAtlas calculates UV coordinates for each vertex of the triangular mesh, ensuring proper texture mapping onto the model.

3) Texture Atlas packing: This step involves packing multiple texture images into a single large texture map, which reduces the number of texture switches during rendering and enhances rendering performance. To efficiently allocate texture space on the texture image, xAtlas^[30] subdivides the triangular mesh into multiple regions, each having its own UV space. The size and shape of these regions are determined based on surface characteristics to ensure even texture allocation.

4) Optimizing texture layout: Once the UV subdivision is completed, xAtlas^[30] determines the texture layout for each region based on their shapes and sizes. This optimization aims to minimize empty areas and wasted texture space.

5) Combining texture images: Finally, xAtlas^[30] combines the texture images from these regions into a single large texture map and generates a new UV mapping that correctly maps each triangle on the 3D model's surface to the appropriate texture region. This new UV mapping and the merged texture images are fine-tuned through trainable parameters to produce the final texture map.

In summary, the process involves generating a UV mapping that links the 3D model's surface to a set of texture regions, packing multiple texture images into a single large texture map, and optimizing the layout of these texture regions to minimize waste. This results in a final texture map that can be applied to the 3D model for rendering with texture information.

3 Existing Problems

Existing indoor 3D reconstruction techniques based on multi-view RGB images have achieved good reconstruction results in certain situations and within a certain range. However, there are still several problems when it comes to reconstructing complex indoor scenes.

Traditional feature-based 3D reconstruction methods face dif-

difficulties in dealing with a large number of textureless areas and repetitive texture areas in indoor scenes, resulting in holes and noise in the reconstruction results. This limits the application of traditional methods in large-scale and complex scenes.

Deep learning-based 3D reconstruction methods typically use computationally expensive structures such as 3D CNNs or transformers, requiring processing a large amount of image data. Generating high-resolution voxel grids also consumes significant storage resources, posing challenges in terms of computational resources and storage space. Additionally, complex scenes and shape variations require more complex and robust deep learning models to capture details and handle changes. Furthermore, deep learning-based methods often require a large amount of annotated data and model training time, which demands substantial computational resources and time.

3D reconstruction methods based on neural implicit surface representation demonstrate better performance in handling complex scenes and shape variations. However, in the absence of boundary information, such as in large scenes or under low lighting conditions, neural implicit surface representation methods may struggle to accurately capture the boundary information of the scene, leading to blurry or incomplete reconstruction results. Moreover, when there are dynamic objects or camera motion in the scene, methods based on neural implicit surface representation may be affected by motion blur. The movement of dynamic objects can result in the discontinuity of point cloud or voxel grid data, which in turn affects the learning of implicit surface functions and the accuracy of reconstruction results. Furthermore, complex indoor scenes typically contain rich details and structures, such as furniture, decorations, and complex textures. Methods based on neural implicit surface representation may struggle to capture these details when dealing with complex scenes, leading to a decrease in the level of reconstruction detail.

4 Future Directions

With the rapid development of deep learning and neural networks, 3D reconstruction methods based on neural implicit surface representation are continuously evolving and improving. The future research directions include:

1) Fusion of stereovision and deep learning: Combining traditional stereovision methods with deep learning techniques implements deep learning models for feature representation and matching, improving the reconstruction results for textureless and repetitive texture areas. For example, CNNs can be used to extract features, followed by the integration of traditional stereovision matching methods for geometric constraint optimization.

2) Adaptive reconstruction algorithms: Adaptive reconstruction algorithms that leverage reinforcement learning methods are developed to learn the optimal reconstruction strategies through interaction with the environment. The algorithm's parameters and strategies can be adjusted based on the complex-

ity and characteristics of the scene. This aims to enhance the robustness and effectiveness of reconstruction, improving reconstruction efficiency for simple scenes while maintaining high-quality reconstruction results for complex scenes.

3) Fusion of cross-modal data: RGB images are combined with other data sources such as depth maps, normal maps and metadata to provide a more comprehensive and diverse information source. Consideration can also be given to incorporating semantic information into the 3D reconstruction process to improve the semantic consistency and accuracy of the reconstruction results. Techniques such as semantic segmentation and object detection can guide the model to better understand and model different objects and scenes during the reconstruction process.

4) Generalization capability of models: Current neural implicit surface reconstruction methods typically require a large amount of training data and need to be retrained for different objects and scenes. The future research direction is to improve the generalization capability of models, enabling them to learn and reconstruct different objects and scenes from limited data and handle complex situations such as different lighting conditions, dynamic scenes, and camera motion. It is also necessary to construct larger and more diverse indoor scenes.

5 Conclusions

This paper presents three major categories of methods for indoor 3D reconstruction using multi-view RGB images: traditional methods based on feature matching, deep learning-based methods, and methods based on neural implicit surfaces. The specific workflows and development status of each method are described, and the existing issues of current methods are analyzed. Future directions are proposed to guide the future development of 3D reconstruction in indoor scenes.

References

- [1] FISHER A, CANNIZZARO R, COCHRANE M, et al. ColMap: a memory-efficient occupancy grid mapping framework [J]. *Robotics and autonomous systems*, 2021, 142: 103755. DOI: 10.1016/j.robot.2021.103755
- [2] CERNEA D. OpenMVS: multi-view stereo reconstruction library [EB/OL]. [2023-05-20]. <https://cdseacave.github.io/openMVS>
- [3] YANG J Y, MAO W, ALVAREZ J M, et al. Cost volume pyramid based depth inference for multi-view stereo [C]//Proc. IEEE/CVF Conference on Computer Vision and Pattern Recognition (CVPR). IEEE, 2020: 4876 - 4885. DOI: 10.1109/CVPR42600.2020.00493
- [4] WEI Z Z, ZHU Q T, MIN C, et al. AA-RMVSNet: Adaptive aggregation recurrent multi-view stereo network [C]//Proc. IEEE/CVF International Conference on Computer Vision (ICCV). IEEE, 2021: 6167 - 6176. DOI: 10.1109/ICCV48922.2021.00613
- [5] LU P, SHENG B, SHI W Z. Scene visual perception and AR navigation applications [J]. *ZTE communications*, 2023, 21(1): 81 - 88. DOI: 10.12142/ZTECOM.202301010
- [6] VASWANI A, SHAZEER N, PARMAR N, et al. Attention is all you need [J]. *Advances in neural information processing systems*, 2017: 30
- [7] DOSOVITSKIY A, BEYER L, KOLESNIKOV A, et al. An image is worth 16×16 words: transformers for image recognition at scale [EB/OL]. (2020-01-

- 22[2023-05-20]. <http://arxiv.org/abs/2010.11929>
- [8] MILDENHALL B, SRINIVASAN P P, TANCIK M, et al. NeRF: representing scenes as neural radiance fields for view synthesis [M]/Lecture Notes in Computer Science. Cham: Springer International Publishing, 2020: 405 – 421. DOI: 10.1007/978-3-030-58452-8_24
- [9] MATURANA D, SCHERER S. VoxNet: a 3D Convolutional Neural Network for real-time object recognition [C]/Proc. IEEE/RSJ International Conference on Intelligent Robots and Systems (IROS). IEEE, 2015: 922 – 928. DOI: 10.1109/IROS.2015.7353481
- [10] WANG N Y, ZHANG Y D, LI Z W, et al. Pixel2Mesh: generating 3D mesh models from single RGB images [C]/European Conference on Computer Vision. Cham: Springer, 2018: 55 – 71. DOI: 10.1007/978-3-030-01252-6_4
- [11] SAYED M, GIBSON J, WATSON J, et al. SimpleRecon: 3D reconstruction without 3D convolutions [M]/Lecture Notes in Computer Science. Cham: Springer Nature Switzerland, 2022: 1 – 19. DOI: 10.1007/978-3-031-19827-4_1
- [12] SUN J M, XIE Y M, CHEN L H, et al. NeuralRecon: real-time coherent 3D reconstruction from monocular video [C]/Proc. IEEE/CVF Conference on Computer Vision and Pattern Recognition (CVPR). IEEE, 2021: 15593 – 15602. DOI: 10.1109/CVPR46437.2021.01534
- [13] YARIV L, GU J T, KASTEN Y, et al. Volume rendering of neural implicit surfaces [C]/Proc. 35th International Conference on Neural Information Processing System. NIPS, 2021: 4805 – 4815
- [14] WANG P, LIU L J, LIU Y, et al. NeuS: learning neural implicit surfaces by volume rendering for multi-view reconstruction [EB/OL]. (2020-06-20) [2023-05-20]. <http://arxiv.org/abs/2106.10689>
- [15] NG P C, HENIKOFF S. SIFT: predicting amino acid changes that affect protein function [J]. *Nucleic acids research*, 2003, 31(13): 3812 – 3814. DOI: 10.1093/nar/gkg509
- [16] BAY H, ESS A, TUYTELAARS T, et al. Speeded-up robust features (SURF) [J]. *Computer vision and image understanding*, 2008, 110(3): 346 – 359. DOI: 10.1016/j.cviu.2007.09.014
- [17] RUBLEE E, RABAUD V, KONOLIGE K, et al. ORB: an efficient alternative to SIFT or SURF [C]/Proc. International Conference on Computer Vision. IEEE, 2011: 2564 – 2571. DOI: 10.1109/ICCV.2011.6126544
- [18] MOULON P, MONASSE P, PERRROT R, et al. OpenMVG: open multiple view geometry [M]/KERAUTRET B, COLOM M, MONASSE P, eds. *Lecture Notes in Computer Science*. Cham: Springer International Publishing, 2017: 60 – 74. DOI: 10.1007/978-3-319-56414-2_5
- [19] WU Z F, SHEN C H, VAN DEN HENGEL A. Wider or deeper: revisiting the ResNet model for visual recognition [J]. *Pattern recognition*, 2019, 90: 119 – 133. DOI: 10.1016/j.patcog.2019.01.006
- [20] BARKAU R L. UNET: one-dimensional unsteady flow through a full network of open channels. User's manual [R]. Hydrologic Engineering Center Davis CA, 1996
- [21] YAO Y, LUO Z X, LI S W, et al. MVSNet: depth inference for unstructured multi-view stereo [C]/European Conference on Computer Vision. Springer, 2018: 785-801. DOI: 10.1007/978-3-030-01237-3_47
- [22] IM S, JEON H G, LIN S, et al. DPSNet: end-to-end deep plane sweep stereo [EB/OL]. (2019-05-02)[2023-05-06]. <http://arxiv.org/abs/1905.00538>
- [23] MUREZ Z, VAN AS T, BARTOLOZZI J, et al. Atlas: end-to-end 3D scene reconstruction from posed images [M]/Lecture Notes in Computer Science. Cham: Springer International Publishing, 2020: 414 – 431. DOI: 10.1007/978-3-030-58571-6_25
- [24] YAN J F, WEI Z Z, YI H W, et al. Dense hybrid recurrent multi-view stereo net with dynamic consistency checking [C]/16th European Conference on Computer Vision. Cham: Springer, 2020: 674-689.10.1007/978-3-030-58548-8_39
- [25] YU Z H, PENG S Y, NIEMEYER M, et al. MonoSDF: exploring monocular geometric cues for neural implicit surface reconstruction [EB/OL]. (2022-06-01)[2023-05-20]. <http://arxiv.org/abs/2206.00665>
- [26] LORENSEN W E, CLINE H E. Marching cubes: a high resolution 3D surface construction algorithm [J]. *ACM SIGGRAPH computer graphics*, 1987, 21(4): 163 – 169. DOI: 10.1145/37402.37422
- [27] SHEN T, GAO J, YIN K, et al. Deep marching tetrahedra: a hybrid representation for high-resolution 3d shape synthesis [J]. *Advances in Neural Information Processing Systems*, 2021, 34: 6087-6101.
- [28] MUNKBERG J, CHEN W Z, HASSELGREN J, et al. Extracting triangular 3D models, materials, and lighting from images [C]/Proc. IEEE/CVF Conference on Computer Vision and Pattern Recognition (CVPR). IEEE, 2022: 8270 – 8280. DOI: 10.1109/CVPR52688.2022.00810
- [29] YARIV L, HEDMAN P, REISER C, et al. BakedSDF: meshing neural SDFs for real-time view synthesis [EB/OL]. (2022-06-01)[2023-05-20]. <http://arxiv.org/abs/2302.14859>
- [30] FAREK J, HUGHES D, SALERNO W, et al. xAtlas: Scalable small variant calling across heterogeneous next-generation sequencing experiments [J]. *GigaScience*, 2023, 12: giac125. DOI: 10.1093/gigascience/giac125

Biographies

LU Ping (lu.ping@zte.com.cn) is the deputy president of ZTE Corporation, where he is also the general manager of the Industrial Digitalization Solution Dept., and the executive deputy director of State Key Laboratory of Mobile Network and Mobile Multimedia Technology. His research interests include cloud computing, big data, augmented reality, and multimedia service-based technologies. He has supported and participated in multiple major national science and technology projects and national science and technology support projects. He has published multiple papers and authored two books.

SHI Wenzhe (shi.wenzhe@zte.com.cn) is a strategy planner of ZTE Corporation where he is also an engineer for XRExplore Platform Product Planning and a member of the National Key Laboratory for Mobile Network and Mobile Multimedia Technology. His research interests include indoor visual AR navigation, SFM 3D reconstruction, visual SLAM, real-time cloud rendering, VR, and spatial perception.

QIAO Xiuquan is currently a full professor with Beijing University of Posts and Telecommunications, China, where he is also the deputy director of the Network Service Foundation Research Center, State Key Laboratory of Networking and Switching Technology. He has authored or co-authored over 60 technical papers in international journals and at conferences, including the *IEEE Communications Magazine*, *Proceedings of IEEE*, *Computer Networks*, *IEEE Internet Computing*, *IEEE Transactions on Automation Science and Engineering*, and *ACM SIGCOMM Computer Communication Review*. His current research interests include the future Internet, services computing, computer vision, distributed deep learning, augmented reality, virtual reality, and 5G networks. Dr. QIAO was a recipient of the Beijing Nova Program in 2008 and the First Prize of the 13th Beijing Youth Outstanding Science and Technology Paper Award in 2016. He served as the associate editor for *Computing* (Springer) and the editor board of *China Communications*.

Intelligence Driven Wireless Networks in B5G and 6G Era: A Survey



GAO Yin^{1,2}, CHEN Jiajun^{1,2}, LI Dapeng^{1,2}

(1. State Key Laboratory of Mobile Network and Mobile Multimedia Technology, Shenzhen 518055, China;

2. Wireless Product R&D Institute, ZTE Corporation, Shanghai 201203, China)

DOI: 10.12142/ZTECOM.202403012

<https://kns.cnki.net/kcms/detail/34.1294.TN.20240903.1032.004.html>,
published online September 3, 2024

Manuscript received: 2024-03-11

Abstract: As the wireless communication network undergoes continuous expansion, the challenges associated with network management and optimization are becoming increasingly complex. To address these challenges, the emerging artificial intelligence (AI) and machine learning (ML) technologies have been introduced as a powerful solution. They empower wireless networks to operate autonomously, predictively, on-demand, and with smart functionality, offering a promising resolution to intricate optimization problems. This paper aims to delve into the prevalent applications of AI/ML technologies in the optimization of wireless networks. The paper not only provides insights into the current landscape but also outlines our vision for the future and considerations regarding the development of an intelligent 6G network.

Keywords: intelligent network; native AI; load prediction; trajectory prediction

Citation (Format 1): GAO Y, CHEN J J, LI D P. Intelligence driven wireless networks in B5G and 6G era: a survey [J]. *ZTE Communications*, 2024, 22(3): 99 – 105. DOI: 10.12142/ZTECOM.202403012

Citation (Format 2): Y. Gao, J. J. Chen, and D. P. Li, "Intelligence driven wireless networks in B5G and 6G era: a survey," *ZTE Communications*, vol. 22, no. 3, pp. 99 – 105, Sept. 2024. doi: 10.12142/ZTECOM.202403012.

1 Introduction

The rapid growth of mobile subscribers and the introduction of numerous new services have led to the continuous expansion of wireless communication networks. In addition, the diversity of network deployment and the increase of network parameters in the 5G era also make network management quite complicated. The large scale and high complexity make it infeasible to achieve the best network optimization solution by human engineers. Fortunately, the advancement of artificial intelligence (AI) and machine learning (ML) technologies has provided a powerful solution to addressing these challenges. AI and ML technologies offer efficient ways to tackle complex problems in wireless communication network management. By leveraging these technologies, the wireless communication network can be autonomous, predicted, on-demand and smart operated, and realize accurate parameter prediction, intelligent resource allocation, and green energy savings, thus greatly enhancing the network performance with less human intervention.

To apply AI/ML to the existing 5G network, the 3rd Generation Partnership Project (3GPP) has also begun the study on

AI/ML topics^[1-3]. In terms of the radio access network (RAN), the enhancement of data collection for intelligence has been studied, including the high-level principles, the functional framework, and scenarios (network energy saving, load balancing, and mobility optimization) for AI-assisted network optimization. The RAN3 work group further discusses the corresponding normative work in Release-18 to enhance the collection of measurement through signaling based on the existing next-generation (NG)-RAN interfaces and architecture. In addition, the research on the intelligence of air interface is also carried out by the RAN1 work group, which studies the lifecycle management, scenarios such as channel state information (CSI) feedback enhancements, beam management and positioning improvement, evaluations for each use case and potential impact to the current specification.

This paper presents the popular application of AI/ML techniques in wireless network optimization and provides our future vision and consideration on a 6G intelligent network. The subsequent sections of this paper are outlined as follows. In Section 2, we review some achievements in AI/ML assisted wireless communication network optimization. Section 3 describes the potential implementation of AI/ML based use cases over existing network architecture. Finally, future vision and consideration are provided in Section 4, followed by the conclusion of this paper in Section 5.

This work was supported in part by the National Natural Science Foundation of China under Grant No. 62201266, and in part by the Natural Science Foundation of Jiangsu Province under Grant No. BK20210335.

2 Applications of AI/ML Techniques in Wireless Network Optimization

In wireless communication systems, AI/ML algorithms have been extensively used for various usage such as traffic load prediction, mobility prediction, radio link failure prediction^[4], positioning^[5], and network slicing resource management^[6]. Various experiments or practices have been carried out to show the potential benefits of AI/ML-assisted wireless network optimization.

2.1 Network Energy Saving

Energy conservation has always been a global and eternal topic in various walks of life. Especially in the mobile communication industry, the relentless expansion of mobile communication networks to meet the demands of an unprecedented surge in mobile subscribers has resulted in a rapid increase in energy consumption. To reduce the huge energy consumption and achieve a greener mobile communication network, numerous research projects have been started with different contribution areas like services, architecture, and intelligence during the past years^[7].

Numerous energy-saving strategies, including symbol shutdown, carrier shutdown, channel shutdown, deep sleep, and symbol aggregation, have been proposed^[8]. However, existing energy conservation is usually vulnerable due to some potential issues such as imprecise traffic prediction, imbalance between performance and efficiency, inflexible parameter adjustment, and localized energy efficiency improvement leading to an overall deterioration^[1]. AI/ML based energy-saving strategies can realize accurate load prediction, flexible parameter optimization, service forecasting, and scene identification, to select the most suitable shut-down schemes for a certain scenario without significantly deteriorating the system performance.

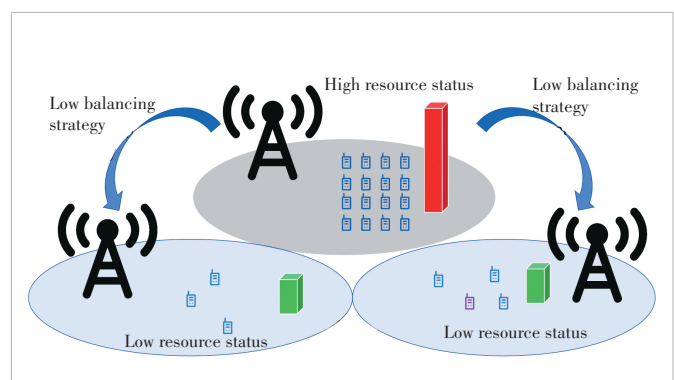
In Ref. [9], the energy-saving performance of strategies including symbol switch-off, channel switch-off, and carrier switch-off with the assistance of Auto Regressive Integrated Moving Average (ARIMA) is evaluated in real scenarios. The results show that the machine learning technique can bring the percentage of the switch-off duration per cell up to 176%, increase the switch-off duration and 1.24 kWh power saving per cell per day without affecting basic key performance indicators (KPIs), and the total electrical saving per week is increased by CNY 2 223 compared with the conventional energy saving strategies^[9]. AI/ML based channel shutdown, symbol shutdown and deep sleep are used in the real test involving 54 active antenna units (AAU) for energy saving, resulting in a reduction of 23.87% in power consumption and an improvement of 23.4% in energy efficiency^[10]. Ref. [11] illustrates an energy-efficiency optimization algorithm through deep reinforcement learning (DRL) by simulation, and shows that the DRL-assisted energy-saving algorithm can bring about 50 W or 40% power savings compared with the initial system. AI-based service awareness, capable of discerning

variations in the energy efficiency of different service types, is integrated with AI-based traffic forecasting for the optimization of energy-saving strategies. This approach results in a daily energy saving of 13.7 kWh, with energy saving increasing by nearly 10%^[12].

2.2 Traffic Load Prediction

Traffic prediction plays a pivotal role in network optimization and serves various use cases, including energy conservation and mobile load balancing. Traditional models such as linear regression and support vector machines (SVM) have reached maturity in traffic load prediction. With the quick evolution of deep learning, increasingly sophisticated algorithms are being employed for more accurate predictions. Load prediction plays a significant role in assisting load balancing as illustrated in Fig. 1.

Several supervised and unsupervised learning algorithms for predicting the resource status on sites are compared in terms of accuracy, time consumption, and memory usage by using the real-world datasets of the wireless Long-Term Evolution (LTE) network, and the results show that the Automated Neural Net (ANN) has the highest prediction accuracy about 80%, and the SVM and Self-Organizing Maps (SOM) can also provide above 70% accuracy^[13]. Ref. [14] proposes a new type of federated learning (FL) mechanism to solve data security and privacy issues in the commonly-used-centralized training models, and the prediction accuracy can reach 86.02%, close to the state-of-the-art FL models while significantly reducing the communication cost. Ref. [15] introduces two models, Ensemble and ResNet, for traffic load prediction, and compares their prediction performance in the same scenario with ARIMA and Prophet as the baseline. The result states that the prediction accuracy of the ensemble model which takes time, space, and historical information into consideration is much higher than ARIMA and Prophet. The calculation complexity of ResNet is significantly lower than that of baseline models, as it can generate results for all cells in a single training session. This characteristic makes it particularly suitable for traffic load prediction tasks involving large datasets.



▲ Figure 1. Benefits to load balancing with assistance of artificial intelligence (AI)/machine learning (ML)

2.3 UE Trajectory Prediction

The ultra-dense network deployment in the 5G mobile communication system consists of numerous small cells to satisfy the requirements of ultra-high reliability, low latency, and high data rate. This can lead to more frequent handovers for high-mobility UE, thus resulting in problems such as high latency, throughput reduction, radio link failure (RLF), and ping-pong effect. Therefore, mobility optimization is of vital importance, and one of the key parts of mobility optimization is UE trajectory prediction. Since human mobility is predictable to some extent, it is feasible to analyze user's mobility patterns through their history trajectory information^[16], and can be enhanced by using machine learning techniques.

Ref. [16] learns the mobility pattern of user equipment (UE) from historical trajectories and predicts its future movement trends using the Long Short Term Memory (LSTM) structure, and the prediction result is used in the proposed intelligent dual connectivity mechanism for handover optimization. The simulation results demonstrate that, even as cell density increases, the average handover prediction accuracy for low-speed users remains high^[16]. Ref. [17] proposes multiple features that combine UE history trajectory with the reference signal receiving power (RSRP) measurement reports from serving and neighbor base stations as input of the sequence-to-sequence model for next-time location prediction, and introduces orientation loss function to analyze the direction of movement. Simulation results show that with RSRP and orientation loss function, the average distance error decreases from 48.634 m to 38.457 m, and the accuracy of predicted connected nodes the next time can be up to 98.26%^[17]. Ref. [18] compares the performance of various models for AI-based mobility prediction, and Bidirectional Long Short Term Memory (Bi-LSTM)-attention shows the highest accuracy up to 91.78%, while ANN consumes the shortest training time due to its low complexity.

3 Implementation of AI/ML Based Use Cases over Network Architecture

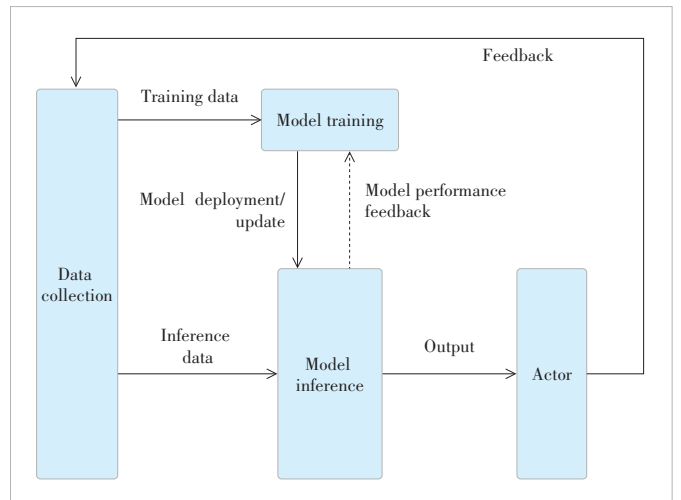
The key to integration between AI/ML and wireless networks is to resolve the issue of how to implement the AI/ML based use cases over existing network architecture. Existing network architecture includes next-generation radio access network (NG-RAN) nodes, UE, and core networks, and each network entity can be in charge of different functions to support AI/ML, e.g., training and inference. Different scenarios may call for various deployment methods for AI/ML models.

A framework for RAN intelligence (Fig. 2) has been described in 3GPP TR 37.817^[1]. The data collection function collects different kinds of data for the AI/ML model, such as measurements from UE or gNBs, predictions or decisions output from AI/ML models, and feedback from the actor, and provides the input data for training and inference function. Input data can be used after the data preparation procedure, such as data pre-processing, is performed by the model training function and

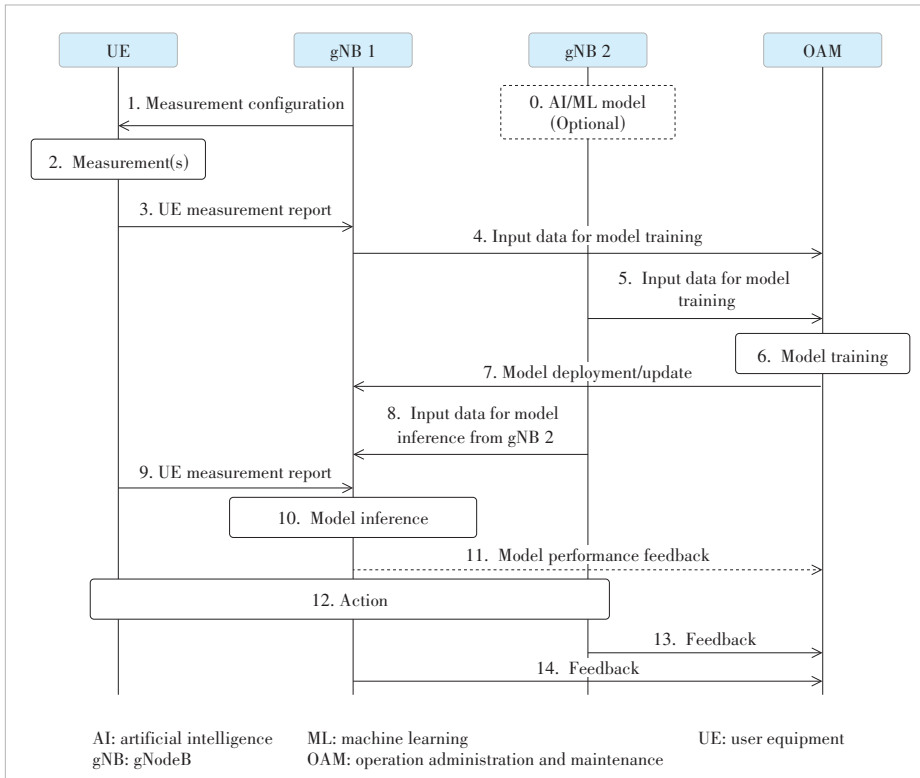
model inference function. The model training function trains, validates and tests the AI/ML model, which will be deployed to the model inference function after these procedures. The model inference function generates predictions or decisions and a trained AI/ML model from the model training function. Additionally, it offers model performance feedback to monitor and optimize model performance. The actor function executes actions based on decisions made by the model inference function and provides feedback to the data collection.

Some enhancements are needed in the current 5G RAN to integrate AI/ML functions. From the perspective of specification, three use cases, i.e., network energy saving, load balancing, and mobility optimization, are first considered to be standardized for supporting AI/ML functions. For these three AI/ML based use cases, model training can be located in either operation administration and maintenance (OAM) or gNB, while the model inference is located in gNB. In the case of centralized unit/distributed unit (CU-DU) split RAN architecture, model training can be located in either OAM or gNB-CU, while the model inference is located in gNB-CU.

Fig. 3 shows the general flow chart of an AI-based use case with model training at OAM and model inference at gNB. UE is currently served by gNB 1, while gNB 2 can be the neighbouring gNB optionally with an AI/ML model. The OAM collects the input data needed for model training, including the measurement report of UE, input data from serving gNB and neighbouring gNB, and performs model training. The trained AI/ML model is then deployed/updated into the gNB 1 (this step is out of the RAN3 Rel-17 scope) for further training or model inference. Based on the local input data from gNB 1 and other indicated input data from UE and gNB 2, gNB 1 performs model inference to make decisions or predictions, and this output can also be the model performance feedback sent to the OAM. The gNB 1 executes the action based on the model inference output and provides feedback to OAM for



▲ Figure 2. Functional framework for radio access network (RAN) intelligence



▲ Figure 3. Deployment of AI/ML functionality: model training at OAM and model inference at next-generation radio access network (NG-RAN)

model performance monitoring and training optimization.

Fig. 4 shows the general flow chart of an AI-based use case with model training and model inference at gNB.

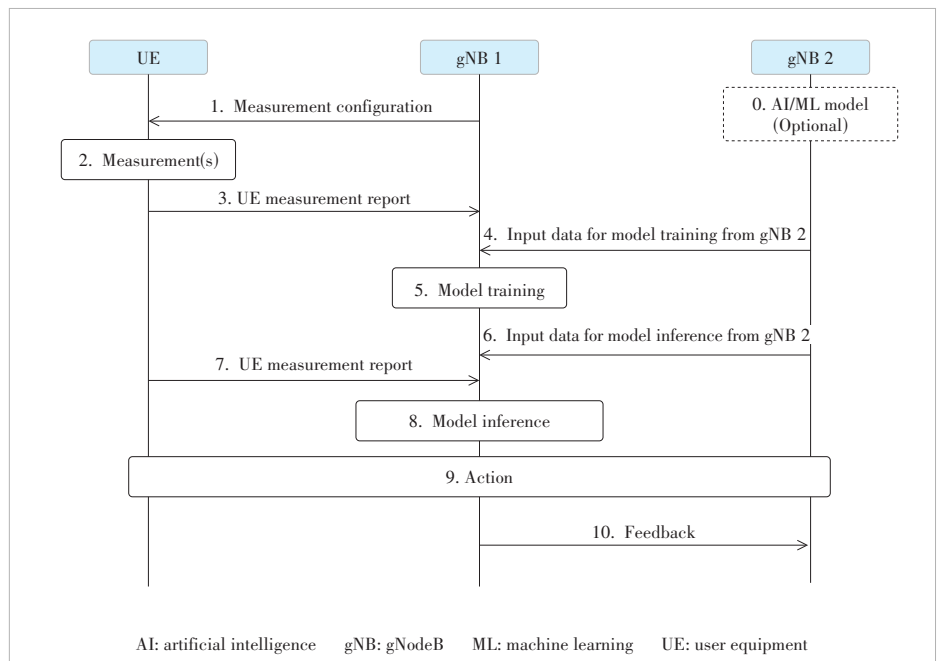
It can be seen that the overall procedure is similar to the previously introduced flow chart. The difference is that since the model training and model inference are both performed in gNB 1, the input data for model training and model inference and the feedback after the action are directly sent to gNB 1.

Across the three AI/ML-based use cases, the predicted resource status, the predicted number of active UEs, predicted radio resource control (RRC) numbers and predicted UE trajectory are considered as types of predicted assistance information to be reported between NG-RAN nodes.

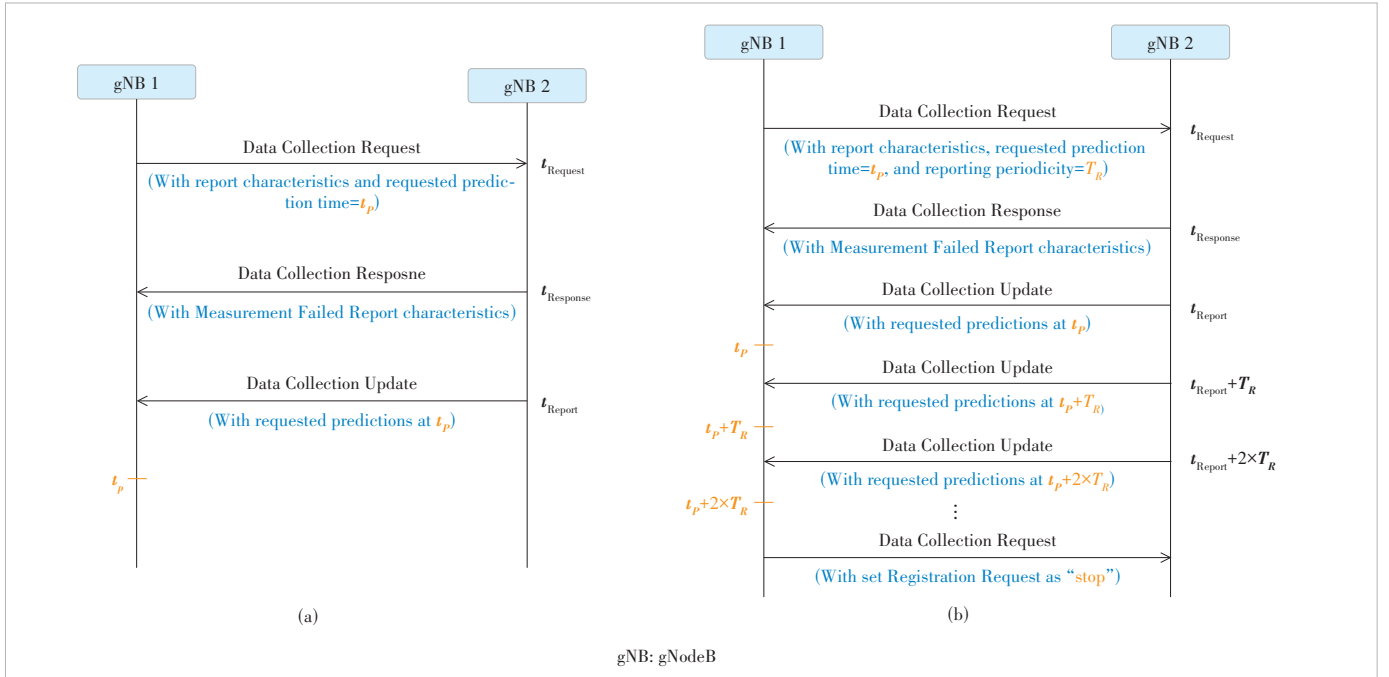
Take predicted resource status information as an example. It can be reported at one time or periodically between NG-RAN nodes. The flow charts of one-time reporting and periodic reporting are shown in Figs. 5(a) and 5(b). In one-time reporting, the

requesting node requests the reporting of predictions by sending the Data Collection Request message and configures the requested prediction time (a specific point of time in the reasonable future for which the prediction information is requested) as t_p . The requested node makes predictions based on its own AI/ML model and reports the successfully initiated predictions in the Data Collection Update message to the requesting node for one time at t_{Report} , which is a time point ahead of t_p . For periodic reporting, the reporting periodicity is also configured in the Data Collection Request message. The requested predictions will be reported every T_R at time points of $t_{Report} + N \times T_R$ ($N = 0, 1, 2, \dots$), corresponding to the requested prediction time of $t_p + N \times T_R$, until the requesting node sends the Data Collection Request message to stop the report.

Meanwhile, UE performance feedback (including average UE throughput DL/UL, average packet delay, and average packet loss), measured UE trajectory, and energy cost are considered measurements to support AI/ML functions, such as model performance evaluation.



▲ Figure 4. Deployment of AI/ML functionality: model training and model inference at next-generation radio access network (NG-RAN)



▲ Figure 5. Flowcharts of transferring predicted information: (a) one-time reporting; (b) periodic reporting

Take the UE performance feedback as an example. It can also be reported at one time or periodically, as illustrated in Figs. 6(a) and Fig. 6(b). Since the UE performance is the average information over a period of time measured at the traffic offloaded neighbouring gNB, a new data collection ID, IE, is included in the Handover Request message as a trigger indication to request the measurement of UE performance at the target gNB after the successful handover, while the configuration of measurement and reporting is still indicated in the Data Collection Request message. In one-time reporting, the target gNB starts the UE performance measurement collection after the successful handover until the measurement collection duration expires, and reports the measured UE performance for one time to the source gNB. In periodic reporting, for one pair of measurement IDs, the reporting periodicity is calculated from the egress of the Data Collection Response message, namely, the UE performance feedback is reported through the Data Collection Update message every T_R at time points of $t_{\text{Response}} + N \times T_R$, which can effectively avoid the signaling storm caused by the UE handed over at different times.

With the introduced solutions to supporting AI/ML functions over the Xn interface between NG-RAN nodes, the RAN node can infer future information, aiding operators in optimizing their network and enhancing the user experience.

4 Future Vision on AI/ML Assisted Wireless Network

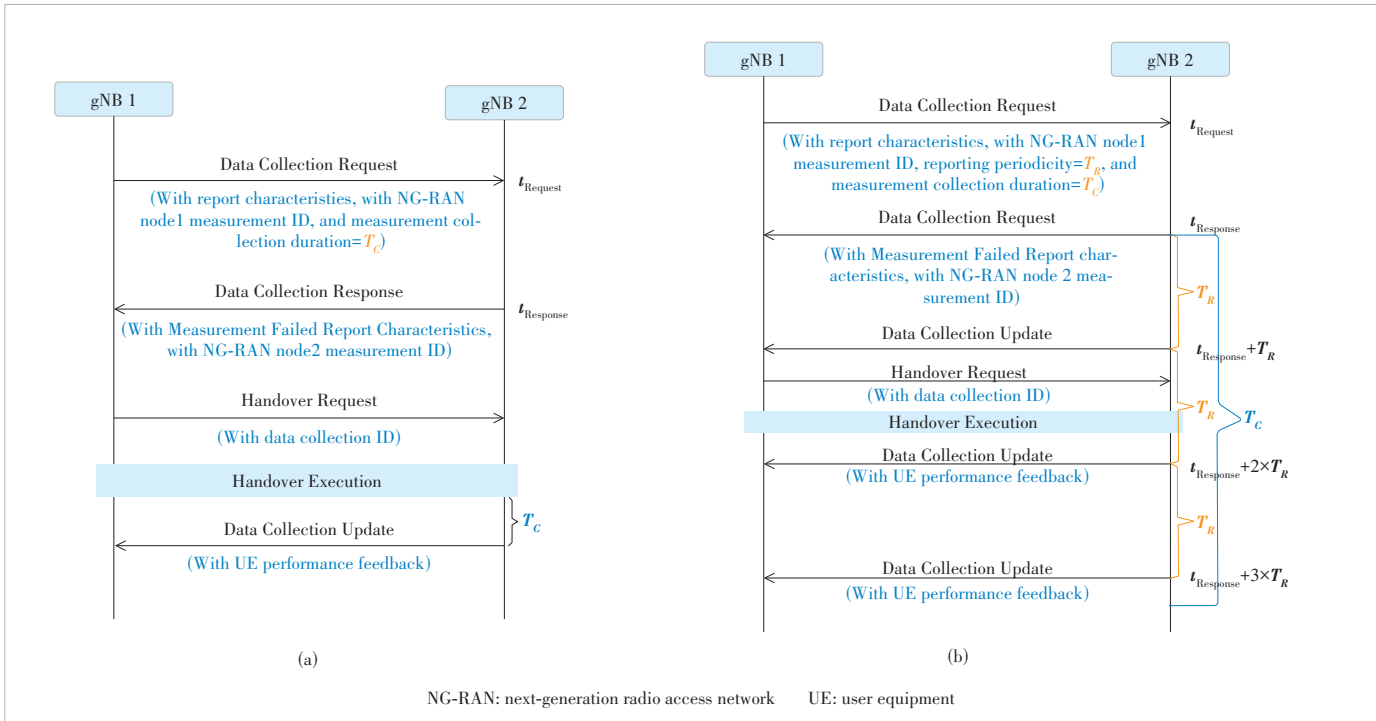
The development of the 6G network is currently a vigorously researched topic in both the telecommunications industry and the academic community. For 6G, there are higher and

more requirements compared to 5G mobile networks in terms of key objectives, such as coverage, speed, latency, capacity, AI, integrated sensing and communication (ISAC), and computing. From our perspective, 6G networks need to achieve seamless human-machine and machine-machine interactive communications, while humans are at the center of control and judgment. Inter-working between humans and machines will become more frequent and broader in the future, not only for the devices bought by people, such as wearable devices and sensing devices, but also for those variant devices in society and industry, e. g., cameras, vehicles, robots, and unmanned aerial vehicles (UAVs). Such collaborative intelligent interaction can be achieved by AI/ML tools based on the amount of data perception, while machine cognition must be handled carefully. During human-machine interaction, three key points need to be considered: intelligence, energy efficiency, and security, as illustrated in Fig. 7.

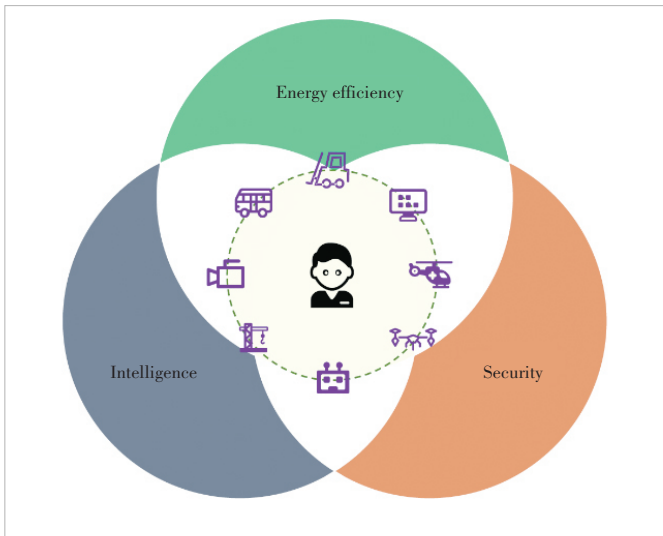
1) Intelligence

In the realm of artificial intelligence, the current focus of 5G is to treat AI as a tool to assist networks in operations such as load balancing, energy efficiency, and mobility optimization. However, with the advent of 6G, the consideration goes beyond treating AI/ML merely as a tool. Instead, the focus shifts towards deeply integrating AI/ML functionalities into the network layer, aiming to achieve native AI.

From now on, artificial intelligence can be divided into data intelligence, perception intelligence, cognitive intelligence, and autonomous intelligence. Data intelligence refers to the ability of computing hardware to analyze and categorize data stored, which can be considered the most fundamental level of



▲ Figure 6. Flow charts of transferring UE performance feedback: (a) one-time reporting; (b) periodic reporting



▲ Figure 7. 6G network: inter-working between human and machine for sustainability

intelligence. Perception intelligence means that computing units have perceptual capabilities to recognize diverse information, such as videos, images, and sounds. From an implementation and security perspective, perception intelligence will become an efficient level of intelligence in 6G networks. By perceiving and analyzing data from various network elements and layers (including communication quality, user experience, use case requirements, etc.), it will make a large number of human-machine interactions more efficient.

2) Energy efficiency

Energy efficiency is one of the key concerns for operators, whether in the current 5G or future 6G networks. For 6G, as there will be an introduction of a larger number of terminal devices and the need to support computing capabilities for AI/ML functions, the substantial increase in data transmission can lead to a significant rise in energy consumption. This increased energy consumption can adversely affect the sustainability of 6G networks and result in a considerable number of carbon emissions. Therefore, energy-saving efficiency strategies need to be further developed. This may involve using artificial intelligence to predict traffic volume and minimize energy consumption or treating energy services as a specific service criterion.

3) Security

6G security aims to ensure that systems are protected against unintended and unauthorized access, safeguarding personal data and sensitive network information. Enhanced encryption algorithms can be used to protect the privacy of data during transmission and storage. In addition, federated learning is leveraged to use the local training and global training mechanisms to protect the privacy data from UE. Blockchain processes data through decentralization and uses distributed data management to protect user privacy.

5 Conclusions

AI/ML-enabled RAN intelligence has the potential to significantly enhance network performance and user experience. This paper aims to delve into a comprehensive overview of

achievements in optimizing wireless communication networks through the application of AI/ML techniques. Additionally, the paper provides an overview of the implementation of AI/ML based use cases over existing network architecture. The inclusion of this aspect underscores the importance of aligning AI/ML advancements with industry standards, ensuring seamless integration and widespread adoption. As computational capabilities continue to strengthen, diverse application scenarios emerge, and standardization progresses, the paper anticipates an escalating role for AI/ML techniques in shaping the landscape of 5G and the imminent 6G era. The convergence of these factors positions AI/ML as a pivotal force, poised to drive innovation and efficiency in next-generation wireless communication networks.

References

- [1] 3rd Generation Partnership Project (3GPP). Study on enhancement for data collection for NR and EN-DC [R]. 3GPP R 37.817, 2022
- [2] CHEN W S, LIN X Q, LEE J, et al. 5G-advanced toward 6G: past, present, and future [J]. *IEEE journal on selected areas in communications*, 2023, 41 (6): 1592 - 1619. DOI: 10.1109/JSAC.2023.3274037
- [3] 3rd Generation Partnership Project (3GPP). Study on artificial intelligence (AI)/machine learning (ML) for NR air interface [R]. 3GPP TR 37.843, 2023
- [4] BOUTIBA K, BAGAA M, KSENTINI A. Radio link failure prediction in 5G networks [C]//Proc. IEEE Global Communications Conference (GLOBECOM). IEEE, 2021: 1 - 6. DOI: 10.1109/GLOBECOM46510.2021.9685587
- [5] BUTT M M, PANTELIDOU A, KOVÁCS I Z. ML-assisted UE positioning: performance analysis and 5G architecture enhancements [J]. *IEEE open journal of vehicular technology*, 2021, 2: 377 - 388. DOI: 10.1109/OJVT.2021.3110134
- [6] DEBBABI F, JMAL R, CHAARI L, et al. Overview of AI-based algorithms for network slicing resource management in B5G and 6G [C]//Proc. International Wireless Communications and Mobile Computing (IWCMC). IEEE, 2022: 330 - 335. DOI: 10.1109/IWCMC55113.2022.9824988
- [7] LARSEN L M P, CHRISTIANSEN H L, RUEPP S, et al. Toward greener 5G and beyond radio access networks: a survey [J]. *IEEE open journal of the communications society*, 2023, 4: 768 - 797. DOI: 10.1109/OJCOMS.2023.3257889
- [8] TAN R M, WU T, SHI Y, et al. Intelligent energy saving solution of 5G base station based on artificial intelligence technologies [C]//Proc. IEEE International Joint EMC/SI/PI and EMC Europe Symposium. IEEE, 2021: 739 - 742. DOI: 10.1109/EMC/SI/PI/EMCEurope52599.2021.9559261
- [9] GAO Y, CHEN J J, LIU Z, et al. Machine learning based energy saving scheme in wireless access networks [C]//Proc. International Wireless Communications and Mobile Computing (IWCMC). IEEE, 2020: 1573 - 1578. DOI: 10.1109/IWCMC48107.2020.9148536
- [10] CHEN J J, GAO Y, LIU Z, et al. Future vision on artificial intelligence assisted green energy efficiency network [J]. *ZTE communications*, 2023, 21 (2): 34 - 39. DOI: 10.12142/ZTECOM.202302006
- [11] GIANOPOULOS A, SPANTIDEAS S, KAPSALIS N, et al. Supporting intelligence in disaggregated open radio access networks: architectural principles, AI/ML workflow, and use cases [J]. *IEEE access*, 2022, 10: 39580 - 39595. DOI: 10.1109/ACCESS.2022.3166160
- [12] TAN R M, SHI Y, FAN Y Y, et al. Energy saving technologies and best practices for 5G radio access network [J]. *IEEE access*, 2022, 10: 51747 - 51756. DOI: 10.1109/ACCESS.2022.3174089
- [13] SHRIVASTAVA P, PATEL S. Selection of efficient and accurate prediction algorithm for employing real time 5G data load prediction [C]//Proc. IEEE 6th International Conference on Computing, Communication and Automation (ICCCA). IEEE, 2021: 572 - 580. DOI: 10.1109/ICCCA52192.2021.9666235
- [14] NAN J H, AI M, LIU A J, et al. Regional-union based federated learning for wireless traffic prediction in 5G-Advanced/6G network [C]//Proc. IEEE/CIC International Conference on Communications in China (ICCC Workshops). IEEE, 2022: 423 - 427. DOI: 10.1109/ICCCWorkshops55477.2022.9896702
- [15] GAO Y, ZHANG M, CHEN J J, et al. Accurate load prediction algorithms assisted with machine learning for network traffic [C]//Proceedings of International Wireless Communications and Mobile Computing (IWCMC). IEEE, 2021: 1683 - 1688. DOI: 10.1109/IWCMC51323.2021.9498910
- [16] WANG C, ZHAO Z, SUN Q, et al. Deep learning-based intelligent dual connectivity for mobility management in dense network [C]//IEEE 88th Vehicular Technology Conference (VTC-Fall). IEEE, 2018: 1 - 5. DOI: 10.1109/VTCFall.2018.8690554
- [17] GAO Y, CHEN J J, LIU Z, et al. Deep learning based location prediction with multiple features in communication network [C]//Proc. IEEE Wireless Communications and Networking Conference (WCNC). IEEE, 2021: 1 - 5. DOI: 10.1109/WCNC49053.2021.9417278
- [18] WANG W H, DUAN X Y, SUN W F, et al. Research on mobility prediction in 5G and beyond for vertical industries [C]//Proc. IEEE/CIC International Conference on Communications in China (ICCC Workshops). IEEE, 2021: 379 - 383. DOI: 10.1109/ICCCWorkshops52231.2021.9538889

Biographies

GAO Yin (gao.yin1@zte.com.cn) received her master's degree in circuit and system from Xidian University, China in 2005. Since 2005, she has been engaged in the study of 4G/5G technology and is currently a wireless expert and project manager at the research center of ZTE Corporation and the State Key Laboratory of Mobile Network and Mobile Multimedia Technology, China. She has authored or co-authored hundreds of proposals for 3GPP meetings and journal papers in wireless communications and has filed more than 200 patents. She has also worked as 3GPP RAN3 Chair since 2017 and was elected as RAN3 Chair in May 2021.

CHEN Jiajun received his master's degree in communication engineer from Shanghai University, China in 2019. He is currently a 5G research engineer at the R&D center of ZTE Corporation and the State Key Laboratory of Mobile Network and Mobile Multimedia Technology, China. His research interests include 5G wireless communications and artificial intelligence.

LI Dapeng received his MS degree in computer science from University of Electronic Science and Technology of China in 2003. He is currently a senior researcher at ZTE corporation and mainly focuses on research and implementation of wireless access network systems.

Secure SSL/TLS Communication System Based on Quantum Keys



WANG Jigang^{1,2}, LU Yuqian³, WEI Liping^{1,2},

JIANG Xinzao³, ZHANG Han^{1,2}

(1. State Key Laboratory of Mobile Network and Mobile Multimedia, Shenzhen 518055, China;

2. Department of Cyberspace Security, ZTE Corporation, Shenzhen 518057, China;

3. School of Cyber Science and Engineering, Southeast University, Nanjing 211102, China)

DOI: 10.12142/ZTECOM.202403013

<https://kns.cnki.net/kcms/detail/34.1294.TN.20240923.1559.002.html>, published online September 23, 2024

Manuscript received: 2023–10–28

Abstract: Secure Sockets Layer (SSL) and Transport Layer Security (TLS) protocols facilitates a secure framework for identity authentication, data encryption, and message integrity verification. However, with the recent development in quantum computing technology, the security of conventional key-based SSL/TLS protocols faces vulnerabilities. In this paper, we propose a scheme by integrating the quantum key into the SSL/TLS framework. Furthermore, the application of post-quantum algorithms is used to enhance and complement the existing encryption suites. Experimental results show that the proposed SSL/TLS communication system based on quantum keys exhibits high performance in latency and throughput. Moreover, the proposed system showcases good resilience against quantum attacks.

Keywords: SSL/TLS protocols; quantum key; post-quantum cryptography

Citation (Format 1): WANG J G, LU Y Q, WEI L P, et al. Secure SSL/TLS communication system based on quantum keys [J]. *ZTE Communications*, 2024, 22(3): 106 – 115. DOI: 10.12142/ZTECOM.202403013

Citation (Format 2): J. G. Wang, Y. Q. Lu, L. P. Wei, et al., “Secure SSL/TLS communication system based on quantum keys,” *ZTE Communications*, vol. 22, no. 3, pp. 106 – 115, Sept. 2024. doi: 10.12142/ZTECOM.202403013.

1 Introduction

In recent years, the development of quantum computing has posed challenges to the security of traditional encryption algorithms. The Secure Sockets Layer (SSL)/Transport Layer Security (TLS) protocol, which is built upon these conventional encryption algorithms, facilitates identity authentication, data encryption, and message integrity verification. During the handshake phase of the SSL/TLS protocol, the client transmits its supported encryption suites to the server. The server, based on its configuration, selects a suite that encompasses authentication algorithms, key exchange algorithms, digest algorithms, and others. These are employed for subsequent processes such as identity authentication, key negotiation, and encrypted communication. Consequently, if the algorithms within the cipher suite harbor known vulnerabilities such as discrete logarithm and prime factorization problems susceptible to the Shor quantum algorithm^[1], the cipher suite may be insecure, thus imperiling the SSL/TLS protocol against potential attacks.

In this paper, we address the aforementioned issues by incorporating quantum key distribution into the SSL/TLS proto-

col. Quantum keys, as supplementary and preferred sources of keys, offer a resilience against quantum attacks. In situations where quantum keys are inaccessible, the system seamlessly transitions to a post-quantum cipher mode. Post-quantum cipher algorithms, similarly fortified against quantum attacks, optimize and complement the original encryption suites of the SSL/TLS protocol. The dynamic switch between quantum keys and post-quantum encryption algorithms ensures constant protection against quantum attacks, enhancing the system’s security and reliability.

This paper is structured as follows: Section 2 introduces the background knowledge of the SSL/TLS protocol, quantum key distribution, and post-quantum encryption algorithms. Section 3 provides an overview of the overall system architecture, detailing the handshake protocol and cipher suite employed in this study. The experimental environment and system modules are presented in Section 4. Section 5 conducts testing and analysis of the system’s performance with regard to handshake latency and post-establishment data throughput. Finally, a comprehensive conclusion is made in Section 6.

2 Background

2.1 SSL/TLS Protocol

The SSL and TLS protocols are secure transport protocols

This work was supported by ZTE Industry-University-Institute Cooperation Funds under Grant No. HC-CN-20221029003.

that reside between the application layer and the transport layer in the TCP/IP protocol stack. The SSL/TLS protocol encompasses two layers of communication. The record protocol offers fundamental security services to various higher-level protocols and defines the format for data transmission^[2]. Moreover, SSL/TLS establishes three higher-level mechanisms involving data encryption, identity authentication, and message integrity verification, thereby ensuring security and data integrity during transmission.

The SSL/TLS protocol negotiates cipher suites and keys through a handshake process between the client and the server. This handshake protocol consists of a series of messages exchanged between the client and server, which can be categorized into four distinct stages.

The first stage initiates the logical connection and establishes relevant security functionalities. It commences with a client “hello” message and concludes with a server “hello” message. During this stage, the client and server negotiate the SSL version for use, session ID, compression methods, and cipher suites. Random numbers are also exchanged. Cipher suites define key exchange algorithms and CipherSpecs, which encompass encryption algorithms, MAC algorithms, and other pertinent information. Supported key exchange methods by the SSL/TLS protocol include Rivest-Shamir-Adleman (RSA), fixed Diffie-Hellman (DH), ephemeral DH, and anonymous DH^[3].

The second stage pertains to server authentication and key exchange. If authentication is required, the server sends its certificate at the beginning of this stage. Any agreed-upon key exchange, apart from anonymous DH, necessitates this certificate message. Subsequently, a server key exchange message is sent. This message is not required if RSA key exchange is employed, or if the server sends a certificate with fixed DH parameters. Additionally, non-anonymous servers can request certificates from clients by sending a certificate request message. This stage ends with a server-done message.

In the third stage, client authentication and key exchange are initiated by the client’s certificate message. Next, the client sends a client key exchange message to create a premaster secret between the client and server. The content of this message varies based on the key exchange method. The exchanged premaster secret will be used by both parties to derive a shared master key. CipherSpec parameters are generated from the master key using hash techniques. These parameters include a client write MAC, a server write MAC, a client write key, a server write key, a client write Initialization Vector (IV), and a server write IV^[4]. Finally, the client sends a certificate verification message to validate its certificate explicitly.

In the fourth stage, the client sending a change-cipher-spec message to transfer the pending CipherSpec state to the current state. Subsequently, a finished message is sent using the new algorithm and key. Finally, the server sends a

change-cipher-spec message to transfer the pending messages to the current CipherSpec, and it also sends its own finished message^[5].

The record protocol in the SSL/TLS framework is established atop a reliable transport protocol (such as TCP) and provides support for fundamental functionalities like data encapsulation, compression, and encryption. One key advantage of SSL/TLS lies in its independence from specific application layer protocols. Higher-level application layer protocols (e.g., HTTP, FTP, Telnet) can seamlessly operate over the SSL/TLS protocol^[6]. The SSL/TLS protocol completes encryption algorithm negotiation, communication key establishment, and server authentication before the communication between application layer protocols begins. As a result, data transmitted by application layer protocols are encrypted, ensuring communication confidentiality.

2.2 Quantum Key Distribution

Quantum Key Distribution (QKD) is theoretically proven to be unconditionally secure, with its security guaranteed by the fundamental principles of quantum mechanics^[7]. QKD utilizes quantum states to encode and transmit information, providing theoretically unconditional secure shared keys for both communicating parties and establishing secure confidential communication. QKD guarantees the security of point-to-point key distribution. The process involves the exchange of quantum bits (qubits) between a quantum transmitter and a quantum receiver through a quantum channel. They further exchange measurement bases through a public channel, perform key sifting, and subsequently perform error correction. This process is designed to detect the presence of potential attackers and determine the final session key.

In the process of QKD, pairs of photons with different polarization states are randomly emitted by quantum devices. On the receiving side, the photon states sent by the quantum devices are measured by randomly selecting measurement bases^[8]. Based on the polarization state of the emitted photon from the quantum device and the orientation of the measurement basis at the receiving side, the information received is determined as either 0 or 1 for each received photon. Moreover, due to the non-cloneability of quantum states, which means they cannot be copied or measured without disrupting their state, any attempt at eavesdropping could potentially alter the quantum states themselves, resulting in a high error rate and thus making eavesdropping detectable. Furthermore, each string of keys is generated randomly, and if intercepted, the communicating parties can detect it and change the password^[9], thus rendering quantum keys non-cloneable and reliable.

Consequently, the distinct advantage of quantum keys is their ability to resist quantum computing attacks, achieved through their inherent properties of single quantum indivisibility and unclonable quantum states^[10]. The combination

of QKD and the one-time pad enables information-theoretic secure encryption, meaning that it remains secure even against adversaries with unlimited computational resources. QKD’s functionality includes symmetric key negotiation and generation, which, when combined with symmetric cipher algorithms, can achieve encryption, decryption, and authentication capabilities.

2.3 Post-Quantum Cryptography

Cryptographic algorithms that can resist attacks from quantum computers are collectively referred to as Post-Quantum Cryptography (PQC). These algorithms have been developed to tackle security threats posed by the emergence of quantum computing^[11]. Post-quantum cryptographic algorithms offer computation speeds surpassing those of existing public key algorithms while maintaining the same level of security. They can be used to replace existing algorithms and protocols, including public key encryption, key exchange, digital signatures, and more.

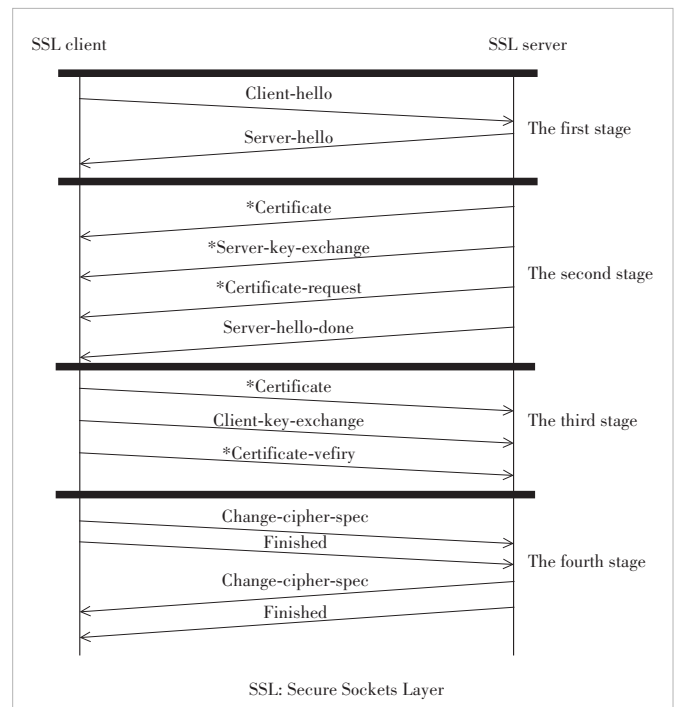
Post-quantum cryptographic algorithms can be categorized into four main classes: lattice-based crypto systems, code-based crypto systems, multivariate crypto systems, and hash-based cryptosystems. Among these, lattice-based post-quantum cryptographic algorithms stand out due to their relative efficiency, versatility, and ability to be highly parallelized^[12]. They strike a better balance between security, key sizes, and computation speed compared to traditional number theory-based constructions. In some cases, lattice-based algorithms can even outperform traditional number theory-based cryptographic algorithms in terms of computation speed. Among various post-quantum cryptographic algorithms, lattice-based ones are more suitable for practical applications when considering the same level of security. The security of lattice-based post-quantum cryptographic algorithms is based on the hardness of solving lattice problems. They achieve smaller public and private key sizes, faster computation speeds, and can be used to construct various cryptographic primitives^[13], making them more suitable for real-world applications. Compared to number-theory-based cryptographic algorithms, lattice-based algorithms offer significantly improved computation speeds and higher security levels.

On July 5th, 2022, NIST announced a selection of algorithms for standardization, which includes CRYSTALS-KYBER for asymmetric encryption and key encapsulation mechanisms, CRYSTALS-Dilithium, FALCON, and SPHINCS+ for digital signatures. Among them, NIST recommends the CRYSTALS-Kyber algorithm for general-purpose encryption of information exchanged over public networks and the other three algorithms for identity authentication. CRYSTALS-Kyber is a lattice-based post-quantum cryptographic algorithm that provides an IND-CCA2 secure key encapsulation mechanism. Its security relies on the difficulty of solving the Module Learning With Errors problem on lat-

tices^[14]. The module is an extension of the ideal lattice and general lattice, while Module Learning with Errors is an extension of Ring Learning with Errors (RLWE). When appropriate parameters are chosen, cryptographic schemes constructed based on Module Learning with Errors (MLWE) provide a good balance between efficiency and security. Therefore, our scheme employs the CRYSTALS-Kyber algorithm based on MLWE to guarantee strong security. CRYSTALS-Kyber includes algorithms for public-private key pair generation, key encapsulation, and ciphertext generation. CRYSTALS-Kyber, as a public key algorithm, can be used in the key negotiation part of the handshake process. It offers the advantages of relatively small encryption keys, small data exchange volume, and fast operation speed while ensuring security. Kyber defines three parameter sets: Kyber512, Kyber768, and Kyber1024. By utilizing post-quantum cryptographic algorithms like Kyber for key exchange and negotiation, systems can more effectively address potential attacks from future quantum computing technologies^[15].

3 System Architecture

The system framework designed in this paper is depicted in Fig. 1. The quantum key storage devices are abstractly represented as a Quantum Key Pool (QKP). When the remaining quantity of quantum keys in the pool meets the demand, the proposed approach utilizes the quantum keys negotiated through the QKD system as the session key for the SSL/TLS protocol. Subsequently, during the encryption of communication data using encryption algorithms, the quantum key serves



▲ Figure 1. SSL/Transport Layer Security (TLS) handshake protocol

as the symmetric key for encryption. In cases where the quantity of quantum keys in the pool falls short of the demand, the application employs post-quantum cryptographic algorithms to optimize and supplement the corresponding cipher suites of the original SSL/TLS protocol. This approach enables resistance against quantum attacks in the post-quantum cryptographic mode, ensuring quantum security in the entire mode.

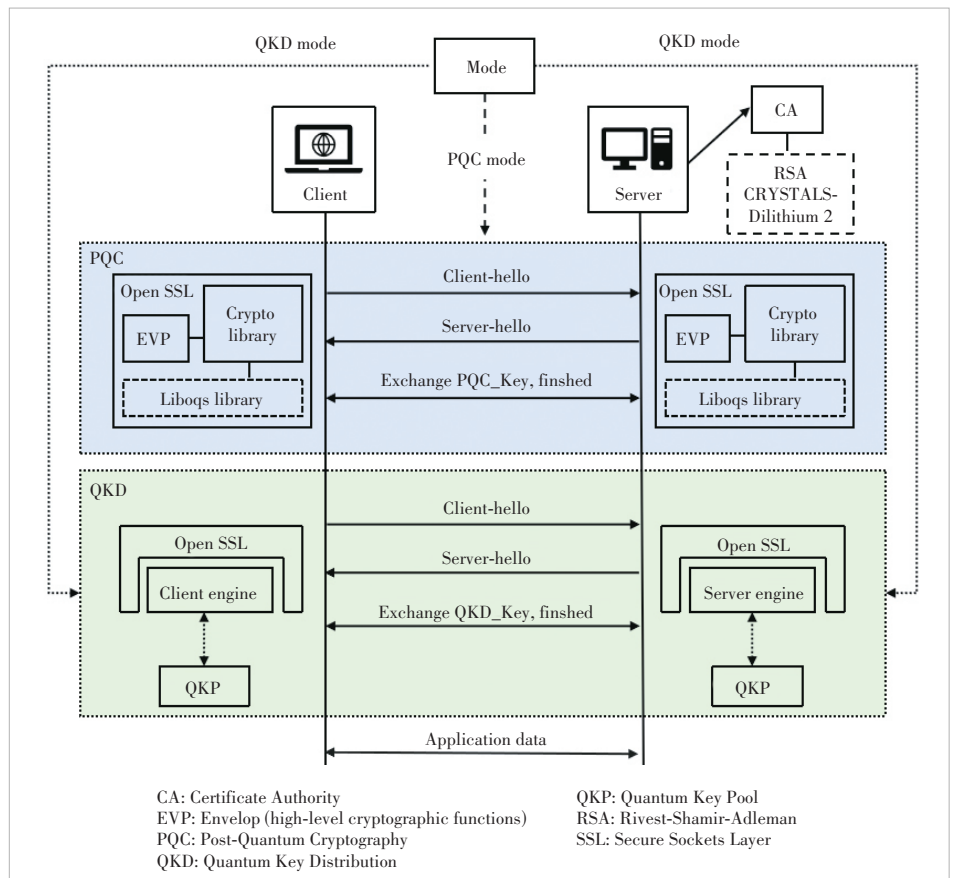
3.1 Handshake Protocol

Keys are stored in pairs between any two QKD nodes. The key pool is divided into multiple virtual spaces based on the source and destination nodes of communication. Keys are placed in the corresponding index-numbered key pool based on the source and destination node identifiers of communication requests. Quantum key distribution devices generate quantum keys and their corresponding identifiers, known as quantum key identifiers, through quantum key negotiation protocols (such as BB84/B92/TF-QKD). These keys and identifiers are then stored in the key pool. The key pool performs unified authentication and management of quantum keys and their corresponding identifiers. Quantum keys are used as session keys for SSL/TLS communication, while key identifiers play a crucial role in obtaining quantum key credentials and ensuring consistency during the SSL/TLS handshake process. The handshake procedure in the quantum key mode is illustrated in Fig. 2.

In the handshake process of the quantum key mode, the client initiates communication by sending an encrypted communication request “Client Hello” to the server. During this process, the client primarily provides information such as the supported protocol version (e. g., TLS 1.3), a randomly generated client nonce, encryption algorithm suites, supported compression methods, and other relevant configurations to the server. Upon receiving the client’s request, the server responds with a message “Server Hello” confirming the use of the encryption communication protocol version (TLS 1.3), a randomly generated server nonce, configurations for server encryption algorithms, and the chosen encryption algorithm suite. The server encrypts the “Server Hello” information using its private key and sends it back to the client, along with its certificate containing the public key. The client verifies the server’s certificate upon

receiving the response. If the certificate is not issued by a trusted authority, the domain name does not match, or the certificate has expired, a warning is displayed to the user, who can decide whether to continue communication. If the certificate is valid, the client extracts the server’s public key from the certificate and decrypts the “Server Hello” message, which was encrypted by the server’s private key. Failure to decrypt indicates a false “Server Hello” message, resulting in the termination of communication.

After the initial authentication, the client sends a request for quantum key allocation to the key pool of the quantum key distribution device. The key pool sends quantum keys and their corresponding key identifiers to the client, providing the client with a pair of quantum keys and their identifiers. The client encrypts the quantum key identifier using a premaster secret and sends it to the server. Upon decryption, the server obtains the quantum key identifier. Following verification of the client’s identity, the server calculates the premaster secret for the current session by combining the previously shared random numbers (client nonce and server nonce). The server then decrypts the quantum key identifier to obtain it. Using the quantum key identifier, the server sends a quantum key extraction request to the key pool, which responds by sending the corresponding quantum key.



▲ Figure 2. Overall system framework

The received quantum key undergoes a hash operation, and its hash is compared to the hash of the quantum key in the client's message to verify consistency. In case of inconsistency, an error message is sent to the server, triggering a quantum key retrieval process.

Once the server notifies the successful negotiation of the quantum key agreement, both parties send change cipher spec notifications to indicate that subsequent message encryption will involve the symmetric encryption method agreed upon and the quantum key. A handshake completion notification is sent, and at this point, both the client and server process the quantum key to obtain a compatible format for the session key.

Considering the possibility of quantum devices experiencing emergencies such as downtime, our system's key pool features a backup function. Periodically, we securely store and backup keys, allowing us to retrieve quantum keys from the key pool's backup. If the client and server cannot obtain the same quantum key due to key pool asynchrony or an insufficient quantity of remaining keys in the pool, we will switch to the classic mode of the SSL/TLS protocol using PQC algorithms. PQC algorithms optimize and supplement the encryption cipher suites of the original SSL/TLS protocol. In this context, a post-quantum cryptographic algorithm, such as CRYSTALS-Kyber, is used to modify the existing SSL/TLS protocol. The SSL/TLS handshake process using post-quantum cryptographic algorithms is illustrated in Fig. 3.

In the handshake procedure of the post-quantum cryptographic mode, the client initially dispatches a "Client Hello" request to initiate encrypted communication with the server. In response, the server reciprocates by sending a "Server Hello" message back to the client, along with its own certificate and static public key (Public_Key_02). Subsequently, the client generates a temporary public-private key pair (Public_Key_01, Secret_Key_01) via the Kyber key generation algorithm. Utilizing Public_Key_02 provided by the server, the client generates a random number K_1 . This number is then subjected to the Kyber encryption algorithm, resulting in the ciphertext C_1 . The client then forwards the temporary public key (Public_Key_01) and ciphertext C_1 to the server. Upon receipt of Public_Key_01 and ciphertext C_1 from the client, the server encrypts the random number K_2 using Public_Key_01 to derive the ciphertext C_2 . Concurrently, it decrypts ciphertext C_1 using its static private key to obtain pre master secret K_1' . Then, the server sends ciphertext C_2

to the client. Subsequently, the client receives ciphertext C_2 from the server and decrypts it using its temporary private key (Secret_Key_01) to extract the pre master secret K_2' . Then, both the server and client perform hash operations on K_1' and K_2' respectively, utilizing the resultant hash value as the session key.

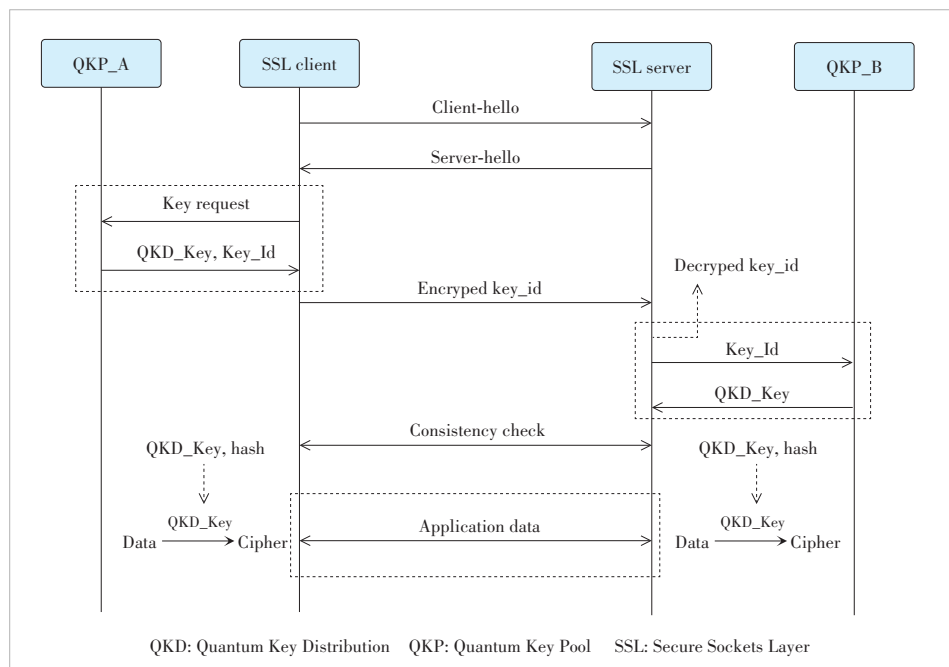
During the handshake process, the generation of public-private key pairs, encryption and decryption of random numbers are performed using the CRYSTALS-Kyber algorithm. Through the Kyber encryption and decryption algorithms, a secure exchange of random numbers used in the SSL/TLS protocol are accomplished between the client and the server. Due to the quantum-resistant properties of the Kyber algorithm, this process is impervious to decryption by quantum attacks.

Finally, both the client and server send change cipher spec notifications to indicate that subsequent message encryption will involve the symmetric encryption method agreed upon and the key derived from the post-quantum cryptographic process. A handshake completion notification is sent, marking the completion of the handshake process in the post-quantum cryptographic mode.

3.2 Encryption Suite

Within the SSL/TLS protocol, the SSL_CIPHER data structure is used to describe a cipher suite, which is composed of a set of cryptographic algorithms including key exchange, authorization, communication encryption, and digest algorithms.

During the communication process between a client and a server, the client initiates the handshake by sending a "Client Hello" packet, containing a list of supported cipher suites. Multiple suites can be separated by symbols, such as



▲ Figure 3. Handshake flow in quantum key mode

TLS_RSA_WITH_AES_128_CBC_SHA(0x002f) and others. The server, based on the cipher suite identifiers and their priority sent by the client, selects a supported cipher suite and includes it in the “Server Hello” response. This agreed cipher suite is ultimately used for the session negotiation between the two parties.

In the quantum cryptographic mode, the following encryption parameters are generated: client MAC, server MAC, client key, server key, client IV, server IV, and pre-master secret. MAC is used to generate message digests. IV is generated only when traditional block cipher encryption is applied to application traffic. When secure encryption and authentication are used, the size of the required write key and MAC must be negotiated during the SSL/TLS protocol handshake.

Each quantum encryption suite must include a key exchange algorithm, a symmetric encryption algorithm, and an authentication algorithm, with the key exchange algorithm employing a quantum-key-based key negotiation algorithm. The server selects a supported cipher suite from the list of available cipher suites. If no compatible cipher suite is found, the server returns a handshake failure alert message and terminates the connection. Cipher suites in the quantum cipher mode are shown in Table 1.

Each post-quantum encryption suite comprises a key exchange algorithm, symmetric encryption algorithm, and message digest algorithm. The key exchange algorithm in these suites employs post-quantum encryption techniques, such as CRYSTALS-Kyber. The message digest algorithm is used for verifying server signatures and can include Rivest-Shamir-Adleman (RSA), Digital Signature Standard (DSS), Elliptic Curve Cryptography (ECC), or their corresponding variant algorithms. The server’s authentication relies on a robust PKI mechanism, encompassing certificate issuance, certificate management, and certificate validity verification. Only after validating the certificate’s legitimacy can the verification of the server’s own signature take place. Cipher suites in the post-quantum cipher mode are shown in Table 2.

▼Table 1. Cipher suites in quantum cipher mode

Grade	Encryption Suite
1	TLS_QKD_SHA_RSA_WITH_OTP_MD5
2	TLS_QKD_DHE_DSS_WITH_DES_CBC_UHAH1
3	TLS_QKD_UHASH1_PSK_WITH_OPT_UHAH2
4	TLS_QKD_MD5_DH_RSA_WITH_AES_128_CBC_SHA

▼Table 2. Cipher suites in post-quantum cipher mode

Grade	Encryption Suite
1	TLS_Kyber_SHA_RSA_WITH_OTP_MD5
2	TLS_Kyber_DHE_DSS_WITH_DES_CBC_UHAH1
3	TLS_Kyber_UHASH1_PSK_WITH_OPT_UHAH2
4	TLS_Kyber_MD5_DH_RSA_WITH_AES_128_CBC_SHA

4 Experiment

4.1 Experiment Environment

Our experimental setup involves two host machines equipped with Core i5-13600 processors, 8 GB of RAM, and 100 GB of disk storage each. Additionally, we have two quantum communication devices employing BB84 protocols. The length of the quantum key generated by quantum communication devices is 256 bit, while the key identifier stored in the quantum key pool is 12 bit. The attenuation in the photon transmission process and finite-size effects may lead to communication delays. Therefore, in our experimental conditions, the quantum channel distance is set to be short-range (within 50 km) with a key rate of 20 kbit/s. The experimental testing is facilitated using the OpenSSL 1.1.1t toolkit.

The testing environment consists of two host machines: the server employs an Ubuntu Server 22.10 operating system, while the client is based on a Windows 11 environment. To capture and analyze network traffic during testing, we utilize the Tshark network capture software.

4.2 Quantum Key Based SSL Communication Module

We leverage the OpenSSL engine mechanism to integrate QKD with the SSL/TLS protocol. This engine mechanism enables third parties to augment OpenSSL with extensions, which can be implemented as dynamic libraries dynamically loaded into OpenSSL^[16]. The engine mechanism seamlessly facilitates encryption using software cryptographic libraries or hardware encryption devices. By overloading the callback functions used for hardware-accelerated DH key exchange, we realize the sharing of quantum keys between communicating parties. Due to the inability of the DH callback function within the engine to distinguish between client and server invocations, we separately implement two independent engines for dynamic loading: one on the client side and the other on the server side. This duality serves to adapt QKD to the SSL/TLS protocol. The callback functions that are overloaded for hardware acceleration encompass the following:

1) `init()`: This function is formerly employed for initializing the engine; post-overloading, it initializes the QKD device.

2) `generate_key()`: This function is used for generating DH private keys and computing public keys using negotiated parameters; upon overloading, the server utilizes a fixed value as the DH private key, invokes `QKD_START()` to acquire the quantum key identifier from the QKD device or USB key as the DH public key, which is subsequently transmitted to the client.

3) `compute_key()`: This function is initially employed for calculating DH shared keys; post-overloading, the client utilizes the DH public key received from the server as the quantum key identifier, passing it as a parameter to `QKD_START()`. Following this, both the server and client individually invoke `QKD_CONNECT()` with the QKD device and input the

quantum key identifier into QKD_GET_KEY(). This procedure retrieves the corresponding quantum key from the QKD device as the DH shared key, culminating with a QKD_CLOSE() invocation.

The QKD API invocation process for both the client and server is depicted in Fig. 4.

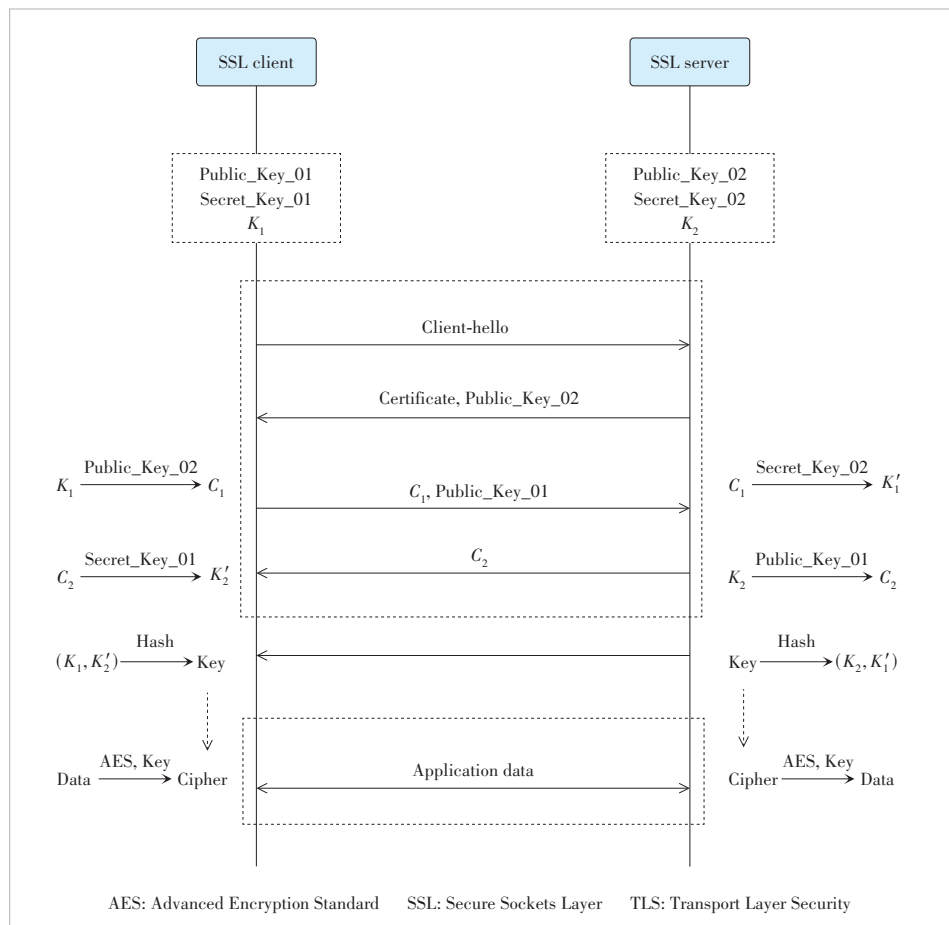
During the process of acquiring quantum keys using the QKD API on both the client and server sides, the SSL server initiates the procedure by invoking QKD_START() with a null value. Consequently, the QKD system returns a new available quantum key identifier to the server. This identifier is stored by the server and then encrypted before being transmitted to the client. Subsequently, the client employs the QKD_START() function with the key identifier as its parameter.

Following these initial steps, both the server and client independently execute QKD_CONNECT() to establish a QKD connection. This connection facilitates the exchange of quantum key identifiers sent by the client and server. This step serves to verify that the client possesses an identical quantum key identifier to that of the server. Ultimately, to conclude the process, both the server and client separately invoke QKD_CLOSE() to terminate the QKD connection.

4.3 Post-Quantum Key Based SSL Communication Module

We extend the encryption module by building upon the OpenSSL Crypto Library and integrating algorithms from the liboqs library. The liboqs library, an open-source C library designed for post-quantum encryption algorithms, is incorporated into the OpenSSL framework as a novel branch. This integration allows the post-quantum cryptographic algorithms from the liboqs library to complement the existing functionality of OpenSSL's Crypto Library. As a result, these post-quantum cryptographic algorithms fortify the SSL/TLS protocol with quantum-resistant capabilities. The communication framework of the SSL/TLS protocol, rooted in post-quantum cryptographic algorithms, is illustrated in Fig. 5.

When higher-level applications invoke the OpenSSL library to facilitate secure encrypted communication via the SSL/TLS protocol, they do not directly engage with the low-level specifics of individual cryptographic algorithms^[17]. Instead, these applications interact with the EVP interface pro-



▲ Figure 4. Handshake flow of the SSL/TLS protocol employing post-quantum cryptographic algorithms

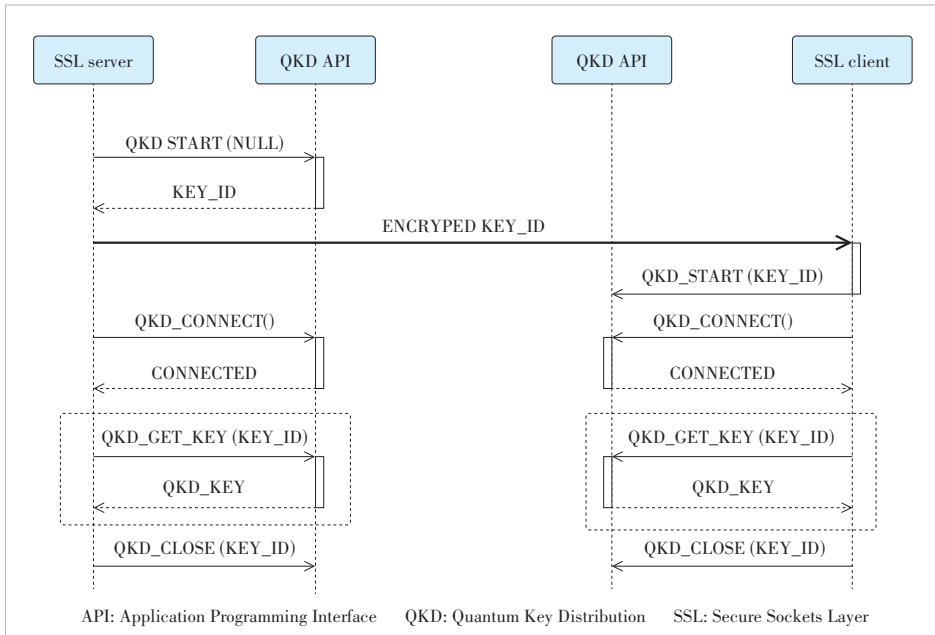
vided by the OpenSSL library. The EVP module encapsulates the intricate details of cryptographic algorithm implementations and offers abstract methods and data types to manage cryptographic operations. The foundational encryption functions required for network protocols are realized through the libcrypto library. This library encompasses the concrete implementations of encryption.

In the context of the SSL/TLS communication module based on post-quantum cryptography, digital signature certificates are generated by a custom certificate authority (CA). The digital signature algorithm utilized is CRYSTALS-Dilithium2. These certificates contain their own public key as well as a random value, serving the purpose of identity authentication.

5 Results and Analysis

We conducted performance testing on the SSL/TLS communication system proposed in this paper. In the tests, the client initiates an SSL/TLS connection request to the server. Both parties establish a secure and reliable SSL/TLS session through the handshake process.

We created an SSL server and an SSL client using the developed communication system tools based on OpenSSL. The



▲ Figure 5. Process of invoking QKD API for the client-side and server-side

server dynamically loaded the server-side engine and awaited connection requests from SSL clients. Subsequently, the client dynamically loaded the client-side engine and initiated an SSL connection to the server.

We employed network packet capture software Tshark to monitor the interaction between the client and server. This allowed us to capture encrypted packets and analyze relevant information such as packet size and timestamps. Through this analysis, we evaluated the system's performance.

As a point of comparison, we also subjected an SSL/TLS communication system using classical cryptographic algorithms to testing. This comparative approach enabled a quantitative assessment of the impact of the quantum key application on the performance of the original protocol. The primary evaluation metrics encompassed the handshake latency between communication parties and the data throughput following the establishment of a secure session between the parties.

5.1 Handshake Delay

We conducted multiple experiments by varying the key negotiation method and the key size to measure handshake la-

▼ Table 3. SSL/TLS communication handshake delay under different key negotiation methods

Key Negotiation Method	Key Size	Handshake Delay/ms
Quantum key distribution	Quantum key 512 kB	16.2
Quantum key distribution	Quantum key 16 kB	15.7
Quantum key distribution	Quantum key 160 B	15.6
Classical public key algorithm	RSA 4 096 bit	15.3
Classical public key algorithm	RSA 2 048 bit	3.7
Classical public key algorithm	RSA 1 024 bit	2.1

SSL: Secure Sockets Layer TLS: Transport Layer Security

tency. Table 3 provides a description of the SSL/TLS communication handshake latency data when employing quantum key distribution as the key negotiation method.

According to the findings presented in Table 3, it is evident that when utilizing quantum key distribution as the key negotiation method for the SSL/TLS protocol, the resulting handshake latency remains consistently around 16 ms. This value is nearly identical to the handshake latency observed when employing classical public key algorithms (4096 bit RSA public keys) as the key negotiation method.

Furthermore, as indicated by the results in Table 3, the handshake latency of SSL/TLS communication generated by classical public key algorithms increases with larger RSA

key sizes. To maintain higher security levels, systems or users are required to continually escalate the size of the RSA public keys they employ. Consequently, in communication environments demanding elevated security standards, the disparity in handshake latency between utilizing quantum key distribution and classical public key algorithms as the key negotiation methods for the SSL/TLS protocol will progressively diminish.

5.2 Data Throughput

When both communicating parties employ the AES algorithm as the encryption method, a higher frequency of key updates enhances communication security. However, the trade-off is that a higher frequency of key updates can lead to a decrease in data throughput for the session between the parties.

The TCP throughput of the network used in our tests was measured at 985 Mbit/s. In the SSL/TLS protocol, we performed key negotiations using both quantum key distribution technology and classical public key algorithms. For quantum key distribution, a key size of 160 B was utilized, while for classical public key algorithms, an RSA key size of 1024 bits was used. The data throughput performance under different key update frequencies, using these two different key negotiation methods, is depicted in Fig. 6.

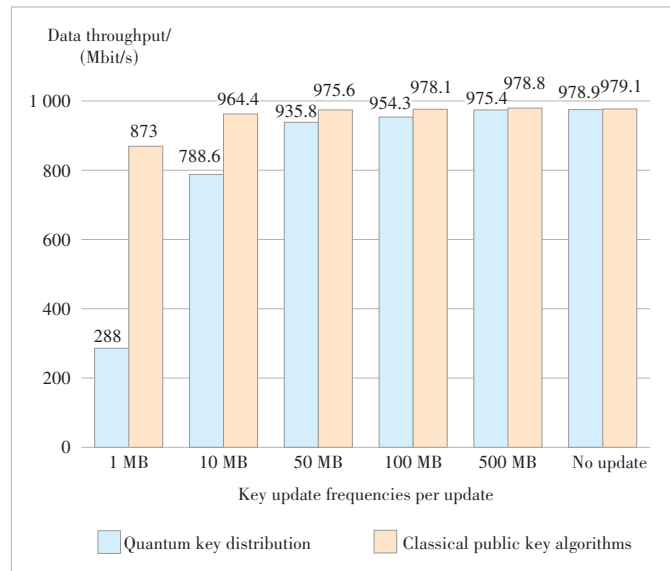
For each transmission of a fixed amount of data by the client (such as 1 MB), a new SSL/TLS session connection is initiated, leading to an update of the AES key.

From Fig. 6, it becomes evident that when transmitting 1 MB of data and utilizing quantum key distribution for key negotiation, a higher frequency of key updates exerts a notable impact on subsequent communication data throughput. However, as the key update frequency reaches 100 MB per update,

the difference in data throughput between the two different key negotiation methods (quantum key distribution and classical public key algorithms) is approximately 3%. When the key update frequency further increases to 500 MB per update, the impact of quantum key distribution on communication data throughput becomes negligible.

5.3 Security Analysis

In the information exchange process of the SSL/TLS communication system described in this paper, the use of the unclonability and tamper-resistance of quantum states ensures the security of information transmission. Currently, several studies^[18-20] have shown that combining QKD with PQC can enhance a network’s resilience to potential quantum computing attacks. In the quantum key distribution process, the key pool stores quantum keys along with key identifiers. These identifiers uniquely represent the quantum keys, which the SSL/TLS protocol’s client and server use to obtain quantum keys as session keys from the quantum key distribution device. In the designed SSL/TLS communication system based on quantum keys, both communication parties transmit encrypted quantum key identifiers during the SSL/TLS handshake, rather than directly transmitting the quantum keys over the channel. Subsequent key consistency checks are then performed. As a result, attackers cannot eavesdrop on the SSL/TLS handshake process to steal or tamper with the quantum keys being used by both parties. Therefore, the SSL/TLS protocol based on quantum keys exhibits the ability to resist quantum attacks on the physical level. At the same time, we recog-



▲ Figure 7. Data throughput under various key update frequencies

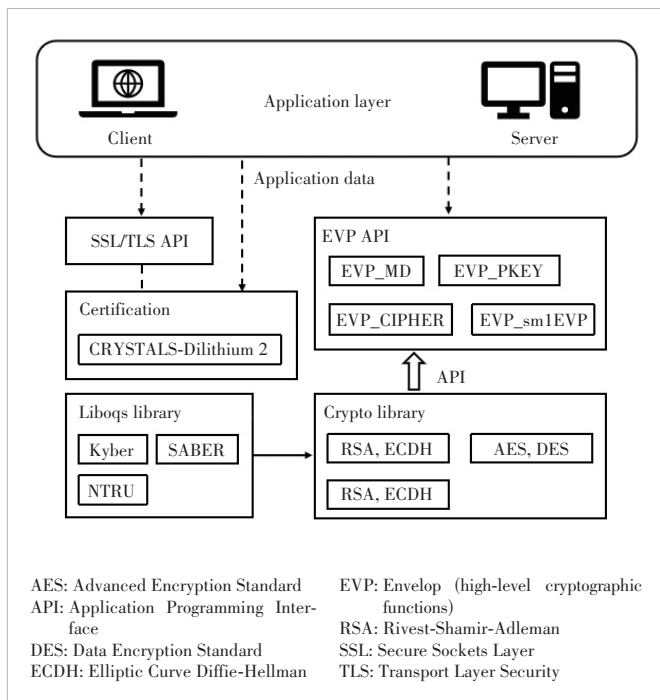
nize that any eavesdropping on the QKD process will alter the quantum states, potentially subjecting QKD-based networks to distributed denial-of-service (DDoS) attacks. In future work, we will implement access control measures to prevent DDoS attacks targeting the QKD process within the network.

The security of post-quantum cryptographic algorithms relies on mathematical problems that current quantum computing cannot efficiently solve. The kyber768 algorithm used in this paper is a lattice-based post-quantum cryptographic algorithm, and its security hinges on the hardness of the MLWE problem on lattices. When appropriate parameters are chosen, there are currently no known classical or quantum algorithms capable of rapidly solving this problem. Consequently, this algorithm offers high security against quantum attacks. Therefore, the SSL/TLS protocol that integrates post-quantum cryptography resists quantum attacks on the mathematical level.

In summary, whether utilizing quantum key distribution technology or employing post-quantum cryptographic algorithms for key negotiation, both approaches guarantee quantum-resistant security performance for the SSL/TLS communication process.

6 Conclusions

This paper presents a novel approach that combines quantum key distribution with post-quantum cryptography in an SSL/TLS protocol secure communication system. By dynamically loading an engine, the integration of key exchange and quantum keys within the SSL/TLS protocol is achieved. Additionally, post-quantum cryptographic algorithms are embedded into the cryptographic suite of the SSL/TLS protocol, thereby expanding its underlying algorithmic capabilities. This extension builds upon the existing SSL/TLS protocol to create a quantum-resistant SSL/TLS communication system,



▲ Figure 6. Communication framework diagram of SSL/TLS protocol based on post-quantum cipher algorithm

while maintaining transparency to upper-layer applications. The significance of this work lies in its potential to advance the adoption of quantum technologies within the SSL/TLS protocol. Through packet analysis of communication data within the test environment, the proposed system demonstrates high performance in handshake latency and throughput.

References

- [1] JOSEPH D, MISOCZKI R, MANZANO M, et al. Transitioning organizations to post-quantum cryptography [J]. *Nature*, 2022, 605(7909): 237 – 243. DOI: 10.1038/s41586-022-04623-2
- [2] DASTRES R, SOORI M. Secure socket layer (SSL) in the network and web security [J]. *International journal of computer and information engineering*, 2020, 14(10): 330 – 333
- [3] DUDDU S, RISHITA SAI A, SOWJANYA C L S, et al. Secure socket layer stripping attack using address resolution protocol spoofing [C]// *Proc. 4th International Conference on Intelligent Computing and Control Systems (ICICCS)*. IEEE, 2020: 973 – 978. DOI: 10.1109/ICICCS48265.2020.9120993
- [4] IBRAHIM A. Secure socket layer: fundamentals and certificate verification [EB/OL]. [2023-08-20]. <https://engrxiv.org/preprint/view/3532/6315>
- [5] AHMAD KHAN N, KHAN A S, KAR H A, et al. Employing public key infrastructure to encapsulate messages during transport layer security handshake procedure [C]// *Proc. Applied Informatics International Conference (AiIC)*. IEEE, 2022: 126 – 130. DOI: 10.1109/AiIC54368.2022.9914605
- [6] SHAKYA S. An efficient security framework for data migration in a cloud computing environment [J]. *Journal of artificial intelligence and capsule networks*, 2019, 1(1): 45 – 53. DOI: 10.36548/jaicn.2019.1.006
- [7] ZENG P, ZHOU H Y, WU W J, et al. Mode-pairing quantum key distribution [J]. *Nature communications*, 2022, 13(1): 3903. DOI: 10.1038/s41467-022-31534-7
- [8] XU F H, MA X F, ZHANG Q, et al. Secure quantum key distribution with realistic devices [J]. *Reviews of modern physics*, 2020, 92(2): 025002. DOI: 10.1103/RevModPhys.92.025002
- [9] MEHIC M, NIEMIEC M, RASS S, et al. Quantum key distribution [J]. *ACM computing surveys*, 2021, 53(5): 1 – 41. DOI: 10.1145/3402192
- [10] MA W K, CHEN B W, LIU L, et al. Equilibrium allocation approaches of quantum key resources with security levels in QKD-enabled optical data center networks [J]. *IEEE Internet of Things journal*, 2022, 9(24): 25660 – 25672. DOI: 10.1109/JIOT.2022.3195104
- [11] EMURA K, MORIAI S, NAKAJIMA T, et al. Cache-22: a highly deployable end-to-end encrypted cache system with post-quantum security [EB/OL]. [2023-08-20]. <https://eprint.iacr.org/2022/220.pdf>
- [12] ALAGIC G, ALPERIN-SHERIFF J, APON D, et al. Status report on the first round of the NIST post-quantum cryptography standardization process [EB/OL]. [2023-08-20]. <https://nvlpubs.nist.gov/nistpubs/ir/2019/NIST.IR.8240.pdf>
- [13] ASIF R. Post-quantum cryptosystems for Internet-of-Things: a survey on lattice-based algorithms [J]. *IoT*, 2021, 2(1): 71 – 91. DOI: 10.3390/iot2010005
- [14] DANG V B, MOHAJERANI K, GAJ K. High-speed hardware architectures and FPGA benchmarking of CRYSTALS-kyber, NTRU, and saber [J]. *IEEE transactions on computers*, 2023, 72(2): 306 – 320. DOI: 10.1109/TC.2022.3222954
- [15] HUANG Y M, HUANG M Q, LEI Z K, et al. A pure hardware implementation of CRYSTALS-KYBER PQC algorithm through resource reuse [J]. *IEICE electronics express*, 2020, 17(17): 20200234. DOI: 10.1587/elex.17.20200234
- [16] JATI A, GUPTA N, CHATTOPADHYAY A, et al. A configurable CRYSTALS-kyber hardware implementation with side-channel protection [J]. *ACM transactions on embedded computing systems*, 2024, 23(2): 1 – 25. DOI: 10.1145/3587037
- [17] WALDEN J. OpenSSL 3.0.0: an exploratory case study [C]// *Proc. 19th International Conference on Mining Software Repositories*. ACM, 2022: 735 – 737. DOI: 10.1145/3524842.3528035
- [18] AHN J, KWON H Y, AHN B, et al. Toward quantum secured distributed energy resources: adoption of post-quantum cryptography (PQC) and quantum key distribution (QKD) [J]. *Energies*, 2022, 15(3): 714. DOI: 10.3390/en15030714
- [19] YANG Y H, LI P Y, MA S Z, et al. All optical metropolitan quantum key distribution network with post-quantum cryptography authentication [J]. *Optics express*, 2021, 29(16): 25859 – 25867. DOI: 10.1364/OE.432944
- [20] WANG L J, ZHANG K Y, WANG J Y, et al. Experimental authentication of quantum key distribution with post-quantum cryptography [J]. *NPJ quantum information*, 2021, 7(1): 67. DOI: 10.1038/s41534-021-00400-7

Biographies

WANG Jigang received his PhD degree in computer science from Harbin Engineering University, China in 2007. From May 2007 to June 2009, he held a postdoctoral position in Institute of Computer Science, Tsinghua University, China. From August 2009, He has been with Cyber Security Product Line, ZTE Corporation as the general manager. His recent research interests include operating systems, network and information security, and artificial intelligence.

LU Yuqian is a master student at School of Cyber Science and Engineering, Southeast University, China. Her research interests include IoT and information security.

WEI Liping received his bachelor's degree in electronic information engineering from Zhejiang University, China in 2005. Since 2020, he has been a product manager of cyber security products at ZTE Corporation. His recent research interests include mobile communication, network and information security, and artificial intelligence.

JIANG Xinzao (230229200@seu.edu.cn) is a PhD student at School of Cyber Science and Engineering, Southeast University, China. His research interests include privacy-preserving computation and IoT.

ZHANG Han received his MSc degree in information technology and management from ITC Institute of Twente University, the Netherlands. He is currently pursuing his PhD degree in School of Cyber Science and Engineering, Southeast University, China. He is a senior system architect of ZTE Corporation, China and the director of Jiangsu Provincial Key Laboratory of Big data Storage and Application, China. He is also an associate researcher at the State Key Laboratory of Mobile Network and Mobile Multimedia Technology, China. His research interests include information security, cloud computing, big data, IoT, 5G technology, and human computer interactions.

Differential Spatial Modulation Mapping Algorithms



WANG Chanfei, CHAI Jianxin, XU Yamei

(College of Computer and Communication, Lanzhou University of Technology, Lanzhou 730050, China)

DOI: 10.12142/ZTECOM.202403014

<https://kns.cnki.net/kcms/detail/34.1294.TN.20240903.1032.004.html>, published online September 3, 2024

Manuscript received: 2024-08-04

Abstract: Differential spatial modulation (DSM) is a multiple-input multiple-output (MIMO) transmission scheme. It has attracted extensive research interest due to its ability to transmit additional data without increasing any radio frequency chain. In this paper, DSM is investigated using two mapping algorithms: Look-Up Table Order (LUTO) and Permutation Method (PM). Then, the bit error rate (BER) performance and complexity of the two mapping algorithms in various antennas and modulation methods are verified by simulation experiments. The results show that PM has a lower BER than the LUTO mapping algorithm, and the latter has lower complexity than the former.

Keywords: spatial modulation (SM); multiple-input multiple-output (MIMO); Look-Up Table Order (LUTO); Permutation Method (PM); mapping algorithm

Citation (Format 1): WANG C F, CHAI J X, XU Y M. Differential spatial modulation mapping algorithms [J]. *ZTE Communications*, 2024, 22 (3): 116 - 122. DOI: 10.12142/ZTECOM.202403014

Citation (Format 2): C. F. Wang, J. X. Chai, and Y. M. Xu, "Differential spatial modulation mapping algorithms," *ZTE Communications*, vol. 22, no. 3, pp. 116 - 122, Sept. 2024. doi: 10.12142/ZTECOM.202403014.

1 Introduction

In order to enhance the transmission rate of wireless communications, various multi-antenna technologies have been proposed, among which spatial modulation (SM) technology^[1-2] has garnered widespread attention due to its innovative nature. As a novel digital modulation method, SM technology conveys additional information through the On/Off states of transmission antennas, achieving an effective balance between spectral efficiency and energy efficiency. This approach reduces the number of radio-frequency chains, thereby decreasing implementation costs, and finds extensive applications across various signal domains, such as frequency, time, code and angle domains. Recent comprehensive review papers^[3-4] have thoroughly delineated the fundamental principles, system design variants, and performance enhancement strategies of SM, providing crucial insights for understanding and advancing this technology. Concurrently, index modulation multiple access (IMMA), envisioned as an advanced technique for future 6G communications, is considered a novel extension of the traditional non-orthogonal multiple access (NOMA). It enhances spectral efficiency and energy efficiency and opti-

mizes system performance and massive connectivity capabilities. Relevant literature^[5-7] has delved deeply into the basic principles of IMMA and investigated its potential applications in various fields such as vehicular networks, reconfigurable intelligent surface (RIS)-aided networks, cooperative networks, and secure networks. Moreover, recent studies^[8-9] have explored the application of index modulation technology in new areas such as green Internet of things (IoT) and dual-hop OFDM relay systems, further highlighting its advantages in improving communication efficiency and performance. These developments not only underscore the significance of index modulation technology in modern wireless communication, but also pave new paths and provide perspectives for its future evolution.

Building on this progress, differential spatial modulation (DSM), an important advancement in spatial modulation techniques, has emerged to address challenges in high-speed channel streaming and complex channel estimation in SM^[10]. DSM introduces differential modulation in the time domain^[11], retaining the benefit of SM's single transmit antenna activation per time slot while effectively avoiding channel estimation^[12]. In a DSM system, the focus is on differential mapping coding at the transmitter^[13] and demodulation at the receiver^[14], with current research primarily directed towards mapping algorithms for antenna activation sequences and the development of efficient detection algorithms at the receiver^[15-17]. As the

This work is supported by the National Natural Science Foundation of China (NSFC) under Grant No. 62061024 and the Project of Gansu Province Science and Technology Department under Grant No. 22ZD6GA055.

number of transmit streams increases with the antennas and modulation sequences, the performance of the DSM system is impacted. To this end, a differential spatial modulation detector with low complexity has been proposed^[18], and algebraic differential spatial modulation has been explored^[19]. A new generalized DSM scheme improving data transmission rates through symbol interleaving techniques is introduced in Ref. [20]. For high mobility scenarios, a low-complexity detector that enhances performance in fast fading channels is proposed^[21], alongside a reordered amplitude phase-shift keying-assisted DSM scheme and a low-complexity detection algorithm^[22], significantly improving performance under fast fading conditions. Differing from previous studies, this paper focuses on the mapping algorithm of DSM^[23], elaborating on the design of the activation sequence for the look-up table order (LUTO) and permutation method (PM) and further designing a mapping table for LUTO when the number of transmit antennas is large. Our simulation validates that, in terms of the bit error rate (BER), PM slightly outperforms LUTO, with the extended PM algorithm showing a slight improvement in system performance compared to existing literature^[16]. Depending on system requirements, different mapping algorithms can be selected in practical applications.

The remainder of this paper is organized as follows. In Section 2, a brief review of a DSM system model is presented. Two mapping algorithms are described in Section 3 and complexity analysis is provided in Section 4. In Section 5, we present the simulation results. The conclusion is given in Section 6.

Notations are as follows: $(\cdot)^T$ and $\text{Tr}(\cdot)$ denote the transpose and trace of the matrix, respectively; $\text{Re}\{\cdot\}$ represents the real component of the argument; the complex number field is denoted with \mathbb{C} .

2 System Model

Consider a fundamental band DSM system with N_T transmit antennas and N_R receive antennas. At the transmitter, the information bits are divided into each of $\log_2(N_T!) + N_T \log_2(M)$ bits in a transmit block^[4] and are transmitted on N_T time slots, where M denotes the modulation order. Note that in the DSM system, the transmitting antennas and the length of a transmitted block is N_T . At the time of transmission duration T , the transmission matrix $\mathbf{S}_T \in \mathbb{C}^{N_r \times N_t}$ is

$$\mathbf{S}_T = \mathbf{S}_{T-1} \mathbf{X}_T, \quad (1)$$

where $\mathbf{X}_T \in \mathbb{C}^{N_r \times N_r}$ is the message matrices. Let $\mathbf{H}_T \in \mathbb{C}^{N_r \times N_r}$ represent the channel matrix. Then the received signal matrix $\mathbf{Y}_T \in \mathbb{C}^{N_r \times N_r}$ can be expressed as

$$\mathbf{Y}_T = \mathbf{H}_T \mathbf{S}_T + \mathbf{N}_T. \quad (2)$$

Assuming that the channel is a flat Rayleigh fading channel, we consider the channel is invariant between two consecu-

tive transmissions^[6], and then we have $\mathbf{H}_T = \mathbf{H}_{T-1}$. Therefore, Eq. (2) can be rewritten as

$$\mathbf{Y}_T = \mathbf{Y}_{T-1} \mathbf{X}_T - \mathbf{N}_{T-1} \mathbf{X}_T + \mathbf{N}_T. \quad (3)$$

The estimation of \mathbf{X}_T based on the maximum likelihood (ML) rule can be expressed as

$$\hat{\mathbf{X}}_T = \underset{\forall \mathbf{X} \in R_M}{\text{argmin}} \left\| \mathbf{Y}_T - \mathbf{Y}_{T-1} \mathbf{X}_T \right\|_F^2. \quad (4)$$

Thus, the optimal detector can be derived as

$$\hat{\mathbf{X}}_T = \underset{\forall \mathbf{X} \in R_M}{\text{argmax}} \text{Tr} \left\{ \text{Re} \left\{ \mathbf{Y}_T^H \mathbf{Y}_{T-1} \mathbf{X}_T \right\} \right\}, \quad (5)$$

where R_M denotes the set consisting of all effective information matrices. At last, the information bits are recovered by de-mapping the estimated antenna activation order. In the following, the mapping algorithms will be formulated.

3 Mapping Algorithms

3.1 LUTO

The LUTO algorithm is an efficient mapping method for matching data symbols to antenna combinations. Specifically, the antenna indices are divided into groups; each group contains several antenna indices, and each bit is used to select a group. The antenna indices within each group are arranged in a certain order, and the order among different groups can be customized as needed. To summarize, the implementation steps of the algorithm are as follows:

Step 1: Predefine an antenna combination mapping table corresponding to each data symbol;

Step 2: Convert the entered data symbols to the desired antenna combination;

Step 3: Map the antenna combinations and transmit the data symbols.

The signal matrix \mathbf{S}_{T+1} is calculated by Eq. (1). Examples of binary phase shift keying (BPSK) and differential transmission processes with $N_T=3$ are shown in Table 1.

Table 2 shows the mapping table for the LUTO algorithm when $N_T=3$. For further study, the matrix of all signals sent by the system is shown in Table 3 when the input bit stream is 00 with BPSK modulation. Normally, the number of table rows is $2^{\log_2(N_T!)}$, and the total number of the mapping schemes generated is $N_T!$. Therefore, part of mapping scheme would be dropped. The formula for discarding the number of mapping schemes can be expressed as

$$L = N_T! - 2^{\log_2(N_T!)}. \quad (6)$$

The table column is related to the modulation order, which is determined by the following steps.

Step 1: Generate the value of the bits to be entered;

▼Table 1. Differential transmission in differential spatial modulation (DSM) with binary phase shift keying (BPSK) modulation and $N_T = 3$

Index t	0	1	2	3
Time interval	0, 1, 2	3, 4, 5	6, 7, 8	9, 10, 11
Input bit	No information sent	01010	10100	11110
Map to X_t	No information sent	$\begin{bmatrix} -1 & & \\ & -1 & \\ & +1 & \end{bmatrix}$	$\begin{bmatrix} & +1 & \\ +1 & & \\ & & +1 \end{bmatrix}$	$\begin{bmatrix} & & -1 \\ +1 & & \\ & & +1 \end{bmatrix}$
Actual transmitted signal matrix S_t	$\begin{bmatrix} +1 & & \\ & +1 & \\ & & +1 \end{bmatrix}$	$\begin{bmatrix} -1 & & \\ & -1 & \\ & +1 & \end{bmatrix}$	$\begin{bmatrix} & -1 & \\ +1 & & \\ & & -1 \end{bmatrix}$	$\begin{bmatrix} & & -1 \\ -1 & & \\ & & -1 \end{bmatrix}$

▼Table 2. Mapping table of LUTO algorithm when $N_T = 3$

Input Bitstream	Antenna Activation Sequence	Block of Information to Send
00	(1, 2, 3)	$\begin{bmatrix} s_1 \\ s_2 \\ s_3 \end{bmatrix}$
01	(1, 3, 2)	$\begin{bmatrix} s_1 \\ s_3 \\ s_2 \end{bmatrix}$
10	(2, 1, 3)	$\begin{bmatrix} s_2 \\ s_1 \\ s_3 \end{bmatrix}$
11	(2, 3, 1)	$\begin{bmatrix} s_2 \\ s_3 \\ s_1 \end{bmatrix}$

▼ Table 3. Matrix of all signals sent with binary phase shift keying (BPSK) modulation and $N_T = 3$ when input bit D is 00

Input Bits	Time Interval 1		Time Interval 2		Time Interval 3		Transmitted Signal Matrix
	Antenna Index	Symbol	Antenna Index	Symbol	Antenna Index	Symbol	
00000	1	-1	2	-1	3	-1	$\begin{bmatrix} -1 & & \\ & -1 & \\ & & -1 \end{bmatrix}$
00001	1	-1	2	-1	3	+1	$\begin{bmatrix} -1 & & \\ & -1 & \\ & & +1 \end{bmatrix}$
00010	1	-1	2	+1	3	-1	$\begin{bmatrix} -1 & & \\ & +1 & \\ & & -1 \end{bmatrix}$
00011	1	-1	2	+1	3	+1	$\begin{bmatrix} -1 & & \\ & +1 & \\ & & +1 \end{bmatrix}$
00100	1	+1	2	+1	3	+1	$\begin{bmatrix} +1 & & \\ & +1 & \\ & & +1 \end{bmatrix}$
00101	1	+1	2	+1	3	-1	$\begin{bmatrix} +1 & & \\ & +1 & \\ & & -1 \end{bmatrix}$
00110	1	+1	2	-1	3	+1	$\begin{bmatrix} +1 & & \\ & -1 & \\ & & +1 \end{bmatrix}$
00111	1	+1	2	-1	3	-1	$\begin{bmatrix} +1 & & \\ & -1 & \\ & & -1 \end{bmatrix}$

Step 2: Derive the maximum binary number from the 0/1 bit sequence based on the input bit value;

Step 3: Convert the maximum binary number to a decimal number;

Step 4: Add one to the resulting decimal number to determine the size of the table column.

As shown in Tables 4 and 5, the antenna activation sequence is given when $N_T = 4$ and $N_T = 5$. When $N_T = 4$, there are $N_T! = 4! = 24$ antenna activation sequences. From Eq. (6), it can be seen that among the 24 antenna activation orders, there will be eight antenna selection options not selected. The last eight of all schemes are generally discarded. The selected mapping scheme is represented by the set $D = \{D_0, D_1, \dots, D_{15}\} = \{(1,2,3,4), (1,2,4,3), (1,3,2,4), (1,3,4,2), (1,4,2,3), (1,4,3,2), (2,1,3,4), (2,1,4,3), (2,3,1,4), (2,3,4,1), (2,4,1,3), (2,4,3,1), (3,1,2,4), (3,1,4,2), (3,2,1,4), (3,2,4,1)\}$. Based on the formula $N_T \log_2(M) = 4 \log_2(2) = 4$, a four-bit sequence is obtained. Converting the largest sequence 1111 to decimal and adding one yields a table with 16 columns. Define that U represents the full modulation symbol mapping scheme. Then, a permutation combination is obtained as $U = \{(-1, -1, -1, -1), (-1, -1, -1, +1), (-1, -1, +1, -1), (-1, -1, +1, +1), (-1, +1, -1, -1), (-1, +1, -1, +1), (-1, +1, +1, -1), (-1, +1, +1, +1), (+1, -1, -1, -1), (+1, -1, -1, +1), (+1, -1, +1, -1), (+1, -1, +1, +1), (+1, +1, -1, -1), (+1, +1, -1, +1), (+1, +1, +1, -1), (+1, +1, +1, +1)\}$. Set $D = \{D_0, D_1, \dots, D_{63}\} = \{(1,2,3,4,5), (1,2,3,5,4), (1,2,4,3,5), (1,2,4,5,3), (1,2,5,3,4), (1,2,5,4,3), (1,3,2,4,5), (1,3,2,5,4), (1,3,4,2,5), (1,3,4,5,2), (1,3,5,2,4), (1,3,5,4,2), (1,4,2,3,5), (1,4,2,5,3), (1,4,3,2,5), (1,4,3,5,2), (1,4,5,2,3), (1,4,5,3,2), (1,5,2,3,4), (1,5,2,4,3), (1,5,3,2,4), (1,5,3,4,2), (1,5,4,2,3), (1,5,4,3,2), (2,1,3,4,5), (2,1,3,4,5), (2,1,3,5,4), (2,1,4,3,5), (2,1,4,5,3), (2,1,5,3,4), (2,1,5,4,3), (2,3,1,4,5), (2,3,1,5,4), (2,3,4,1,5), (2,3,4,5,1), (2,3,5,1,4), (2,3,5,4,1), (2,4,1,3,5), (2,4,1,5,3), (2,4,3,1,5), (2,4,3,5,1), (2,4,5,1,3), (2,4,5,3,1), (2,5,1,3,4), (2,5,1,4,3), (2,5,3,1,4), (2,5,3,4,1), (2,5,4,1,3), (2,5,4,3,1), (3,1,2,4,5), (3,1,2,5,4), (3,1,4,2,5), (3,1,4,5,2), (3,1,5,4,2), (3,1,5,2,4), (3,2,1,4,5), (3,2,1,5,4), (3,2,4,1,5), (3,2,4,5,1), (3,2,5,2,4), (3,2,5,4,1), (3,4,2,1,5), (3,4,2,5,1), (3,4,5,1,2)\}$.

From Eq. (6), it can be seen that by bringing $N_T = 5$ into $5! - 2^{\log_2(5!)} = 56$, there are 56 antenna activation sequences that will not be selected. Set U is arranged in the same way as $N_T = 4$. For $N_T = 4, 5$, each information block carries 8 and 11 data bits in the BPSK scheme of LUTO, respectively. It can be seen that as N_T and M increase, the transmission efficiency

▼Table 4. All the signal schemes of Look-Up Table Order (LUTO) with binary phase shift keying (BPSK) modulation and $N_T = 4$

		U										
		U_0	U_1	U_2	U_3	...	U_6	U_7	...	U_{13}	U_{14}	U_{15}
D	D_0	00000000	00000001	00000010	00000011	...	00000110	00000111	...	00001101	00001110	00001111
	D_1	00010000	00010001	00010010	00010011	...	00010110	00010111	...	00011101	00011110	00011111
	D_2	00100000	00100001	00100010	00100011	...	00100110	00100111	...	00101101	00101110	00101111

	D_6	01100000	01100001	01100010	01100011	...	01100110	01100111	...	01101101	01101110	01101111
	D_7	01110000	01110001	01110010	01110011	...	01110110	01110111	...	01111101	01111110	01111111

	D_{13}	11000000	11000001	11000010	11000011	...	11000110	11000111	...	11001101	11001110	11001111
	D_{14}	11010000	11010001	11010010	11010011	...	11010110	11010111	...	11011101	11011110	11011111
	D_{15}	11110000	11110001	11110010	11110011	...	11110110	11110111	...	11111101	11111110	11111111

▼Table 5. All the signal schemes of Look-Up Table Order (LUTO) with binary phase shift keying (BPSK) modulation and $N_T = 5$

		U									
		U_0	U_1	U_2	...	U_{14}	U_{15}	...	U_{29}	U_{30}	U_{31}
D	D_0	0000000000	0000000001	0000000010	...	0000000110	0000000111	...	0000001101	0000001110	0000001111
	D_1	0000010000	0000010001	0000010010	...	0000010110	0000010111	...	0000011101	0000011110	0000011111
	D_2	0000100000	0000100001	0000100010	...	0000100110	0000100111	...	0000101101	0000101110	0000101111

	D_{14}	0011100000	0011100001	0011100010	...	0011100110	0011100111	...	0011101101	0011101110	0011101111
	D_{15}	0011110000	0011110001	0011110010	...	0011110110	0011110111	...	0011111101	0011111110	0011111111

	D_{30}	0111100000	0111100001	0111100010	...	0111100110	0111100111	...	0111101101	0111101110	0111101111
	D_{31}	0111110000	0111110001	0111110010	...	0111110110	0111110111	...	0111111101	0111111110	0111111111

	D_{61}	1111010000	1111010001	1111010010	...	1111010110	1111010111	...	1111011101	1111011110	1111011111
	D_{62}	1111100000	1111100001	1111100010	...	1111100110	1111100111	...	1111101101	1111101110	1111101111
D_{63}	1111110000	1111110001	1111110010	...	1111110110	1111110111	...	1111111101	1111111110	1111111111	

increases. The table size is $16 \times 16 = 256$ when $N_T = 4$. When $N_T = 5$, the table size is $32 \times 64 = 2048$. As the transmitting antennas increase by one, the size of the table increases by 1792 cells. Specifically, the size of the table increases exponentially with the transmitting antennas.

3.2 Permutation Method

From the previous subsection, it can be seen that the LUTO is not applicable to the case where the number of transmitting antennas is large. Thus, PM is introduced. This method forms a point-to-point mapping by permuting the order of N_R numbers. First, an integer m is mapped into a sequence, $a^{(m)} = (a_1^{(m)}, \dots, a_N^{(m)})$, which is a set of permutations $\{1, \dots, N_R\}$. For N_R , $m \in [0, N_R! - 1]$ can be represented as a sequence $a^{(m)}$ of length N_R . In short, the algorithm is implemented as follows.

Step 1: The input sequence is converted to an integer m .

Step 2: Integer m is converted to the sequence $b^m = (b_1^m, \dots, b_{N_1}^m)$, and the conversion is shown as

$$m = b_1^m (N_R - 1)! + \dots + b_{N_T}^m 0! \quad (7)$$

Take the largest b_1^m satisfying $b_1^m (N_1 - 1) \leq n_1$, and continue to find b_2^m satisfying $b_2^m (N_T - 2)! \leq m - b_1^m (N_T - 1)!$. And then all the b^m elements are computed in turn.

Step 3: the factorial sequence b^m is mapped into the arrangement $a^{(m)}$. Here $\Theta = (1, 2, \dots, N_R)$ is defined as an ordered list, its first element index is 0, and the formula for converting b^m to $a^{(m)}$ is shown as

$$a_i^m = \Theta_{b_i^m}, \quad 1 \leq i \leq N_T \quad (8)$$

so that the element $\Theta_{b_i^m}$ will be removed from list 1, and then each element of $a^{(m)}$ is obtained in a recursive way.

4 Complexity Analysis

The experimental platform utilizes the Windows 10 operating system, the programming environment is MATLAB 2016, and the CPU employed is an Intel Core i9-13900. Specifically, these configurations are detailed in Table 6.

Table 7 compares the program running times of the PM al-

▼Table 6. Configuration of the test host

CPU Type	Core Count	Thread Count	Core Types	Performance-Core Frequency	RAM
Core i9-13900	24	32	Alder Lake (12-th generation)	2.00 GHz	32 GB

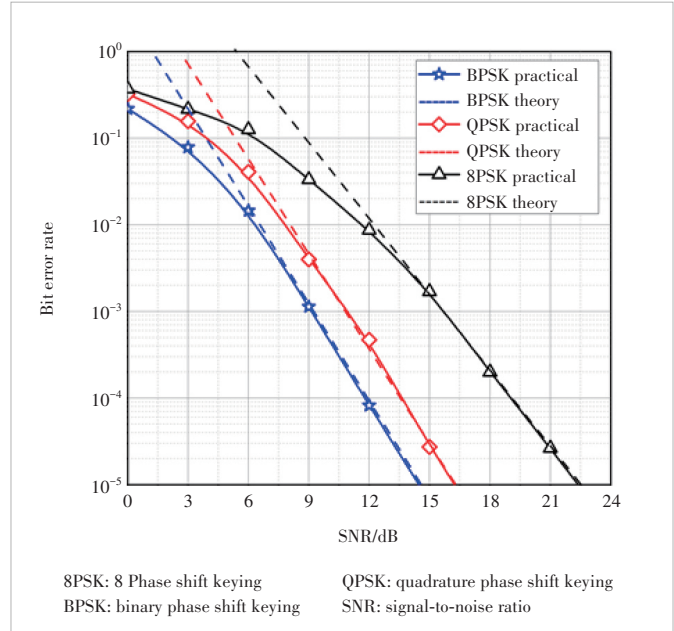
▼Table 7. Performance test results

Test Items	Program Running Time/s	Test Items	Program Running Time/s
PM BPSK $N_T = 3 N_R = 1$	6.76	LUTO BPSK $N_T = 3 N_R = 1$	4.47
PM BPSK $N_T = 3 N_R = 2$	112.95	LUTO BPSK $N_T = 3 N_R = 2$	30.45
PM BPSK $N_T = 3 N_R = 3$	213.68	LUTO BPSK $N_T = 3 N_R = 3$	67.37
PM QPSK $N_T = 3 N_R = 1$	15.01	LUTO QPSK $N_T = 3 N_R = 1$	5.47
PM QPSK $N_T = 3 N_R = 2$	363.52	LUTO QPSK $N_T = 3 N_R = 2$	46.82
PM QPSK $N_T = 3 N_R = 3$	816.58	LUTO QPSK $N_T = 3 N_R = 3$	89.67
PM 8PSK $N_T = 3 N_R = 1$	44.54	LUTO 8PSK $N_T = 3 N_R = 1$	11.59
PM 8PSK $N_T = 3 N_R = 2$	370.16	LUTO 8PSK $N_T = 3 N_R = 2$	41.83
PM 8PSK $N_T = 3 N_R = 3$	1 969.85	LUTO 8PSK $N_T = 3 N_R = 3$	375.57
PM BPSK $N_T = 4 N_R = 1$	24.26	LUTO BPSK $N_T = 3 N_R = 1$	20.51
PM BPSK $N_T = 4 N_R = 2$	472.79	LUTO BPSK $N_T = 4 N_R = 2$	249.37
PM BPSK $N_T = 4 N_R = 3$	962.76	LUTO BPSK $N_T = 4 N_R = 3$	334.52
PM BPSK $N_T = 4 N_R = 4$	1 145.05	LUTO BPSK $N_T = 4 N_R = 4$	481.76
PM QPSK $N_T = 4 N_R = 1$	249.45	LUTO QPSK $N_T = 4 N_R = 1$	173.50
PM 8PSK $N_T = 4 N_R = 1$	1 323.63	LUTO 8PSK $N_T = 4 N_R = 1$	625.83
PM BPSK $N_T = 5 N_R = 1$	127.07	LUTO BPSK $N_T = 5 N_R = 1$	96.36
PM QPSK $N_T = 5 N_R = 1$	1 981.00	LUTO QPSK $N_T = 5 N_R = 1$	896.64
PM 8PSK $N_T = 5 N_R = 1$	56 551.78	LUTO 8PSK $N_T = 5 N_R = 1$	15 637.95

8PSK: 8 Phase shift keying
 BPSK: binary phase shift keying
 LUTO: Look-Up Table Order

PM: Permutation Method
 QPSK: quadrature phase shift keying

gorithm and the LUTO algorithm under different conditions. From the table, it is evident that the LUTO algorithm outperforms the PM algorithm in terms of running time. This advantage becomes more pronounced as the number of antennas and the level of modulation order increase. This is because when the number of transmitting antennas is small, the LUTO algorithm does not incur any additional time complexity. However, as the number of antennas grows, the space complexity required by the LUTO algorithm increases exponentially. The PM algorithm, which converts the input bit stream into a signal matrix without using lookup tables, significantly reduces spatial complexity.



▲ Figure 1. Simulation and theoretical results of Look-Up Table Order (LUTO) with $N_T = 4$ and $N_R = 4$

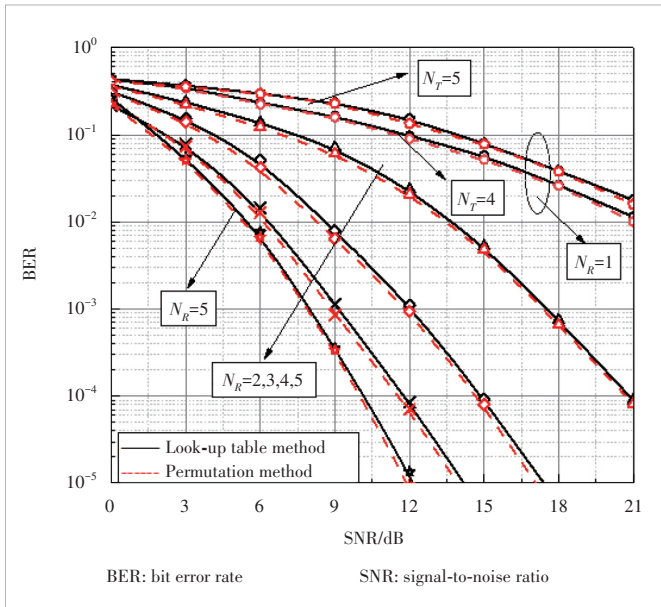
5 Simulation Results and Discussion

In this section, we simulate and evaluate the BER performance of the DSM. The quasi-static Rayleigh flat fading channel is used in the experiments.

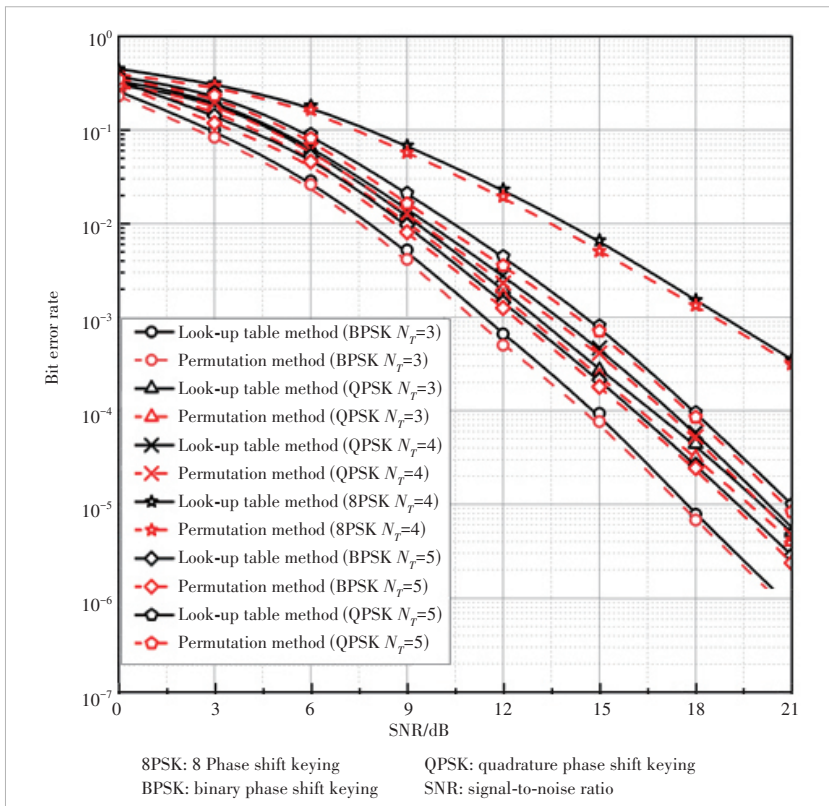
Fig. 1 gives the theoretical and simulation results of the LUTO for BPSK, QPSK and 8PSK modulation in DSM systems. It shows the performance of the DSM system when $N_T = 4$ and $N_R = 4$. It can be seen that the higher the order of symbol modulation, the higher the data rate of the DSM system transmits.

Fig. 2 gives the comparative results of BER performance of DSM with $N_T = 4, 5$ and $N_R = 1, 2, 3, 4, 5$ for PM and LUTO under BPSK modulation. At $BER = 10^{-1}$, it can be seen that the SNR gain of the PM is slightly better than that of the LUTO for $N_R = 1, N_T = 4$ and $N_T = 5$. As the number of receiving antennas increases, the SNR gain of the PM gradually increases. The simulations show that the system performance is affected by the number of transmitting antennas. As the transmitting antenna number increases, the diversity gain increases.

Fig. 3 gives the BER performance of PM and LUTO in DSM with different modulations for $N_T = 3, 4, 5, N_R = 3$. When $N_T = 4$, there is roughly a 5.9 dB SNR loss at $BER = 10^{-3}$ for 8PSK compared to QPSK modulation. When $N_T = 5$, there is roughly 2.4 dB SNR loss for QPSK modulation compared to BPSK modulation at $BER = 10^{-3}$.



▲ Figure 2. BER performance of DSM with Permutation Method (PM) and Look-Up Table Order (LUTO) with BPSK modulation



▲ Figure 3. Simulation and theoretical results of the system with different modulation for different differential spatial modulation (DSM) with $N_r = 3$

6 Conclusions

In this paper, the design of DSM's mapping algorithms, LUTO and PM, particularly when used with a high number of antennas, is further expanded upon. A detailed description

and performance analysis of these two mapping algorithms are presented. Simulation results show that the PM algorithm is slightly better than the LUTO algorithm in terms of BER, although its implementation is more complicated. The LUTO algorithm, on the other hand, is relatively simple but requires additional lookup table storage space. The selection of the appropriate method should be based on the specific situation.

References

- [1] DI RENZO M, HAAS H, GRANT P M. Spatial modulation for multiple-antenna wireless systems: A survey [J]. *IEEE communications magazine*, 2011, 49(12): 182 – 191. DOI: 10.1109/MCOM.2011.6094024
- [2] MESLEH R Y, HAAS H, SINANOVIC S, et al. Spatial modulation [J]. *IEEE transactions on vehicular technology*, 2008, 57(4): 2228 – 2241. DOI: 10.1109/TVT.2007.912136
- [3] WEN M W, ZHENG B X, KIM K J, et al. A survey on spatial modulation in emerging wireless systems: Research progresses and applications [J]. *IEEE journal on selected areas in communications*, 2019, 37(9): 1949 – 1972. DOI: 10.1109/JSAC.2019.2929453
- [4] LI J, DANG S P, WEN M W, et al. Index modulation multiple access for 6G communications: Principles, applications, and challenges [J]. *IEEE network*, 2023, 37(1): 52 – 60. DOI: 10.1109/MNET.002.2200433
- [5] LI J, DANG S P, YAN Y E, et al. Generalized quadrature spatial modulation and its application to vehicular networks with NOMA [J]. *IEEE transactions on intelligent transportation systems*, 2021, 22(7): 4030 – 4039. DOI: 10.1109/TITS.2020.3006482
- [6] LI J, DANG S P, HUANG Y, et al. Composite multiple-mode orthogonal frequency division multiplexing with index modulation [J]. *IEEE transactions on wireless communications*, 2023, 22(6): 3748 – 3761. DOI: 10.1109/TWC.2022.3220752
- [7] WEN M W, LI J, DANG S P, et al. Joint-mapping orthogonal frequency division multiplexing with subcarrier number modulation [J]. *IEEE transactions on communications*, 2021, 69(7): 4306 – 4318. DOI: 10.1109/TCOMM.2021.3066584
- [8] WEN M W, LIN S E, KIM K J, et al. Cyclic delay diversity with index modulation for green Internet of Things [J]. *IEEE transactions on green communications and networking*, 2021, 5(2): 600 – 610. DOI: 10.1109/TGCN.2021.3067705
- [9] WEN M W, CHEN X, LI Q, et al. Index modulation aided subcarrier mapping for dual-hop OFDM relaying [J]. *IEEE transactions on communications*, 2019, 67(9): 6012 – 6024. DOI: 10.1109/TCOMM.2019.2920642
- [10] JEGANATHAN J, CHRAYEB A, SZCZECINSKI L. Spatial modulation: optimal detection and performance analysis [J]. *IEEE communications letters*, 2008, 12(8): 545 – 547. DOI: 10.1109/LCOMM.2008.080739
- [11] BIAN Y Y, WEN M W, CHENG X, et al. A differential scheme for Spatial Modulation [C]//*Proc. IEEE Global Communications Conference (GLOBECOM)*. IEEE, 2013: 3925 – 3930. DOI: 10.1109/GLOCOM.2013.6831686
- [12] ISHIKAWA N, SUGIURA S. Unified differential spatial modulation [J]. *IEEE wireless communications letters*, 2014, 3(4): 337 – 340. DOI: 10.1109/LWC.2014.2315635

- [13] BIAN Y Y, CHENG X, WEN M W, et al. Differential spatial modulation [J]. IEEE transactions on vehicular technology, 2015, 64(7): 3262 – 3268. DOI: 10.1109/TVT.2014.2348791
- [14] LI J, WEN M W, CHENG X, et al. Differential spatial modulation with gray coded antenna activation order [J]. IEEE communications letters, 2016, 20(6): 1100 – 1103. DOI: 10.1109/LCOMM.2016.2557801
- [15] ZHANG M, WEN M W, CHENG X, et al. A dual-hop virtual MIMO architecture based on hybrid differential spatial modulation [J]. IEEE transactions on wireless communications, 2016, 15(9): 6356 – 6370. DOI: 10.1109/TWC.2016.2583423
- [16] RAJASHEKAR R, XU C, ISHIKAWA N, et al. Algebraic differential spatial modulation is capable of approaching the performance of its coherent counterpart [J]. IEEE transactions on communications, 2017, 65(10): 4260 – 4273. DOI: 10.1109/TCOMM.2017.2720170
- [17] XU C, WANG L, NG S X, et al. Soft-decision multiple-symbol differential sphere detection and decision-feedback differential detection for differential QAM dispending with channel estimation in the face of rapidly fading channels [J]. IEEE transactions on wireless communications, 2016, 15(6): 4408 – 4425. DOI: 10.1109/TWC.2016.2541665
- [18] WEI R Y, TSAI Y W, CHEN S L. Improved schemes of differential spatial modulation [J]. IEEE access, 2021, 9: 97120 – 97128. DOI: 10.1109/ACCESS.2021.3095531
- [19] WEN M W, CHENG X, BIAN Y Y, et al. A low-complexity near-ML differential spatial modulation detector [J]. IEEE signal processing letters, 2015, 22(11): 1834 – 1838. DOI: 10.1109/LSP.2015.2425042
- [20] WEI R Y, CHEN S L, LIN Y H, et al. Bandwidth-efficient generalized differential spatial modulation [J]. IEEE transactions on vehicular technology, 2023, 72(1): 601 – 610. DOI: 10.1109/TVT.2022.3202912
- [21] XIU H T, YU D Z, GAO P Y, et al. An enhanced system model for differential spatial modulation system under fast fading channels and a corresponding DFDD based low-complexity detector [J]. IEEE transactions on vehicular technology, 2024, 73(2): 2227 – 2235. DOI: 10.1109/TVT.2023.3316275
- [22] YANG L, XIU H T, YU D Z, et al. Reordered amplitude phase shift keying aided differential spatial modulation: DFDD-based low-complexity detector and performance analysis over fading channels [J]. IEEE transactions on wireless communications, 2022, 21(10): 7913 – 7925. DOI: 10.1109/TWC.2022.3162834
- [23] WEI R Y. Differential encoding by a look-up table for quadrature-amplitude modulation [J]. IEEE transactions on communications, 2011, 59(1): 84 – 94. DOI: 10.1109/TCOMM.2010.102910.100061

Biographies

WANG Chanfei (wangchanfei@163.com) received her MS degree in communication and information systems from Lanzhou University of Technology, China in 2008 and PhD degree from Beijing University of Posts and Telecommunications (BUPT), China in 2016. She is currently an associate professor and a master's degree supervisor with the College of Computer and Communication, Lanzhou University of Technology. Her research interest is signal detection in communication system.

CHAI Jianxin is currently pursuing his master's degree in the Department of Communication Engineering, Lanzhou University of Technology, China. His research interests include differential spatial modulation and signal detection and estimation.

XU Yamei received her PhD degree from Xidian University, China. She is currently an associate professor and the master's degree supervisor with the College of Computer and Communication, Lanzhou University of Technology, China. Her research interest is pattern recognition.

The 1st Youth Expert Committee

for Promoting Industry-University-Institute Cooperation

Director CHEN Wei, Beijing Jiaotong University
Deputy Director QIN Xiaoqi, Beijing University of Posts and Telecommunications
LU Dan, ZTE Corporation

Members (Surname in Alphabetical Order)

CAO Jin Xidian University
CHEN Li University of Science and Technology of China
CHEN Qimei Wuhan University
CHEN Shuyi Harbin Institute of Technology
CHEN Siheng Shanghai Jiao Tong University
CHEN Wei Beijing Jiaotong University
GUAN Ke Beijing Jiaotong University
HAN Kaifeng China Academy of Information and Communications Technology
HE Zi Nanjing University of Science and Technology
HOU Tianwei Beijing Jiaotong University
HU Jie University of Electronic Science and Technology of China
HUANG Chen Purple Mountain Laboratories
LI Ang Xi'an Jiaotong University
LIU Chunsen Fudan University
LIU Fan Southern University of Science and Technology
LIU Junyu Xidian University
LU Dan ZTE Corporation
LU Youyou Tsinghua University
NING Zhaolong Chongqing University of Posts and Telecommunications
QI Liang Shanghai Jiao Tong University
QIN Xiaoqi Beijing University of Posts and Telecommunications
QIN Zhijin Tsinghua University
SHI Yinghuan Nanjing University
TANG Wankai Southeast University
WANG Jingjing Beihang University
WANG Xinggang Huazhong University of Science and Technology
WANG Yongqiang Tianjin University
WEN Miaowen South China University of Technology
WU Qingqing Shanghai Jiao Tong University
WU Yongpeng Shanghai Jiao Tong University
XIA Wenchao Nanjing University of Posts and Telecommunications
XU Mengwei Beijing University of Posts and Telecommunications
XU Tianheng Shanghai Advanced Research Institute, Chinese Academy of Sciences
YANG Chuanchuan Peking University
YIN Haifan Huazhong University of Science and Technology
YU Jihong Beijing Institute of Technology
ZHANG Jiao Beijing University of Posts and Telecommunications
ZHANG Yuchao Beijing University of Posts and Telecommunications
ZHANG Jiayi Beijing Jiaotong University
ZHAO Yuda Zhejiang University
ZHAO Zhongyuan Beijing University of Posts and Telecommunications
ZHOU Yi Southwest Jiaotong University
ZHU Bingcheng Southeast University

ZTE COMMUNICATIONS

中兴通讯技术(英文版)

ZTE Communications has been indexed in the following databases:

- Abstract Journal
- Cambridge Scientific Abstracts (CSA)
- China Science and Technology Journal Database
- Chinese Journal Fulltext Databases
- Index Copernicus
- Scopus
- Ulrich's Periodicals Directory
- Wanfang Data
- WJCI 2021-2023

Industry Consultants:

DUAN Xiangyang, GAO Yin, HU Liujun, HUA Xinhai, LIU Xinyang, LU Ping, SHI Weiqiang, TU Yaofeng, WANG Huitao, XIONG Xiankui, ZHAO Yajun, ZHAO Zhiyong, ZHU Xiaoguang

ZTE COMMUNICATIONS

Vol. 22 No. 3 (Issue 88)

Quarterly

First Issue Published in 2003

Supervised by:

Anhui Publishing Group

Sponsored by:

Time Publishing and Media Co., Ltd.

Shenzhen Guangyu Aerospace Industry Co., Ltd.

Published by:

Anhui Science & Technology Publishing House

Edited and Circulated (Home and Abroad) by:

Magazine House of ZTE Communications

Staff Members:

General Editor: WANG Xiyu

Editor-in-Chief: WANG Li

Executive Editor-in-Chief: HUANG Xinming

Editorial Director: LU Dan

Editor-in-Charge: ZHU Li

Editors: REN Xixi, XU Ye, YANG Guangxi

Producer: XU Ying

Circulation Executive: WANG Pingping

Assistant: WANG Kun

Editorial Correspondence:

Add: 12F Kaixuan Building, 329 Jinzhai Road,

Hefei 230061, P. R. China

Tel: +86-551-65533356

Email: magazine@zte.com.cn

Website: <http://zte.magtechjournal.com>

Annual Subscription: RMB 120

Printed by:

Hefei Tiancai Color Printing Company

Publication Date: September 25, 2024

China Standard Serial Number: ISSN 1673-5188
CN 34-1294/TN